Characterization of Point Contact Germanium Detectors and Development of Signal Readout Electronics for LEGEND

Frank Edzards

Max Planck Institute for Physics
Technical University of Munich

MAX PLANCK INSTITUTE FOR PHYSICS

CHARACTERIZATION OF POINT CONTACT GERMANIUM DETECTORS AND DEVELOPMENT OF SIGNAL READOUT ELECTRONICS FOR LEGEND

FRANK ARNE EDZARDS

Vollständiger Abdruck der von der Fakultät für Physik

der Technischen Universität München

zur Erlangung des akademischen Grades

Doktor der Naturwissenschaften (Dr. rer. nat.)

genehmigten Dissertation.

Vorsitzender:
apl. Prof. Dr. Norbert Kaiser

Prüfer der Dissertation:
1. Prof. Dr. Susanne Mertens
2. Prof. Dr. Lothar Oberauer

Die Dissertation wurde am 05.05.2021 bei der Technischen Universität München eingereicht und durch die Fakultät für Physik am 12.07.2021 angenommen.

ABSTRACT

The Large Enriched Germanium Experiment for Neutrinoless ββ Decay, LEGEND, is a tonne-scale experimental program to search for neutrinoless double beta ($0\nu\beta\beta$) decay in the isotope ^{76}Ge with an unprecedented sensitivity. Building on the success of the low-background ^{76}Ge-based GERDA and MAJORANA DEMONSTRATOR experiments, the LEGEND collaboration is targeting a signal discovery sensitivity beyond 10^{28} yr on the decay half-life with approximately $10\,\mathrm{t}\cdot\mathrm{yr}$ of exposure. An essential prerequisite to achieve this ambitious goal is the reduction of backgrounds.

In the first phase of the experiment, LEGEND-200, alpha- and beta-induced surface backgrounds are anticipated to be among the dominant contributions. The investigation of these backgrounds is one of the main objectives of this work. To this end, the response of a p-type point contact germanium detector to alpha and beta particles is studied in detail. It is shown that the passivated detector surface is prone to effects such as charge build-up leading to a radial-dependent behavior of important pulse shape parameters. The validity of the surface charge model is verified in dedicated pulse shape simulations.

Another important role to enhance the experiment's sensitivity plays signal readout electronics. The readout system needs to be placed as close as possible to the detectors to reduce the electronic noise and to enable the application of background rejection analysis techniques. However, the proximity also poses unique challenges for the radiopurity of the electronics. In LEGEND-200, an improved charge sensitive amplifier based on implementations by the predecessor experiments, GERDA and MAJORANA DEMONSTRATOR, that fulfills the requirements will be used. Within this work, data of a first full chain integration test are analyzed. It is shown that the novel readout system features an excellent performance.

For the final stage of the experiment, LEGEND-1000, backgrounds must be decreased even further. To reduce the component originating from the signal readout electronics, the use of an application-specific integrated circuit (ASIC) amplifier located very close to the detector is foreseen. ASIC technology allows the implementation of the entire amplifier into a single low-mass, low-background chip while maintaining the spectral and noise performance achieved with conventional solutions. In this work, the feasibility of operating a large-scale germanium detector with a commercially available readout ASIC is demonstrated. It is shown that an excellent performance exceeding the requirements can be obtained. Finally, a first prototype of an ASIC specifically developed to meet the demands of LEGEND-1000 is characterized.

ZUSAMMENFASSUNG

Das Large Enriched Germanium Experiment for Neutrinoless ββ Decay, LEGEND, ist ein experimentelles Programm im Tonnenmaßstab, das nach dem neutrinolosen doppelten Betazerfall ($0\nu\beta\beta$) im Isotop ^{76}Ge mit bisher unerreichter Sensitivität suchen wird. Aufbauend auf dem Erfolg der Vorgängerexperimente, GERDA und MAJORANA DEMONSTRATOR, setzt sich die LEGEND Kollaboration eine Signalsensitivtät größer als 10^{28} Jahre bezogen auf die Halbwertszeit des Zerfalls für eine Exposition von etwa $10\,\mathrm{t}\cdot\mathrm{yr}$ zum Ziel. Eine wesentliche Voraussetzung, um dieses ambitionierte Ziel zu erreichen, ist die Reduzierung des Untergrunds.

In der ersten Phase des Experiments, LEGEND-200, werden Alpha- und Beta-induzierte Oberflächenuntergründe zu den dominierenden Beiträgen gehören. Eines der Hauptziele dieser Arbeit ist die Untersuchung dieser Untergründe. Hierfür wird das Verhalten eines p-Typ Punktkontakt-Germaniumdetektors in Bezug auf Alpha- und Beta-Teilchen im Detail untersucht. Die Messungen zeigen, dass die passivierte Detektoroberfläche anfällig für Effekte wie Oberflächenaufladung ist, was in einer radialen Abhängigkeit wichtiger Pulsformparameter resultiert. Die Gültigkeit des Oberflächenladungsmodells wird mittels Pulsformsimulationen validiert.

Eine weitere wichtige Rolle zur Steigerung der experimentellen Sensitivität spielt die Auslese-elektronik. Das Auslesesystem muss so nah wie möglich an den Detektoren platziert werden, um das elektronische Rauschen zu reduzieren und die Anwendung von Analysemethoden zur Untergrundreduzierung zu ermöglichen. Allerdings stellt diese Nähe auch spezielle Anforderungen an die radioaktive Reinheit der Elektronik. In LEGEND-200 wird ein verbesserter Ladungsverstärker basierend auf Implementierungen der Vorgängerexperimente, GERDA und MAJORANA DEMONSTRATOR, verwendet, der diese Anforderungen erfüllt. Im Rahmen dieser Arbeit werden Daten eines ersten Integrationstests mit vollständigem Signalpfad analysiert. Es wird gezeigt, dass das neue Auslesesystem eine exzellente Leistung aufweist.

Für die finale Phase des Experiments, LEGEND-1000, müssen die Untergründe noch weiter verringert werden. Um den von der Ausleseelektronik stammenden Anteil zu reduzieren, ist die Verwendung eines Verstärkers basierend auf einer anwendungsspezifischen integrierten Schaltung (ASIC) vorgesehen, der in unmittelbarer Nähe zum Detektor platziert wird. Die ASIC-Technologie ermöglicht die Implementierung des gesamten Verstärkers in einem einzigen Chip mit geringer Masse und niedrigem Untergrund unter Beibehaltung der spektralen Leisung, die mit herkömmlichen Verstärkern erzielt wird. Im Rahmen dieser Arbeit wird demonstriert, dass das Auslesen eines Germaniumdetektors mit einem kommerziell erhältlichen ASIC praktikabel ist. Es wird gezeigt, dass eine exzellente, die Anforderungen übertreffende Leistung erreicht werden kann. Abschließend wird ein erster ASIC-Prototyp charakterisiert, der speziell entwickelt wurde, um die Anforderungen von LEGEND-1000 zu erfüllen.

PUBLICATIONS

Part of the results obtained within the framework of this thesis were already published in scientific journals and are publicly available:

CORRESPONDING AUTHOR, PEER REVIEWED

F. Edzards *et al.*: *Development of signal readout electronics for LEGEND-1000.* J. Phys. Conf. Ser., Vol. 1468, 2020. doi:10.1088/1742-6596/1468/1/012114

F. Edzards *et al.*: *Investigation of ASIC-based signal readout electronics for LEGEND-1000.* J. Instr., Vol. 15, 2020. doi:10.1088/1748-0221/15/09/P09022

F. Edzards (for the LEGEND collaboration): *The Future of Neutrinoless Double Beta Decay Searches with Germanium Detectors.* J. Phys. Conf. Ser., Vol. 1690, 2020. doi:10.1088/1742-6596/1690/1/012180

F. Edzards *et al.*: *Surface characterization of p-type point contact germanium detectors.* 2021. arXiv:2105.14487

No one who achieves success does so without acknowledging the help of others. The wise and confident acknowledge this help with gratitude.

— Alfred N. Whitehead

ACKNOWLEDGMENTS

The completion of this thesis could not have been possible without the participation and assistance of many people. Their contributions are sincerely appreciated and gratefully acknowledged.

SUSANNE MERTENS I would like to express my sincere gratitude to you for giving me the unique opportunity to work in the highly interesting field of neutrino physics. I am deeply indebted to you for your stimulating suggestions, constant encouragement and guidance that helped me in all the time of research of this thesis. You were the one who inspired me to see and do things I never thought possible. I highly appreciate leaving me the freedom to test and develop new ideas.

DAVID C. RADFORD I would like to thank you for countless interesting and extremely helpful discussions, and for improving my comprehension of germanium detectors considerably. Your help to better understand PPC detector surface effects was indispensable. Moreover, I highly acknowledge your support in pulse shape simulations using `Siggen`. I appreciate your very motivating nature!

MICHAEL WILLERS I am very grateful to you for being a great and patient supervisor during my research stays at Berkeley Lab. I would also like to thank you for improving my hardware expertise considerably, for our efficient cooperation in writing the manuscript on signal readout electronics, and for proofreading parts of this thesis.

BJÖRN LEHNERT I highly acknowledge your support in analyzing and understanding PPC detector surface effects. In particular, I would like to thank you for the very stimulating and interesting physics discussions which quite often took a considerable amount of time. Finally, a big thank you for proofreading parts of this thesis.

MARTIN SLÉZAK Your endless help in fixing any software-related issue was indispensable. In addition, I highly appreciate our great photography discussions and sessions, and the associated longest *Minuspunkt* (circumnavigating the globe). Your feedback on parts of this thesis is very much appreciated.

CHRISTIAN KARL I am extremely grateful to you for your coding help and for speeding up my nested for-loops. A big thank you also for the introduction of Bavarian culture into our group and for many useful hiking recommendations. Finally, I would like to thank you for the great ambiance in our office.

LUKAS HAUERTMANN I am very thankful for the great time we spent together in the GALATEA laboratory. Furthermore, I would like to thank you for our fruitful discussions and for taking care of the GALATEA GEANT4 simulations.

YOANN KERMAÏDIC Our discussions on the Post-GERDA Test data analysis turned out to be extremely fruitful and purposeful. Many thanks also for proofreading parts of this thesis.

THIBAUT HOUDY Je te remercie beaucoup d'avoir répondu à toutes mes questions en ce qui concerne le logiciel GEANT4. En outre, je te suis extrêmement reconnaissant pour nos discussions franco-allemandes. Finalement, je tiens à te remercier pour corriger parties de cette thèse.

ALAN POON I am very grateful to you for giving me the unique opportunity to conduct several research stays at Berkeley Lab. The research environment was very stimulating and enriching. Finally, I would like to thank you for your outstanding academic support.

PAUL BARTON You greatly contributed to this work by giving me the unique opportunity to perform ASIC characterization measurements at Berkeley Lab. Many thanks for training me on signal readout electronics, for countless electronics-related discussions, and for providing scientific advice on our ASIC manuscript.

MARCOS TURQUETI Thank you very much for your endless help in setting up and optimizing the qAMP preamplifier, for many helpful discussions, and for improving my knowledge in analog and digital electronics considerably. Muito obrigado!

DAVID FINK I am very thankful for your initial assistance in the lab, particularly for your help to gain a better understanding of ASIC-based signal readout electronics.

KATRIN AND TRISTAN GROUP I am deeply indebted to our research group at MPP for the great and stimulating research environment and all the social events (barbecue parties, skiing excursions, etc.). In addition, I would particularly like to thank Tim Brunst, Daniel Siegmann, and Korbinian Urban for proofreading parts of this thesis.

GEDET GROUP A big thank you to the whole group, particularly Iris Abt, for the great gesture of integrating me into your activities! I highly appreciate the great times we spent together at the LEGEND collaboration meetings and other conferences. In addition, I would like to thank you for opening me the doors to your facilities and all the invaluable help with conducting and understanding measurements with GALATEA.

E15 GROUP AT TUM I would like to thank the whole group, particularly Stefan Schönert, Tommaso Comellato, Oskar Moras, Mario Schwarz, Christoph Wiesinger, and Patrick Krause for many useful discussions, for opening me the doors to their labs, and for their help in setting up the test stands. I am also grateful for the great times we spent together at the LEGEND collaboration meetings.

STUDIENSTIFTUNG DES DEUTSCHEN VOLKES I am very thankful to the German Academic Scholarship Foundation for providing me a doctoral scholarship giving me the unique opportunity to fully focus on my research work. Moreover, I highly appreciate the excellent idealistic support, including language courses, summer academies, excursions, educational lectures, etc.

Finally, I must express my profound gratitude to my lovely wife *Marta Edzards*, my *parents*, and my *sister* for providing me with unfailing support and continuous encouragement throughout my years of study and through the process of researching and writing this thesis. This accomplishment would not have been possible without you. Thank you very much!

Frank Edzards

CONTENTS

ACRONYMS

aGe	Amorphous germanium
AC	Anti-coincidence (cut)
ADC	Analog-to-digital converter
AGS	Alternating Gradient Synchrotron
ASIC	Application-specific integrated circuit
BAO	Baryonic acoustic oscillations
BEGe	Broad energy germanium (detector)
BI	Background index
BNL	Brookhaven National Laboratory
BSM	Beyond Standard Model (physics)
CKM	Cabibbo-Kobayashi-Maskawa (matrix)
CMB	Cosmic microwave background
CMOS	Complementary metal-oxide-semiconductor
CSA	Charge sensitive amplifier
CSDA	Continuous slowing down approximation
CT	Charge trapping
CTA	Cherenkov Telescope Array
DAQ	Data acquisition (system)
DCR	Delayed charge recovery
DEP	Double escape peak
EC	Electron capture
EMI	Electromagnetic interference
ENC	Equivalent noise charge
ENIG	Electroless nickel immersion gold
ESD	Electrostatic discharge sensitive device
FE	Front-end (electronics)
FEP	Full energy peak
FADC	Flash analog-to-digital converter
FWHM	Full width at half maximum
ftp	fixed-time-pickoff (trapezoid)
GELATIO	GERDA Layout for input output
GERDA	Germanium detector array
HdM	Heidelberg-Moscow (experiment)
HPGe	High-purity germanium
HV	High voltage
HWHM	Half width at half maximum
IBD	Inverse beta decay
IC	Integrated circuit
ICP-MS	Inductively coupled plasma mass spectrometry
ICPC	Inverted coaxial point contact (detector)

IGEX	International Germanium Experiment
IIR	Infinite impulse response (filter)
IO	Inverted neutrino mass ordering
IR	Infrared
JFET	Junction gate field-effect transistor
KATRIN	Karlsruhe Tritium Neutrino (experiment)
LAr	Liquid argon
LEP	Large electron-positron (collider)
LBNL	Lawrence Berkeley National Laboratory
LDO	Low-dropout (regulator)
LEGEND	Large Enriched Germanium Experiment for Neutrinoless $\beta\beta$ Decay
LMFE	Low-mass front-end (electronics)
LN_2	Liquid nitrogen
LNGS	Laboratori Nazionali del Gran Sasso
LSB	Left side band
MCA	Multichannel analyzer
MJD	MAJORANA DEMONSTRATOR
MMC	Metallic magnetic calorimeter
MOSFET	Metal-oxide-semiconductor field-effect transistor
MPP	Max Planck Institute for Physics
MSE	Multi-site event
MSW	Mikheyev-Smirnov-Wolfenstein (effect)
NME	Nuclear matrix element
NO	Normal neutrino mass ordering
NTD	Neutron-transmutation-doped
PCB	Printed circuit board
PEI	Polyetherimide
PEN	Polyethylene naphthalate
PGT	Post-GERDA test
PMNS	Pontecorvo-Maki-Nakagawa-Sakata (matrix)
PMT	Photomultiplier (tube)
PONaMa1	PPC detector from ORTEC made from Natural Material
PPC	P-type point contact (detector)
PSA	Pulse shape analysis
PSD	Pulse shape discrimination
PSS	Pulse shape simulations
PTFE	Polytetrafluoroethylene (Teflon)
PZ	Pole-zero
RMS	Root mean square
ROI	Region of interest (of $0\nu\beta\beta$ decay)
RSB	Right side band
SEP	Single escape peak
SiPM	Silicon photomultiplier
SIS	Source insertion system

SM	Standard Model (of particle physics)
SMD	Surface-mount device
SNO	Sudbury Neutrino Observatory
SNR	Signal-to-noise ratio
SSE	Single-site event
SSM	Standard Solar Model
SURF	Sanford Underground Research Facility
TES	Transition-edge sensor
TMP	Turbomolecular pump
TPB	Tetraphenyl butadiene
TPC	Time projection chamber
TTX	Tetratex
TUBE	TUM Upside-down BEGe (scanning system)
TUM	Technical University of Munich
UG LAr	Underground liquid argon
WIMP	Weakly interacting massive particle
WLSR	Wavelength-shifting reflector

Part I

PREAMBLE

1

INTRODUCTION AND OBJECTIVES

Since its experimental discovery in 1956 [1–3], our knowledge and understanding of the neutrino has increased enormously. However, there are still a number of fundamental open questions in the field of neutrino physics. First and foremost, the absolute neutrino mass is not yet known. A closely related question deals with the intrinsic nature of neutrinos, i.e. if they are their own antiparticles and thus Majorana fermions. The answer to these questions could unravel some of the most pressing mysteries in particle physics and cosmology, such as the question of the origin of particle mass, and the matter/antimatter asymmetry of our universe.

The observation of neutrino oscillations proves that the neutrino mass is non-zero [4–7]. However, oscillation experiments are not sensitive to the absolute mass scale. Three complementary approaches are currently being pursued to determine the neutrino mass: 1) direct mass measurements using single beta decay and electron capture, 2) indirect mass determination via astrophysical and cosmological observables, and 3) search for neutrinoless double beta ($0\nu\beta\beta$) decay. Direct neutrino mass measurements set an upper limit, constraining the neutrino mass to be at least five orders of magnitude smaller than the mass of the lightest charged fermion, the electron [8]. The smallness of the neutrino mass is closely intertwined with the question about the Majorana nature of the neutrino. While all known charged fermions are distinct from their antiparticle, the unique fact that neutrinos are electrically neutral provokes the question whether they may be identical to their own antiparticles. Currently, the most practical way to ascertain whether neutrinos are Majorana particles is the search for $0\nu\beta\beta$ decay. The decay violates lepton number conservation by two units and its observation would have major implications on our understanding of the origin of matter in our universe. Together with cosmological observations and direct neutrino mass measurements, it could also provide information on the absolute neutrino mass scale [9, 10].

One of the most promising technologies to search for $0\nu\beta\beta$ decay are high-purity germanium (HPGe) detectors. The Large Enriched Germanium Experiment for Neutrinoless $\beta\beta$ Decay, LEGEND, pursues a phased approach to realize a tonne-scale $0\nu\beta\beta$ decay search with HPGe detectors [11–14]. To reach the ambitious targeted signal discovery sensitivity beyond 10^{28} yr on the decay half-life, ultra-low background requirements have to be met. Consequently, the reduction of backgrounds is one of the main challenges to be addressed.

Background projections for the first phase of the experiment, LEGEND-200, anticipate alpha- and beta-induced surface backgrounds to be among the dominant contributions. One of the main objectives of this work is to gain a better understanding of these backgrounds. In this context, the response of a p-type point contact (PPC) germanium detector to alpha and beta particles hitting the passivated surface was studied in detail. The corresponding work included the experimental realization and the data analysis. In particular, a highly customized analysis framework has been developed. A related goal of this work is to model and verify the measurement results via dedicated Monte Carlo and pulse shape simulations.

Another important role to minimize backgrounds and to maximize the experiment's discovery sensitivity plays signal readout electronics. The charge sensitive amplifier (CSA) should be placed as close as possible to the HPGe detector to minimize stray input capacitance and thus electronic noise. This also enhances the bandwidth of the system (faster signal rise times), which is important for the successful application of pulse shape discrimination (PSD) techniques to reject background events [15, 16]. However, a close proximity of the CSA to the detector is in conflict with the stringent radiopurity requirements. Any component close to the detectors contributes to

the background and can reduce the experimental sensitivity [16, 17]. Therefore, the material mass and the volume of the CSA must be small. In addition, radiopure components must be used. In LEGEND-200, a novel readout system based on implementations by the predecessor experiments, the Germanium Detector Array (GERDA) and MAJORANA DEMONSTRATOR experiments, will be used. The CSA consists of a first stage very close to the detectors (several cm) which is based on MAJORANA DEMONSTRATOR's low-noise, low-mass front-end (LMFE) readout electronics [18], and a second stage farther away which is based on the preamplifier of the GERDA experiment [19, 20]. One of the main aims of this work is to characterize the performance of the novel readout electronics. In this context, calibration and physics data of the Post-GERDA test, a full chain integration test with about 18 kg detector mass, were analyzed. Based on the improved noise situation compared to the GERDA experiment, one of the goals was to demonstrate the feasibility of applying a charge trapping correction for the recently developed inverted coaxial point contact (ICPC) detector geometry [21]. Moreover, performance metrics of a backup CSA were studied in bench tests.

In the final phase of LEGEND, LEGEND-1000, the total background level needs to be reduced by another order of magnitude compared to LEGEND-200. Therefore, additional background rejection techniques are required. From the readout electronics point of view, this can be supported by using state-of-the-art application-specific integrated circuit (ASIC) technology. The technology enables the implementation of the entire CSA into a single low-mass, low-background chip while maintaining the performance of conventional amplifiers. One of the main objectives of this work was to demonstrate the feasibility of operating a large-scale HPGe detector together with a readout ASIC. To study key electronic parameters, and to validate the viability of background rejection capabilities, a PPC detector was equipped with a commercially available ASIC CSA, the XGLab CUBE ASIC [22, 23]. To verify that the chip fulfills the stringent background requirements, an extensive radiopurity assay campaign was conducted. Currently, a customized readout ASIC that specifically meets the electronics requirements of LEGEND-1000 is being developed. Within this work, the characteristics of a first prototype of this chip are investigated.

This thesis is organized as described in the following.

I PREAMPLE In **Ch.** 2, a general introduction to neutrino physics and neutrino mass with a focus on $0\nu\beta\beta$ decay is given. In addition, the current status and prospects of various $0\nu\beta\beta$ decay searches are discussed. **Ch.** 3 focuses on the properties and the working principle of semiconductor detectors. Here, the interaction processes of particles with matter are reviewed and HPGe detectors are introduced. The radioactive backgrounds typically encountered in ^{76}Ge-based $0\nu\beta\beta$ decay searches and their rejection strategies are discussed in **Ch.** 4. Moreover, the physics programs of the GERDA experiment, the MAJORANA DEMONSTRATOR, and of LEGEND are presented.

II CHARACTERIZATION OF POINT CONTACT GERMANIUM DETECTORS The relevance of alpha and beta surface backgrounds in LEGEND-200 is elaborated in **Ch.** 5. In particular, the phenomenology of surface effects on the passivated surface of PPC detectors is discussed. The measurement setup including the scanning facility, the detector, the radioactive sources, and the signal readout electronics used to characterize these surface effects is described in **Ch.** 6. Furthermore, the data analysis procedures and the detector performance in the experimental setup are reviewed in this chapter. The results of surface characterization measurements with alpha and beta particles are presented in **Chs.** 7 and 8, respectively. Finally, the results of an extensive simulation campaign are compared to the measurement results in **Ch.** 9.

III DEVELOPMENT OF SIGNAL READOUT ELECTRONICS FOR LEGEND In **Ch.** 10, the basics of signal readout electronics for $0\nu\beta\beta$ decay searches are discussed. The chapter focuses on the readout architecture, charge sensitive amplifiers, and on electronic noise. Signal readout electronics for LEGEND-200 is part of **Ch.** 11. Here, analysis results of the Post-GERDA test and characterization measurement results of a backup amplifier are presented. Signal readout electronics for LEGEND-1000 is the subject of **Ch.** 12. The chapter summarizes the requirements on a readout ASIC for the application in LEGEND and presents characterization measurements of two ASIC prototypes.

IV SUMMARY AND CONCLUSIONS The main results obtained within the scope of this work are summarized in **Ch.** 13.

2

NEUTRINO PHYSICS

The neutrino is one of the most abundant particles in our universe. In the well-established Standard Model[1] (SM) of particle physics [24], the spin-1/2 fermion comes in three distinct flavors in accordance with the charged leptons: the electron (e), the muon (μ), and the tau lepton (τ). Moreover, it is electrically neutral, is treated as massless, and interacts only via the weak force and gravitation. Lepton number[2] is conserved within each family, and neutrinos have left-handed helicity[3], whereas antineutrinos have right-handed helicity [25]. Due to the very weak interaction with matter, it is challenging to detect and study neutrinos. As an example, the cross section of neutrinos with energies of a few MeV from a reactor is on the order of $\sigma_{\overline{\nu}p} \approx 10^{-44}\,\mathrm{cm}^2$, whereas the cross section for the corresponding electromagnetic process at similar energies is $\sigma_{\gamma p} \approx 10^{-25}\,\mathrm{cm}^2$ [26, 27]. Despite many recent experimental efforts, some of the neutrino's most fundamental properties are still unknown. Notably, these include the actual, but very tiny mass (as proven by the observation of neutrino oscillations), and whether it is a Majorana fermion, i.e. its own antiparticle, or not.

This chapter gives a brief introduction to neutrino physics with a focus on neutrino mass and double beta decay, which is of particular importance for the work presented in this thesis. In **Ch.** 2.1, a historical summary of the discoveries in neutrino physics will be given. The phenomenon of neutrino mixing and oscillations, whereby neutrinos undergo flavor transitions as they propagate over long distances, is described in **Ch.** 2.2. **Ch.** 2.3 focuses on neutrino mass and its determination via single beta decay and cosmological observables. The physics of (neutrinoless) double beta decay is discussed in detail in **Ch.** 2.4.

2.1 HISTORICAL OVERVIEW

The existence of the neutrino was first postulated by W. Pauli in the year 1930 to explain the observed continuous electron energy spectrum in single beta decay, in contrast to the expectation of a monochromatic spectrum for the anticipated two-body decay [28]. Only by introducing a third, electrically neutral particle emitted along with the electron, energy conservation was restored. This particle, originally denoted as "neutron", should have spin-1/2, and should not travel at the speed of light. In 1932, the neutron was discovered by J. Chadwick [29, 30] and the particle postulated by Pauli was renamed neutrino (ν). A first theoretical description of single beta decay was given in 1934 by E. Fermi [31]:

$$(Z, A) \rightarrow (Z+1, A) + e^- + \overline{\nu}_e. \tag{2.1}$$

Here, Z denotes the atomic number, A the mass number of the nucleus, e^- the electron, and $\overline{\nu}_e$ the electron antineutrino. Only in the year 1956, the electron antineutrino ($\overline{\nu}_e$) was discovered experimentally [1–3]. The groups led by C. L. Cowan Jr. and F. Reines used a setup in the vicinity of the Savannah River nuclear reactor. It consisted of a water target with dissolved cadmium chloride ($CdCl_2$) between layers of scintillating material, read out by photomultiplier tubes (PMTs). Electron antineutrinos from the nuclear fission reaction were detected via inverse beta decay (IBD):

$$\overline{\nu}_e + p \rightarrow e^+ + n. \tag{2.2}$$

1 The SM is a gauge theory based on the symmetry group $SU(3)_C \times SU(2)_L \times U(1)_Y$.

2 The lepton number describes the difference between the number of leptons and the number of antileptons in an elementary particle reaction. Lepton number conservation states that in any physical process the sum of lepton numbers before and after the interaction are equal.

3 The helicity is the projection of the spin onto the direction of the momentum. The helicity of massive particles depends on the reference frame. For massless particles, helicity is identical to chirality. While helicity is a property of the particle itself, chirality is a frame-independent property of the interaction.

The measurement was possible through the detection of both the prompt positron (e^+) signal (annihilating with an electron and producing a pair of photons) and the delayed coincident de-excitation of Cd after neutron (n) capture. For his discovery, Reines was awarded the Nobel Prize in Physics in 1995.

The muon neutrino (ν_μ) was discovered in the year 1962 at the Alternating Gradient Synchrotron (AGS) at Brookhaven National Laboratory (BNL) by M. Schwartz, L. M. Lederman and J. Steinberger [32]. In the experiment, a 15 GeV proton beam was shot onto a beryllium target. The interactions there produced charged pions that subsequently decayed producing neutrinos. All particles except the neutrinos were stopped by a steel shield in front of the detector. The detector itself was a spark chamber consisting of several aluminum plates separated by gas-filled gaps. The existence of a second neutrino flavor was deduced by observing long muon tracks (created in charged current interactions of muon neutrinos), and only a few electron neutrinos via electromagnetic showers of electrons [32]. The three scientists were awarded the Nobel Prize in 1988.

After the discovery of the tau lepton in 1975 [33], the existence of a corresponding third neutrino, the tau neutrino (ν_τ), was anticipated. It was finally discovered in the year 2000 at Fermilab with the DONUT (Direct observation of the nu tau) experiment [34] and confirmed the existence of the last lepton within the Standard Model (SM) of particle physics. This is due to the fact that based on measurements of the width of the Z^0 resonance at the Large Electron-Positron (LEP) collider, the number of active light neutrinos was determined to be $N = 2.9840 \pm 0.0082$ [35].

Since the discovery of the neutrino, its nature has been studied in detail. In 1958, the experiment by M. H. Goldhaber *et al.* proved that the helicity of the electron neutrino ν_e is negative [25]. This was later confirmed also for ν_μ [36] and ν_τ [37, 38]. Therefore, the conclusion was drawn that in nature neutrinos only occur as left-handed particles or as right-handed antiparticles.

2.2 NEUTRINO MIXING AND OSCILLATIONS

For many years, it was assumed that neutrinos were massless fundamental particles. Due to the fact that in the SM neutrinos only appear with negative helicity, neutrino mass generation via Yukawa coupling is not allowed[4]. The picture drastically changed with the observation of neutrino oscillations providing compelling experimental evidence for a small, yet non-zero neutrino mass. This also points towards a mass creation mechanism beyond the SM (BSM).

SOLAR NEUTRINO PROBLEM Nuclear fusion reactions in the Sun produce a large flux of electron neutrinos ν_e (mainly via the pp-chain). The neutrinos propagate from the center of the Sun to the Earth and can be observed with sufficiently massive detectors [39]. First theoretical calculations of the neutrino flux were provided by J. Bahcall in the scope of the Standard Solar Model (SSM) [40, 41]. On the experimental side, R. Davis Jr. designed one of the first solar neutrino detectors based on a radiochemical technique, located in the Homestake mine[5] in South Dakota, to test the predictions [4, 42]. The experiment measured the solar neutrino flux (mostly ^{8}B neutrinos) by counting the number of ^{37}Ar atoms produced in the IBD reaction

$$\nu_e + {}^{37}\mathrm{Cl} \rightarrow {}^{37}\mathrm{Ar} + e^- . \tag{2.3}$$

As opposed to the prediction of 1.7 interactions per day, a rate of only 0.48 ± 0.04 neutrino interactions per day was observed [39, 43, 44]. The apparent deficit of solar neutrinos became known as the solar neutrino problem. In the subsequent GALLEX (1991 – 1996) [45], GNO (1998 – 2002) [46], SAGE (1990 – 2006) [47, 48], and Borexino (2007 – today) [49–51] experiments measuring solar pp-neutrinos, the deviation from the SSM prediction was confirmed.

A possible solution to the problem was that neutrinos produced in a particular flavor (electron flavor for the solar neutrinos) can convert into neutrinos of a different flavor during their propagation over long distances, e.g. $\nu_e \leftrightarrow \nu_\mu$. This mechanism is nowadays referred to as neutrino

4 In the SM, mass comes from the spontaneous symmetry breaking via Yukawa interaction of the left-handed doublet with the right-handed singlet. Since there are no right-handed neutrinos in the SM, there is no renormalizable gauge-invariant operator for tree level neutrino mass generation.

5 The experiment was carried out deep underground to eliminate backgrounds from cosmic rays.

oscillation. Measuring only weak interactions mediated by charged currents, Davis' experiment was only sensitive to electron neutrinos and could not detect neutrinos of a different flavor. The solar neutrino problem was resolved experimentally in 2001 by the Sudbury Neutrino Observatory (SNO). By also measuring neutral current and elastic scattering reactions using a Cherenkov detector deploying 1 kt of heavy water with dissolved NaCl (to capture the neutrons of the neutral current interaction), the experiment was sensitive to all neutrino species and measured the entire neutrino flux. The experimental results confirmed the missing electron neutrinos and validated the appearance of muon and tau neutrinos in their place [6, 7]. For his pioneering contributions to astrophysics, in particular for the detection of solar neutrinos, R. Davis was awarded the Nobel Prize in 2002.

Independently, neutrino oscillations were also measured for atmospheric neutrinos by the Super-Kamiokande experiment [5]. Atmospheric neutrinos are created in the decay of charged pions ($\pi^{\pm}$) and kaons ($K^{\pm}$) that are produced when cosmic rays interact with air molecules in the upper atmosphere. In the subsequent decay of muons, additional neutrinos are created. The expected flavor ratio is $\nu_\mu : \nu_e = 2 : 1$. Super-Kamiokande used 50 kt of ultra-pure water as a detection medium in a large underground tank equipped with 11200 PMTs. The experiment was sensitive to high-energetic electron and muon neutrinos via charged current reactions. The associated charged leptons produced in these reactions were detected via the Cherenkov light they emitted in the water. By resolving the direction of the interactions, neutrino oscillations were studied by comparing the neutrino flux from different zenith angles. For the electron neutrino flux, no angular dependence and no deviation from the expected magnitude was observed. In contrast, the muon neutrino flux was smaller than expected and showed a directional dependence, i.e. the flux coming from the sky directly above the experiment was higher than the flux coming from the opposite side of the Earth [52]. These observations were attributed to neutrino oscillations with a flavor transition $\nu_\mu \to \nu_\tau$ (Super-Kamiokande was not sensitive to tau neutrinos). For the discovery of neutrino oscillations, A. McDonald (SNO) and T. Kajita (Super-Kamiokande) were awarded the Nobel Prize in 2015.

THEORY OF NEUTRINO OSCILLATIONS Neutrino-antineutrino transitions $\nu \leftrightarrow \overline{\nu}$ were already suggested by B. Pontecorvo in 1958 in analogy to transitions in the $K^0/\overline{K}^0$ system [53]. A few years later, he revived this idea as a possible solution to the solar neutrino problem [54, 55]. Neutrino oscillations arise from the fact that the neutrino flavor eigenstates $|\nu_l\rangle$ ($l = e, \mu, \tau$) are not equal to the neutrino mass eigenstates $|\nu_i\rangle$ ($i = 1, 2, 3$). Instead, the flavor eigenstates are a quantum mechanical superposition of the mass eigenstates:

$$|\nu_l\rangle = \sum_{i=1}^{3} U_{li}^{*} \, |\nu_i\rangle \, . \tag{2.4}$$

Here, U_{li}^{*} denotes a complex 3×3 matrix, the so-called Pontecorvo-Maki-Nakagawa-Sakata (PMNS) matrix which relates the flavor to the mass eigenstates. It is the analogue of the Cabibbo-Kobayashi-Maskawa (CKM) matrix describing mixing in the quark sector [56, 57]. Assuming the existence of only three neutrino mass eigenstates and unitarity of the mixing matrix, it can be parameterized by three different mixing angles ($\theta_{12}, \theta_{13}, \theta_{23}$) and, depending on whether the massive neutrinos are Dirac or Majorana particles, cf. **Ch.** 2.3.1, by one or three complex CP-violating phases (δ, α, β) [58]:

$$U = \begin{pmatrix} U_{e1} & U_{e2} & U_{e3} \\ U_{\mu 1} & U_{\mu 2} & U_{\mu 3} \\ U_{\tau 1} & U_{\tau 2} & U_{\tau 3} \end{pmatrix} \tag{2.5}$$

$$= \underbrace{\underbrace{\begin{pmatrix} c_{12}c_{13} & s_{12}c_{13} & s_{13}e^{-i\delta} \\ -s_{12}c_{23} - c_{12}s_{23}s_{13}e^{i\delta} & c_{12}c_{23} - s_{12}s_{23}s_{13}e^{i\delta} & s_{23}c_{13} \\ s_{12}s_{23} - c_{12}c_{23}s_{13}e^{i\delta} & -c_{12}s_{23} - s_{12}c_{23}s_{13}e^{i\delta} & c_{23}c_{13} \end{pmatrix}}_{\text{Dirac}} \operatorname{diag}\left(1, e^{i\alpha}, e^{i\beta}\right)}_{\text{Majorana}} , \tag{2.6}$$

where $s_{ij} = \sin\theta_{ij}$ and $c_{ij} = \cos\theta_{ij}$ with $\theta_{ij} = [0, \pi/2]$. The phase $\delta = [0, 2\pi]$ is the so-called Dirac phase and describes CP violation in the lepton sector. The phase factors α and β are called Majorana

Table 2.1: Overview of the three-flavor neutrino oscillation parameters for the normal (NO) and inverted mass ordering (IO) regimes. All values are derived from a global analysis and represent best-fit values. Data from [60].

Parameter	Best fit ($\pm 1\sigma$)	
	NO	IO
θ_{12} (°)	$33.44^{+0.78}_{-0.75}$	$33.45^{+0.78}_{-0.75}$
θ_{13} (°)	$8.57^{+0.13}_{-0.12}$	8.61 ± 0.12
θ_{23} (°)	$49.0^{+1.1}_{-1.4}$	$49.3^{+1.0}_{-1.12}$
δ (°)	195^{+51}_{-25}	286^{+27}_{-32}
$\Delta m^2_{21} (10^{-5}\,\mathrm{eV}^2)$	$7.42^{+0.21}_{-0.20}$	
$\Delta m^2_{3l} (10^{-3}\,\mathrm{eV}^2)$	$+2.514^{+0.028}_{-0.027}$	-2.497 ± 0.028

phases and they are physically meaningful only if neutrinos are Majorana particles, i.e. their own antiparticles. This also means that these phases are zero if the neutrino is a Dirac particle.

In order to see the salient features of neutrino oscillations, we simplify the treatment by considering the case of only two neutrino flavor eigenstates (ν_α, ν_β) with a single mixing angle (θ). The probability for an oscillation can then be expressed as [59]:

$$P(\nu_\alpha \to \nu_\beta) \approx \sin^2(2\theta) \sin^2\left(1.27 \cdot \Delta m^2\,[\mathrm{eV}^2] \cdot \frac{L\,[\mathrm{km}]}{E\,[\mathrm{GeV}]}\right). \tag{2.7}$$

Here, Δm^2 denotes the mass squared difference between the two mass eigenstates, E the neutrino energy, and L the baseline length of the oscillation, i.e. the distance traveled by the neutrino between the source and detector. The equation shows that neutrino flavor transitions only occur if the mass squared difference Δm^2 is non-zero. This implies that in the case of three neutrino flavors, at least two mass eigenstates need to be non-zero. In addition, **Eq.** (2.7) shows that the oscillation amplitude is sensitive to the mixing angle, while the mass squared difference can be inferred from the oscillation length. Therefore, by measuring the oscillation pattern, the neutrino oscillation parameters can be determined.

NEUTRINO OSCILLATION PARAMETERS AND MASS ORDERING Neutrino oscillation experiments provide information on the mixing angles, the Dirac phase, and the mass squared differences $\Delta m^2_{ij} = m^2_i - m^2_j, i \neq j$. Since neutrino oscillations are an interference effect, they are not sensitive to the absolute neutrino mass scale. In the case of three-flavor neutrino mixing, there are only two independent neutrino mass squared differences $\Delta m^2_{21} \neq 0$ and $\Delta m^2_{31} \approx \Delta m^2_{32} \neq 0$. The mass squared difference Δm^2_{21} is measured by solar neutrino oscillation experiments [61–63], whereas the mass squared differences Δm^2_{31} and Δm^2_{32} are obtained from atmospheric neutrino oscillation experiments [64, 65]. Likewise, the angles θ_{12} and θ_{23} are measured in solar neutrino and atmospheric neutrino oscillation experiments, respectively. Therefore, the mass squared differences are often denoted as $\Delta m^2_{21} = \Delta m^2_\odot$ and $\Delta m^2_{31} = \Delta m^2_A$, whereas the angles are denoted as $\theta_{12} = \theta_\odot$ and $\theta_{23} = \theta_A$ [66]. The oscillation parameters are also measured in reactor neutrino [67–70] and accelerator neutrino [71, 72] experiments. An overview of the most recent values is listed in **Tab.** 2.1.

While the sign of Δm^2_{21} is known through the Mikheyev-Smirnov-Wolfenstein (MSW) effect, a matter resonance effect in the Sun modifying neutrino oscillations [73], experiments measuring oscillation parameters are currently not sensitive to the sign of $\Delta m^2_{31(2)}$. Therefore, the two possible signs translate into two types of neutrino mass ordering, see **Fig.** 2.1. Assuming that $m_1 < m_2$ so that $\Delta m^2_{21} > 0$ [66], we obtain the following two possibilities:

1. Normal mass ordering (NO): m_1 is the mass of the lightest eigenstate, $m_1 < m_2 < m_3$, $\Delta m^2_{31} = \Delta m^2_A > 0$,
2. Inverted mass ordering (IO): m_3 is the mass of the lightest eigenstate, $m_3 < m_1 < m_2$, $\Delta m^2_{32} = \Delta m^2_A < 0$.

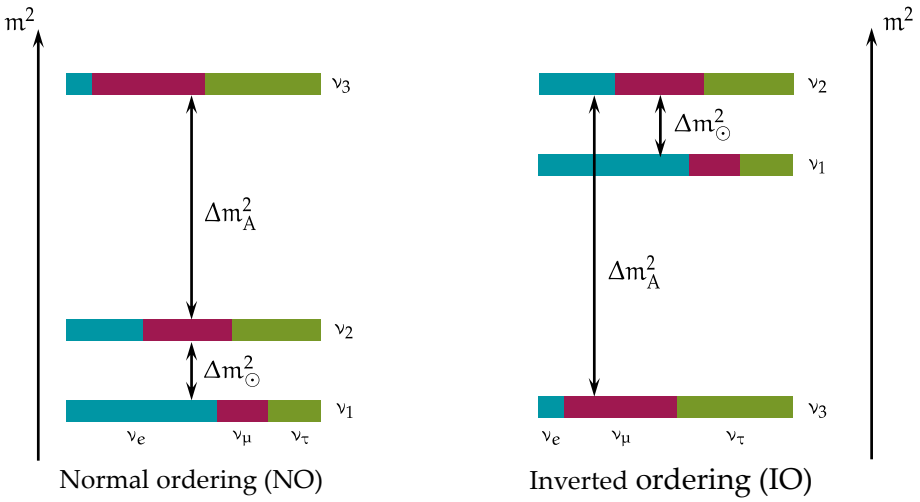

Figure 2.1: Possible orderings of the neutrino mass for three-flavor neutrino oscillations. The normal ordering (NO) refers to the case in which $m_1 < m_2 < m_3$, whereas in the inverted ordering (IO) $m_3 < m_1 < m_2$. The neutrino mass eigenstates are a superposition of the flavor eigenstates, and vice versa.

Depending on the value of the lightest neutrino mass $m_{\text{lightest}} = \min(m_i)$, the mass eigenvalues for the different mass orderings can then be expressed as [66]

$$\text{NO}: m_1 = m_{\text{lightest}}, \quad m_2 = \sqrt{m_1^2 + \Delta m_{21}^2}, \quad m_3 = \sqrt{m_1^2 + \Delta m_{31}^2}, \tag{2.8}$$

$$\text{IO}: m_1 = \sqrt{m_3^2 + \Delta m_{23}^2 - \Delta m_{21}^2}, \quad m_2 = \sqrt{m_3^2 + \Delta m_{23}^2}, \quad m_3 = m_{\text{lightest}}. \tag{2.9}$$

Current global fits of neutrino oscillation data slightly favor the NO regime over the IO one [60, 74]. However, more dedicated future experiments are required to unravel the question of the neutrino mass ordering [75].

2.3 NEUTRINO MASS

The observation of neutrino oscillations has proven that at least two out of the three neutrinos are massive particles. However, as pointed out in **Ch.** 2.2, neutrino oscillation experiments are only sensitive to the mass squared differences and not to the absolute mass scale. With a mass at least five orders of magnitude smaller than the mass of an electron, see **Fig.** 2.2, neutrinos are a clear exemption in the SM. On the one hand, its tiny mass makes the neutrino one of the most interesting particles, one that might be a portal to BSM physics. On the other hand, the small mass leads to major challenges in its experimental determination. Three complementary approaches are currently being pursued:

1) Direct kinematical inference of neutrino mass via single beta decay and electron capture,

2) indirect mass determination via astrophysical and cosmological observables,

3) search for neutrinoless double beta ($0\nu\beta\beta$) decay.

The following sections describe the foundations of these neutrino mass determination techniques. First, in **Ch.** 2.3.1, the Dirac or Majorana nature of neutrinos will be discussed briefly. **Ch.** 2.3.2 focuses on the mass determination via direct measurements. The indirect mass determination via cosmology is detailed in **Ch.** 2.3.3. Finally, a dedicated chapter, **Ch.** 2.4, focuses on the physics of double beta decay.

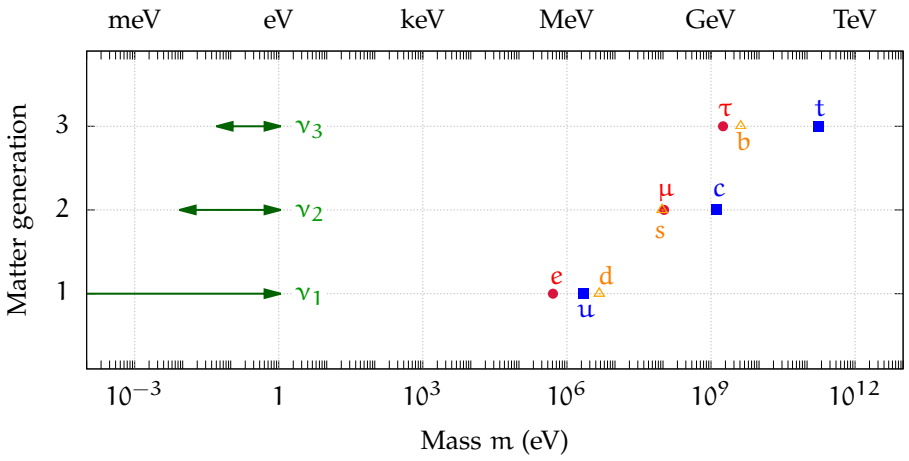

Figure 2.2: Comparison of the masses of the fundamental fermions. The graph shows that the three neutrinos ν_i ($i = 1, 2, 3$) have a mass at least five orders of magnitude smaller than the masses of the charged fermions. Data from [76].

2.3.1 *Dirac and Majorana neutrinos*

To unravel the question of the origin of neutrino mass and to understand the underlying particle physics interactions, it is important to investigate the nature of the neutrino. Of particular interest is whether it is a Dirac fermion, i.e. a particle that is distinct from its antiparticle ($\nu \neq \bar{\nu}$), or a Majorana fermion, i.e. a particle that is identical to its antiparticle ($\nu = \bar{\nu}$).

DIRAC AND MAJORANA MASS TERMS By introducing a right-chiral neutrino singlet (ν_R) in the SM, neutrino masses can be generated via the Higgs mechanism with Yukawa interactions. This avoids the need for the introduction of a bare mass term and preserves renormalizability. Since in the SM neutrinos exclusively appear as left-handed particles, right-handed neutrinos must be sterile singlets and cannot interact weakly [25, 77, 78]. The Dirac neutrino mass term in the extended SM Lagrangian is of the form

$$\mathcal{L}_D^{\text{mass}} \propto -m_D(\bar{\nu}_R \nu_L + \bar{\nu}_L \nu_R), \tag{2.10}$$

where m_D denotes the coupling strength of the neutrino spinor to the Higgs field, i.e. the Dirac neutrino mass, and ν_L, ν_R are chiral projections of the neutrino spinors. According to **Eq.** (2.10), Dirac mass terms are only possible in the presence of right-chiral neutrino fields and left-chiral antineutrino fields. The Dirac mass m_D is proportional to the product of the vacuum expectation value $v \approx \mathcal{O}(100\,\text{GeV})$ of the Higgs field and the Yukawa coupling y:

$$m_D \propto v \cdot y. \tag{2.11}$$

Given current upper limits on the neutrino mass of $\mathcal{O}(1\,\text{eV})$, the Yukawa coupling would have to be on the order of $y \approx 10^{-12}$, a value unnaturally small compared to the one of other particles obtaining their mass via the same mechanism. The necessity of this fine-tuning of the neutrino Yukawa coupling constant is typically considered as a strong argument against a SM origin of neutrino mass [79].

If the neutrino is a Majorana particle, however, lepton number violating mass terms of the form

$$\mathcal{L}_{M,L}^{\text{mass}} \propto -\frac{M_L}{2}\left(\bar{\nu}_L^C \nu_L + \bar{\nu}_L \nu_L^C\right) \tag{2.12}$$

can be constructed. Here, the superscript C represents charge conjugation. Moreover, if we again introduce a right-chiral neutrino singlet, also mass terms of the following form are possible:

$$\mathcal{L}_{M,R}^{\text{mass}} \propto -\frac{M_R}{2}\left(\bar{\nu}_R^C \nu_R + \bar{\nu}_R \nu_R^C\right). \tag{2.13}$$

Since this term does not require any interaction with the Higgs field, the Majorana mass M_R can be arbitrarily large.

SEESAW MECHANISM The various mass terms discussed above can be combined and written compactly using the following matrix representation:

$$\mathcal{L}^{\text{mass}} = -\frac{1}{2}\begin{pmatrix}\overline{\nu}_L & \overline{\nu}_R^C\end{pmatrix}\underbrace{\begin{pmatrix}M_L & m_D\\ m_D & M_R\end{pmatrix}}_{\mathcal{M}}\begin{pmatrix}\nu_L^C\\ \nu_R\end{pmatrix} + \text{h.c.} \tag{2.14}$$

By using the simplified assumption that $M_L = 0, m_D \ll M_R$, and diagonalizing the mass matrix $\mathcal{M}$, we obtain the eigenvalues

$$m_1 = \frac{m_D^2}{M_R} \quad \text{and} \quad m_2 = M_R\left(1 + \frac{m_D^2}{M_R^2}\right) \approx M_R, \tag{2.15}$$

which is called the Seesaw type I mechanism [80–83]. The first mass m_1 corresponds to a light eigenstate, whereas m_2 corresponds to a heavy one. Therefore, the mechanism provides a natural way of generating a small neutrino mass, while the Yukawa coupling constant is compatible with those of other particles. It should be noted that there are also other types of Seesaw mechanisms that are not discussed here. More detailed information can be found in [84].

2.3.2 *Direct neutrino mass measurements*

One way of probing the neutrino mass is via precision measurements of the kinematics of single beta decay or electron capture (EC). Such direct neutrino mass searches have the advantage that they are model-independent and do not depend on the nature of the neutrino. In contrast, they give the weakest limits on the neutrino mass [9]. The mass observable in both cases is the effective mass m_β of the electron (anti)neutrino, which is the incoherent sum of the neutrino mass eigenstates (each eigenstate contributes individually but cannot be resolved experimentally at the moment):

$$m_\beta = \sqrt{\sum_{i=1}^{3} |U_{ei}|^2 \, m_i^2}. \tag{2.16}$$

In single beta decay, the released energy Q_β is shared between the decay products. The daughter nucleus receives a recoil energy E_{rec}, while the remaining energy, the so-called endpoint E_0, is split between the electron and the electron antineutrino with energies E_e and $E_{\bar{\nu}}$ [85]:

$$E_0 = Q_\beta - E_{\text{rec}} = E_e + E_{\bar{\nu}}. \tag{2.17}$$

Since the emitted antineutrino takes away at least the energy corresponding to its rest mass, the maximum energy the electron can receive is $E_0 - m_\beta$. Consequently, a non-vanishing neutrino mass distorts the electron energy spectrum in the vicinity of the endpoint, as illustrated in **Fig.** 2.3. Typically, the isotope tritium is used for direct neutrino mass searches using single beta decay. This is due to its short half-life ($T_{1/2} = 12.3\,\text{yr}$) and a comparably low endpoint ($E_0 \approx 18.6\,\text{keV}$). The recent most stringent upper limit on the electron antineutrino mass was obtained by the world-leading Karlsruhe Tritium Neutrino (KATRIN) experiment, the successor of the Mainz and Troitsk experiments, with $m_\beta < 1.1\,\text{eV}$ (90% CL) [8]. After an effective data taking time of three years, KATRIN targets to reach a final sensitivity on the neutrino mass of $0.2\,\text{eV}$.

A related and complementary approach for direct neutrino mass searches is the measurement of electron capture reactions, commonly using the nuclide ^{163}Ho. The imprint of the neutrino mass is comparable to the one in single beta decay, i.e. a spectral distortion in the region of the decay energy Q_{EC}. The electron capture spectrum is measured calorimetrically (source embedded in absorber), i.e. the energy released in the absorber is converted into a temperature rise read out by a sensitive thermo sensor. To this end, the ECHo experiment uses metallic magnetic calorimeters (MMCs) [86], whereas HOLMES uses transition-edge sensors (TESs) [87]. The experiments are designed to reach sub-eV sensitivity on the electron neutrino mass.

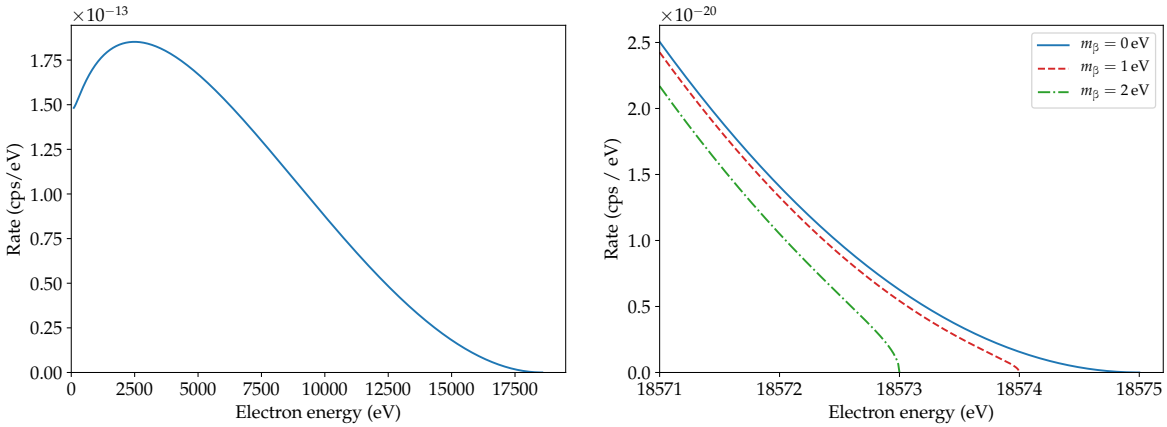

(a) Full spectrum.

(b) Endpoint region.

Figure 2.3: Differential electron energy spectrum of single beta decay of tritium ($^3\mathrm{H} \rightarrow {}^3\mathrm{He} + e^- + \overline{\nu}_e$). The signature of an electron antineutrino with a mass of $m_\beta = 1\,\mathrm{eV}$ ($m_\beta = 2\,\mathrm{eV}$) can be clearly identified by the spectral distortion in the vicinity close to the endpoint as shown in the right plot. Data provided by C. Karl.

2.3.3 *Cosmology*

Another probe of neutrino mass is provided by cosmological observations, in particular cosmological structure formation. Due to their vast abundance[6], neutrinos had a significant impact on the structure formation in the early universe. After decoupling from the early universe plasma at timescales of about 1 s, neutrinos were still relativistic over a long period of time with a large free streaming length[7]. The structures that we observe today were formed by small density fluctuations that grew in size due to gravitational clustering. By acting as hot dark matter, relic neutrinos mitigated this growth by washing-out structures (carrying away matter) on scales smaller than the free streaming length. The relic neutrino contribution to the non-relativistic energy density is accessible via cosmology by measuring the matter distribution of the universe. Finite neutrino mass results in a suppression of the matter power spectrum at small scales [88]. The relevant observable is the sum of the three neutrino mass eigenstates:

$$m_\Sigma = \sum_{i=1}^{3} m_i. \tag{2.18}$$

Assuming the existence of three massive neutrinos and the validity of the ΛCDM model, by combining data from measurements of the cosmic microwave background (CMB), polarization, gravitational lensing effects, as well as large scale structure information from baryonic acoustic oscillations (BAO), a very stringent upper limit of $m_\Sigma < 0.12\,\mathrm{eV}$ (95% CL) is obtained [66, 89]. It should be noted here that other combinations of astrophysical data or the introduction of additional cosmological parameters[8] give much less stringent limits. A current more conservative limit is on the order of $m_\Sigma < 0.3\,\mathrm{eV}$ [9]. In general, one of the drawbacks of neutrino mass determination via cosmology is the strong dependence of the results on the underlying cosmological model.

6 Today there are about 339 relic neutrinos/cm^3 from the Big Bang in the cosmos [59].
7 The free streaming length is the distance a neutrino can travel before it gets non-relativistic.
8 The minimal cosmological model uses $\geqslant 6$ parameters, e.g. Hubble constant, baryonic matter fraction, etc.

2.4 DOUBLE BETA DECAY

2.4.1 *Overview*

TWO-NEUTRINO DOUBLE BETA DECAY Typically, a nucleus with an excess of neutrons gradually converts into a more stable nucleus via single beta decay, cf. **Ch.** 2.1. In some (even-even) nuclei, however, single beta decay is energetically forbidden or highly suppressed, while the simultaneous occurrence of two beta decays, the so-called two-neutrino double beta decay ($2\nu\beta\beta$ decay) is the only SM-allowed decay mode, see **Fig.** 2.4. In this rare nuclear decay, two neutrons in the parent nucleus (A, Z) are converted into two protons in a daughter nucleus $(A, Z+2)$ via the weak interaction, and two electrons, as well as two electron antineutrinos are emitted:

$$2n \rightarrow 2p + 2e^- + 2\bar{\nu}_e. \tag{2.19}$$

The process is visualized in **Fig.** 2.5 and the corresponding Feynman diagram is illustrated in **Fig.** 2.6a. Since two leptons and two antileptons are emitted, lepton number is conserved ($\Delta L = 0$).

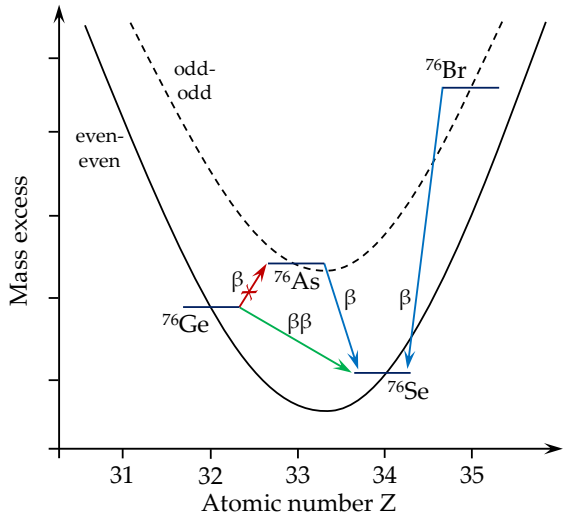

Figure 2.4: Mass parabolas for even-even and odd-odd nuclei (using the example of isobars with mass number $A = 76$). Isobars with even mass and atomic number lie on a lower parabola compared to those with odd atomic number. Typically, transitions between the curves are realized via single beta decay. In some cases, however, the neighboring isobar is energetically higher and single beta decay is forbidden, e.g. $^{76}\text{Ge} \not\rightarrow {}^{76}\text{As}$. Then, two-neutrino double beta decay is the only allowed decay mode.

Two-neutrino double beta decay is a second-order weak process that was first proposed in 1935 by M. Goeppert-Mayer [90]. So far, it has been observed experimentally in more than ten isotopes (e.g. ^{76}Ge, ^{130}Te, ^{136}Xe, etc.) with a typical half-life of $T^{2\nu}_{1/2} > 10^{18}$ yr [91]. The properties of commonly studied isotopes are listed in **Tab.** 2.2. The decay rate or inverse of the half-life of $2\nu\beta\beta$ decay can be expressed as [92]

$$\Gamma^{2\nu} = \frac{1}{T^{2\nu}_{1/2}} = G^{2\nu} \cdot g_A^4 \cdot |m_e c^2 \cdot M^{2\nu}|^2, \tag{2.20}$$

where $G^{2\nu}$ denotes the phase space factor, g_A the axial-vector coupling constant, m_e the electron mass, and $M^{2\nu}$ the nuclear matrix element (NME). The estimation of the axial-vector coupling constant is matter of debate: When comparing the measured and predicted $2\nu\beta\beta$ decay rates of several isotopes, the experimental values are systematically smaller than the estimated ones. This problem could be due to a quenching of g_A, induced by limitations inherent to the underlying models, many-body currents or non-nucleonic degrees of freedom [93, 94]. While for a free nucleon the coupling constant has a value of $g_A \approx 1.27$ [95], measured $2\nu\beta\beta$ decay rates can be described in terms of the effective coupling constant

$$g_A^{\text{eff}} = g_A \cdot A^{-\gamma}, \tag{2.21}$$

where γ takes values in the range $0.12 \leqslant \gamma \leqslant 0.18$, depending on the nuclear model used [96–98]. Novel ab-initio calculations can model these effects in the NME and have shown that for single beta decay, the discrepancy between experimental and theoretical decay rates can be resolved [99]. This might be also the case for double beta decay in the near future. First results are already available for the isotope ^{48}Ca [100].

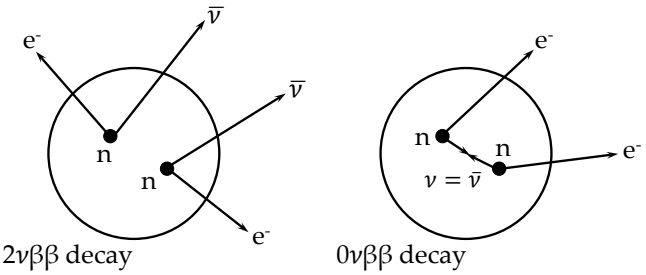

Figure 2.5: Schematic illustration of two-neutrino double beta decay ($2\nu\beta\beta$ decay) and neutrinoless double beta decay ($0\nu\beta\beta$ decay). Both processes are characterized by the simultaneous decay of two neutrons in one nucleus into two protons. $2\nu\beta\beta$ decay is accompanied by the emission of two electron antineutrinos and two electrons. In contrast, in $0\nu\beta\beta$ decay only two electrons are emitted.

In $2\nu\beta\beta$ decay, the energy is shared between the two electrons and the two electron antineutrinos in the final state (the nuclear recoil can be neglected). Therefore, the sum of the electron energy is a continuum ranging from 0 keV to the $Q_{\beta\beta}$-value of the decay, see **Fig.** 2.7. The spectral shape of the continuous energy spectrum can be approximated by the following empirical relationship [101]:

$$\frac{dN}{dE} \approx E \cdot \left(Q_{\beta\beta} - E\right)^5 \cdot \left(E^4 + 10E^3 + 40E^2 + 60E + 30\right). \tag{2.22}$$

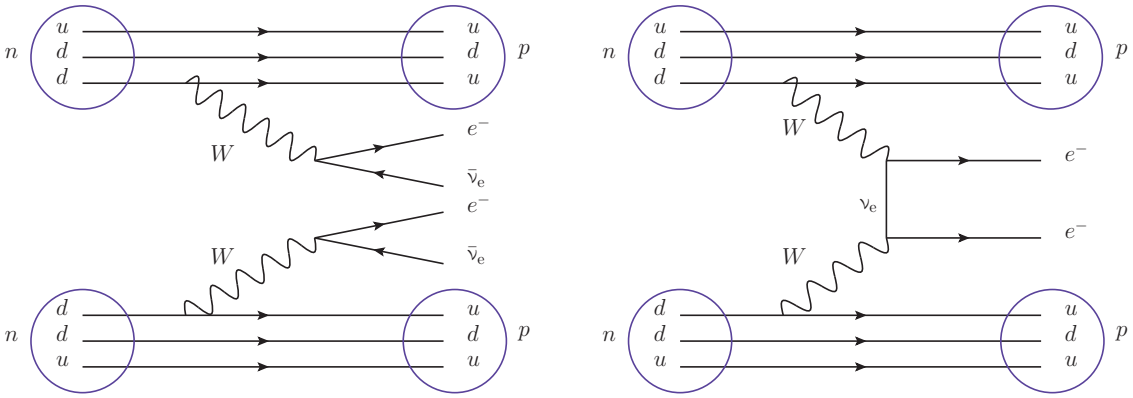

(a) Two-neutrino double beta decay ($2\nu\beta\beta$ decay).

(b) Neutrinoless double beta decay ($0\nu\beta\beta$ decay).

Figure 2.6: Feynman diagrams of (a) $2\nu\beta\beta$ decay and (b) $0\nu\beta\beta$ decay assuming light neutrino exchange.

NEUTRINOLESS DOUBLE BETA DECAY Neutrinoless double beta decay ($0\nu\beta\beta$ decay) is a hypothetical lepton number-violating process ($\Delta L = +2$) that is forbidden in the SM and has not yet been observed. It was proposed by W. H. Furry in 1939 [122–124]. Currently, the search for $0\nu\beta\beta$ decay is the most practical way of establishing that massive neutrinos are Majorana fermions [66]. In the decay, two neutrons in the parent nucleus are converted into two protons in a daughter nucleus and two electrons are emitted:

$$2n \rightarrow 2p + 2e^-. \tag{2.23}$$

The process is visualized in **Fig.** 2.5 and the corresponding Feynman diagram is shown in **Fig.** 2.6b. The decay can only occur if the virtual neutrino emitted at the first vertex is absorbed as a virtual antineutrino at the second vertex. This is only possible if the neutrino is identical to its antiparticle, and thus a Majorana fermion, cf. **Ch.** 2.3.1. Independent of the mechanism inducing it, the observation of $0\nu\beta\beta$ decay would not only prove the Majorana nature of the neutrino, but also the existence

Table 2.2: Overview and properties of commonly studied ββ-decaying isotopes. The table lists the isotopes including their decays and natural abundances [111], the $Q_{\beta\beta}$-values [112], the phase space factors $G^{0\nu}$ [92], the nuclear matrix elements $M^{0\nu}$ for light neutrino exchange [113–121], and the half-lives $T^{2\nu}_{1/2}$ of 2νββ decay.

Isotope and decay	Isotopic abundance (%)	$Q_{\beta\beta}$ (keV)	$G^{0\nu}$ ($10^{-15}\,\mathrm{yr}^{-1}$)	$\lvert M^{0\nu}\rvert$	$T^{2\nu}_{1/2}$ (yr)
$^{48}\mathrm{Ca} \rightarrow {}^{48}\mathrm{Ti}$	0.187(21)	4268.08(8)	24.81	0.30 – 2.94	$(6.4^{+0.7}_{-0.6}\,{}^{+1.2}_{-0.9}) \cdot 10^{19}$ [102]
$^{76}\mathrm{Ge} \rightarrow {}^{76}\mathrm{Se}$	7.73(12)	2039.060(10)	2.363	2.66 – 6.04	$(1.926 \pm 0.094) \cdot 10^{21}$ [103]
$^{82}\mathrm{Se} \rightarrow {}^{82}\mathrm{Kr}$	8.73(22)	2997.9(5)	10.16	2.72 – 5.40	$(8.60 \pm 0.03^{+0.19}_{-0.13}) \cdot 10^{19}$ [104]
$^{96}\mathrm{Zr} \rightarrow {}^{96}\mathrm{Mo}$	2.80(9)	3356.03(7)	20.58	2.83 – 6.47	$(2.35 \pm 0.14 \pm 0.16) \cdot 10^{19}$ [105]
$^{100}\mathrm{Mo} \rightarrow {}^{100}\mathrm{Ru}$	9.82(31)	3034.36(17)	15.92	3.90 – 6.58	$(7.12^{+0.18}_{-0.14} \pm 0.10) \cdot 10^{18}$ [106]
$^{116}\mathrm{Cd} \rightarrow {}^{116}\mathrm{Sn}$	7.49(18)	2813.49(13)	16.70	3.10 – 5.52	$(2.63^{+0.11}_{-0.12}) \cdot 10^{19}$ [107]
$^{130}\mathrm{Te} \rightarrow {}^{130}\mathrm{Xe}$	34.08(62)	2527.510(10)	14.22	1.70 – 6.41	$(8.2 \pm 0.2 \pm 0.6) \cdot 10^{20}$ [108]
$^{136}\mathrm{Xe} \rightarrow {}^{136}\mathrm{Ba}$	8.8573(44)	2457.8(3)	14.58	1.11 – 4.77	$(2.165 \pm 0.016 \pm 0.059) \cdot 10^{21}$ [109]
$^{150}\mathrm{Nd} \rightarrow {}^{150}\mathrm{Sm}$	5.638(28)	3371.38(20)	63.034	1.71 – 5.46	$(9.34 \pm 0.22^{+0.62}_{-0.60}) \cdot 10^{18}$ [110]

of BSM physics that could explain the dominance of baryonic matter over antimatter in our universe via Leptogenesis [84]. In particular, a lepton-number violating process could be linked to Baryon number violation via standard model sphaleron processes, i.e. non-perturbative solutions to the electroweak field equations [88, 125, 126]. Together with the two other Sakharov conditions (C and CP violation, interactions out of thermal equilibrium), these are necessary (but not sufficient) criteria for the dynamic production of a baryon asymmetry [127]. Moreover, together with measurements from cosmology and direct neutrino mass measurements, 0νββ decay can provide information on the absolute neutrino mass scale and ordering, cf. **Ch.** 2.4.2. In general, the decay can be mediated by various mechanisms. The simplest is based on the exchange of light massive Majorana neutrinos. Other channels involve non-standard interactions such as right-handed currents or the exchange of supersymmetric particles [9, 128], and are not considered here. Independent of the mediating mechanism, any realization that allows 0νββ decay to occur would result in a non-zero effective Majorana mass term as described by the Schechter-Valle theorem [123, 129].

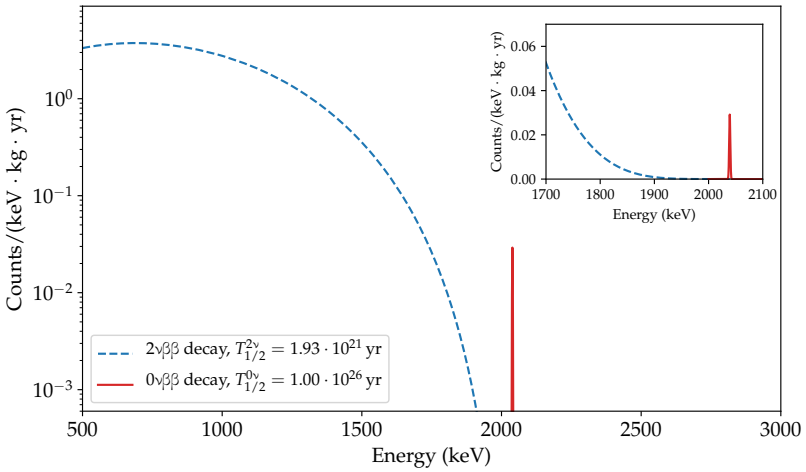

Figure 2.7: Experimental signature of 0νββ decay: Gaussian peak at the $Q_{\beta\beta}$-value ($Q_{\beta\beta} \approx 2039$ keV for ^{76}Ge) for a given half-life $T^{0\nu}_{1/2}$ above the two-neutrino double beta decay (2νββ decay) continuum. The peak width and amplitude (see inset) are determined by the finite energy resolution of the detectors. The expected distribution of 2νββ decay events is shown assuming the half-life measured by the GERDA experiment [103, 130]. Data provided by Y. Kermaïdic.

The final state of 0νββ decay consists of the daughter nucleus and two electrons. Due to the huge mass difference between the nucleus and the two emitted leptons (typically five orders of magnitude), the nuclear recoil can be neglected [58, 94]. Therefore, since there are no neutrinos in the

final state, the emitted electrons share the total energy $Q_{\beta\beta}$ released in the decay. Consequently, the experimental signature of $0\nu\beta\beta$ decay is a mono-energetic peak centered at the $Q_{\beta\beta}$-value as illustrated in **Fig.** 2.7. The $Q_{\beta\beta}$-value is usually well measured, e.g. in high-precision atomic traps, and the peak width is solely determined by the finite energy resolution of the detectors in $0\nu\beta\beta$ decay experiments [9]. The expected half-lives of $0\nu\beta\beta$ decay are much higher than in the case of $2\nu\beta\beta$ decay, since $T^{0\nu}_{1/2}$ is inversely proportional to the square of the neutrino mass, cf. **Ch.** 2.4.2. Therefore, the rejection of backgrounds, particularly in the region of interest (ROI) around the $Q_{\beta\beta}$-value, is of major importance in $0\nu\beta\beta$ decay searches.

2.4.2 *Effective Majorana mass*

In the following, it is assumed that $0\nu\beta\beta$ decay is mediated by the exchange of light Majorana neutrinos and that only the three known neutrinos participate in the process. The mass observable in $0\nu\beta\beta$ decay is the effective Majorana mass $\langle m_{\beta\beta}\rangle$. It can be related to the decay rate ($\Gamma^{0\nu}$) or inverse of the decay half-life ($T^{0\nu}_{1/2}$) via

$$\Gamma^{0\nu} = \frac{1}{T^{0\nu}_{1/2}} = g_A^4 \cdot G^{0\nu} \cdot |M^{0\nu}|^2 \cdot \frac{\langle m_{\beta\beta}\rangle^2}{m_e^2} \quad \Leftrightarrow \quad \langle m_{\beta\beta}\rangle = \frac{m_e}{g_A^2 \cdot |M^{0\nu}|} \cdot \sqrt{\frac{1}{T^{0\nu}_{1/2} \cdot G^{0\nu}}}. \tag{2.24}$$

Here, $G^{0\nu} = G^{0\nu}(Q_{\beta\beta}, Z) \propto Q^5_{\beta\beta}$ describes the phase space factor that depends on the $Q_{\beta\beta}$-value and on the atomic number Z [9]. Moreover, $\left|M^{0\nu}\right|$ denotes the NME describing the nuclear structure of the parent, intermediate, and daughter nuclei. For the axial-vector coupling constant, it is current convention to use an unquenched value[9] of $g_A \approx 1.27$ [95]. The phase space factor is calculable precisely and recent calculations state a value of $G^{0\nu} = 2.363 \cdot 10^{-15}\,\mathrm{yr}^{-1}$ for the isotope ^{76}Ge [92]. In contrast, the NME is obtained from nuclear theory (many-body problem) and its calculation has large theoretical uncertainties. Depending on the actual nuclear model[10], values differ by a factor of two to three. More accurate calculations[11] are highly desirable since the NME is crucial for the interpretation of the effective Majorana mass. More detailed information on the current status of NME calculations for different $0\nu\beta\beta$-decaying isotopes can be found in [95, 113, 117, 121, 131]. For the isotope ^{76}Ge, values in the range $2.66 \leqslant \left|M^{0\nu}\right| \leqslant 6.04$ are currently considered [113, 115].

From the theoretical point of view, the effective Majorana mass is a coherent[12] sum of the different neutrino mass eigenstates m_i weighted with the neutrino mixing matrix elements U_{ei}:

$$\langle m_{\beta\beta}\rangle = \left|\sum_i U_{ei}^2 m_i\right| = \left|\sum_i |U_{ei}|^2\, m_i e^{i\alpha_i}\right|. \tag{2.25}$$

In the three-flavor case together with the standard parameterization in **Eq.** (2.6), this can be written as

$$\langle m_{\beta\beta}\rangle = \left|m_1 |U_{e1}|^2 + m_2 |U_{e2}|^2 e^{2i\alpha} + m_3 |U_{e3}|^2 e^{2i\beta}\right|. \tag{2.26}$$

Even though this allows for cancellations, a full cancellation is only possible for a limited range of m_1 in the NO regime. **Fig.** 2.8 shows a geometrical interpretation of **Eq.** (2.26) as a vector sum. Expanding **Eq.** (2.26) using **Eq.** (2.6) and the substitutions $2\alpha(\beta) \to \alpha(\beta)$ and $2(-\delta+\beta) \to \beta$ yields

$$\langle m_{\beta\beta}\rangle = \left|c_{12}^2 c_{13}^2 m_1 + s_{12}^2 c_{13}^2 m_2 e^{i\alpha} + s_{13}^2 m_3 e^{i\beta}\right| \tag{2.27}$$

$$= \sqrt{a_1^2 + a_2^2}, \tag{2.28}$$

where

$$a_1 = c_{12}^2 c_{13}^2 m_1 + s_{12}^2 c_{13}^2 m_2 \cos\alpha + s_{13}^2 m_3 \cos\beta, \tag{2.29}$$

$$a_2 = s_{12}^2 c_{13}^2 m_2 \sin\alpha + s_{13}^2 m_3 \sin\beta. \tag{2.30}$$

9 As of yet it is unknown if the quenching in $2\nu\beta\beta$ and $0\nu\beta\beta$ decay is the same.

10 The four main models are the quasi-particle random phase approximation (QRPA), the nuclear shell model (NSM), the interacting boson model (IBM), and the energy density functional (EDF). It is generally accepted that all these models neglect certain aspects of nuclear physics, different in each case [10].

11 The difficulty of NME calculations arises from the fact that one has to deal with a many-body problem, i.e. the initial- and final-state nuclear wave functions need to be known. Currently, precise calculations of the nuclear structure are only possible for systems characterized by a low mass number [9].

12 The term coherent refers to the CP-violating phases in the PMNS matrix that can lead to a destructive interference.

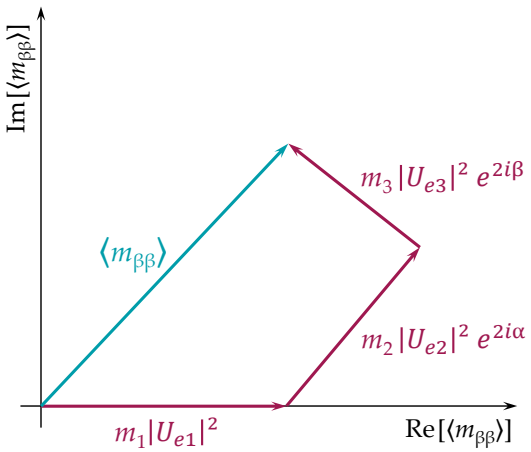

Figure 2.8: Interpretation of the effective Majorana mass $\langle m_{\beta\beta}\rangle$ as a vector sum. The m_1 component has no Majorana phase (choice in PMNS matrix).

The effective Majorana mass in **Eq.** (2.28) can be expressed as a function of other neutrino mass observables. **Fig.** 2.9 shows the allowed $\langle m_{\beta\beta}\rangle$ parameter space as a function of the lightest neutrino mass m_{lightest}, the neutrino mass m_β from direct mass measurements, and the sum m_Σ of the neutrino mass eigenstates. The bands corresponding to the NO and IO are based on the definitions in **Eqs.** (2.8) and (2.9), respectively. The size of the bands are driven by the unknown Majorana phases α and β that are varied in the interval $[0, 2\pi]$.

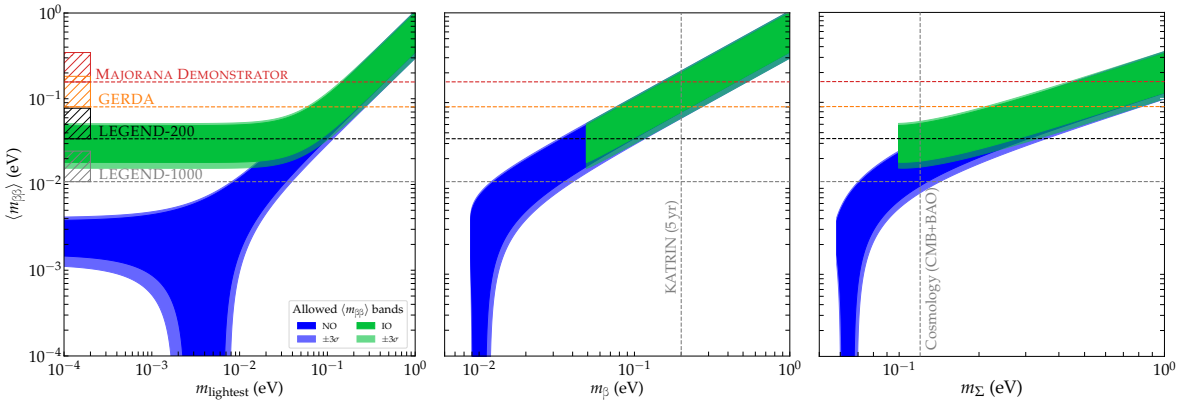

(a) $\langle m_{\beta\beta}\rangle$ vs m_{lightest}. (b) $\langle m_{\beta\beta}\rangle$ vs m_β. (c) $\langle m_{\beta\beta}\rangle$ vs m_Σ.

Figure 2.9: Correlation of the different neutrino mass observables: (a) Effective Majorana mass $\langle m_{\beta\beta}\rangle$ as a function of the lightest neutrino mass m_{lightest}, (b) the neutrino mass m_β from direct mass measurements, and (c) the sum m_Σ of the neutrino mass eigenstates. The plots show the allowed $\langle m_{\beta\beta}\rangle$ regions for the normal ordering (NO, blue bands) and the inverted ordering (IO, green bands). The bands correspond to the best fit values of neutrino oscillation parameters from [76]. The phases α and β are varied in the interval $[0, 2\pi]$. 3σ uncertainty bands are obtained by propagating the uncertainties on the mixing angles and squared mass differences. The plots also show the allowed $\langle m_{\beta\beta}\rangle$ ranges of former (GERDA, MAJORANA DEMONSTRATOR), current (LEGEND-200), and future (LEGEND-1000) ^{76}Ge-based $0\nu\beta\beta$ decay experiments (with the horizontal dashed lines representing the lower bounds). Moreover, the sensitivity of the KATRIN experiment on m_β, and the most stringent limit from cosmological observations on m_Σ are indicated by the vertical lines. Plot first introduced in [132].

As can be seen from the figure, in the NO for values $m_{\text{lightest}} \lesssim 10^{-3}$ eV, the effective Majorana mass is distributed on a flat area. In the range 10^{-3} eV $\lesssim m_{\text{lightest}} \lesssim 10^{-2}$ eV, $\langle m_{\beta\beta}\rangle$ can vanish due to the combination of Majorana phases, even though all m_i are non-vanishing. For higher values of m_{lightest}, the IO and NO bands are overlapping. This region corresponds to the so-called quasi-degenerate regime in which the overall mass scale dominates the ordering, i.e. $m_1 \approx m_2 \approx m_3$

(mass splittings do not play a role). The plots also show that a limit on the effective Majorana mass of $\langle m_{\beta\beta}\rangle \lesssim 20\,\text{meV}$ would disfavor Majorana neutrinos in the IO. This can be tested with future $0\nu\beta\beta$ decay experiments, e.g. LEGEND-1000, cf. **Ch.** 4.3.2, that will fully cover the IO range. The $\langle m_{\beta\beta}\rangle$ ranges of former, current, and future ^{76}Ge-based $0\nu\beta\beta$ decay experiments shown in **Fig.** 2.9 were calculated using **Eq.** (2.24). The sizes of these ranges reflect the large uncertainties of the NMEs. Current experiments probe values of the effective Majorana mass of $\mathcal{O}(100\,\text{meV})$. The figure also indicates the predicted sensitivity of direct neutrino mass measurements with the KATRIN experiment ($m_\beta = 0.2\,\text{eV}$), cf. **Ch.** 2.3.2, and the most stringent limit on the sum of the neutrino masses obtained from cosmological observations ($m_\Sigma < 0.12\,\text{eV}$), cf. **Ch.** 2.3.3. It is worthwhile to mention that currently there are no tensions between the different mass observables [133].

2.4.3 *Experimental sensitivity*

One of the key parameters in experimental $0\nu\beta\beta$ decay searches is the sensitivity on the half-life $T^{0\nu}_{1/2}$. An expression for the sensitivity can be derived by comparing the number of expected signal events (N_S) to the number of background events (N_B). The former quantity is given by the product of the initial number $N_{\beta\beta}$ of $0\nu\beta\beta$-decaying isotopes, the probability $P(t)$ to decay after a certain measurement time t, and the total detection efficiency ϵ_{det}:

$$N_S = N_{\beta\beta} \cdot P(t) \cdot \epsilon_{\text{det}}. \tag{2.31}$$

The probability can be calculated according to

$$P(t) = \frac{1}{\tau}\int_0^t \exp\left(-\frac{t'}{\tau}\right) dt' = 1 - \exp\left(-\frac{t}{\tau}\right) \approx \frac{t}{\tau}, \tag{2.32}$$

where $\tau = T^{0\nu}_{1/2}/\log(2)$. In the last step, a Taylor expansion was used for the exponential since $t \ll \tau$. The initial number of isotopes in a material with total mass M, atomic mass m_a and enrichment fraction f_{enr} can be expressed as [58]

$$N_{\beta\beta} = \frac{M}{m_a} \cdot f_{\text{enr}}. \tag{2.33}$$

Therefore, the number of expected signal events can be written as

$$N_S = \frac{\log(2)}{m_a} \cdot \frac{f_{\text{enr}} \cdot \epsilon_{\text{det}}}{T^{0\nu}_{1/2}} \cdot M \cdot t. \tag{2.34}$$

The product $M \cdot t$ of the detector mass and the measurement time is usually denoted as exposure. On the other side, the number of background events induced by cosmic radiation and radioactive contaminations is given by [58]

$$N_B = BI \cdot \Delta E \cdot M \cdot t, \tag{2.35}$$

where BI denotes the background index (usually expressed in terms of $\text{cts}/(\text{keV}\cdot\text{kg}\cdot\text{yr})$ or equally $\text{cts}/(\text{FWHM}\cdot t\cdot\text{yr})$), representing the background level in the ROI, and ΔE a certain energy window around the $Q_{\beta\beta}$-value (typically chosen equal to the energy resolution of the detector). For a signal discovery (evidence), the number of signal events (N_S) needs to be 5σ (3σ) away from the number of background events (N_B). Assuming Poissonian statistics and using **Eqs.** (2.34) and (2.35), one obtains at the $3\,\sigma$ level

$$N_S > 3\sqrt{N_B} \tag{2.36}$$

$$\Leftrightarrow T^{0\nu}_{1/2}(3\sigma\ \text{DS}) \propto \frac{\log(2)}{m_a} \cdot f_{\text{enr}} \cdot \epsilon_{\text{det}} \cdot \sqrt{\frac{M\cdot t}{BI\cdot\Delta E}} \tag{2.37}$$

For the next generation of $0\nu\beta\beta$ decay experiments, it is crucial to stay in a background-free regime, i.e. in an environment in which the BI is so low that the expected number of background events is below one count ($N_B \lesssim 1$) within the energy region of interest at a given exposure $M \cdot t$. In this case, the sensitivity scales linearly with the exposure. The two different cases can be summarized as follows:

$$T^{0\nu}_{1/2}(3\sigma\ \text{DS}) \propto \begin{cases} f_{\text{enr}} \cdot \epsilon_{\text{det}} \cdot \sqrt{\frac{M\cdot t}{BI\cdot\Delta E}}, & \text{with background,} \\ f_{\text{enr}} \cdot \epsilon_{\text{det}} \cdot M \cdot t, & \text{background-free.} \end{cases} \tag{2.38}$$

As can be seen from **Eq.** (2.38), there are several ways to increase the experimental sensitivity. In particular, it is preferable to have a high enrichment fraction f_{enr}, a high detection efficiency ϵ_{det}, a large exposure $M \cdot t$, a low background index BI, and a good energy resolution ΔE. Future $0\nu\beta\beta$ decay experiments will operate some hundred kilograms (up to the tonne-scale) of isotope mass for several years. In the presence of backgrounds, the sensitivity scales with the square root of the exposure. This decreases the signal discovery sensitivity considerably as shown for the example of the isotope ^{76}Ge in **Fig.** 2.10.

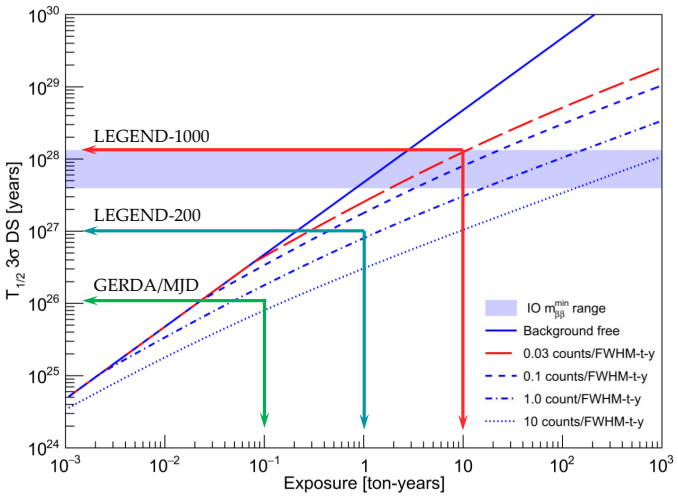

Figure 2.10: Signal discovery sensitivity for the isotope ^{76}Ge as a function of exposure. To increase the discovery sensitivity, one needs to stay close to the background-free regime (solid blue line). The presence of backgrounds (dashed lines) reduces the sensitivity considerably. The blue band shows the allowed region of the inverted mass ordering regime corresponding to an effective Majorana mass of $\langle m_{\beta\beta} \rangle = 10 - 17$ meV (assuming the worst case nuclear matrix element and an unquenched axial-vector coupling constant g_A). The width of the band is due to the uncertainty of the matrix element. The red lines indicate the goal of LEGEND-1000 with a targeted background of BI < 0.03 cts/(FWHM $\cdot$ t $\cdot$ yr) and a sensitivity on the half-life of $T^{0\nu}_{1/2} > 10^{28}$ yr. Adpated from [134–136].

2.4.4 *Status and prospects of $0\nu\beta\beta$ decay searches*

2.4.4.1 *Overview*

A vigorous worldwide experimental program is currently underway to search for the rare $0\nu\beta\beta$ decay in several candidate isotopes (e.g. ^{76}Ge, ^{82}Se, ^{100}Mo, etc.). In this section, some design-considerations of $0\nu\beta\beta$ decay experiments are discussed, including the choice of isotopes and the various detection technologies.

ISOTOPE CHOICES The properties of some of the commonly studied $\beta\beta$-decaying isotopes are summarized in **Tab.** 2.2. Given **Eq.** (2.38), to increase the experimental sensitivity on the $0\nu\beta\beta$ decay half-life, an ideal isotope should be deployable in large quantity. Moreover, there should be the possibility to enrich the material at reasonably low cost. Most of the candidate isotopes have abundances between $\sim 0.19\%$ (^{48}Ca) and $\sim 34\%$ (^{130}Te). The $Q_{\beta\beta}$-values of the considered isotopes are in the range $2\,\text{MeV} \lesssim Q_{\beta\beta} \lesssim 4\,\text{MeV}$, see **Tab.** 2.2. An optimal $0\nu\beta\beta$ decay isotope would have a $Q_{\beta\beta}$-value above the endpoint of environmental radioactivity background. Since most of the typical radioactive contaminants do not emit radiation above the 2.6 MeV ^{208}Tl gamma line, a reaction endpoint higher than this value is preferred. The correlation between the $Q_{\beta\beta}$-value and the isotopic abundance of various isotopes is depicted in **Fig.** 2.11. Finally, the selected technology should encompass a high energy resolution, and a high detection efficiency. The latter can be significantly enhanced by using a source medium that is equal to the detector medium.

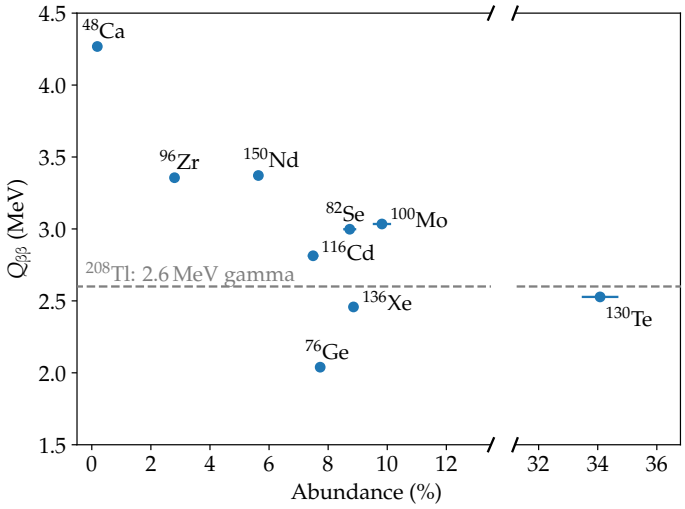

Figure 2.11: Correlation between the $Q_{\beta\beta}$-value and the isotopic abundance of various $\beta\beta$-decaying isotopes. The grey dashed line indicates the 2.6 MeV ^{208}Tl gamma line. In general, the higher the natural abundance and the $Q_{\beta\beta}$-value, the more suited is the isotope. Data from [111, 112].

Unfortunately, there is no isotope that combines all favorable properties, and design choices have to be made to optimize a subset of these parameters [9, 137]. Since designing a $0\nu\beta\beta$ decay experiment essentially depends on the characteristics of the selected isotope, various detection technologies have been developed. Much experimental progress has been made since the first searches for $0\nu\beta\beta$ decay were performed [138–140]. Nowadays, the main technologies used within the field may be classified as semiconductor detectors, cryogenic bolometers, isotope-loaded liquid scintillator detectors, time projection chambers (TPCs), and tracking calorimeters [9, 10]. Semiconductor detectors are of particular importance for the work presented in this thesis and are addressed in detail in **Ch. 3**. The other technologies will be discussed briefly in the following paragraphs. The most stringent current limits on the $0\nu\beta\beta$ decay half-life and the effective Majorana mass of various isotopes are listed in **Tab. 2.3**. Furthermore, an overview of the experimental landscape of current and future $0\nu\beta\beta$ decay experiments is shown in **Fig. 2.12**.

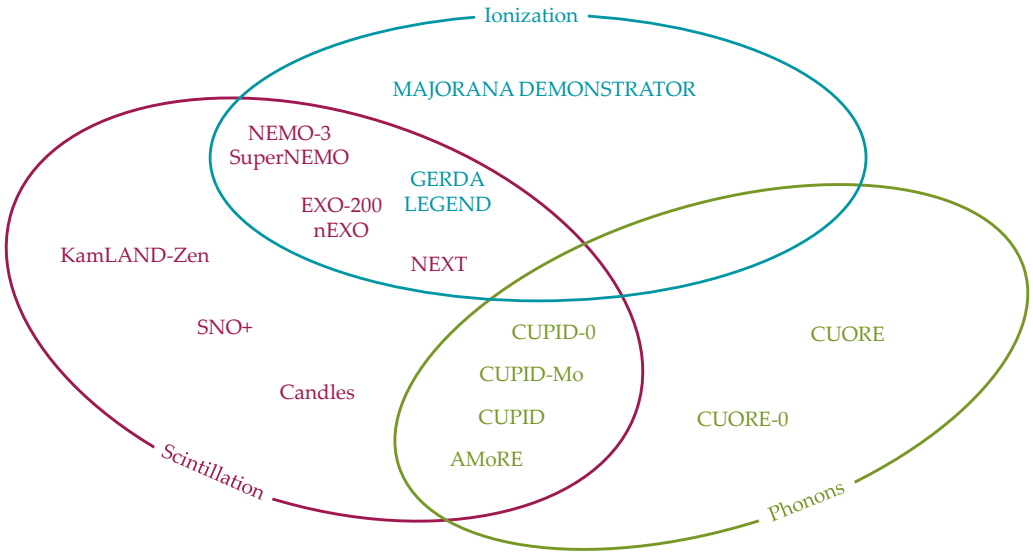

Figure 2.12: Landscape of current and future $0\nu\beta\beta$ decay experiments. The experiments are categorized according to their detection technique: ionization, scintillation (light), and phonons (heat). Several experiments deploy various techniques to increase their experimental sensitivity. Plot idea from [141].

Table 2.3: Overview of limits on the $0\nu\beta\beta$ decay half-life $T^{0\nu}_{1/2}$ (90% CL) and on the effective Majorana mass $\langle m_{\beta\beta}\rangle$ (assuming light Majorana neutrino exchange) from recent measurements for the isotopes ^{76}Ge, ^{82}Se, ^{100}Mo, ^{130}Te, and ^{136}Xe.

Isotope	Experiment	$T^{0\nu}_{1/2}$ (10^{25} yr)	$\langle m_{\beta\beta}\rangle$ (meV)
^{76}Ge	GERDA [130]	>18	$<79-180$
	MAJORANA DEM. [142]	>2.7	$<200-433$
^{82}Se	CUPID-0 [143]	>0.35	$<311-638$
^{100}Mo	NEMO-3 [144]	>0.11	$<330-620$
	CUPID-Mo [145]	>0.14	$<310-540$
^{130}Te	CUORE [146]	>3.2	$<75-350$
^{136}Xe	EXO-200 [147]	>3.5	$<93-286$
	KamLAND-Zen [148]	>10.7	$<61-165$

CRYOGENIC BOLOMETERS Bolometers are cryogenic detectors that are operated at temperatures of $\sim 10-20$ mK. Typically, they consist of an absorber crystal (e.g. TeO_2, $^{116}CdWO_4$, $Zn^{82}Se$, $Li_2{}^{100}MoO_4$, etc.) containing the $\beta\beta$-decaying isotope. The absorber is connected to a low-temperature thermal bath via a thermal coupling. Energy depositions are registered as a temperature rise on the order of 100 µK/MeV. To read out the minuscule temperate change, highly sensitive phonon sensors such as neutron-transmutation-doped (NTD) Ge or Si thermistors, MMCs, and TESs are used. Due to excellent counting statistics in the phonon channel, bolometers have an excellent energy resolution comparable to the one of semiconductor detectors [9, 149].

The CUORE (Cryogenic Underground Observatory for Rare Events) experiment at the underground Laboratori Nazionali del Gran Sasso (LNGS) in Italy operates an array consisting of 988 TeO_2 absorber crystals with a total mass of about 206 kg of candidate isotope ^{130}Te. The bolometers are cooled to a temperature of ~ 11 mK using a ^{3}He/^{4}He dilution refrigerator. In the latest data release, encompassing a total exposure of $M \cdot t = 372.5\,\mathrm{kg}\cdot\mathrm{yr}$, a lower limit on the $0\nu\beta\beta$ decay half-life of ^{130}Te of $T^{0\nu}_{1/2} > 3.2\cdot 10^{25}$ yr (90% CL) was obtained. In addition, a background of $\mathrm{BI} = (1.38\pm 0.07)\cdot 10^{-2}\,\mathrm{cts}/(\mathrm{keV}\cdot\mathrm{kg}\cdot\mathrm{yr})$ was observed in the ROI, largely dominated by alpha particles emitted at the detector surface [146]. By using scintillating absorber crystals and measuring both the heat and light signal, particle identification and discrimination becomes possible: Surface alphas can be suppressed since they emit a different amount of light than beta and gamma particles [150]. This approach is currently being pursued by the CUPID collaboration that plans to operate an array of 1500 scintillating $Li_2{}^{100}MoO_4$ crystals with a total mass of 250 kg of ^{100}Mo (enrichment $> 95\%$) [151]. A similar effort is pursued by the AMoRE collaboration that deploys 100 kg of ^{100}Mo in $> 95\%$ enriched $Ca^{100}MoO_4$ crystals at Y2L in South Korea [152].

SCINTILLATOR DETECTORS Even though liquid scintillator detectors have a comparably poor energy resolution, they are an attractive technology for $0\nu\beta\beta$ decay searches since they allow for relatively simple mass scalability. The scintillating liquid is used as a matrix for the $\beta\beta$-decaying isotope and can be purified to very low radioactive levels. Energy depositions are registered via the detection of the (typically wavelength-shifted) scintillation light using photosensors such as PMTs [9].

The KamLAND-Zen collaboration deploys several tonnes of liquid scintillator doped with ^{136}Xe contained in a transparent nylon mini-balloon. The mini-balloon is suspended in liquid scintillator at the center of an outer balloon. In the KamLAND-Zen 400 experiment, $320-380$ kg of ^{136}Xe were loaded in two phases from 2011 to 2015. A lower limit on the decay half-life of $T^{0\nu}_{1/2} > 1.07\cdot 10^{26}$ yr (90% CL) was obtained for an exposure of $M\cdot t = 504\,\mathrm{kg}\cdot\mathrm{yr}$ [148]. Currently, the KamLAND-Zen 800 experiment operates 750 kg of ^{136}Xe in a new clean mini-balloon. In the future, the collaboration plans to operate over one tonne of enriched xenon with an improved energy resolution in the KamLAND2-Zen experiment.

The SNO+ experiment at SNOLAB in Canada consists of a 12 m diameter acrylic vessel filled with 780 t of tellurium-loaded liquid scintillator. The scintillation light is read out by ~9300 inward facing PMTs. A first loading with 0.5% in natural tellurium has started in 2019 [153].

TIME PROJECTION CHAMBERS The main appeal of time projection chambers (TPCs) as detectors for $0\nu\beta\beta$ decay searches is the combination of mass scalability and the possibility of enhanced background discrimination capabilities. TPCs use a detection medium, typically xenon, that allows to simultaneously read out the scintillation and the ionization signal. While the ionization electrons are drifted towards an electrode (charge collection grid) by means of an electric field, the prompt scintillation light is detected via photosensors. The combination of these signals allows for energy and position reconstruction. Moreover, the different ionization-to-scintillation ratios for alpha and beta/gamma particles can be exploited to reject backgrounds. Xenon TPCs have several additional advantages: the isotope can be enriched, is easy to purify, is self-shielding, and can be built for both liquid and gas phases [9].

In the EXO-200 experiment, 110 kg of liquid xenon, enriched to 80.6% in ^{136}Xe, were operated in a cylindrical single-phase TPC. Data taking proceeded in two phases and ended in 2018. For a total exposure of $M \cdot t = 234.1\,\mathrm{kg \cdot yr}$, no statistically significant evidence for $0\nu\beta\beta$ decay was observed. A lower limit on the decay half-life of $T^{0\nu}_{1/2} > 3.5 \cdot 10^{25}\,\mathrm{yr}$ (90% CL) was obtained. The planned tonne-scale successor to EXO-200, nEXO, targets a sensitivity on the a half-life of about 10^{28} yr [9, 109, 147, 154].

The NEXT collaboration plans to operate a high-pressure gas-phase xenon TPC. In this less dense detection environment, individual electron tracks can be resolved. This allows for an excellent event topology reconstruction and thus additional background rejection. NEXT-100, a pilot project at LSC in Spain, has just started operation [9, 155, 156]. A similar approach is currently being pursued at CJPL with PandaX III [157].

TRACKING CALORIMETERS In contrast to the detection technologies discussed above, in tracking calorimeters the $\beta\beta$-decaying source is not equal to the detector. Typically, a multilayer detection strategy is applied: A thin foil of source material is surrounded by a low-pressure gas tracker (electron track reconstruction) and a calorimetric layer (energy reconstruction). While the technique provides excellent topological information, mass scalability is rather limited [9].

The NEMO-3 facility studied multiple $0\nu\beta\beta$ decay isotopes, mostly ^{100}Mo. A demonstrator module of the next-generation detector, SuperNEMO, with 6.3 kg of ^{82}Se is currently under commissioning at the LSM underground laboratory in France [102, 110, 144, 158, 159].

2.4.4.2 $0\nu\beta\beta$ *decay searches in* ^{76}*Ge*

ADVANTAGES OF THE ISOTOPE ^{76}GE The search for $0\nu\beta\beta$ decay with germanium semiconductor detectors has a 50 year-long history. This can be related to the fact that germanium as an isotope with 32 protons and 44 neutrons has several advantages. First, germanium detectors are an established radiation detection technology with an excellent energy resolution of about 0.1% FWHM (full width at half maximum) in the ROI at the $Q_{\beta\beta}$-value of $Q_{\beta\beta} = 2039.06\,\mathrm{keV}$ [189]. This is important to effectively suppress the intrinsic background contribution from $2\nu\beta\beta$ decay, particularly events from the high-energy tail, see **Fig.** 2.7. In addition, germanium detectors are intrinsically pure (impurities are removed during crystal growing) and can be enriched from 7.7% to above 92% in the $\beta\beta$-decaying isotope ^{76}Ge [9, 190]. Another advantage is that the detector is equal to the source. This translates into a high signal detection efficiency of $\epsilon_{\mathrm{det}} \approx 80\%$ [94]. Furthermore, germanium has a high density and thus a large stopping power. The topology of a $0\nu\beta\beta$ decay event in the detector is an energy deposition at a single site. This can be exploited to apply pulse shape discrimination (PSD) methods to powerfully reject background events with a different event topology (e.g. Compton-scattered gammas or surface events), cf. **Ch.** 4.1.2. Due to the distinct advantages discussed above, germanium detectors constitute one of the most auspicious technologies for next-generation $0\nu\beta\beta$ decay searches exploiting the tonne-scale.

Table 2.4: Chronology of lower limits on the $0\nu\beta\beta$ decay half-life $T^{0\nu}_{1/2}$ of the isotope ^{76}Ge. The claims from part of the HdM collaboration are denoted as HdM-KK.

Experiment	Date	$T^{0\nu}_{1/2}$ (yr)
Milano	1967	$> 3.1 \cdot 10^{20}$ (68% CL) [140]
Milano	1970	$> 1.2 \cdot 10^{21}$ (68% CL) [160]
Milano	1973	$> 5.0 \cdot 10^{21}$ (68% CL) [161]
PNL-USC	1983	$> 1.7 \cdot 10^{22}$ (90% CL) [162]
Caltech	1984	$> 1.7 \cdot 10^{22}$ (68% CL) [163]
GDK	1984	$> 3.2 \cdot 10^{22}$ (68% CL) [164]
Milano	1984	$> 5.0 \cdot 10^{22}$ (68% CL) [165]
Milano	1984	$> 1.2 \cdot 10^{23}$ (68% CL) [166]
PNL-USC	1985	$> 7.0 \cdot 10^{22}$ (68% CL) [167]
PNL-USC	1985	$> 1.16 \cdot 10^{23}$ (68% CL) [168]
Milano	1986	$> 1.65 \cdot 10^{23}$ (68% CL) [169]
Gotthard	1989	$> 2.7 \cdot 10^{23}$ (68% CL) [170]
ITEP/YePI	1990	$> 1.3 \cdot 10^{24}$ (68% CL) [171]
Gotthard	1992	$> 6.0 \cdot 10^{23}$ (68% CL) [172]
HdM	1992	$> 1.4 \cdot 10^{24}$ (90% CL) [173]
HdM	1995	$> 5.6 \cdot 10^{24}$ (90% CL) [174]
IGEX	1996	$> 4.2 \cdot 10^{24}$ (90% CL) [175]
HdM	1997	$> 7.4 \cdot 10^{24}$ (90% CL) [176]
IGEX	1999	$> 8.0 \cdot 10^{24}$ (90% CL) [177]
IGEX	2000	$> 1.57 \cdot 10^{25}$ (90% CL) [178]
HdM	2001	$> 1.9 \cdot 10^{25}$ (90% CL) [179]
HdM-KK	2001	$(1.5^{+1.6}_{-0.5}) \cdot 10^{21}$ [180]
IGEX	2003	$> 1.6 \cdot 10^{25}$ (90% CL) [181]
HdM-KK	2004	$(1.19^{+0.37}_{-0.23}) \cdot 10^{25}$ [182]
HdM-B	2005	$> 1.55 \cdot 10^{25}$ (90% CL) [183]
HdM-KK	2006	$(2.23^{+0.44}_{-0.31}) \cdot 10^{25}$ [184]
GERDA	2013	$> 2.1 \cdot 10^{25}$ (90% CL) [185]
GERDA	2017	$> 5.3 \cdot 10^{25}$ (90% CL) [186]
MJD	2018	$> 1.9 \cdot 10^{25}$ (90% CL) [187]
GERDA	2018	$> 8.0 \cdot 10^{25}$ (90% CL) [188]
MJD	2019	$> 2.7 \cdot 10^{25}$ (90% CL) [142]
GERDA	2019	$> 0.9 \cdot 10^{26}$ (90% CL) [133]
GERDA	2020	$> 1.8 \cdot 10^{26}$ (90% CL) [130]

HISTORICAL OVERVIEW A chronology of the searches for $0\nu\beta\beta$ decay in the isotope ^{76}Ge and the associated lower limits on the decay half-life are listed in **Tab.** 2.4. In addition, a graphical representation of the chronology is shown in **Fig.** 2.13. First experiments searching for the rare decay started in the $1960-70$'s. A research group at Milano University obtained a lower limit of $T^{0\nu}_{1/2} > 3.1 \cdot 10^{20}$ yr (68% CL) on the $0\nu\beta\beta$ decay half-life. Subsequent experimental efforts by various groups led to lower limits of $T^{0\nu}_{1/2} \gtrsim 10^{23}$ yr. The sensitivity could be enhanced significantly, since experiments started their operation in underground laboratories [160]. In addition, the introduction of germanium detectors enriched up to about 85% in the isotope ^{76}Ge further increased the experimental sensitivity [171]. In the 1990's, the Heidelberg-Moscow (HdM) and the International Germanium Experiment (IGEX) collaboration operated several enriched detectors successfully for

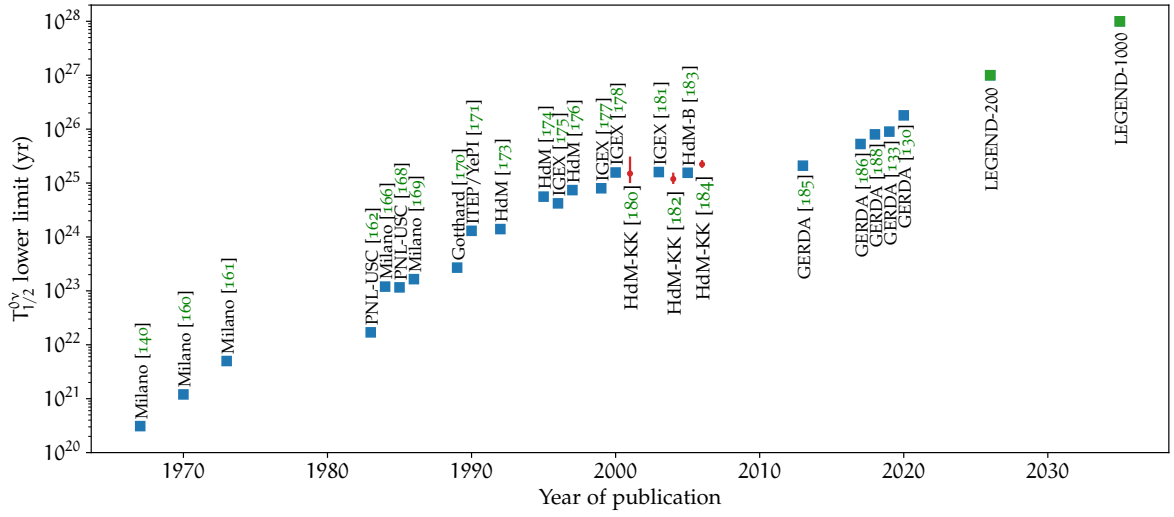

Figure 2.13: Chronology of lower limits on the $0\nu\beta\beta$ decay half-life of the isotope ^{76}Ge. Values are taken from **Tab.** 2.4. For several publications per year, only the strongest limit is illustrated. The limits up to 1992 correspond to 68% CL, while the more recent values correspond to 90% CL. The three claims of part of the HdM collaboration are shown with red error bars. The values for LEGEND are targeted sensitivities. Plot idea from [94].

about a decade. They obtained limits on the decay half-life on the order of $T^{0\nu}_{1/2} \gtrsim 10^{24} - 10^{25}$ yr. In the years 2001, 2004 and 2006, H. V. Klapdor-Kleingrothaus and part of the HdM collaboration claimed the discovery of $0\nu\beta\beta$ decay with half-lives as reported in **Tab.** 2.4 [180, 182, 184]. Strong criticism was raised with respect to the deployed analysis procedures [191]. Recent results by the Germanium Detector Array (GERDA) experiment, cf. **Ch.** 4.2.1, and the MAJORANA DEMONSTRATOR, cf. **Ch.** 4.2.2, exclude these claims. The GERDA experiment obtained a lower limit on the decay half-life of $T^{0\nu}_{1/2} \gtrsim 1.8 \cdot 10^{26}$ yr [130], the current best sensitivity of any $0\nu\beta\beta$ decay experimental program. In the future, the Large Enriched Germanium Experiment for Neutrinoless $\beta\beta$ Decay (LEGEND) will continue the search for the decay in the isotope ^{76}Ge [11–14]. Pursuing a staged approach, the collaboration is targeting a signal discovery sensitivity on the decay half-life of higher than 10^{28} yr. The rich physics program of LEGEND is presented in detail in **Ch.** 4.3.

3

SEMICONDUCTOR DETECTORS

Semiconductor detectors such as high-purity germanium (HPGe) detectors have been deployed successfully in many radiation detection applications for decades. This is due to several distinct advantages including a high energy resolution (many information carriers per pulse), fast timing characteristics, and flexible geometries [192].

In this chapter, the working principle and characteristics of semiconductor detectors with a focus on HPGe detectors for ^{76}Ge-based $0\nu\beta\beta$ decay searches will be discussed. It should be noted here that other semiconductor technologies such as CdZnTe [193] or complementary metal-oxide-semiconductor (CMOS) pixel arrays [194] are also deployed to search for $0\nu\beta\beta$ decay [9]. However, they are still in an early development stage and will not be discussed here.

In **Ch.** 3.1, the interaction of particles with matter is reviewed. The characteristics of semiconductor materials and the principle of semiconductor detectors are described in **Ch.** 3.2. Finally, the properties of HPGe detectors are discussed in **Ch.** 3.3.

3.1 INTERACTION OF PARTICLES WITH MATTER

A comprehensive knowledge of the interaction of particles with matter is important to understand the radiation detection with semiconductor detectors. Depending on the properties of the incoming particle and the characteristics of the absorber material, different interaction processes are possible.

3.1.1 *Alpha particles*

Heavy charged alpha particles (masses $\gtrsim 1\,\mathrm{GeV}$) traversing through matter interact electromagnetically with the shell electrons of the atoms. They lose their energy through inelastic collisions with the electrons leading to ionized atoms [39, 94]. For a single charged particle with velocity $v = \beta c$ traversing a material with number density N and atomic number Z, the ionization energy loss dE per unit path length dx traversed is described by the Bethe formula [192]:

$$-\left\langle \frac{dE}{dx} \right\rangle = \frac{4\pi e^4 z^2}{m_e v^2} NZ \left[\log\left(\frac{2 m_e v^2}{I} \right) - \log\left(1-\beta^2\right) - \beta^2 \right]. \tag{3.1}$$

Here, ze describes the charge of the incoming particle in multiples of the electron charge ($z = 2$ for alpha particles), m_e the electron rest mass, and I the average excitation and ionization potential of the absorber material. The equation assumes that the mass of the incoming particle is much higher than the electron mass. As a result, the energy transferred to the electron per interaction is much smaller than the kinetic energy of the particle itself. In particular, the deflection of the incoming heavy particle is negligible. The product NZ represents the electron density of the absorber material. Materials with higher densities have a higher stopping power. Alpha particles with a charge of $z = 2$ ionize strongly due to the z^2-dependence in **Eq.** (3.1). Therefore, they have a short mean free path and their interaction basically takes place at a single site [39, 94, 192]. The average path length of alpha particles in materials can be approximated by the continuous slowing down approximation[1] (CSDA) range. The CSDA range of alpha particles in germanium and liquid argon (LAr) is shown in **Fig.** 3.1a. The plot shows that in both media alpha particles with an energy of a few MeV only traverse up to several tens of micrometers.

1 The approximation assumes that the energy loss rate at every point along the track is equal to the total stopping power [195].

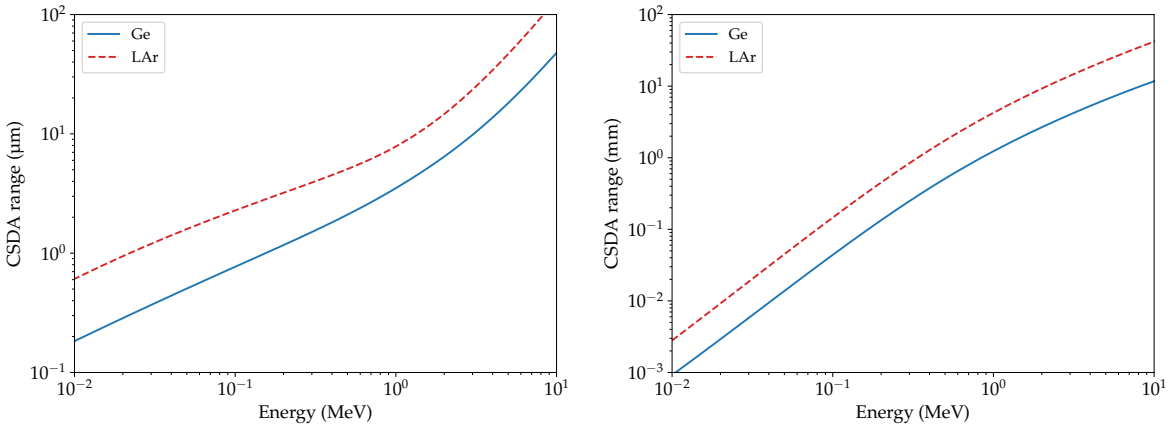

(a) CSDA range of alpha particles in Ge and LAr.

(b) CSDA range of electrons in Ge and LAr.

Figure 3.1: Ranges of (a) alpha particles and (b) electrons in germanium (Ge) and liquid argon (LAr). The range is expressed in terms of the continuous slowing down approximation (CSDA). Data from [196].

3.1.2 *Electrons and positrons*

Electrons interact with matter via ionization or Bremsstrahlung. Compared to heavy charged particles, such as alpha particles, they lose their energy at a lower rate. Since the electron mass is equal to that of the orbital electrons with which it is interacting, the assumptions made in **Ch.** 3.1.1 are no longer valid. More specifically, a larger fraction of the electron energy can be lost and the deflection angle can be large [94, 192]. The energy loss due to ionization and excitation in this case is more complex than for heavy charged particles and is reviewed in detail in [192].

The energy loss of electrons at low energies is dominated by ionization. Above a certain energy, the critical energy E_c, the main energy loss mechanism is Bremsstrahlung, whereby the electron radiates a photon in the electrostatic field of a nucleus. The critical energy E_c, at which both processes contribute equally, is related to the charge Z of the nucleus and can be approximated by [39]

$$E_c \approx \frac{800\,\mathrm{MeV}}{Z}, \quad E_c^{\mathrm{Ge}} \approx 25\,\mathrm{MeV}. \tag{3.2}$$

Therefore, for electrons with energies up to a few MeV interacting in germanium, the energy loss is driven by ionization. As for alpha particles, the average path length of electrons in materials can be approximated by the CSDA range, see **Fig.** 3.1b. It can be observed that in germanium and in liquid argon, electrons with an energy of a few MeV traverse up to several millimeters.

Most of the aforementioned processes are also valid for an incoming positron. However, when the positron is almost at rest ($E_{e^+} \lesssim 10\,\mathrm{keV}$) and encounters another electron, they annihilate and two 511 keV photons are emitted back to back [94].

3.1.3 *Gamma radiation*

Gamma radiation is highly penetrating and its interaction with matter strongly depends on the energy, and on the atomic number of the considered material. In radiation detection measurements, the following interaction mechanisms are relevant:

1) Photoelectric absorption,

2) incoherent scattering (Compton scattering),

3) pair production and pair annihilation.

At low energies, photoelectric absorption is dominant, whereas at higher energies pair production has the largest cross section. Incoherent scattering is prevalent at intermediate energies. The attenuation law of gamma rays in terms of the mass attenuation is given by the Beer-Lambert law [192]:

$$I(x) = I_0 e^{-(\mu/\rho)\lambda}, \quad \lambda = \rho x. \tag{3.3}$$

Here, $I(x)$ denotes the radiation intensity in the absorber, I_0 the initial intensity, and μ/ρ the mass attenuation coefficient, with μ the linear attenuation coefficient, and ρ the mass density of the medium. The attenuation coefficient can be expressed as a sum of the cross sections of the different processes:

$$\frac{\mu}{\rho} \propto \sum_i \sigma_i \propto \sigma_{PA} + \sigma_{IS} + \sigma_{PP}, \tag{3.4}$$

where $\sigma_{PA}, \sigma_{IS}, \sigma_{PP}$ describe the cross sections corresponding to photoelectric absorption, incoherent scattering, and pair production. The total mass attenuation coefficient of germanium as a function of the photon energy is illustrated in **Fig.** 3.2. As can be seen, at the $Q_{\beta\beta}$-value of ^{76}Ge, incoherent scattering is the dominant process, while photoelectric absorption and pair production are subdominant.

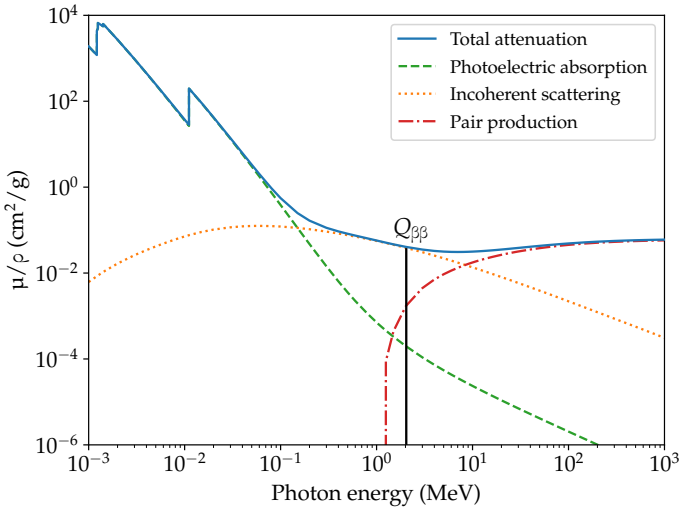

Figure 3.2: Attenuation coefficient μ/ρ in germanium as a function of the photon energy. The total attenuation is proportional to the sum of the cross sections corresponding to photoelectric absorption, incoherent scattering, and pair production/annihilation. At the $Q_{\beta\beta}$-value of ^{76}Ge, incoherent scattering is the dominant process. Data from [197].

PHOTOELECTRIC ABSORPTION At low photon energies (in germanium up to about 150 keV, see **Fig.** 3.2), photoelectric absorption is the dominant interaction mechanism. In this process, incident gamma radiation interacts with an atom of the absorbing material. The complete photon energy is transferred to one of the shell electrons which is subsequently emitted. The interaction creates an excited absorber atom with a vacancy in one of its bound shells. The de-excitation is realized through the emission of characteristic X-ray photons or Auger electrons. If photoelectric absorption takes place in a radiation detector and the full electron energy is absorbed in the active volume, a characteristic peak, the full energy peak (FEP), will be present in the energy spectrum [94, 192].

COMPTON SCATTERING At higher photon energies, incoherent scattering (Compton scattering) becomes relevant. In germanium, incoherent scattering is the dominating interaction process in the energy range from about 150 keV to 8 MeV, see **Fig.** 3.2. An incident gamma ray photon scatters off a bound (incoherent scattering) or free electron (Compton scattering) in the absorbing material, see **Fig.** 3.3. It is deflected through an angle θ ($0 \leqslant \theta \leqslant \pi$) with respect to its original direction. The

electron recoils and carries away an angle-dependent portion of the initial photon energy E_γ. The energy E'_γ of the scattered photon can be related to E_γ via [192]

$$E'_\gamma = \frac{E_\gamma}{1 + \frac{E_\gamma}{m_e c^2}(1 - \cos\theta)}, \tag{3.5}$$

where the term $m_e c^2$ denotes the rest mass of the electron. The electron recoil energy E_e is then given by $E_e = E_\gamma - E'_\gamma$. As can be deduced from **Eq.** (3.5), for small scattering angles θ only a small amount of energy is transferred to the recoil electron. Since the electron and the scattered photon share the energy, Compton scattering manifests itself as a continuum (Compton continuum) in the energy spectrum measured with a radiation detector. The maximum electron recoil energy is obtained in the case of a total deflection ($\theta = \pi$):

$$\max(E_e) = E_e(\theta = \pi) = \frac{2E_\gamma^2}{2E_\gamma + m_e c^2}. \tag{3.6}$$

In the energy spectrum, this leads to a visible shoulder (Compton edge) at the energy $\max(E_e)$ associated with a photon peak at the energy E_γ [94].

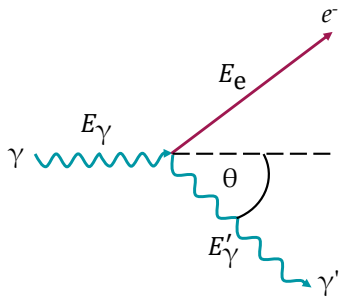

Figure 3.3: Simplified illustration of Compton scattering. An incoming photon scatters off an electron and is then deflected through an angle θ.

PAIR PRODUCTION AND PAIR ANNIHILATION If the photon energy is at least as high as twice the rest mass energy of the electron ($2 \cdot 511\,\text{keV} = 1022\,\text{keV}$), the mechanism of pair production becomes relevant. In germanium, the process is dominant for photon energies above ~8 MeV, see **Fig.** 3.2. A photon interacts with a nucleus in the absorbing material and is converted into an electron-positron pair (pair production), see **Fig.** 3.4. The pair shares the energy

$$E_{\text{pair}} = E_\gamma - 2m_e c^2. \tag{3.7}$$

After slowing down, the positron annihilates with another electron (pair annihilation) and emits two 511 keV photons back to back (for reasons of conservation of momentum):

$$e^+ + e^- \rightarrow 2\gamma. \tag{3.8}$$

The production of these photons creates a distinct event topology in a germanium detector. If pair production and pair annihilation take place outside the detector, one of the two photons may enter the active volume and fully deposit its energy. This leads to a characteristic gamma peak at 511 keV in the energy spectrum, the annihilation peak. On the other side, if the processes take place inside the detector volume, the following scenarios are possible:

1) If the two gammas are fully absorbed in the active volume, a gamma peak corresponding to the full initial energy E_γ becomes visible in the energy spectrum, the full energy peak (FEP).

2) In contrast, if one gamma escapes the detector and the other one is fully absorbed, an energy equal to $E_\gamma - 511\,\text{keV}$ is detected. This peak is called the single escape peak (SEP).

3) Finally, if both gammas escape the detector, an energy of $E_\gamma - 2 \cdot 511\,\text{keV}$ is detected and leads to the so-called double escape peak (DEP).

Naturally, there is also the possibility that only a fraction of the energy of the annihilation photons is deposited in the detector. In theses cases, energy depositions in the ranges $[E_\gamma - 511\,\text{keV} : E_\gamma]$ or $[E_\gamma - 2 \cdot 511\,\text{keV} : E_\gamma - 511\,\text{keV}]$ are detected. The various spectral features discussed above are illustrated in **Fig.** 3.5 using the example of the energy spectrum of a ^{228}Th calibration measurement.

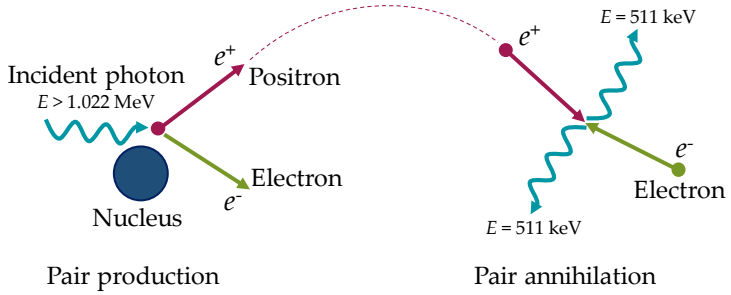

Figure 3.4: Illustration of the processes pair production and pair annihilation. When an incident photon interacts with the nucleus, an electron-positron pair is produced. After the positron is stopped, it can form positronium together with another electron. This system is unstable and the particles annihilate each other emitting two 511 keV gammas back to back. Plot idea from [198].

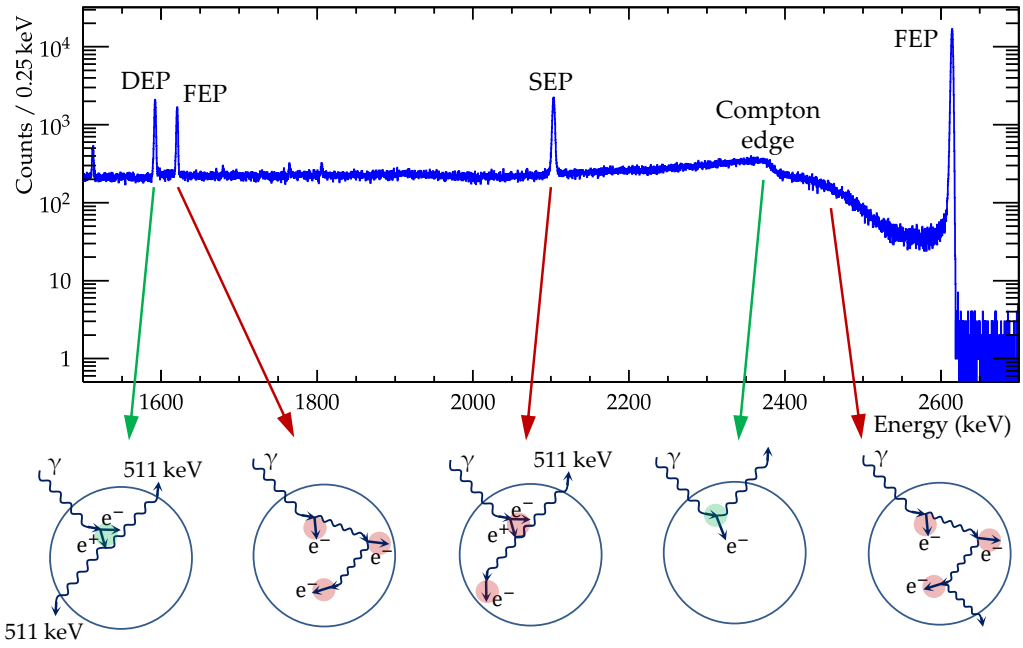

Figure 3.5: Energy spectrum of a ^{228}Th calibration measurement illustrating spectral features of gamma ray interactions. The full energy peak (FEP) corresponds to events whose energy is fully absorbed in the detector. The single escape peak (SEP) is due to events in which one of the annihilation photons escapes the detector and the energy of the other one is fully absorbed. For events in the double escape peak (DEP), both annihilation photons escape the detector. Events close to the Compton edge are characterized by a close to maximal deflection angle. Events above this edge are due to multiple Compton scatterings. Plot idea from [199].

3.2 DETECTOR BASICS

In the following paragraphs, the basics of semiconductor detectors with a focus on germanium detectors will be discussed. The explanations mostly follow those in [94, 192, 200].

BAND STRUCTURE The energy of electrons within a solid is confined to energy bands. Bands corresponding to different energies are separated by a gap. The highest, yet occupied band is called valence band, whereas the next higher-lying, non-populated band is called conduction band. The gap between these bands is referred to as band gap (E_g). Its size determines whether the material is classified as an insulator, a semiconductor, or a conductor [192]. The band structure corresponding to these different types is illustrated in **Fig.** 3.6.

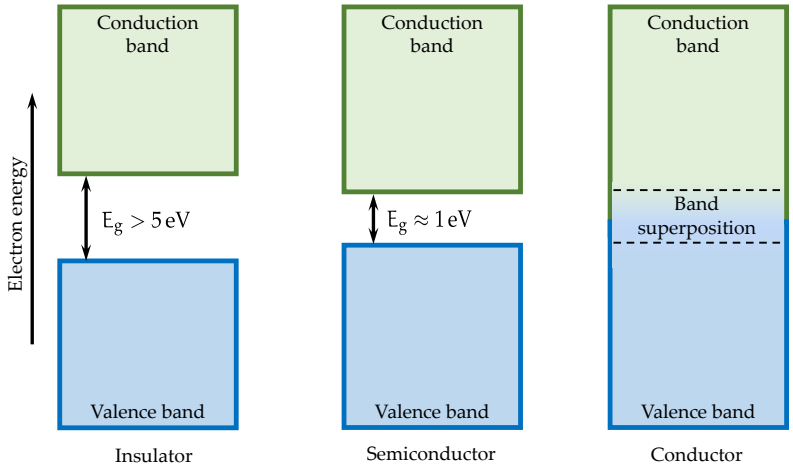

Figure 3.6: Band structure in solids for an insulator, a semiconductor, and a conductor. While insulators are characterized by a relatively large gap between the valence and the conduction band of $E_g > 5\,eV$, semiconductors have a smaller band gap of $E_g \approx 1\,eV$. In conductors, the valence and conduction bands are superimposed.

In conductors, the electrons can move easily between the valence and conduction bands via thermal excitation. For an insulator, the band gap is large and the electrons from the valence band cannot move into the conduction band (thermal excitation cannot overcome the energy barrier). In contrast, for a semiconductor, the band gap is smaller and if a valence electron gains sufficient thermal energy, it can be elevated into the conduction band, see **Fig.** 3.7a. The thermal excitation not only creates an electron in the conduction band, but also an associated vacancy (hole) in the valence band. The combination of the two is called electron-hole pair. The probability for an electron to jump from the valence band to the conduction band is described by a Boltzmann distribution [192]:

$$P(T) \propto T^{3/2} \exp\left(-\frac{E_g}{2kT}\right). \tag{3.9}$$

Here, T is the temperature, and k the Boltzmann constant. A graphic representation of this equation using the example of germanium is shown in **Fig.** 3.7b. It can be observed that above a certain temperature, the current induced by electrons moving to the conduction band increases strongly. This quantity is called leakage current. When a semiconductor is used as a radiation detector, cf. **Ch.** 3.3, the leakage current is a source of noise. Since too high a leakage current prevents it from being functional, the detector needs to be operated at low (cryogenic) temperatures.

The band gap in semiconductor materials can be used for particle detection. If a charged particle or a gamma ray enters the material, valence electrons are excited into the conduction band. A certain number N of electron-hole pairs is created which is directly proportional to the absorbed energy E and the average energy ϵ necessary to create one electron-hole pair:

$$N = \frac{E}{\epsilon}. \tag{3.10}$$

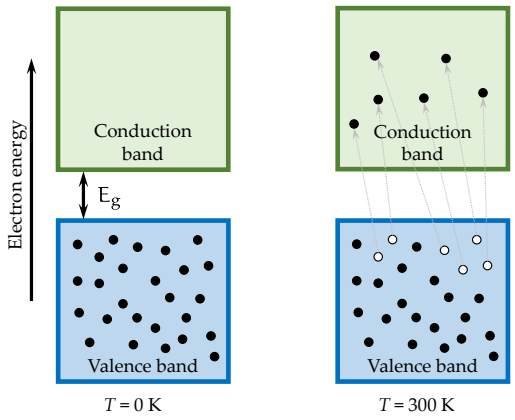

(a) Thermal excitation in a semiconductor.

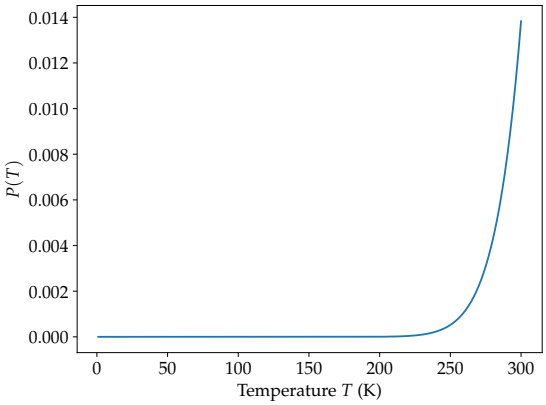

(b) Transition probability from valence to conduction band.

Figure 3.7: (a) In semiconductors, electrons can move from the valence to the conduction band by thermal excitation. (b) The probability $P(T)$ for an electron to jump to the conduction band is temperature-dependent and can be described by a Boltzmann distribution, shown here for the example of germanium. At higher temperatures, semiconductors start to become more conductive.

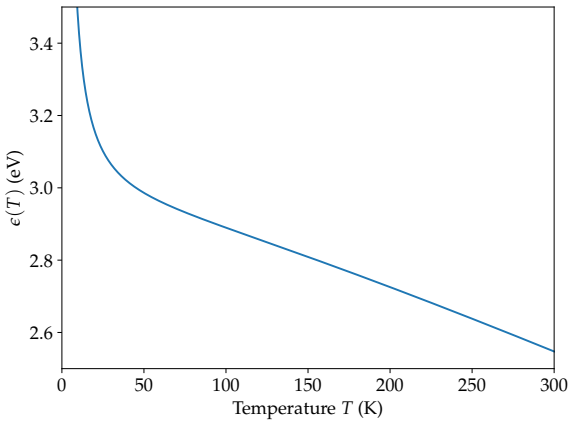

(a) Parameterization of $\epsilon(T)$.

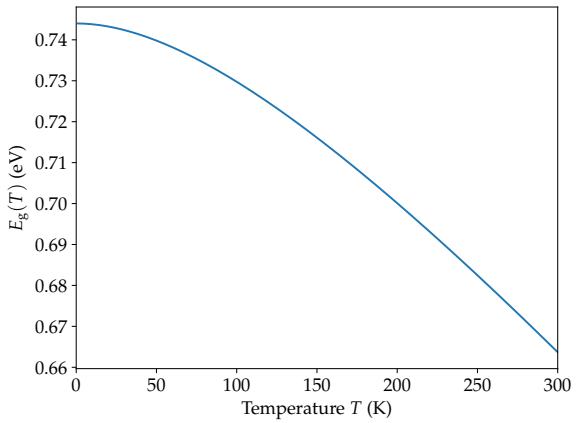

(b) Parameterization of $E_g(T)$.

Figure 3.8: Parameterization of (a) the average energy $\epsilon(T)$ necessary for the creation of an electron-hole pair, and (b) of the band gap $E_g(T)$ in germanium. At higher temperatures, less energy is required for the creation of an electron-hole pair. In addition, the band gap also decreases with increasing temperature.

In the presence of an external electric field, the electrons are collected to the anode, while the holes are collected to the cathode. This enables to measure the deposited energy and to use the semiconductor as a detector. To enhance the detection efficiency, the number of electron-hole pairs should be as high as possible. For a given amount of absorbed energy, this can be realized with a low value of ϵ. For germanium, a commonly used parameterization of ϵ is given by [94, 201]:

$$\epsilon(T) = 2.2 \cdot E_g(T) + 1.99 \cdot E_g^{3/2}(T) \cdot \exp\left(4.75 \frac{E_g(T)}{T}\right). \tag{3.11}$$

Moreover, the temperature-dependent band gap can be described by Varshni's empirical relation [202, 203]:

$$E_g(T) = E_g(0) - \frac{\alpha T^2}{T + \beta} \tag{3.12}$$

$$= 0.744\,\text{eV} - \frac{4.774 \cdot 10^{-4}\,\text{eV/K}^2 \cdot T^2}{T + 235\,\text{K}} \quad \text{for germanium.} \tag{3.13}$$

Table 3.1: Properties of the semiconductor materials silicon and germanium. The quantity Z denotes the atomic number, ρ the density at $T = 300\,K$, ϵ the average energy required for the production of an electron-hole pair, and E_g the band gap. The values of ϵ, E_g, and the mobilities are given for the typical operating temperatures of silicon ($T = 300\,K$) and germanium detectors ($T = 77\,K$). Data from [192].

Material	Z	ρ (g/cm^3)	ϵ (eV)	E_g (eV)	Mobility ($cm^2/(V \cdot s)$) Electrons	Holes
Silicon	14	2.33	3.62	1.106	1350	480
Germanium	32	5.32	2.96	0.73	$3.6 \cdot 10^4$	$4.2 \cdot 10^4$

Graphical representations of these parameterizations are shown in **Fig.** 3.8. As can be observed in **Fig.** 3.8a, ϵ decreases with increasing temperature. Consequently, to increase the available number of electron-hole pairs, an operation of the detector at higher temperatures would be preferred. On the other hand, with increasing temperature also the band gap E_g decreases, see **Fig.** 3.8b. A smaller band gap increases the probability that an electron jumps from the valence to the conduction band resulting in elevated leakage currents. Therefore, to optimize the detection efficiency, a compromise has to be found. Typically, germanium detectors are operated at liquid nitrogen (LN_2) temperature ($T = 77\,K$), where $\epsilon = 2.96\,eV$ and $E_g = 0.73\,eV$, or at LAr temperature ($T = 87\,K$). In contrast, silicon detectors are often operated at room temperature ($T = 300\,K$), where $\epsilon = 3.62\,eV$ and $E_g = 1.106\,eV$ [192]. The main properties of the semiconductor materials silicon and germanium are summarized in **Tab.** 3.1.

IMPURITIES AND DOPING So far, our discussion was based on the assumption of an ideal semiconductor which at zero temperature has no conductivity. However, in nature, ideal crystals without any impurities do no exist. Small residual crystal impurities are always present and affect the band levels and band gap, and hence the conductivity. The impurities can be divided into acceptor and donor impurities, providing additional holes or electrons, respectively. If an acceptor atom (e.g. boron) with three valence electrons is inserted into a four-valent crystal lattice, e.g. germanium, an additional hole is available, see **Fig.** 3.9a. This is called a p-type crystal due to the presence of positive acceptor impurities. Similarly, if a donor atom with either one (e.g. lithium) or five valence electrons (e.g. arsenic) is inserted into a four-valent crystal lattice, one additional electron is generated, see **Fig.** 3.9b. This is called an n-type crystal due to the presence of negative donor impurities. Generally, acceptor and donor impurities are both present in the crystal lattice. The intentional introduction of impurities into the lattice is called doping. Doping can be used to compensate for an imbalance of the impurities. In addition, it is typically used to make electrical contact with semiconductor devices [94, 192].

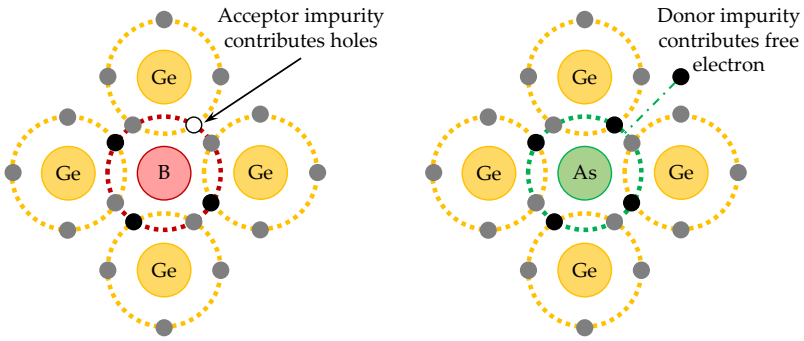

(a) Acceptor impurity.

(b) Donor impurity.

Figure 3.9: (a) Acceptor and (b) donor impurity in a four-valent crystal lattice (using the example of germanium). Acceptor and donor atoms provide additional holes or electrons, respectively. Plot idea from [204].

DIODE AND DEPLETION The combination of a p-type and an n-type semiconductor material creates an electrostatic system called diode, see **Fig.** 3.10. At the junction between these materials, the p-n-junction, free holes and electrons diffuse into the opposite material and recombine. This results in a depletion region which is used as the active volume of a semiconductor detector. The depleted zone is typically small but can be extended by applying an electric voltage to the diode. To this end, the voltage is applied in a reverse bias configuration, i.e. the negative terminal is applied to the p-type side, while the positive terminal is applied to the n-type side. Thereby, the electrons and holes are attracted to the opposite sides. The size of the depletion region increases with increasing bias voltage and decreasing net impurity concentration. The voltage, at which a full depletion of the detector is obtained is called depletion voltage. As soon as a reverse bias voltage is applied, a semiconductor detector behaves as a capacitor with capacitance C_D.

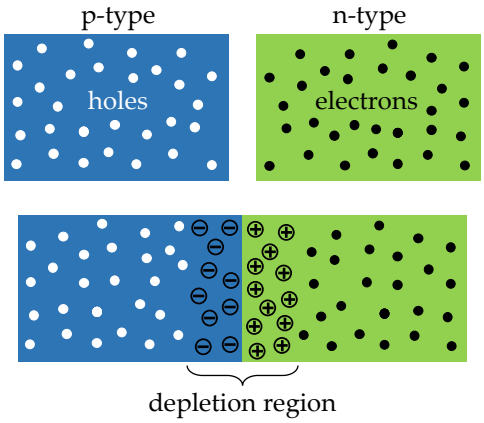

Figure 3.10: Combining p-type and n-type semiconductor materials to form a diode. At the junction between the materials, a depletion region is created.

3.3 HIGH-PURITY GERMANIUM DETECTORS

Germanium detectors are typically fabricated from a single crystal of p-type material. The signal readout contact (p^+ contact) is formed by a p-type junction obtained via boron implantation (thickness of $\sim 100\,\text{nm}$). In contrast, the bias voltage electrode (n^+ electrode) is formed by an n-type junction realized by drifting lithium on the surface (thickness of $1-2\,\text{mm}$). While the signal readout contact is at zero electric potential, a positive high voltage (HV) is applied to the n-type junction. If a charged particle or gamma radiation enters the active detector volume, charge carriers (electron-hole pairs) are created along the trajectory. Charge carriers with the same polarity start drifting towards the electrodes following the electric field lines. For a detector made from p-type material, the holes are collected to the p^+ signal readout contact, whereas the electrons drift towards the lithiated n^+ electrode, see **Fig.** 3.11. In general, the collection of holes (for p-type bulk material) is favored over the collection of electrons (for n-type bulk material) since hole trapping is less pronounced than electron trapping. Consequently, by using p-type bulk materials, a more efficient charge collection and hence a better detector performance can be achieved [192].

High-purity germanium (HPGe) detectors are semiconductor detectors with a very high purity (up to 12 N). The typical impurity concentration is of $\mathcal{O}(10^{10}\,\text{atoms/cm}^3)$. Therefore and because of the high mobility of the charge carriers, it is possible to construct large detectors with masses of $\mathcal{O}(1\,\text{kg})$. In the following sections, the signal formation in HPGe detectors, as well as the different detector geometries deployed in former and current $0\nu\beta\beta$ decay experiments will be presented.

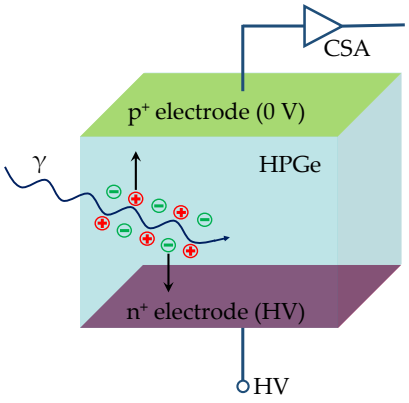

Figure 3.11: Working principle of a semiconductor detector. If gamma radiation or a charged particle enters the detector, it creates electron-hole pairs along its trajectory. While the electrons drift to the n^+ electrode, the holes are collected to the p^+ contact. The collected charge is read-out via a charge sensitive amplifier (CSA).

3.3.1 *Signal formation and weighting potential*

As discussed above, electron-hole pairs are created when energy is deposited in the detection volume by an incident particle. As soon as the charge carriers start drifting to the electrodes, the signal formation process begins: The movement of the holes and electrons induces mirror charges at the electrodes. Once the last carrier has arrived at its collecting electrode, the process of charge induction ends [192]. The temporal development of the induced charge Q, and of the associated instantaneous current I is described by the Shockley-Ramo theorem [94, 205, 206]:

$$Q(t) = q \cdot [WP(\vec{r}_h(t)) - WP(\vec{r}_e(t))], \tag{3.14}$$

$$I(t) = q \cdot \left[\vec{E}(\vec{r}_h(t)) \cdot \vec{v}_h(t) - \vec{E}(\vec{r}_e(t)) \cdot \vec{v}_e(t)\right]. \tag{3.15}$$

Here, q denotes the charge generated by the incoming particle, $WP(\vec{r})$ and $\vec{E}(\vec{r})$ the weighting potential and the weighting field at position $\vec{r}$, and $\vec{r}_{h(e)}(t)$ and $\vec{v}_{h(e)}(t)$ the position and velocity of the hole (electron) cloud at time t, respectively. The dimensionless weighting potential describes how strongly the charge at a given detector position couples to the electrode. It only depends on the detector dimensions and the contact geometry, and can be computed by solving the Laplace equation:

$$\nabla^2 WP = 0, \tag{3.16}$$

with the boundary conditions that the voltage on the electrode for which the induced charge is to be calculated is unity ($WP = 1$), and the voltage on all other electrodes is zero ($WP = 0$). For most of the detector geometries, the equation can only be solved numerically. The weighting field is finally obtained as the gradient of the weighting potential [192].

3.3.2 *Detector geometries*

In this section, detector geometries typically deployed in ^{76}Ge-based $0\nu\beta\beta$ decay searches are discussed. A graphical representation of the geometries and the associated weighting potentials is shown in **Fig.** 3.12. The drift of the charge carriers in the detector is driven by the presence of the electric field. The saturated drift velocity is of $\mathcal{O}(0.1\,\mathrm{mm/ns})$, and taking into account the typical detector dimensions of $\mathcal{O}(1\,\mathrm{cm})$, the charge is fully collected in a time period of $\mathcal{O}(100\,\mathrm{ns})$ [149].

3.3.2.1 *Semi-coaxial detectors*

One of the first detector geometries deployed in ^{76}Ge-based $0\nu\beta\beta$ decay searches is the (semi-)coaxial detector [173, 207, 208]. The geometry is characterized by a cylindrical shape with a concentric bore hole, see **Fig.** 3.12a. The p^+ signal readout electrode is obtained via boron implantation and fully

extends over the bore hole. This is necessary to ensure a depletion of the entire detection volume. In contrast, the n^+ contact is formed by the lithiated outer lateral and top surface. The two electrodes are separated by a small groove that is typically passivated. While the p^+ contact is at zero potential, a positive bias voltage is applied to the n^+ contact. Due to their large readout electrode, semi-coaxial detectors have a comparably large capacitance of $C_D \approx \mathcal{O}(10\,\mathrm{pF})$. Since the detector capacitance is proportional to the electronic noise, see **Ch.** 10.3.3, semi-coaxial detectors have a rather poor energy resolution. In addition, due to a complicated shape of the weighting field inside the detector, it is challenging to deploy background rejection methods based on the signal shape. Semi-coaxial detectors have been extensively deployed in the GERDA experiment, cf. **Ch.** 4.2.1.

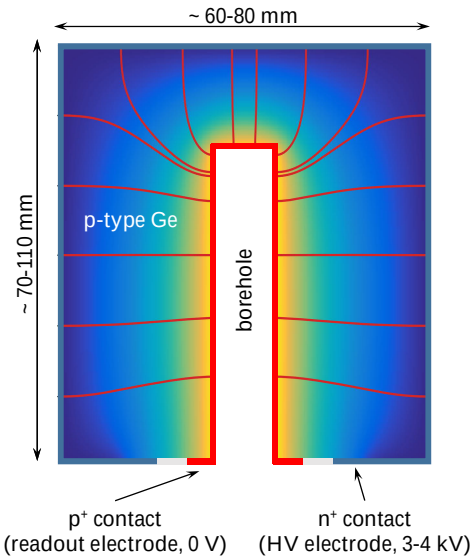

(a) Semi-coaxial detector.

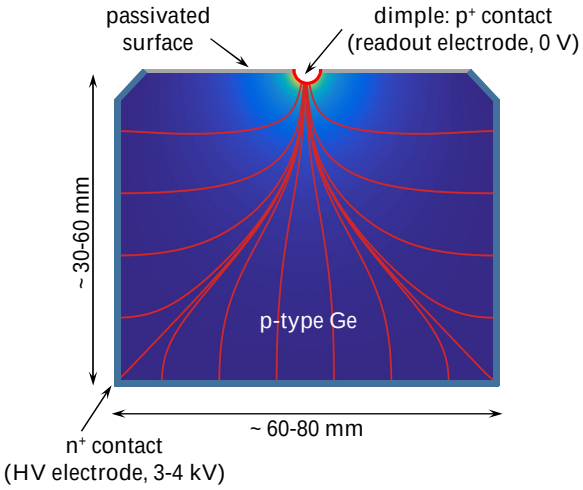

(b) P-type point contact (PPC) detector.

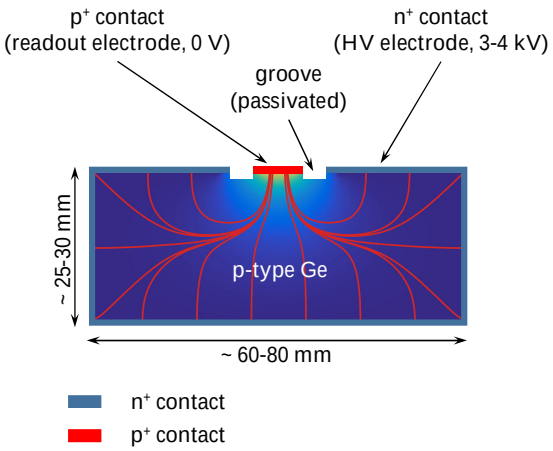

(c) Broad energy germanium (BEGe) detector.

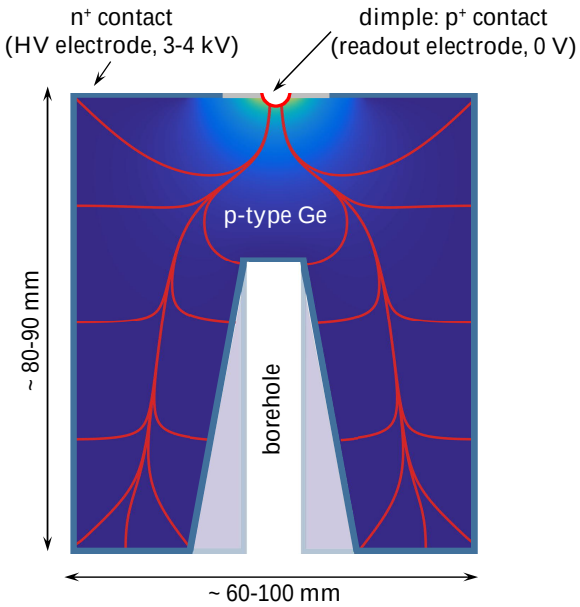

(d) Inverted coaxial point contact (ICPC) detector.

Figure 3.12: Overview of the detector types typically used in ^{76}Ge-based $0\nu\beta\beta$ decay searches: (a) Semi-coaxial, (b) PPC, (c) BEGe, and (d) ICPC detector. The figure shows the electrode arrangements and indicates typical dimensions. Moreover, the weighting potential inside the detector (blue and yellow areas correspond to low and high values, respectively), and the drift paths (red thin lines) are illustrated.

3.3.2.2 *P-type point contact (PPC) detectors*

Former experiments almost exclusively used the widespread semi-coaxial detector design. To account for the comparably poor energy resolution and background rejection capabilities of this detector geometry, novel germanium detectors with smaller capacitances have been developed. One example is the p-type point contact (PPC) HPGe detector [209]. Just as the semi-coaxial detector, it has a cylindrical shape but is shorter in length, see **Fig.** 3.12b. While the n^+ contact extends over the lateral and bottom detector surface, the p^+ electrode (point contact) is formed by a small dimple (ORTEC design) or spot (flat) contact (Mirion design) located in the center of the top surface[2]. The point contact size (radius of $3-4\,\text{mm}$, depth of $1-2\,\text{mm}$) is significantly smaller compared to the one of typical traditional semi-coaxial detectors. Therefore, PPC detectors have a lower capacitance ($C_D \approx 1-2\,\text{pF}$ at full depletion) resulting in lower electronic noise, and thus in a better energy resolution. Moreover, PPC detectors can be operated at lower energy thresholds ($< 1\,\text{keV}$) which makes them suitable for rare-event searches at small energies [142]. Another advantage of this type of detector is the enhanced capability of applying background rejection methods based on the shape of the signals (pulse shape). This is due to the specific geometry and arrangement of the electrodes leading to a strong weighting field close to the readout contact and to a relatively low field elsewhere. As a result, the signal shape of events that deposit their energy at a single location (single-site events, indicator for $0\nu\beta\beta$ decay signal events) in the detector is almost independent of the location of the energy deposition. This can be used to discriminate these events from those depositing their energy at multiple sites (multi-site events, e.g. Compton-scattered photon, indicator for background events), cf. **Ch.** 4.1.2. All these advantages make the PPC detector an excellent radiation detection instrument that is widely used in nuclear and particle physics experiments, including searches for $0\nu\beta\beta$ decay [15, 142, 187], low-energy nuclear recoils such as in dark matter [210, 211], and coherent elastic neutrino-nucleus scattering [212, 213].

3.3.2.3 *Broad energy germanium (BEGe) detectors*

Just as PPC detectors, broad energy germanium (BEGe) detectors have a low detector capacitance ($C_D \approx 3-5\,\text{pF}$ at full depletion) and enhanced PSD capabilities. The detector geometry encompasses a cylindrical shape with a comparably short length, see **Fig.** 3.12c. Compared to PPC detectors, the p^+ signal readout electrode (concentric disc) has a larger radius (up to 7 mm). It is separated from the n^+ contact by an insulating, passivated groove with a typical depth of 2 mm, and an outer diameter of 21 mm. The n^+ contact covers the bottom and lateral surface and extends up to the groove. Therefore, BEGe detectors are less sensitive to surface backgrounds. In addition, the n^+ electrode wrap-around creates a funnel effect by pushing the holes towards the center of the detector. Independent of their starting point, the holes then drift along fixed drift paths to the p^+ readout electrode [214, 215]. As for the PPC detector geometry, this enables the efficient rejection of backgrounds.

3.3.2.4 *Inverted coaxial point contact (ICPC) detectors*

An efficient way to improve the signal discovery sensitivity of $0\nu\beta\beta$ decay searches is to increase the isotope mass, cf. **Ch.** 2.4.3. Detectors with higher masses could reduce the number of required channels, in particular the number of amplifiers, cables, detector holders, etc. and thus the overall background. Unfortunately, the size of PPC and BEGe detectors cannot be increased further. This would result in regions of undepleted material (pinch-off regions) in the active volume when biasing the detector. Moreover, in some regions the electric field could be too low resulting in charge trapping (CT) and in a poor energy resolution. The inverted coaxial point contact (ICPC) detector is a detector design that was proposed recently [21]. It features a cylindrical shape with a length about twice as long as BEGe detectors, see **Fig.** 3.12d. The p^+ contact is located on the top surface and separated from the n^+ electrode by an insulating groove or a passivation layer. The detector comprises a concentric bore hole (on the opposite side of the readout contact) which is required to optimize the electric field inside the detector and to avoid undepleted regions. In addition, the detector geometry can be tuned by adapting its length, diameter, well depth, p^+ point contact diameter, etc. The ICPC detector has the same advantages as PPC and BEGe detectors (low capacitance, low threshold, background rejection capabilities, etc.), but at the same time allows for much larger detector masses

2 Here, the top surface is defined as the surface with the higher impurity concentration of the crystal.

up to 3 kg [216]. Compared to PPC and BEGe detectors, the surface to volume ratio is $30-40\%$ smaller making them less susceptible to surface backgrounds. However, due to their extended size, the timing characteristics of ICPC detectors are quite different from those of the other geometries. In particular, drift times are comparably long (up to 2 µs) so that collective effects such as diffusion and self-repulsion of the charge cloud become relevant [217]. The ICPC detector geometry is the baseline design to be used in LEGEND.

4

THE LARGE ENRICHED GERMANIUM EXPERIMENT FOR $0\nu\beta\beta$ DECAY

This chapter focuses on former and present state-of-the-art experiments searching for $0\nu\beta\beta$ decay in the isotope ^{76}Ge. First, radioactive backgrounds encountered in the experiments and their rejection strategies are discussed in **Ch.** 4.1. The European-based GERDA and the US-based MAJORANA DEMONSTRATOR experiments will be reviewed in **Ch.** 4.2. Finally, the Large Enriched Germanium Experiment for Neutrinoless $\beta\beta$ Decay (LEGEND), the successor of the two previously mentioned experiments, will be introduced in **Ch.** 4.3.

4.1 BACKGROUNDS IN $0\nu\beta\beta$ DECAY SEARCHES

4.1.1 *Overview*

BACKGROUND SOURCES A simplified illustration of the background sources typically encountered in ^{76}Ge-based $0\nu\beta\beta$ decay searches is shown in **Fig.** 4.1. One of the main background sources can be attributed to the primordial, natural radioactivity in the HPGe detector itself, and in nearby components. In particular, the radioactive decay chains of the isotopes ^{232}Th and ^{238}U lead to gamma backgrounds with energies above 2 MeV. At the $Q_{\beta\beta}$-value, the decays of ^{208}Tl and ^{214}Bi are of major concern since they can deposit energy extraneously in the ROI. A further background is due to alpha and beta surface events. While alpha backgrounds are caused by surface contaminations with radon isotopes and their progeny, particularly ^{222}Rn and ^{210}Po, a problematic beta background in LAr cryostats is caused by the decay of the long-lived isotope ^{42}Ar and its daughter ^{42}K. Alpha and beta surface backgrounds will be discussed in detail in **Ch.** 5. Radioactive backgrounds also arise from cosmogenic activation while the detectors and other materials are above ground: High-energetic neutrons and muons create radioactive isotopes such as ^{68}Ge and ^{60}Co that decay and lead to beta and gamma backgrounds in the ROI. Muon-induced backgrounds can be also generated at depth. By hitting the rocks, low- and high-energy secondaries such as neutrons are produced. These in turn lead to additional backgrounds via de-excitation and capture reactions [58].

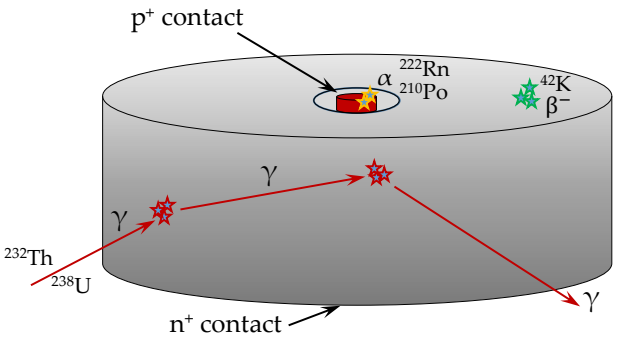

Figure 4.1: Radioactive backgrounds encountered in $0\nu\beta\beta$ decay searches with germanium detectors. Gammas typically deposit energy at various positions in the detector via Compton scattering. Backgrounds arising from alpha and beta particles can be assigned to surface backgrounds.

BACKGROUND REDUCTION STRATEGIES To maximize the signal discovery sensitivity, the next generation of ^{76}Ge-based $0\nu\beta\beta$ decay experiments needs to deploy sophisticated background reduction strategies. To this end, several active and passive background mitigation techniques have

been developed. First, ultra-pure and low-mass materials (detector holders, readout electronics, etc.) are used to reduce the impact of backgrounds from the natural U and Th chains. In this context, radiopurity assay results from prior generations of low-background experiments aid the material selection process. Besides, low-activity passive shielding materials such as copper, lead, water, etc. are deployed to reduce backgrounds originating farther away from the active detector volume, e.g. neutron backgrounds from rock surroundings. At the same time, some of these materials can be used as an active veto system to reject cosmic ray backgrounds. When handling the materials, care must be taken to maintain their cleanliness and to avoid surface contaminations [9]. To minimize backgrounds originating from cosmogenic activation, the above-ground time of the detectors and other materials needs to be minimized. Moreover, low-background physics experiments are commonly carried out in underground laboratories. This reduces the cosmic muon flux and its related induced activities.

4.1.2 *Pulse shape discrimination*

While $0\nu\beta\beta$ decay is a localized phenomenon, i.e. the electrons emerging from the decay deposit their energy within a small volume of $\mathcal{O}(1\,\mathrm{mm}^3)$, gamma backgrounds feature multiple interaction sites from Compton scattering, cf. **Ch.** 3.1.3. In order to fulfill the ultra-low background requirements for $0\nu\beta\beta$ decay searches, it is important to appropriately discriminate these background events from signal events. A powerful background rejection method is based on the analysis of the shape of the signal pulses, commonly referred to as pulse shape analysis (PSA) or pulse shape discrimination (PSD). PPC, BEGe and ICPC detectors, cf. **Ch.** 3.3.2, are ideally suited for the application of PSD techniques. For these point contact detectors, the weighting potential is strong and highly localized in the vicinity of the p^+ signal readout electrode, see **Fig.** 3.12. In contrast, it is relatively low elsewhere in the active volume. As a consequence, the signal shape of an event with a single energy deposition location in the detector (single-site event, SSE) is almost independent of its point of origin. In contrast, an event with multiple energy deposition locations in the detector (multi-site event, MSE) has a different signal shape. Waveform examples for a SSE and a MSE are shown in **Fig.** 4.2. The difference in the signal shape can be seen clearly, with two distinct interactions evident in the MSE. $0\nu\beta\beta$ decay signal-like events occur at a single location in the germanium crystal and are thus SSEs. In contrast, background events (from gamma ray interactions) typically deposit energy at multiple locations in the detector and are thus MSEs [16].

A commonly used discriminative quantity of the signal pulse shape is the ratio A/E of the maximum amplitude of the current pulse (A) and the amplitude (energy) of the charge pulse (E). The A/E distribution of SSEs is narrow and only slightly dependent on the energy, see **Fig.** 4.3. In contrast, the A/E distribution of MSEs is broad and located at lower values due to the reduced maximum current amplitude compared to SSEs. This also holds true for n^+ surface events: Holes created in the $\sim$1 mm-thick n^+ lithium layer first diffuse into the detector bulk and then drift to the p^+ readout electrode. Due to the diffuse character of the initial charge propagation, the charge collection time of n^+ surface events is longer compared to the one of normal bulk events, see **Fig.** 4.2. These slow pulses have characteristic low A/E values that can be used to efficiently discriminate n^+ surface backgrounds. Eventually, events close to the p^+ contact have very short drift times in a strong weighting field. Consequently, these events have high A values resulting in $A/E > 1$ values.

In practice, ^{228}Th is an isotope often used for defining A/E cuts. In the radioactive decay of the isotope to the stable nucleus ^{208}Pb, see decay chain in **Fig.** 6.4, high-energy gammas with an energy of 2614.5 keV are produced. In the detector, they are likely to undergo pair production producing an electron-positron pair, cf. **Ch.** 3.1.3. The positron stops and annihilates with another electron leading to the subsequent emission of two 511 keV gammas back to back. These gammas can either fully deposit their energy in the detector (full energy peak at 2614.5 keV, FEP) or either one or both gamma(s) escape(s) the detector. If only one gamma escapes the detector, an energy of $2614.5\,\mathrm{keV} - 511\,\mathrm{keV} = 2103.5\,\mathrm{keV}$ (single escape peak, SEP) is deposited in the detector. In contrast, if both gammas escape the active volume, an energy of $2614.5\,\mathrm{keV} - 2 \cdot 511\,\mathrm{keV} = 1592.5\,\mathrm{keV}$ (double escape peak, DEP) is deposited in the detector. While the DEP is a good indicator for SSEs (energy deposition only by the initial electron), the SEP is used as an indicator for MSEs (energy deposition at multiple sites) [16].

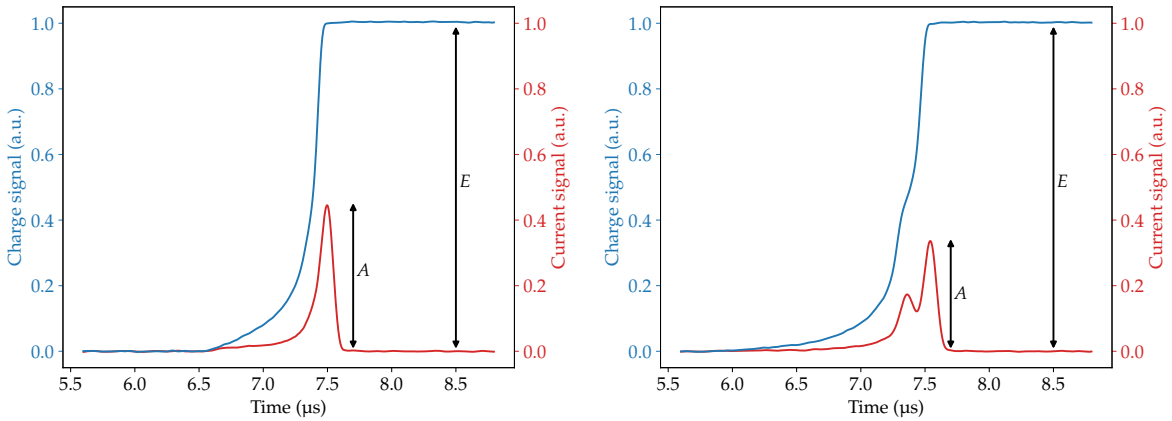

(a) Single-site event (SSE).

(b) Multi-site event (MSE).

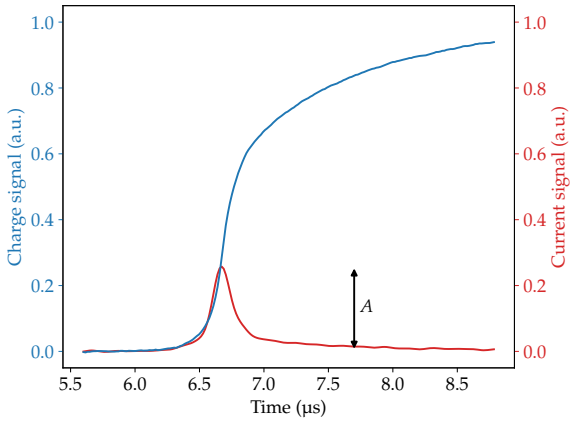

(c) n^+ surface event.

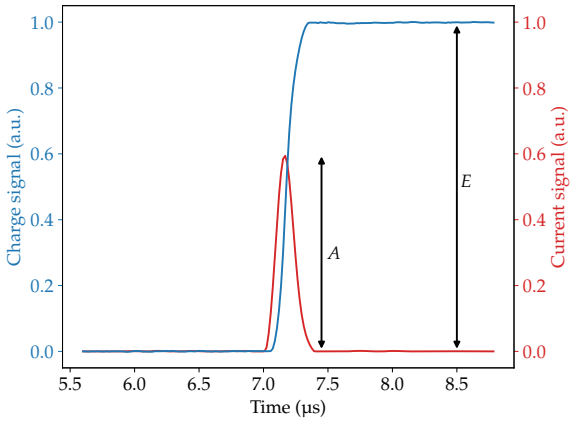

(d) p^+ event.

Figure 4.2: Charge and current signals corresponding to a (a) single-site event, (b) multi-site event, (c) n^+ surface event, and (d) p^+ event. The charge signals were measured with a PPC detector. The current pulse (red curve) corresponds to the time derivative of the charge pulse (blue curve). The different signal shapes of the event classes can be clearly identified by the different maximal heights A of the current pulses.

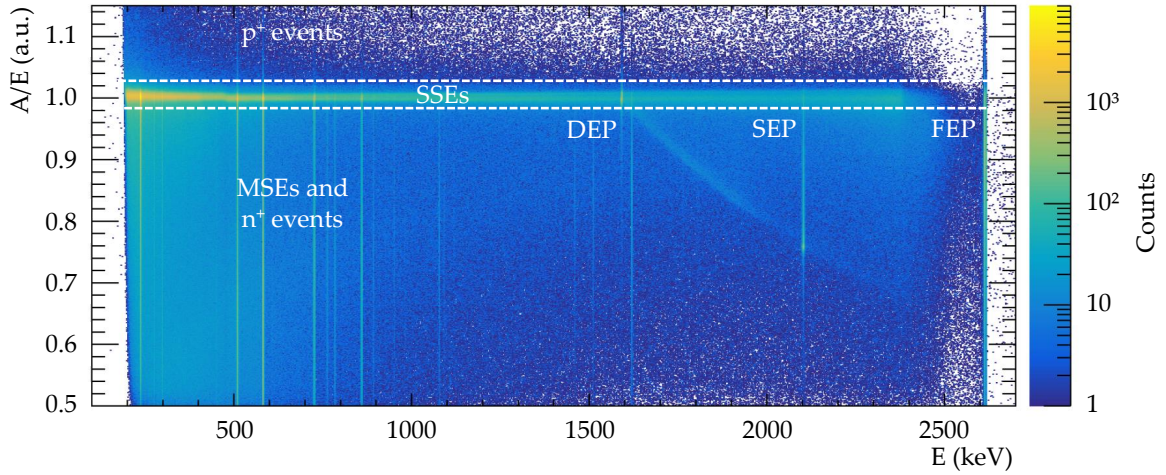

Figure 4.3: Example for the normalized A/E distribution as a function of energy for a ^{228}Th calibration measurement. While single-site events (SSEs) are located along $A/E = 1$, multi-site events (MSEs) and n^+ surface events have $A/E < 1$. Events close to the p^+ signal readout contact are characterized by $A/E > 1$.

In the data analysis, the A/E pulse shape discriminator is tuned such that 90% of the SSEs (signal-like events) in the DEP survive. The survival efficiencies ε_{PSD} of events in the Compton continuum, SEP and FEP are computed accordingly. Usually, the number of MSEs in the SEP can be reduced to below 10% [142]. A detailed description of the quantitative procedure can be found in **Ch.** B.1 in the appendix.

4.2 PREDECESSOR EXPERIMENTS

4.2.1 *GERDA*

OVERVIEW The GERmanium Detector Array (GERDA) experiment was a low-background experiment searching for $0\nu\beta\beta$ decay in the isotope ^{76}Ge using HPGe detectors [185, 186, 218, 219]. It was located at LNGS in Italy. A rock overburden of 3500 m water equivalent (m.w.e.) reduced hadronic components of cosmic ray showers and the muon flux at the experiment by about six orders of magnitude to a residual level of $\Phi_\mu \approx 1.25\,\text{muons}/(\text{m}^2\,\text{h})$. The bare HPGe detectors were operated in a $64\,\text{m}^3$ cryostat (inner diameter of 4 m) filled with LAr (quality 5.0). The experiment has been designed using a multi-layer (shielding) structure, see **Fig.** 4.4.

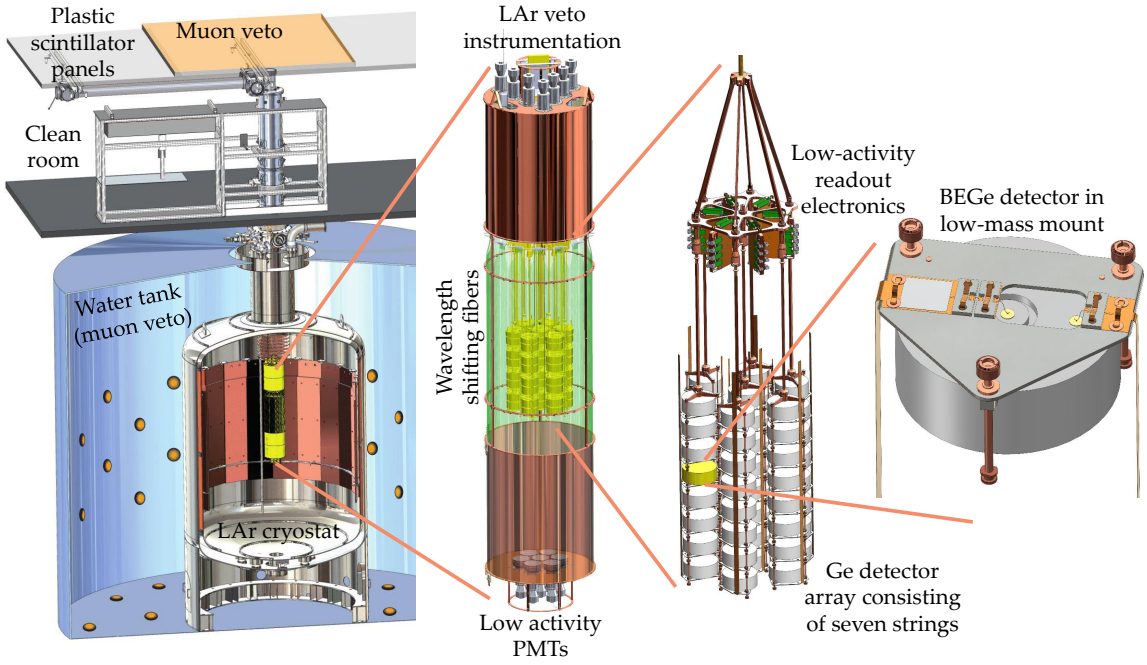

Figure 4.4: Overview of the experimental setup of the GERDA experiment in the Phase II-configuration. The different components are described in detail in the text. Adapted from [186].

In the final configuration of the experiment, the detectors were assembled into seven 40 cm-long strings, six of them being arranged in a hexagonal structure and the seventh string located in the center. Each string was surrounded by a nylon cylinder (mini shroud) limiting the direct contact of the detectors to the LAr volume. Thereby, the accumulation of radioactive ions such as ^{42}K ions at the outer detector surfaces leading to undesired surface backgrounds could be reduced. The detectors were placed on low-mass mono-crystalline silicon plates, supported by copper rods. To read out the diodes, custom-designed signal readout electronics consisting of two amplification stages was used [19, 20]. The LAr served as a cooling medium and at the same time acted as an active shield against external backgrounds. In particular, the LAr scintillation light was used as an anti-coincidence (AC) veto for events releasing their energy in both the detectors and the cryogenic liquid (e.g. gamma ray events undergoing Compton scattering). The LAr cryostat itself was surrounded by a 10 m diameter tank filled with $590\,\text{m}^3$ of ultra-pure water produced by the Borexino and XENON water plants [219–221]. It shielded the experiment from external ionizing radiation and neutron backgrounds from the rock surroundings. The tank was instrumented with 66 PMTs to veto residual cosmic muons reaching the experiment via the detection of Cherenkov light.

Table 4.1: Main results of the GERDA experiment. The table lists the exposure $M \cdot t$, the background index BI, the lower limit on the decay half-life $T^{0\nu}_{1/2}$ (90% CL), and the upper limit on the effective Majorana mass $\langle m_{\beta\beta} \rangle$ for the different phases of the experiment. The actual phase includes the results of previous phases.

	$M \cdot t$ (kg · yr)	BI (cts/(keV · kg · yr))	$T^{0\nu}_{1/2}$ (yr)	$\langle m_{\beta\beta} \rangle$ (meV)
Phase I [185]	21.6	$1 \cdot 10^{-2}$	$> 2.1 \cdot 10^{25}$	$< 200 - 400$
Phase II a [186]	34.4	$0.7 \cdot 10^{-3}$	$> 5.3 \cdot 10^{25}$	$< 150 - 330$
Phase II b [188]	46.7	$1.0 \cdot 10^{-3}$	$> 8.0 \cdot 10^{25}$	$< 120 - 260$
Phase II c [133]	82.4	$0.6 \cdot 10^{-3}$	$> 0.9 \cdot 10^{26}$	$< 100 - 230$
Phase II final [130]	127.2	$5.2 \cdot 10^{-4}$	$> 1.8 \cdot 10^{26}$	$< 79 - 180$

A clean room above the water tank with a lock system surrounded by a glove box was used for the assembly and deployment of the HPGe detectors and the readout electronics. The detector array was routed through the lock system to the center of the cryostat. On top of the experimental setup, a complementary muon veto was installed [185, 186, 222]. The rejection efficiency for muons with potential energy depositions was ~99.2% [223]. The GERDA experiment has been conceived in two phases that will be discussed in the following paragraphs. The main experimental results are summarized in **Tab.** 4.1

GERDA PHASE I In the first phase of the GERDA experiment, HPGe detectors with a total mass of 21.3 kg were operated in the time period from November 2011 to June 2013. Eight of the detectors were reprocessed enriched p-type semi-coaxial detectors (17.67 kg) inherited from the former Heidelberg-Moscow [208] and IGEX experiments [207]. In addition, five enriched broad energy germanium (BEGe) detectors (3.63 kg) serving as prototypes for Phase II were installed in July 2012 [185, 219, 224]. After about 1.6 years of operation, a lower limit on the $0\nu\beta\beta$ decay half-life of ^{76}Ge of $T^{0\nu}_{1/2} > 2.1 \times 10^{25}$ yr (90% CL) was obtained for an exposure of $M \cdot t = 21.6\,\text{kg} \cdot \text{yr}$. In addition, a background index (BI) of $\text{BI} = 1 \cdot 10^{-2}\,\text{cts}/(\text{keV} \cdot \text{kg} \cdot \text{yr})$ at the $Q_{\beta\beta}$-value has been reached [185, 186].

GERDA PHASE II The second phase of the GERDA experiment started in December 2015. The ultimate goal was to improve the half-life sensitivity of the decay to a level of $T^{0\nu}_{1/2} > 10^{26}$ yr for about $M \cdot t = 100\,\text{kg} \cdot \text{yr}$ of exposure by reducing the background level by one order of magnitude [186]. The main objectives of Phase II were to increase the isotope mass, further reduce the material mass, and use materials with a higher radiopurity [219]. To this end, 30 custom-designed enriched BEGe detectors (total mass of 20 kg, average mass of 667 g/detector, produced by Canberra) with optimized energy resolution and enhanced PSD capabilities were installed [215]. Five of these detectors have already been deployed in Phase I. In addition, novel low-mass detector holders, and an enhanced contacting solution (wire-bonded detectors instead of spring-loaded contacts) were introduced. To further suppress backgrounds, a veto system to detect the LAr scintillation light was implemented. This enabled the identification of events depositing energy in both the LAr volume and the detectors, and their rejection based on anti-coincidence (AC) analysis cuts. The LAr scintillation light was detected by a system consisting of light-guiding fibers surrounding the detector strings read out at both ends by silicon photomultipliers (SiPMs) and low-background PMTs. To facilitate the readout of the scintillation light, the fibers, the nylon cylinders, the PMTs, as well as other surfaces were coated with tetraphenyl butadiene (TPB) shifting the wavelength of the scintillation light from $\lambda = 128\,\text{nm}$ to $\lambda \approx 400\,\text{nm}$ [186].

Initially, Phase II was running from December 2015 to April 2018. During this period, 7 semi-coaxial (15.6 kg mass) and 30 BEGe detectors (20 kg mass) were operated. Including the results from GERDA Phase I, for a total exposure of $M \cdot t = 82.4\,\text{kg} \cdot \text{yr}$, no signal was observed in the ROI. The sensitivity on the decay half-life based on a Frequentist analysis was $T^{0\nu}_{1/2} > 0.9 \cdot 10^{26}$ yr (90% CL) and the corresponding background index was $\text{BI} = 0.6 \cdot 10^{-3}\,\text{cts}/(\text{keV} \cdot \text{kg} \cdot \text{yr})$ [133, 188].

As of May 2018, the central string with natural germanium detectors was replaced by a string with five enriched ICPC detectors (total mass of 9.6 kg). Moreover, the geometrical coverage of the fiber curtain was improved [130]. Data taking was then continued from July 2018 to November 2019. The total available enriched germanium exposure after the final data release was $M \cdot t = 127.2\,\text{kg} \cdot \text{yr}$ (combining Phase I and II data). The final energy spectrum before and after all analysis cuts is shown in **Fig.** 4.5. In the analysis window (1930 keV to 2190 keV, with the exclusion of two known gamma lines at 2104 ± 5 keV and 2119 ± 5 keV), 13 events were found after the application of analysis cuts. However, at the $Q_{\beta\beta}$-value, the $0\nu\beta\beta$ decay analysis yielded no signal, setting a novel lower limit on the decay half-life of $T^{0\nu}_{1/2} > 1.8 \cdot 10^{26}$ yr (90% CL) with a median sensitivity of $1.8 \cdot 10^{26}$ yr (90% CL) [130]. The limit on the decay half-life can be converted into an upper limit on the effective Majorana mass as described in **Ch.** 2.4.2. Depending on the NME range, an upper limit of $\langle m_{\beta\beta} \rangle < 79 - 180$ meV is obtained, similar to the limits obtained by experiments searching for $0\nu\beta\beta$ decay in other isotopes, cf. **Tab.** 2.3. In addition, GERDA achieved an unprecedentedly low background level of $\text{BI} = 5.2^{+1.6}_{-1.3} \cdot 10^{-4}$ cts/(keV · kg · yr) [130]. So far, this background is the lowest value in the signal ROI, when normalized with the FWHM, that has been achieved by any $0\nu\beta\beta$ decay experiment.

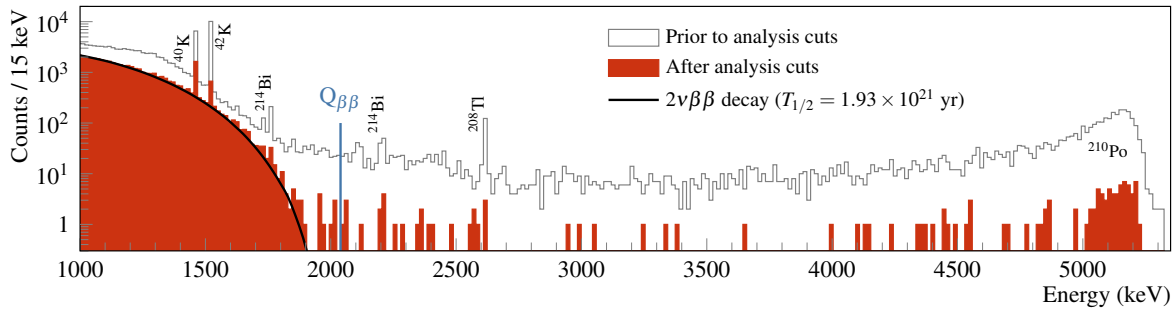

Figure 4.5: Final energy spectrum of the GERDA experiment before and after analysis cuts. The count rate at small energies can be mostly attributed to $2\nu\beta\beta$ decay. Source: [130].

4.2.2 Majorana Demonstrator

OVERVIEW The Majorana Demonstrator (MJD) was an array consisting of 58 PPC HPGe detectors (total detector mass of 44.1 kg) searching for $0\nu\beta\beta$ decay in the isotope ^{76}Ge. The experiment was located at the Sanford Underground Research Facility (SURF) in Lead, South Dakota. It was located deep underground at the 4850-foot (4260 m.w.e.) level of the mine ensuring that the muon flux reaching the experiment was reduced by more than six orders of magnitude. The experiment was built with the goal of demonstrating that backgrounds can be low enough to justify the construction of a tonne-scale germanium experiment. Moreover, a variety of low-energy and new exotic physics studies such as the search for light weakly interacting massive particles (WIMPs) and solar axions were targeted. The experiment used a number of ultra-low activity materials, and methods to reduce radioactive backgrounds: underground electroformed copper mounts for the detectors, low-mass front-end (LMFE) signal readout electronics, low-mass cables and connectors, customized flange connections, etc. [15, 142, 225, 226].

The experimental setup consisted of two independent vacuum cryostats which were made from high-purity electroformed copper. Each cryostat hosted seven arrays of enriched and natural PPC detectors. The detectors had masses of $0.5 - 1.1$ kg each. In total, there were 29.7 kg of enriched ^{76}Ge crystals ($88.1 \pm 0.7\%$) and 14.4 kg of natural Ge (7.8% ^{76}Ge). The cryostats were encapsulated in a compact graded shield composed of various materials (multi-layer structure). The first layers consisted of low-background passive electroformed copper. The copper shield in turn was contained within 45 cm of high-purity lead shielding. The lead shield was enclosed within a radon exclusion volume that was surrounded by an active 4π muon veto. The muon veto itself was enclosed in polyethylene (poly shield) used for neutron moderation. Each of the two modules was equipped with a calibration system consisting of ^{228}Th line sources that could be inserted in helical tubes

surrounding the cryostats [142]. An overview and photographs of the experimental setup are shown in **Fig.** 4.6 and **Fig.** 4.7, respectively.

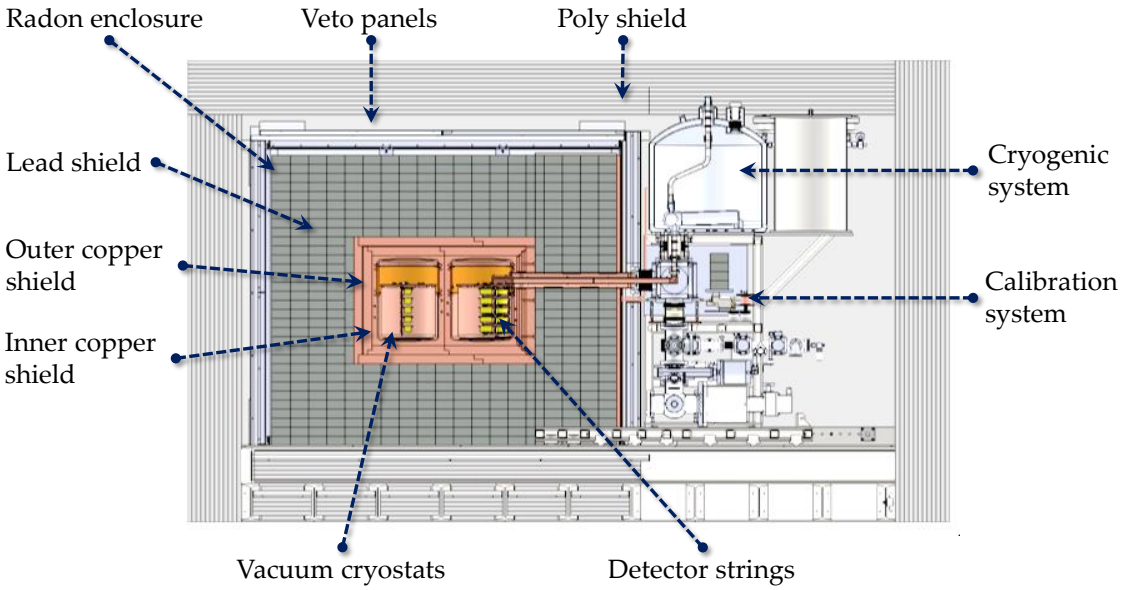

Figure 4.6: Overview of the experimental setup of the MAJORANA DEMONSTRATOR. Figure courtesy of the MJD collaboration.

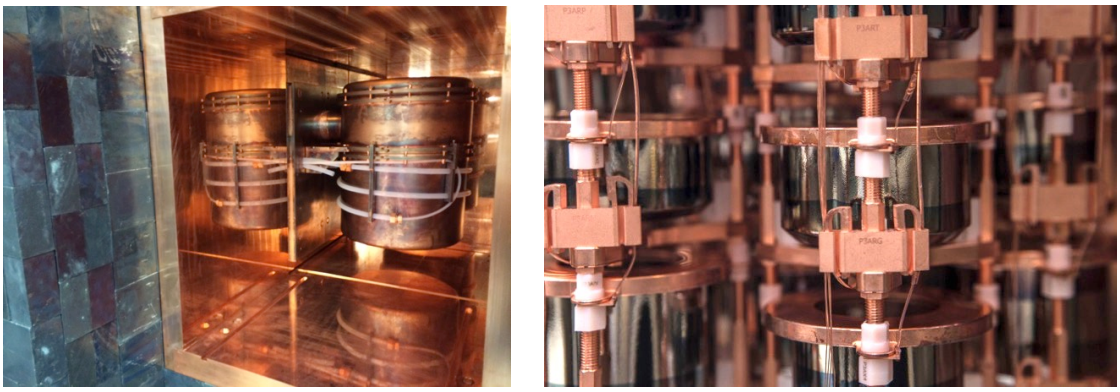

(a) Vacuum cryostat.

(b) Detector strings.

Figure 4.7: Photographs showing parts of the MAJORANA DEMONSTRATOR. (a) The experimental setup consists of two vacuum cryostats which are surrounded by a multi-layer shielding structure. (b) The PPC detectors are assembled into several strings that are supported by copper structures. Image courtesy of the MJD collaboration.

RESULTS The MAJORANA DEMONSTRATOR has started taking data in 2015 (first with only one of the two cryostats). The construction was completed by early 2017 [9]. In an initial data release corresponding to an exposure of $M \cdot t = 9.95\,\mathrm{kg \cdot yr}$, no candidate events were observed. A lower limit on the $0\nu\beta\beta$ decay half-life of $T^{0\nu}_{1/2} > 1.9 \times 10^{25}\,\mathrm{yr}$ (90% CL) was obtained. Moreover, a background index of $\mathrm{BI} = 1.6^{+1.2}_{-1.0} \cdot 10^{-3}\,\mathrm{cts/(keV \cdot kg \cdot yr)}$ at the $Q_{\beta\beta}$-value has been achieved [187].

The latest data release corresponds to an exposure of $M \cdot t = 26\,\mathrm{kg \cdot yr}$ [142]. The energy spectrum after data cleaning cuts and after all analysis cuts (including PSD cuts) is shown in **Fig.** 4.8. In the signal ROI (360 keV window in the energy range from 1950 keV to 2350 keV, with regions excluded due to gamma backgrounds and a 10 keV blinding window centered around $Q_{\beta\beta}$), with 0.653 events expected from the estimated background, one event was observed corresponding to a background of $\mathrm{BI} = (6.1 \pm 0.8) \cdot 10^{-3}\,\mathrm{cts/(keV \cdot kg \cdot yr)}$. For an optimized measurement configuration, with an exposure of $M \cdot t = 21.3\,\mathrm{kg \cdot yr}$, a background of $\mathrm{BI} = (4.7 \pm 0.8) \cdot 10^{-3}\,\mathrm{cts/(keV \cdot kg \cdot yr)}$

was reported. The observed lower limit on the 0νββ decay half-life is $T^{0\nu}_{1/2} > 2.7 \cdot 10^{25}$ yr (90% CL) with a median sensitivity of $4.8 \cdot 10^{25}$ yr (90% CL). Depending on the NME, this translates into an effective Majorana mass of $\langle m_{\beta\beta} \rangle < 200 - 433$ meV [142].

The PPC detectors in the MAJORANA DEMONSTRATOR have achieved an unprecedented energy resolution of 2.53 ± 0.08 keV FWHM at the $Q_{\beta\beta}$-value, the best resolution among all 0νββ decay experiments [142].

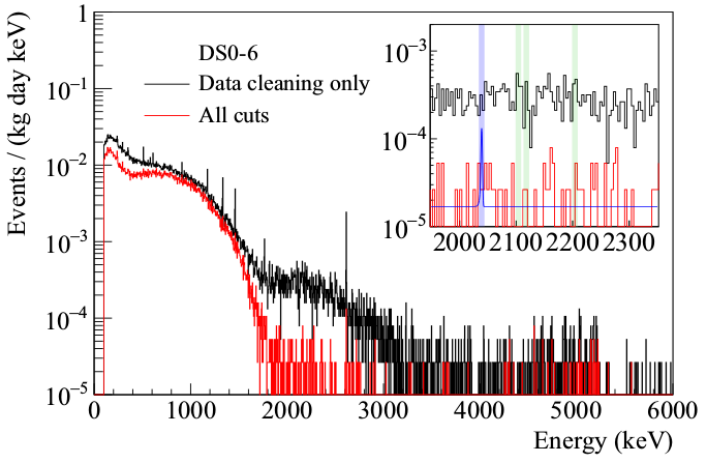

Figure 4.8: Energy spectrum of the MAJORANA DEMONSTRATOR above 100 keV of all data sets for an exposure of $M \cdot t = 26\,\text{kg} \cdot \text{yr}$. The spectrum is shown after data cleaning and muon veto cuts (black line), and after all analysis cuts (red line), including PSD cuts. The inset shows the spectrum in the region of interest. Source: [142].

4.3 LEGEND

The Large Enriched Germanium Experiment for Neutrinoless ββ Decay (LEGEND) pursues a tonne-scale search for 0νββ decay in the isotope ^{76}Ge utilizing the best technologies from the GERDA and MAJORANA DEMONSTRATOR experiments, as well as contributions from other groups. The mission statement of the collaboration is to develop a phased, ^{76}Ge-based double-beta decay experimental program with discovery potential at a half-life beyond 10^{28} years, using existing resources as appropriate to expedite physics results. To achieve this ambitious goal, LEGEND pursues a phased approach [11–14, 136].

4.3.1 *LEGEND-200*

In the first phase of the experimental program, LEGEND-200, up to 200 kg of HPGe detectors will be operated for a time period of about five years in the existing GERDA infrastructure at LNGS. The targeted total exposure is $M \cdot t = 1\,\text{t} \cdot \text{yr}$. LEGEND-200 largely follows the background-free experimental design established by former experiments. Just as in the GERDA experiment, the bare diodes will be deployed in LAr which acts both as a cooling medium and as an active shielding, cf. **Ch.** 4.2.1. At the same time, ultra-high radiopurity materials for all internal structures and custom-designed low-noise signal readout electronics as in the MJD will be used, cf. **Ch.** 4.2.2. The cryostat will be modified such that it can accommodate up to 200 kg of HPGe detectors arranged in several strings, see **Figs.** 4.9 and 4.10, with up to 12 detectors per string.

TECHNOLOGICAL IMPROVEMENTS To increase the active mass relative to the amount of instrumentation, an intensive use of ICPC detectors with a total mass of $\sim 130 - 140$ kg (1.5 – 3 kg each) is foreseen. These detectors are currently being fabricated by multiple vendors. About 70 kg of detector mass will be taken over from GERDA and the MJD. The LAr veto system will be improved to optimize the detection efficiency of the scintillation light. In particular, the detector strings will be arranged in a circular configuration (with maximum one inner string) enhancing the light collection efficiency. This will be supported by the installation of a novel wavelength-shifting reflec-

tor (WLSR) surrounding the fibers. The WLSR consists of a copper shroud as a mechanical structure for a ~250 µm-thick Tetratex (TTX) polytetrafluoroethylene (PTFE) fabric, vacuum-evaporated with TPB. Its purpose is to shift the wavelength of the LAr scintillation light, and to reflect visible light. Another improvement in LEGEND-200 will be the use of LAr with a higher optical purity to increase the attenuation length (> 60 cm for 128 nm scintillation light). To further reduce the electronic noise and to improve the energy resolution, as well as the PSD performance, an improved signal readout electronics solution will be used. One of the main objectives of this work was to characterize the performance of the novel readout electronics. This will be discussed in more detail in **Ch.** 11.

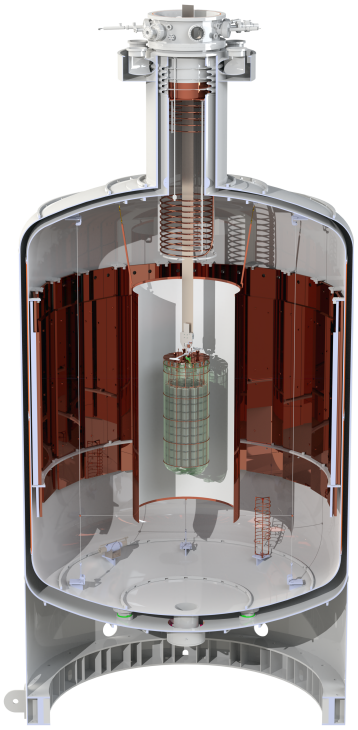

Figure 4.9: Three-dimensional rendering of the LEGEND-200 setup. Rendering provided by P. Krause and M. Willers.

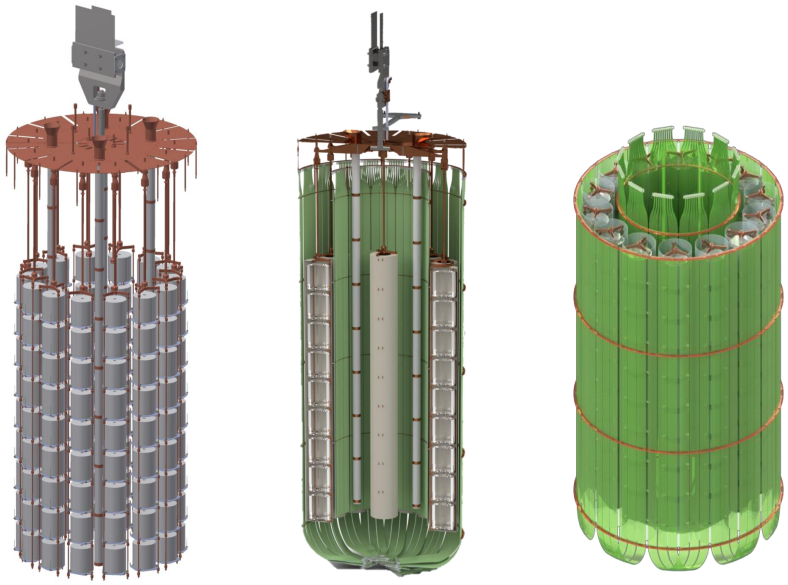

Figure 4.10: Artistic views of the LEGEND-200 setup. The figures show details of the detector array configuration (circular arrangement of strings), and of the LAr veto system (light-guiding fibers). Figures provided by M. Busch and M. Willers.

The detector units will be placed on low-mass base plates made from active and transparent polyethylene naphthalate (PEN), replacing the inactive silicon plates from the GERDA experiment. Since the PEN plates are scintillating, they enhance the light collection efficiency [227]. **Fig.** 4.11 shows a drawing and a photograph of the low-mass PEN detector plate for LEGEND-200. Finally, a modified clean room, a novel lock system, new detector mounts, and a novel data acquisition (DAQ) system will be deployed.

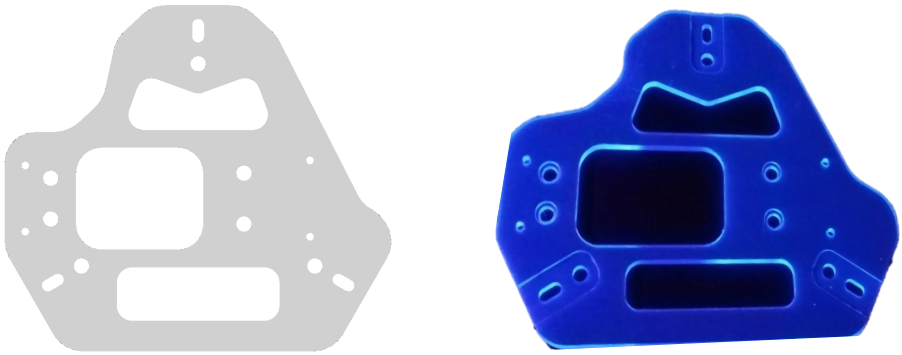

Figure 4.11: Drawing (left) and photograph (right) of a low-mass PEN detector plate for LEGEND-200. The scintillating properties of the material in the blue region can be seen clearly. Figures provided by L. Manzanillas.

BACKGROUND MODEL In LEGEND-200, the overall background is intended to improve by a factor of more than two compared to the background achieved in the GERDA experiment to a level of[1]

$$\mathrm{BI} < 2 \cdot 10^{-4}\,\mathrm{cts}/(\mathrm{keV}\cdot\mathrm{kg}\cdot\mathrm{yr}) \tag{4.1}$$

$$\Leftrightarrow \mathrm{BI} < 0.6\,\mathrm{cts}/(\mathrm{FWHM}\cdot\mathrm{t}\cdot\mathrm{yr}). \tag{4.2}$$

Within a live time of about five years, this will allow to reach the targeted signal discovery sensitivity on the decay half-life of $T^{0\nu}_{1/2} > 10^{27}$ yr, see **Figs.** 2.10 and 4.12. Background estimations based on Monte Carlo simulations and material screening measurements demonstrate that the background goal is projected to be met. A total background of $\mathrm{BI}_{\mathrm{tot}} \approx 10^{-4}\,\mathrm{cts}/(\mathrm{keV}\cdot\mathrm{kg}\cdot\mathrm{yr})$ is anticipated, see **Fig.** 4.13.

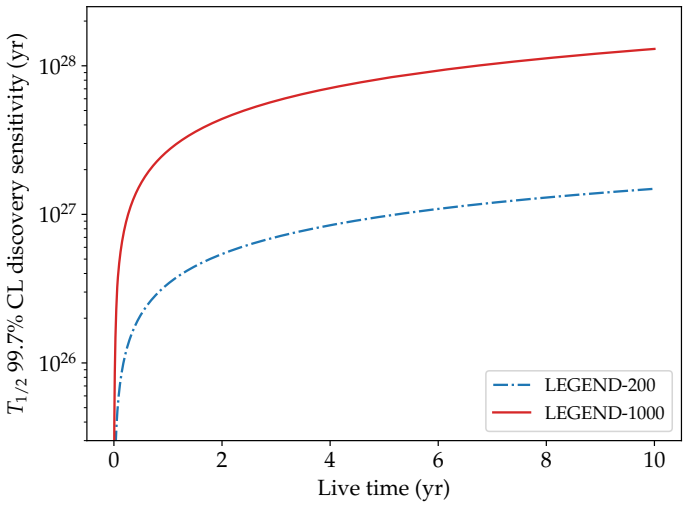

Figure 4.12: Evolution of the signal discovery sensitivity versus live time of LEGEND. The sensitivity is computed assuming a simple counting analysis and using the inversion of Poissonian probabilities as described in [134]. Data provided by M. Agostini.

1 The background index in units of $\mathrm{cts}/(\mathrm{keV}\cdot\mathrm{kg}\cdot\mathrm{yr})$ can be transformed to the units of $\mathrm{cts}/(\mathrm{FWHM}\cdot\mathrm{t}\cdot\mathrm{yr})$ by scaling with the targeted energy resolution at the $Q_{\beta\beta}$-value.

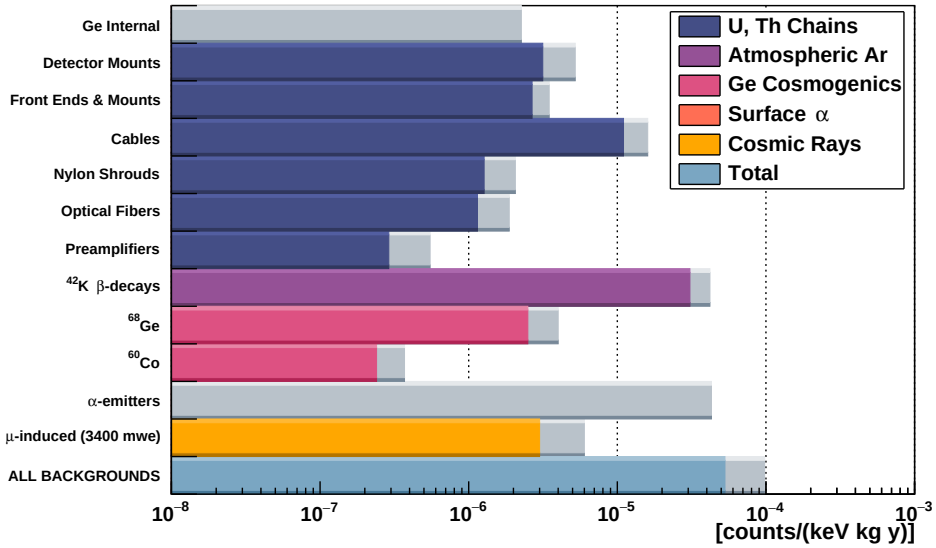

Figure 4.13: Anticipated backgrounds in LEGEND-200. Colored bars provide the estimated background contributions, while grey bars indicate 1σ uncertainties due to uncertainties in the screening measurements and Monte Carlo simulations. For the contributions of U, Th internal to germanium detectors, and for the alpha emitters on detector surfaces, only upper limits are estimated. Plot courtesy of the LEGEND collaboration.

Given the upper limits, surface backgrounds due to ^{42}K beta decays and alpha emitters (mainly ^{222}Rn, ^{210}Po) are the dominant background contributions that could account for up to 85% of the anticipated total background. One of the main aims of this work was to better understand these backgrounds. To this end, the response of a PPC detector to alpha and beta particles was studied in detail in a vacuum test facility. A related goal was to model and verify the measurement results via dedicated simulations. This will be discussed in more detail in **Chs.** 5-9.

STATUS The construction of LEGEND-200 is currently ongoing at LNGS. A first commissioning phase of the DAQ system, the calibration system, and the improved signal readout electronics has started in February 2020. During first test measurements under realistic conditions (called Post-GERDA test, PGT), the detector types to be deployed in LEGEND-200 were operated successfully. Within the framework of this thesis, a dedicated software framework has been developed to analyze the measurement data. The corresponding results are discussed in detail in **Ch.** 11.2. Data taking of LEGEND-200 is intended to start in 2021.

4.3.2 *LEGEND*-1000

In the final stage of LEGEND, LEGEND-1000, the collaboration plans to operate up to 1000 kg of HPGe detectors for a time period of 10 years [136]. Thus, the targeted total exposure is $M \cdot t = 10\,t \cdot yr$. Although several options are still under consideration, an initial baseline design has been established which foresees the operation of the bare germanium detectors in LAr [136]. The design aims at deploying $\sim 200 - 300$ ICPC detectors with a mass of $\sim 2 - 3$ kg each. To this end, HPGe detectors with a total mass of $\sim 850 - 870$ kg need to be produced, while detectors with a total mass of $\sim 130 - 150$ kg will be taken over from LEGEND-200. It is intended to install the detectors in four or five batches with loads of 250 kg or 200 kg each in separate 3 m^3 volumes of the cryostat (re-entrant tubes). This strategy will allow LEGEND to start taking data with the completed batches in parallel to the continuous procurement of detectors. Artistic views of the experimental setup are shown in **Fig.** 4.14. The baseline design of LEGEND-1000 is strongly informed by the GERDA and MAJORANA DEMONSTRATOR experiments. Furthermore, it will take advantage of developments for LEGEND-200.

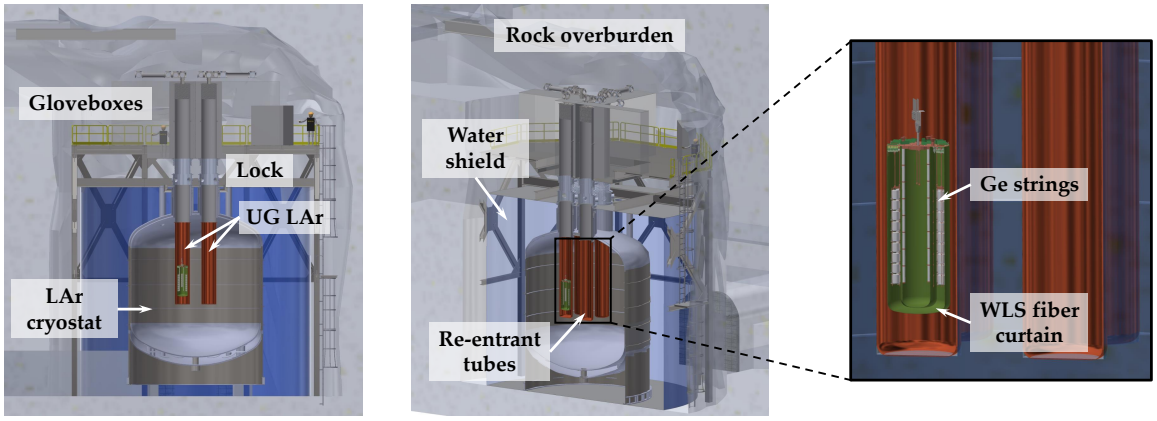

Figure 4.14: Artistic views of the LEGEND-1000 setup. The detector strings will be installed in several re-entrant tubes made from ultra-pure electroformed copper, and filled with underground LAr. The re-entrant tubes themselves are deployed in a cryostat filled with standard LAr. The LAr cryostat is surrounded by a water tank. Figures provided by M. Busch.

BACKGROUND MODEL In LEGEND-1000, the overall background level is intended to be further reduced by an order of magnitude compared to LEGEND-200 to a level of

$$\mathrm{BI} < 1 \cdot 10^{-5}\,\mathrm{cts/(keV \cdot kg \cdot yr)} \tag{4.3}$$

$$\Leftrightarrow \mathrm{BI} < 0.03\,\mathrm{cts/(FWHM \cdot t \cdot yr)}. \tag{4.4}$$

Within a live time of about ten years, the corresponding targeted signal discovery sensitivity on the decay half-life is $T^{0\nu}_{1/2} > 10^{28}$ yr. This fully covers the IO regime, see **Figs.** 2.9 and 2.10. An overview of the anticipated background components is shown in **Fig.** 4.15.

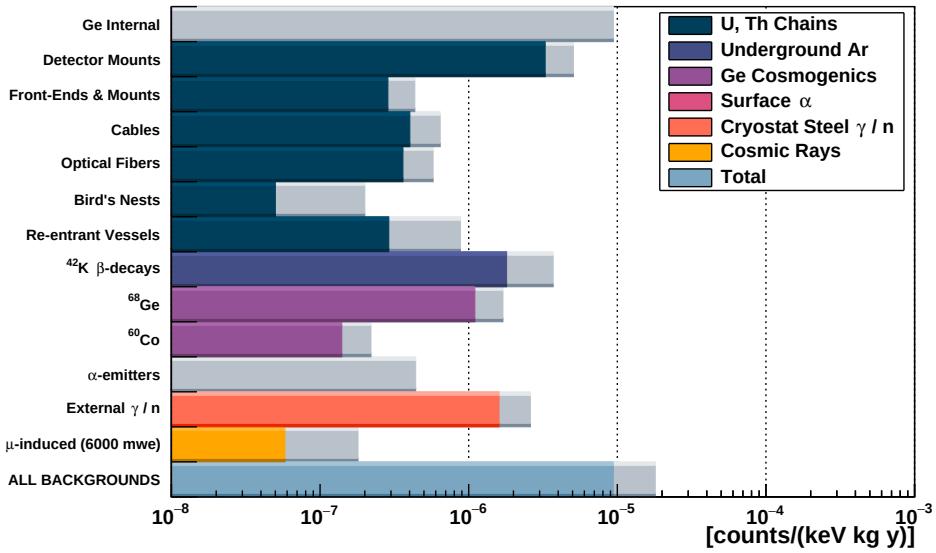

Figure 4.15: Anticipated backgrounds in LEGEND-1000. Colored bars provide the estimated background contributions, while grey bars indicate 1σ uncertainties due to uncertainties in the screening measurements and Monte Carlo simulations. For the contributions of U, Th internal to germanium detectors, and for the alpha emitters on detector surfaces, only upper limits are estimated. Plot courtesy of the LEGEND collaboration.

To achieve the ambitious background goal, additional background reduction techniques are required. Due to the foreseen exclusive use of ICPC detectors, surface alpha backgrounds can be reduced considerably. Moreover, a reduction of the background caused by the radioactive decay of ^{42}K can be achieved by using underground liquid argon (UG LAr). Due to its extraction from deep mines,

UG LAr has a low content of the isotope ^{39}Ar and probably also ^{42}Ar. However, alternative mitigation strategies are also being pursued. These include the option to increase the thickness of the lithiated n^+ electrode, or to use a PEN encapsulation for the HPGe detectors. Muon-induced backgrounds will be reduced by selecting a host lab with a higher depth. Currently, several locations for LEGEND-1000 are being reviewed. Another potential lever to further reduce backgrounds is the signal readout electronics. The LEGEND-1000 baseline design envisages the use of a custom-designed application-specfic integrated circuit (ASIC) readout scheme. ASIC technology, cf. **Ch.** 10.2.3, allows the implementation of the entire charge sensitive amplifier (CSA) into a single low-mass chip while maintaining the spectral and noise performance achieved with conventional solutions [16]. One of the main objectives of this work was to demonstrate the feasibility of operating a large-scale germanium detector together with a readout ASIC. More details of the signal readout electronics of LEGEND-1000 are discussed in **Ch.** 12.

Part II

CHARACTERIZATION OF POINT CONTACT GERMANIUM DETECTORS

In LEGEND-200, alpha- and beta-induced surface backgrounds are anticipated to be among the dominant contributions. One of the main objectives of this work is to gain a better understanding of surface effects. To this end, the response of a p-type point contact germanium detector to alpha and beta particles hitting the passivated surface is studied in detail. In the following chapters, it is shown that the passivation layer is prone to effects such as charge build-up leading to a radial-dependent degradation of various pulse shape parameters. It is demonstrated that independent of the sign of the surface charges, surface alpha events exhibit a delayed charge recovery effect that can be exploited to reject them. Moreover, it is shown that all alpha particles are sensitive to surface effects, whereas beta particles with high penetration depths are mostly insensitive to these effects. Therefore, their discrimination at the passivated surface is expected to be challenging.

5

SURFACE BACKGROUNDS IN LEGEND-200

This chapter discusses the relevance of surface backgrounds in LEGEND-200. In **Ch.** 5.1, a brief overview of alpha and beta surface backgrounds is given. The phenomenology and importance of PPC detector surface effects is reviewed in **Ch.** 5.2. Finally, the delayed charge recovery (DCR) effect, a phenomenon that can be used to effectively reject surface alpha events, is introduced in **Ch.** 5.3.

5.1 OVERVIEW

As already discussed in **Ch.** 4.1, ^{76}Ge-based $0\nu\beta\beta$ decay searches are prone to backgrounds arising from energy depositions at the detector surfaces. According to the LEGEND-200 background model, see **Fig.** 4.13 in **Ch.** 4.3.1, alpha and beta surface backgrounds are anticipated to be among the dominant contributions. For the surface alphas, a maximum background contribution of $\mathrm{BI}_\alpha \lesssim 4.3 \cdot 10^{-5}\,\mathrm{cts}/(\mathrm{keV}\cdot\mathrm{kg}\cdot\mathrm{yr})$ is expected. The surface betas are assumed to contribute with a maximum background of $\mathrm{BI}_\beta \lesssim 4.0 \cdot 10^{-5}\,\mathrm{cts}/(\mathrm{keV}\cdot\mathrm{kg}\cdot\mathrm{yr})$. Together, the surface backgrounds could account for up to 85 % of the anticipated total background $\mathrm{BI}_{\mathrm{tot}} \approx 10^{-4}\,\mathrm{cts}/(\mathrm{keV}\cdot\mathrm{kg}\cdot\mathrm{yr})$ in LEGEND-200. Consequently, a precise understanding and modeling of these backgrounds is crucial.

5.1.1 *Alpha backgrounds*

Alpha backgrounds in LEGEND-200 are expected to be predominantly caused by the decay of radon isotopes and their progeny, particularly ^{222}Rn. Radon is a radioactive noble gas which is created naturally as part of the decay chains of uranium and thorium. During the production processing of a HPGe detector, it is exposed to air and undergoes various mechanical and chemical treatments. A slight radon contamination of the detector (surface) is unavoidable. Furthermore, radon contamination and outgassing of parts close to the detectors in the experimental environment can also lead to undesired alpha backgrounds. A simplified decay scheme of ^{222}Rn is illustrated in **Fig.** 5.1.

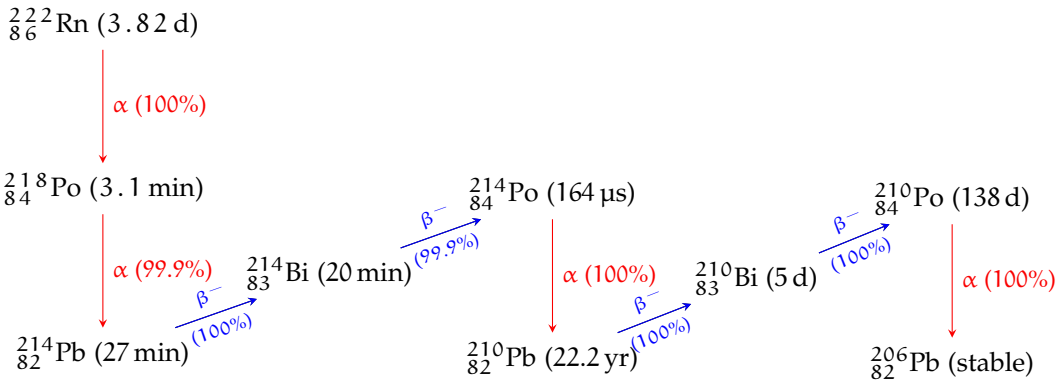

Figure 5.1: Decay scheme of ^{222}Rn. The isotope decays via several alpha and beta decays to the stable nucleus ^{206}Pb. The numbers in parentheses denote the half-lives of the (daughter) isotopes. Data from [112].

As can be seen from the scheme, the isotopes with the longest half-lives are ^{210}Pb ($T_{1/2} = 22.2\,\mathrm{yr}$) and ^{210}Po ($T_{1/2} = 138\,\mathrm{d}$). The other isotopes have shorter half-lives and decay quickly. Due to its long half-life, the isotope ^{210}Pb accumulates. In subsequent decays, the isotope ^{210}Po is of

major concern. During its decay to the stable isotope ^{206}Pb, an alpha particle with an energy of $E_\alpha = 5407.5\,\text{keV}$ is emitted [112]. If the energy of the alpha particle is degraded, it can lead to a background in the ROI. The degradation can be caused by the alpha particle losing energy in the material from which it is emitted, by losing energy in layers on or close to the detector surface, or by charge trapping or charge loss due to dead regions in the detector [228, 229].

In germanium, the penetration depth of an alpha particle with an energy of $E_\alpha \approx 5\,\text{MeV}$ is on the order of 20 µm, cf. **Ch.** 3.1.1. Due to their short penetration depth, all alphas are assumed to be prone to surface effects. Alpha events occur at a single site in the active detector volume.

ALPHA BACKGROUNDS IN LEGEND-200 The estimation of PPC detector alpha backgrounds in LEGEND-200 is based on the extrapolation of alpha backgrounds measured in the MAJORANA DEMONSTRATOR[1]. After the application of PSD cuts (but before the application of dedicated alpha cuts), a background of $BI_0 = 6.95 \cdot 10^{-2}\,\text{cts}/(\text{keV}\cdot\text{kg}\cdot\text{yr})$ was observed in the signal ROI [230, 231]. In the following, it is assumed that the remaining events are all alphas (overestimation), and that they are distributed homogeneously on the passivated detector surface. Moreover, if we assume a survival fraction of Γ_α for the alphas after the additional application of alpha cuts, the background index can be expressed as $BI_1 = BI_0 \cdot \Gamma_\alpha$. Finally, by taking into account that $m_{PPC} \approx 30\,\text{kg}$ out of $M_{L200} \approx 200\,\text{kg}$ detector mass will be PPC detectors, a background of $BI_2 = BI_1 \cdot m_{PPC}/M_{L200}$ is obtained. **Fig.** 5.2 shows the background index BI_2 as a function of the alpha survival fraction Γ_α for various BI_0. Given the MJD background index BI_0, to achieve the anticipated alpha background goal of $BI_\alpha \lesssim 4.3 \cdot 10^{-5}\,\text{cts}/(\text{keV}\cdot\text{kg}\cdot\text{yr})$, an alpha survival fraction of $\Gamma_\alpha \approx 0.4\%$ is required [231]. Scenarios with a decreased or an increased background index BI_0 change the allowed alpha survival fraction only slightly. Assuming that all other backgrounds in the LEGEND-200 background model are fixed, the maximum allowed alpha survival fraction is of $\mathcal{O}(< 1\%)$. It should be noted here that these estimations are very rough approximations that have to be treated with caution (e.g. the different measurement environment is not taken into account). However, the background estimations demonstrate that the rejection of surface alpha events (survival fractions on the sub-percent level) is crucial to achieve the total background goal. Finally, the impact on the analysis may be reduced by separating the PPC and the other detector types into different datasets.

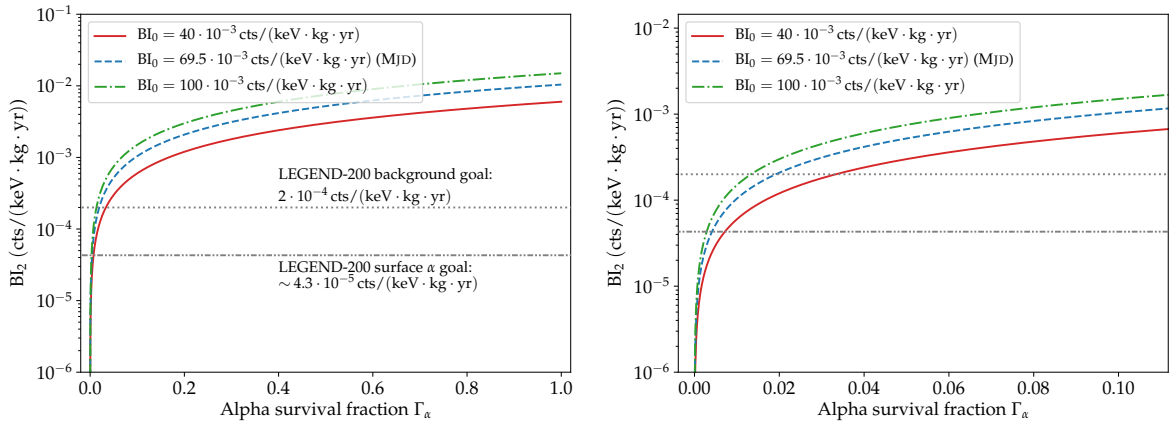

(a) Full Γ_α range.

(b) Relevant Γ_α range.

Figure 5.2: Anticipated alpha backgrounds (PPC detectors) in LEGEND-200 as a function of the alpha survival fraction. The background index BI_2 is shown for various initial backgrounds BI_0. In addition, the LEGEND-200 total background goal (grey dotted line), and the alpha background goal (grey dashed line) are indicated. The right plot shows a zoom of the relevant alpha survival fraction range.

1 The estimation of alpha backgrounds in LEGEND-200 for the BEGe and ICPC detectors is based on GERDA measurements.

5.1.2 *Beta backgrounds*

Beta backgrounds in LEGEND-200 are expected to be caused by radioactive decays of the isotopes ^{42}Ar and ^{42}K. The long-lived isotope ^{42}Ar ($T_{1/2} = 32.9\,\text{yr}$) is naturally abundant in LAr (when sourced from the atmosphere). It is produced by cosmogenic activation and decays via single beta decay to the short-lived daughter ^{42}K ($T_{1/2} = 12.36\,\text{h}$), see **Fig.** 5.3. The decay energy of $Q_\beta = 599\,\text{keV}$ is too low to create a background event in the ROI at the $Q_{\beta\beta}$-value of ^{76}Ge. However, subsequent beta decays of the short-lived daughter ^{42}K with a decay energy of $Q_\beta = 3525.4\,\text{keV}$ are a potential source of background. With a probability of 81.9%, ^{42}K decays directly to the ground state of ^{42}Ca. ^{42}K can also decay to an excited state of ^{42}Ca followed by the transition to the ground state emitting a gamma. The most prominent decay has a probability of 17.6% and is accompanied by a 1524.6 keV gamma. During the decay, also ^{42}K ions are produced which are a further background source. Within the LAr volume, K^- ions are attracted by the positive bias voltage applied to the n^+ electrodes of the detectors. This can be partly mitigated by wrapping the detector strings with nylon cylinders that create a mechanical barrier preventing a drift of the ions to the detector surfaces, cf. **Ch.** 4.2.1 [229].

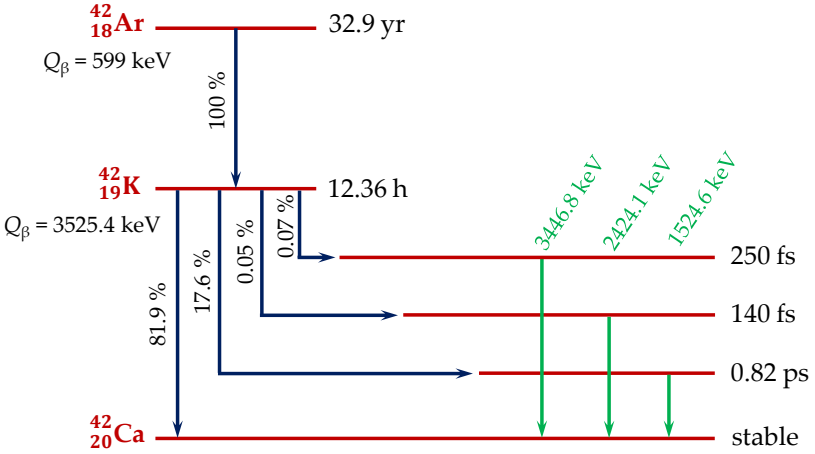

Figure 5.3: Simplified decay scheme of $^{42}\text{Ar} \rightarrow {}^{42}\text{K} \rightarrow {}^{42}\text{Ca}$. The beta decay of ^{42}K ($Q_\beta = 3525.4\,\text{keV}$) to ^{42}Ca is accompanied by the emission of gammas with energies up to 3446.8 keV, well above the $Q_{\beta\beta}$-value of the isotope ^{76}Ge. Scheme adapted from [232, 233].

Within the LAr volume, the path length of beta particles from ^{42}K decays is less than 1.6 cm [222]. Hence, they are only detected if the decay happens within a distance of a few centimeters to the detector surface. Independent of where the beta particles hit the surface, they can lead to background events. However, when impinging on the thick n^+ lithium layer, surface beta events have a characteristic slow rising signal shape which can be used to discriminate against them, cf. **Ch.** 4.1.2.

The main difference between alpha and beta surface events is their penetration depth into the germanium detector. In contrast to alpha particles, electrons from beta decay penetrate deeper, typically up to several mm depending on their energy, cf. **Ch.** 3.1.2. Therefore, not all beta particles show the characteristics of events close to the surface, i.e. some are less affected by surface effects.

BETA BACKGROUND IN LEGEND-200 The PPC detector beta backgrounds in LEGEND-200 can be estimated in a similar way as the alpha backgrounds, i.e. they are based on the extrapolation of ^{42}K beta backgrounds measured in the GERDA experiment. Before the application of analysis cuts, a background of $\text{BI}_0 \approx 6 \cdot 10^{-3}\,\text{cts}/(\text{keV} \cdot \text{kg} \cdot \text{yr})$ was observed on the detector n^+ surface [135, 222]. Extrapolating to the passivated surface of PPC detectors, a projected background index of $\text{BI}_0 \approx 1.5 \cdot 10^{-3}\,\text{cts}/(\text{keV} \cdot \text{kg} \cdot \text{yr})$ is obtained. If we further assume a beta survival fraction Γ_β after the application of PSD cuts, the background index can be expressed as $\text{BI}_1 = \text{BI}_0 \cdot \Gamma_\beta$. Taking also into account the PPC detector mass, we finally obtain $\text{BI}_2 = \text{BI}_1 \cdot m_{\text{PPC}}/M_{\text{L200}}$. **Fig.** 5.4 shows the background index BI_2 as a function of the beta survival fraction Γ_β for various BI_0. To achieve the anticipated beta background goal of $\text{BI}_\beta \lesssim 4.0 \cdot 10^{-5}\,\text{cts}/(\text{keV} \cdot \text{kg} \cdot \text{yr})$, a PPC detector beta survival fraction of $\Gamma_\beta \lesssim \mathcal{O}(10\%)$ is required. The less stringent value compared to the alpha survival fraction is due to the anticipated smaller background index BI_0. Based on the experience gained in

the GERDA experiment, a global beta survival fraction of $\Gamma_\beta \approx \mathcal{O}(1-2\%)$ after the application of PSD cuts is currently being expected [135, 231, 233].

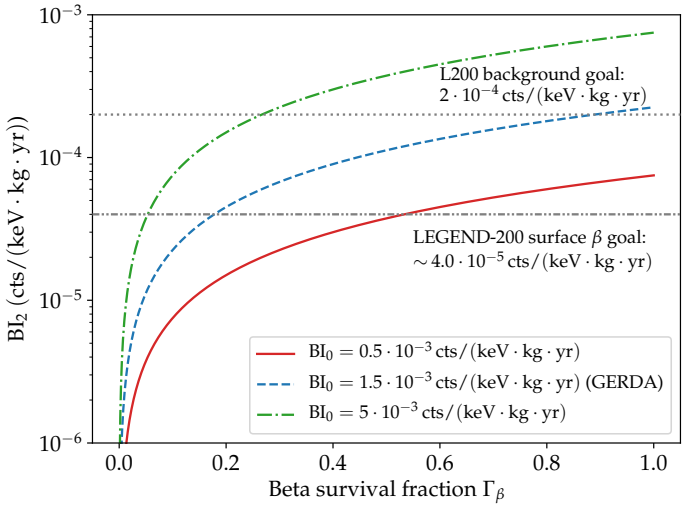

Figure 5.4: Anticipated beta backgrounds (PPC detectors) in LEGEND-200 as a function of the beta survival fraction. The background index BI_2 is shown for various initial backgrounds BI_0. In addition, the LEGEND-200 total background goal (grey dotted line), and the beta background goal (grey dashed line) are indicated.

5.2 PPC DETECTOR SURFACE EFFECTS

Compared to other germanium detector geometries, cf. **Ch.** 3.3.2, PPC detectors have a large passivated surface, usually on the order of $30-40\,\mathrm{cm}^2$. This surface extends over the horizontal top surface, see **Fig.** 6.2, excluding the p^+ contact. Typically, the passivated surface is made from sputtered silicon oxide or amorphous germanium (aGe). This layer has a high resistivity and is left floating, i.e. it is at an undefined electric potential. While the n^+ contact is insensitive to surface alpha events (alpha particles cannot penetrate the few mm-thick lithium-drifted layer), beta particles entering through this surface lead to characteristically slow pulses (they need to penetrate the transition layer) with a reduced current amplitude. Hence, these events have smaller A/E values than SSEs and can be discriminated against by applying PSD cuts. In contrast, the passivated surface and the point contact are highly sensitive to alpha and beta surface events [229].

Since the passivation layer is left floating, it is susceptible to charge build-up. A non-zero charge on the passivated surface, which for example can be induced by charged-up nearby materials at non-zero potentials, changes the electric field in the vicinity of this surface and thus affects the signal formation. Without any charge build-up, the electric field lines close to the passivated surface are mostly parallel to that surface. In the presence of surface charges, however, the field has a strong perpendicular component, modifying the hole and electron drift paths [229].

One of the main aims of this work is to study the impact of surface effects on various pulse shape parameters so that surface backgrounds can be efficiently rejected. To this end, a surface charge model is used whose properties are discussed in the following paragraphs.

NEGATIVE SURFACE CHARGES If the passivated surface is charged negatively, $\sigma < 0$, the holes created during a particle interaction in the detector do not drift directly to the p^+ contact, but are attracted to the passivated surface, see **Fig.** 5.5a. At the surface, they drift very slowly parallel along it in the direction of the point contact and can get trapped by surface charges, surface imperfections, and the amorphous germanium layer. The drift of the holes along the surface to the point contact usually takes much longer than typical event drift times, particularly if the interaction position is located at large radii. Consequently, the holes are not collected, at least not in the time in which the signal is recorded. This means that the signal development is driven by the collection of electrons drifting to the n^+ contact.

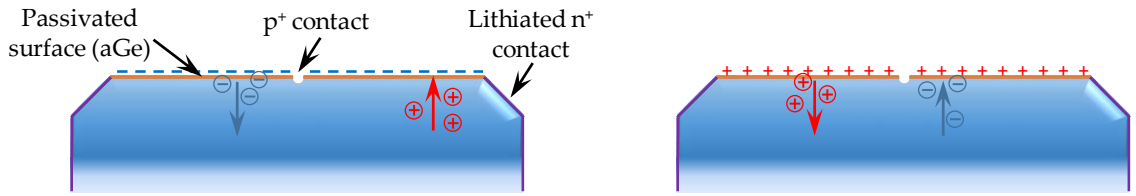

(a) Negative surface charges ($\sigma < 0$). (b) Positive surface charges ($\sigma > 0$).

Figure 5.5: Effect of (a) negative and (b) positive charges on the passivated surface of a PPC detector. In the case of negative (positive) surface charges, holes (electrons) are attracted to the surface, whereas electrons (holes) are repelled. Published in [229].

Due to the presence of negative surface charges, the electrons are repelled from the surface. Simulated electron drift paths are shown in **Fig.** 5.6a. As can be seen, the paths which normally run mostly parallel to the surface are modified by the presence of surface charges, i.e. they are shifted into the bulk. According to the Shockley-Ramo theorem, cf. **Ch.** 3.3.1, for a deposited charge q, the time-dependent charge signal $s(t)$ induced at the p^+ contact can be described by

$$s(t) = q\,[WP(\vec{r}_h(t)) - WP(\vec{r}_e(t))] \tag{5.1}$$
$$= q\,[WP(\vec{r}_h(t)) - WP(\vec{r}_0)] - q\,[WP(\vec{r}_e(t)) - WP(\vec{r}_0)]\,, \tag{5.2}$$

where $WP(\vec{r}_0)$ is the weighting potential at the initial charge deposition location, and the subscripts h and e denote the hole and electron contributions, respectively. After the charge collection is completed for both holes and electrons (time t_c), the equation simplifies to

$$s(t_c) = q\,[1 - WP(\vec{r}_0)] - q\,[0 - WP(\vec{r}_0)] = q. \tag{5.3}$$

This relationship is valid since, by definition, the weighting potential at the p^+ contact is unity ($WP(\vec{r}_h(t_c^h)) = 1$), whereas it is zero at the n^+ contact ($WP(\vec{r}_e(t_c^e)) = 0$). Consequently, the contribution of the electrons to the charge signal development between t_0 (onset of charge collection) and the time t_c^e at which the electrons are collected can be expressed as (total collected electron charge):

$$s_e(t_c^e) \approx q\,WP(\vec{r}_0). \tag{5.4}$$

In contrast, the contribution of the holes can be described by (total collected hole charge):

$$s_h(t_c^h) \approx q(1 - WP(\vec{r}_0)), \tag{5.5}$$

but in the case of negative surface charges is close to zero[2]. In general, close to the passivated surface, the weighting potential strongly depends on the radius r. As shown in **Fig.** 5.7, the weighting potential $WP(r)|_{z=0}$ close to the p^+ contact is close to one. With increasing radial position, the weighting potential drops quickly. The term $1 - WP(r)|_{z=0}$ shows the opposite behavior, i.e. it increases with radius. As discussed above, for a negative charge build-up on the surface, the hole contribution to the signal development at higher radial positions is negligible. Hence, the measured energy is primarily determined by the collected electron charge and follows the radial dependence of $WP(\vec{r}_0)$, cf. **Eq.** (5.4).

POSITIVE SURFACE CHARGES For a positive charge build-up on the passivated detector surface, $\sigma > 0$, the electrons created during a particle interaction are attracted to the surface and the holes are repelled, see **Fig.** 5.5b. Analogous to the explanation for negative surface charges, at small radial positions, the electrons are no longer fully collected to the n^+ contact. The signal development is then primarily due to the collection of holes drifting along modified paths to the p^+ contact, see **Fig.** 5.6b. Following the radial dependence of the weighting potential, cf. **Eq.** (5.5), at small radii, a degraded energy is expected. With increasing radius, the energy increases.

2 Since in the presence of negative surface charges the holes are not collected ($\vec{r}_h(t_c^h) \approx \vec{r}_0$), their contribution to the signal development in the notation introduced in **Eq.** (5.2) is close to zero.

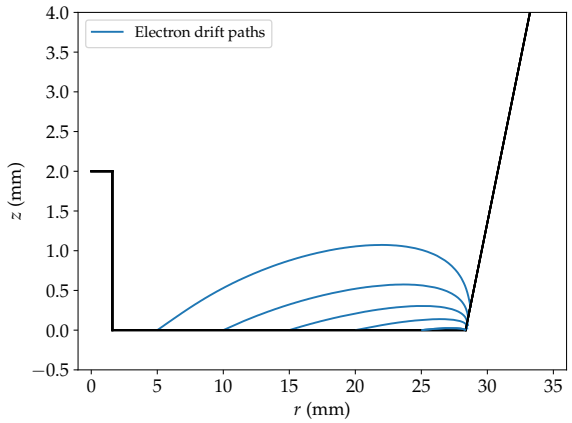

(a) Negative surface charges ($\sigma = -0.3 \cdot 10^{10}\,\mathrm{e/cm^2}$).

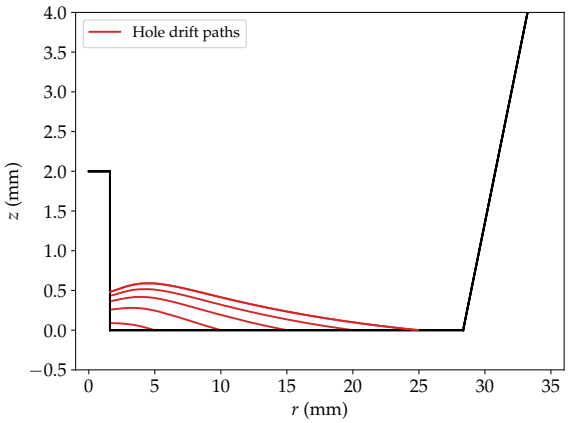

(b) Positive surface charges ($\sigma = +0.3 \cdot 10^{10}\,\mathrm{e/cm^2}$).

Figure 5.6: Simulated electron and hole drift paths for (a) negative and (b) positive charges on the passivated detector surface. The black lines indicate the detector contour, the passivated surface is at $z = 0$. In the presence of negative (positive) surface charges, the holes (electrons) are attracted to the surface. It can be observed how the drift paths are affected by surface charges, i.e. without surface charges the drift would be mostly parallel to the surface. Drift paths were simulated using `mjd_siggen` [234]. Published in [229].

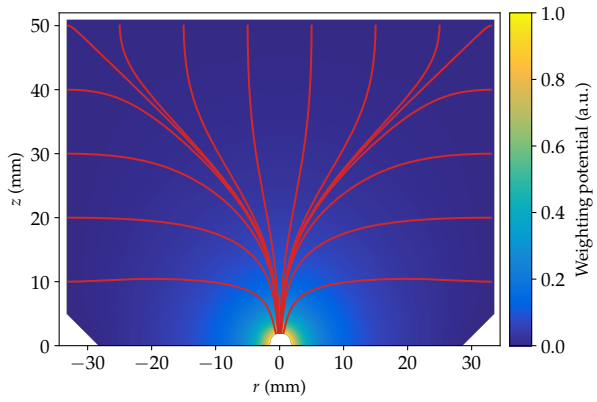

(a) Weighting potential in (r, z) plane.

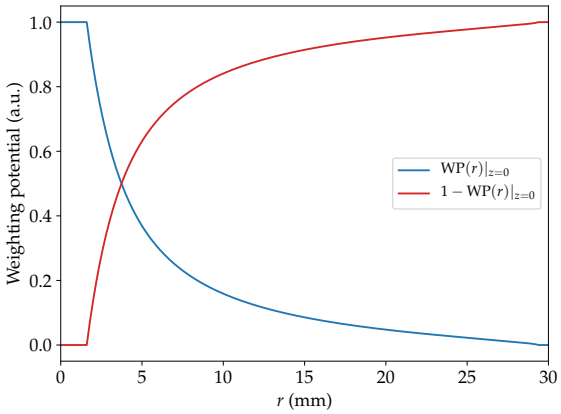

(b) Weighting potential at $z = 0\,\mathrm{mm}$.

Figure 5.7: (a) Simulated weighting potential (WP) of the PONaMa1 detector in the (r, z) plane. The red lines indicate the hole drift paths for interactions near the outer surface. (b) Radial dependence of the WP at the passivated surface, i.e. at $z = 0\,\mathrm{mm}$. The WP was simulated using `mjd_fieldgen` [234]. Published in [229].

IMPACT OF SURFACE CHARGES ON ALPHA AND BETA PARTICLES Due to the small penetration depth of alpha particles in germanium, it is expected that almost all charge carriers are affected by the surface effects described above. In the case of negative surface charges, it is expected that the alpha energy approximately follows the radial dependence of the weighting potential, i.e. it decreases sharply with increasing radius. This is illustrated schematically in **Fig.** 5.8, where the signals of point-like charges with a small penetration depth ($z_0 = 16\,\mu\mathrm{m}$) for a homogeneously distributed surface charge ($\sigma = -0.3 \cdot 10^{10}\,\mathrm{e/cm^2}$) at varying radii were simulated. It can be observed that 1) at higher radial positions the hole component does not contribute to the signal development any longer[3], and 2) the signal amplitude and thus the energy decreases considerably with increasing radius.

In general, beta electrons have higher penetration depths than alpha particles. It is assumed that only electrons in close proximity to the detector surface are affected by surface effects. Electrons with higher penetration depths are not influenced by the presence of surface charges and are collected normally to the electrodes.

3 Using the notation introduced in **Eq.** (5.2), the contribution is close to zero, otherwise it would be constant over time.

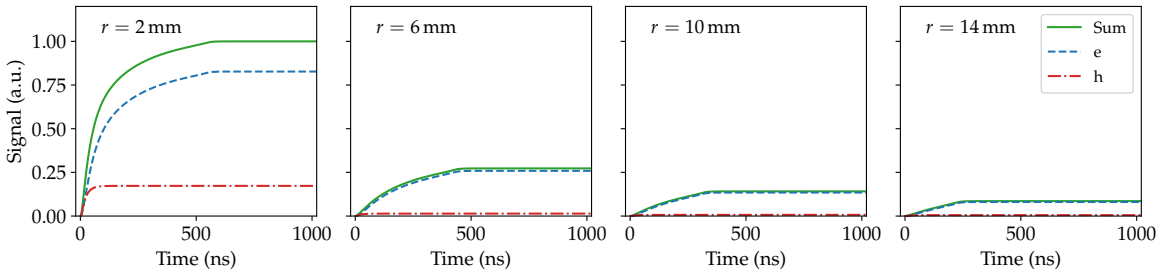

Figure 5.8: Simulated alpha event waveforms in the presence of negative charges on the passivated detector surface ($\sigma = -0.3 \cdot 10^{10}$ e/cm^2) at various radial positions. Point-like charges were started at a depth of $z_0 = 16\,\mu$m. The total signal corresponds to the sum of the electron (e) and hole (h) signals as defined in **Eq.** (5.2). At small radii, the holes still contribute to the signal development. At higher radial positions, the signal development is primarily based on the collection of electrons. Due to the radial dependence of the weighting potential, this component and thus the total signal amplitude fall sharply with increasing radius. The waveforms were simulated using `mjd_siggen` [234]. Published in [229].

5.3 DELAYED CHARGE RECOVERY

Delayed charge recovery (DCR) describes the phenomenon of an extra slow charge collection component for surface alpha events [142, 228, 235]. Compared to events in the detector bulk (e.g. gamma events), the presence of a delayed charge collection component for surface alpha events modifies the waveform tail, see **Fig.** 5.9. The plot shows that the tail of the pole-zero-corrected waveform still increases after the charge collection in the detector bulk has been completed. In contrast, for a gamma event with the same energy in the detector bulk the tail slope stays constant. This distinct pulse shape makes the DCR effect a powerful tool to identify and reject surface alpha events on the passivated surface of PPC detectors [229].

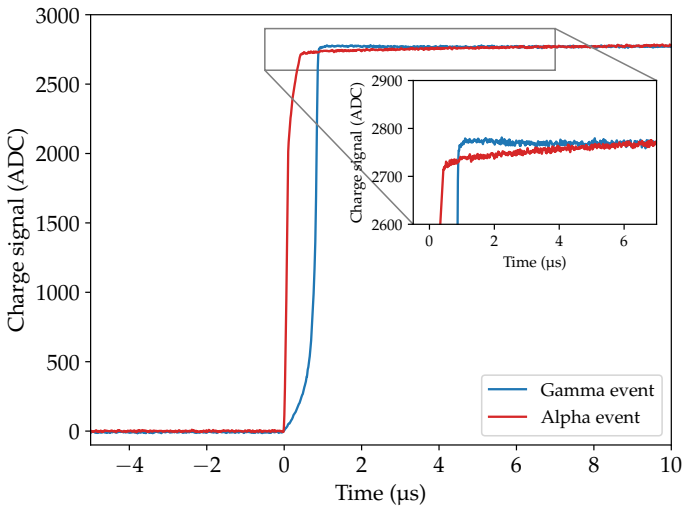

Figure 5.9: Waveform examples for a bulk gamma event (blue curve) and a surface alpha event (red curve) with the same energy. The waveforms were measured with the PPC detector under study. For the baseline and pole-zero-corrected alpha signal, a slowly rising waveform tail can be observed (see inset). This slowly rising component can be explained by the presence of a delayed charge recovery (DCR). Due to its proximity to the p^+ readout electrode, the drift time of the surface alpha event is shorter (steeply rising leading edge) than the one of the gamma bulk event. Published in [229].

There are two mechanisms that can potentially explain the DCR effect for surface alpha events [229]:

1) A certain fraction of charges created during the alpha interaction is trapped in a $\mathcal{O}(\mu m)$-thick region at or near the passivated surface. In this case, the DCR effect corresponds to a slow re-release of these charges into the detector bulk (with a certain release time τ_r) and their subsequent drift to the electrodes.

2) Charges created on or close to the passivated surface have a mobility significantly reduced compared to the drift velocity in the detector bulk [236]. In this case, the DCR effect corresponds to a slow drift of charges along the passivated surface to the electrodes.

Typically, the charge drift along the passivated surface takes much longer than the waveform digitization time. Until recently, it was assumed that the main component leading to a delayed charge collection is due to the trapping and the subsequent slow re-release of charges at the passivated surface. In previous measurements, a charge re-release time on the order of several microseconds was observed. In addition, the fraction of charge re-released into the detector bulk was on the order of a few percent [228, 235]. However, dedicated pulse shape simulations including the effects of diffusion and self-repulsion, cf. **Ch.** 9.3.4, have demonstrated that surface drifts can also have an impact [237].

6

MEASUREMENT SETUP

This chapter describes the experimental setup used for the PPC detector surface characterization measurements. After an overview of the test facility in **Ch.** 6.1, the properties of the investigated HPGe detector and its installation in the experimental setup are described in **Ch.** 6.2. The characteristics of the radioactive sources used for the measurements are reviewed in **Ch.** 6.3, while details of the readout electronics and of the data acquisition system are reported in **Ch.** 6.4. The data analysis procedures are discussed in **Ch.** 6.5. Finally, an overview of the PPC detector performance in the test facility is presented in **Ch.** 6.6.

6.1 GALATEA SCANNING FACILITY

The GALATEA (GermAnium LAser TEst Apparatus) facility at Max Planck Institute for Physics (MPP) is a fully automated multi-purpose scanning test stand that was built to investigate bulk and surface effects of HPGe detectors [238, 239]. Due to its versatility, it allows for almost complete scans of the detector surface with radioactive alpha, beta, and gamma sources. An overview of the experimental setup is shown in **Fig.** 6.1.

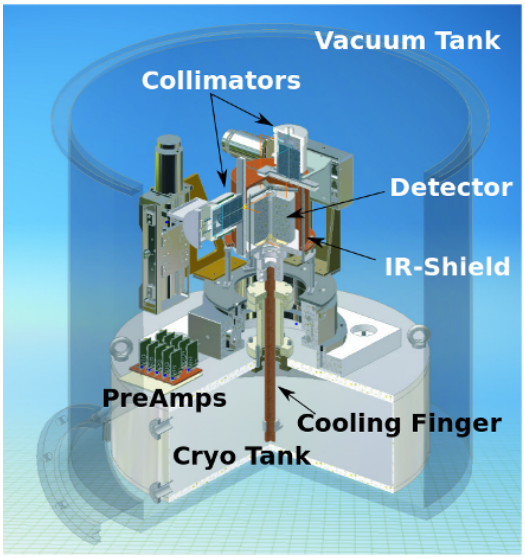

Figure 6.1: Overview of the vacuum cryostat of the GALATEA scanning facility. The germanium detector is cooled via a copper or aluminum holding structure connected to a cooling finger submerged into a cryo tank filled with liquid nitrogen. A copper hat is used as an infrared shield. The radioactive sources used for scanning the detector surface are installed in a top and side collimator. Source: [238].

The core of the test stand is a customized stainless steel vacuum cryostat with a large experimental volume hosting the germanium detector, the radioactive source(s) (usually mounted in a top and/or a side collimator), and the signal readout electronics. The detector under investigation can be mounted in an aluminum or a copper holding structure. This structure is used for cooling the detector and is connected to a copper cooling finger submerged into a tank filled with LN_2. The cryo tank is located inside the vacuum cryostat and is refilled automatically using a feedthrough. The germanium detector is shielded against infrared (IR) radiation by a 4 mm-thick cylindrical copper hat. Several layers of super-insulation foil wrapped around the inner wall of the vacuum cryostat act as further thermal insulation. The copper IR shield has two slits (one on the side of

the hat, the other one on top) along which the collimators with the radioactive sources are guided during surface scan measurements. The top slit has a width of 2.0 mm, a length of 43.5 mm, and extends from the center to the outside. The side slit has a width of 2.0 mm, a length of 76.5 mm, and extends from top to bottom. The collimators are mounted on a slider made from Murtfeldt material with a low sliding friction coefficient [240].

A system consisting of three independent stages allows for an almost complete scan of the detector surface. One stage can rotate the IR shield through 360° with respect to the detector enabling azimuthal scans. The additional two linear stages are used to move the top collimator along the top surface (top scans), and the side collimator along the lateral surface (side scans). The temperature inside the cryostat is measured by several PT100 sensors at various locations (detector holder, detector PTFE support structure, IR shield, stage of rotational motor, cryostat). The cryostat is evacuated using a pumping unit consisting of a forepump (Kashiyama NeoDry 30C) and a turbomolecular pump (Pfeiffer TMH 521 P). In order to minimize microphonic noise, the pumps are turned off during the measurement periods. To this end, a shutter connecting the vacuum tank with the pumping unit is closed. The pressure inside the vacuum cryostat is measured with a vacuum gauge installed in the vessel lid. Further details of the GALATEA test facility can be found in [238, 239].

6.2 PONAMA1 IN GALATEA

For the surface characterization measurements in GALATEA, a PPC germanium detector with natural isotopic composition was used (PONaMa1, acronym for PPC detector from ORTEC made from Natural Material). The detector was developed as a prototype for the enriched HPGe detectors that were operated in the MAJORANA DEMONSTRATOR (future-operated in LEGEND-200) and closely resembles their properties. An overview of the specifications and dimensions of the detector under study can be found in **Fig.** 6.2. While the n^+ contact is lithiated (thickness of 1.1 mm), the p^+ readout contact is 0.3 µm boron-implanted. The passivated surface separating the p^+ contact from the n^+ electrode is made from sputtered aGe with a thickness of about 100 nm and an area of about 37 cm^2. The manufacturer's recommended bias voltage is 2.0 kV.

Property	Value
Mass	1.0 kg
Inner diameter a	58.9 mm
Outer diameter b	68.9 mm
Length c	52.0 mm
Length d	47.0 mm
Deadlayer (Ge/Li) e	1.1 mm
Dimple depth f	2.0 mm
Dimple diameter g	3.2 mm

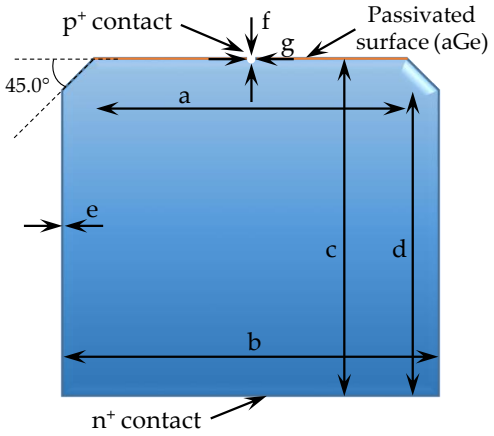

Figure 6.2: Parameters and sketch of the PONaMa1 detector. Published in [229].

To allow for an easy scan of the passivated detector surface in the GALATEA facility, the detector was installed with the point contact facing up, see **Fig.** 6.3. The detector was mounted in a modified copper cylinder of a standard vendor-cryostat detector mount. Its side walls were insulated from the cylinder through a thin sheet of PTFE insulation around the perimeter. The n^+ electrode was connected to the HV module (iseg NHQ 206L) via a spring-loaded pin located at the detector bottom surface. Likewise, connection to the p^+ contact was established with a pogo pin that was held in a narrow PTFE bar mounted on top of the detector. The PTFE holding structure was also used to guide the signal cable. The PTFE bar had a width of 5.1 mm, a height of 5.0 mm, and a distance of about 3.1 mm from the detector surface. For the surface scan measurements at small radial positions, the bar created a shaded area on the detector surface thereby decreasing the event rate. An illustration showing all relevant dimensions can be found in **Fig.** A.1 in the appendix.

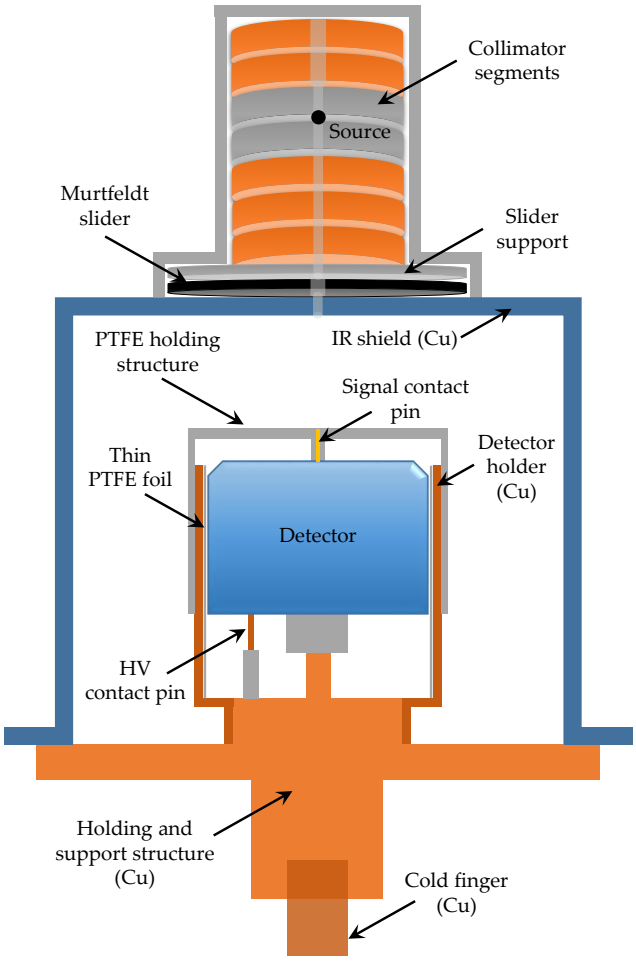

Figure 6.3: Simplified sectional view of the PONaMa1 detector in the GALATEA scanning facility. The detector is mounted in a copper structure that is cooled via liquid nitrogen. It is surrounded by a copper IR shield. In the scan measurements, the detector surface is irradiated by a radioactive source installed in a suitable collimator mounted on top of the IR shield. For reasons of visual clarity, the side collimator is not shown (not relevant to this work). The figure is not to scale. Published in [229].

6.3 RADIOACTIVE SOURCES

Various radioactive sources were used to study the characteristics of background events on the passivated surface of the PONaMa1 detector. For the investigation of surface alpha and surface beta events, ^{241}Am and ^{90}Sr sources were used, respectively. In addition, a ^{228}Th source was installed for calibration purposes and to validate PSD capabilities. In the following paragraphs, the properties of the aforementioned isotopes will be discussed briefly.

AMERICIUM-241 The radioactive isotope ^{241}Am ($T_{1/2} = 432.6\,\text{yr}$) mainly decays via alpha decay to ^{237}Np. The decay is accompanied by a weak gamma ray byproduct [112]:

$$^{241}\text{Am} \rightarrow {}^{237}\text{Np} + {}^{4}_{2}\alpha + \gamma\,(59.54\,\text{keV}). \tag{6.1}$$

The most prominent alpha decay has an energy of $E_\alpha = 5485.56\,\text{keV}$ and a branching ratio of 84.8% [112]. While in air alpha particles with an energy of a few MeV travel several centimeters, in solids like germanium, they only penetrate several tens of micrometers, cf. **Ch.** 3.1.1. Consequently, alpha sources like ^{241}Am are ideally suited for the investigation of surface effects.

STRONTIUM-90 The radioactive isotope ^{90}Sr ($T_{1/2} = 28.9\,\text{yr}$) exclusively decays to ^{90}Y via single beta decay [112]:

$$^{90}\text{Sr} \rightarrow {}^{90}\text{Y} + e^- + \bar{\nu}_e \quad (100\%, Q_\beta = 545.9\,\text{keV}). \tag{6.2}$$

The isotope ^{90}Y ($T_{1/2} = 2.67\,\mathrm{d}$) in turn undergoes beta decay to the ground state of ^{90}Zr [112]:

$$^{90}\mathrm{Y} \rightarrow {}^{90}\mathrm{Zr} + \mathrm{e}^- + \bar{\nu}_\mathrm{e} \quad (99.99\%, Q_\beta = 2278.5\,\mathrm{keV}). \tag{6.3}$$

For the measurements in GALATEA, ^{90}Sr sources were used to study surface beta effects. They provide an appropriate proxy for the ^{42}K-induced backgrounds encountered in realistic experimental environments.

THORIUM-228 The radioactive isotope ^{228}Th ($T_{1/2} = 1.9\,\mathrm{yr}$) decays via several alpha and beta decays to the stable nucleus ^{208}Pb. The decay chain is illustrated in **Fig.** 6.4. During the decays, various excited energy states are produced that emit gamma radiation when returning back to the ground state. Most of the gamma rays are emitted after the decays of ^{212}Bi and ^{208}Tl. Due to several distinct advantages, the isotope is often used as a calibration source for HPGe detectors:

1) First and foremost, the ^{228}Th energy spectrum has several intense gamma lines in a wide energy range (from about 200 keV up to 2.6 MeV) which enables a precise energy calibration. The most prominent gamma lines are listed in **Tab.** 6.1.

2) Secondly, ^{228}Th can be used to define quality cuts for the discrimination of signal events from background events. This is possible due to a high statistics DEP at the energy $E = 1592.5\,\mathrm{keV}$ which is used as a proxy for signal-like events, cf. **Ch.** 4.1.

3) Finally, ^{228}Th has a half-life long enough so that it can be used as an energy and PSD calibration source over a reasonable period of time.

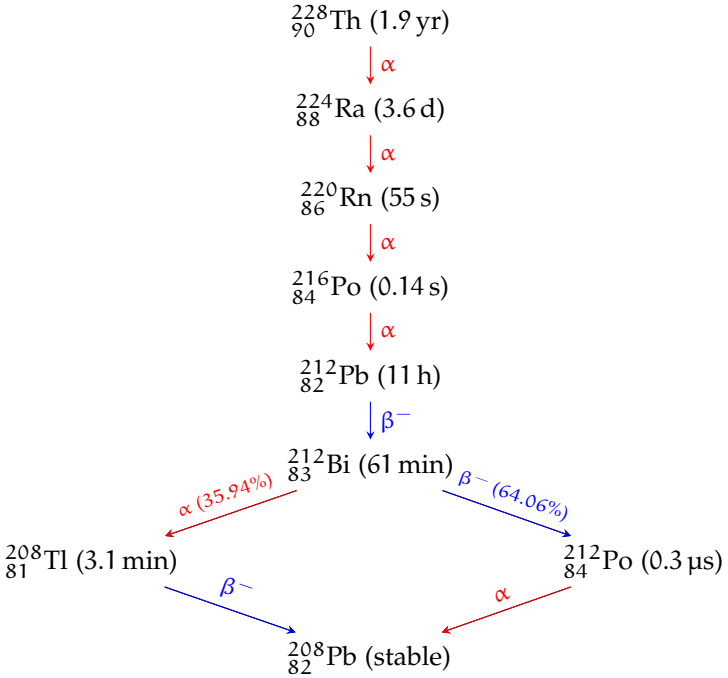

Figure 6.4: Decay scheme of the ^{228}Th isotope. The radionuclide decays via several alpha and beta decays to the stable nucleus ^{208}Pb. The numbers in parentheses denote the half-lives of the (daughter) isotopes. Scheme adapted from [94].

Table 6.1: Most dominant gamma lines (energy and intensity) of the ^{228}Th decay chain. Data from [112].

Isotope	Energy (keV)	Intensity (%)	Isotope	Energy (keV)	Intensity (%)
^{212}Pb	238.632 ± 0.002	43.6 ± 0.5	^{212}Bi	785.37 ± 0.08	1.102 ± 0.013
^{208}Tl	277.371 ± 0.005	6.6 ± 0.3	^{208}Tl	860.557 ± 0.004	12.5 ± 0.1
^{212}Pb	300.087 ± 0.010	3.30 ± 0.04	^{212}Bi	893.408 ± 0.005	0.378 ± 0.019
^{208}Tl	510.77 ± 0.10	22.60 ± 0.20	^{212}Bi	952.120 ± 0.011	0.17 ± 0.03
	511	Annihilation	^{212}Bi	1078.62 ± 0.10	0.564 ± 0.019
^{208}Tl	583.187 ± 0.002	85.0 ± 0.3	^{208}Tl	1592.511 ± 0.010	DEP
^{137}Cs	661.657 ± 0.003	85.1 ± 0.2	^{212}Bi	1620.50 ± 0.10	1.47 ± 0.03
^{212}Bi	727.330 ± 0.009	6.67 ± 0.09	^{208}Tl	2103.511 ± 0.010	SEP
^{208}Tl	763.13 ± 0.08	1.79 ± 0.03	^{208}Tl	2614.511 ± 0.010	99.754 ± 0.004

6.4 READOUT ELECTRONICS AND DATA ACQUISITION

For the surface characterization measurements of the PONaMa1 detector in GALATEA, the signal readout electronics was installed in the vacuum cryostat. It consisted of two stages: a front-end section located in close proximity to the p^+ readout contact of the detector, and a preamplifier farther away. In the context of $0\nu\beta\beta$ decay searches, the spatial separation of the readout electronics has several advantages. This will be discussed in more detail in **Ch.** 10. In GALATEA, the resistive-feedback amplifier had a decay time of $\tau \approx R_f C_f \approx 50\,\mu s$. A HV filter was used to suppress high-frequency noise potentially introduced by the bias voltage supply. A simplified schematic of the readout electronics is shown in **Fig.** 6.5. It should be noted here that the preamplifier was optimized for detectors with higher capacitances than the investigated one. This mismatch might be one of the reasons for the relatively high noise levels encountered in the measurements, cf. **Ch.** 6.6.

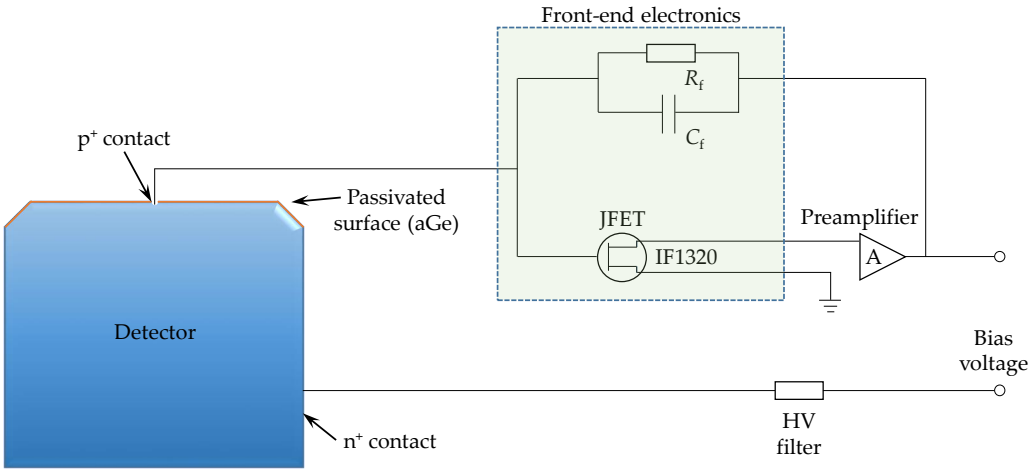

Figure 6.5: Simplified schematic of the signal readout electronics used for the surface characterization measurements of the PONaMa1 detector in GALATEA. It consists of a front-end electronics stage located in close proximity to the p^+ contact and a preamplifier stage farther away.

Data were acquired with a Struck 14-bit SIS3316 flash analog-to-digital converter (FADC). The FADC digitized the analog signals with a sampling frequency of 250 MHz. Every waveform consists of 5000 samples and has a total trace length of 20 µs. Therefore, one sample represents a time interval of 4 ns. The acquisition window was divided into about one third of pre-trigger and two thirds of post-trigger region, with the start time t_0 of the waveform located at $t_0 \approx 6.8\,\mu s$. All waveform traces were stored on disk for offline data analysis.

6.5 DATA ANALYSIS PROCEDURES

This section describes the analysis procedures and routines of the data acquired with the PONaMa1 detector in GALATEA. A simplified overview of the analysis chain is shown in **Fig.** 6.6. In the scope of this thesis, a highly customized `Python` code has been developed for the analysis of the measurement data. A modified version of the code was also used for the analysis of the Post-GERDA test data, cf. **Ch.** 11.2.

ANALYSIS AND DATA STRUCTURE The data analysis is organized hierarchically using `Tier`-levels comparable to those in the GERDA data analysis [241]. The raw waveforms, the timestamps, and the online event energies (in ADC units) acquired with the FADC are initially stored in a binary format (`Tier0` level). For reasons of data handling, the data files are converted into the `hdf5` format (`Tier1` level). In the next stage of the analysis chain, the `Tier2` level, various waveform computations are performed. These are described in detail in the following paragraphs. The outputs of the `Tier2` analysis are saved as `hdf5` files and can eventually be used for high-level data analyses (`Tier3` level), e.g. energy calibration, PSD techniques, etc.

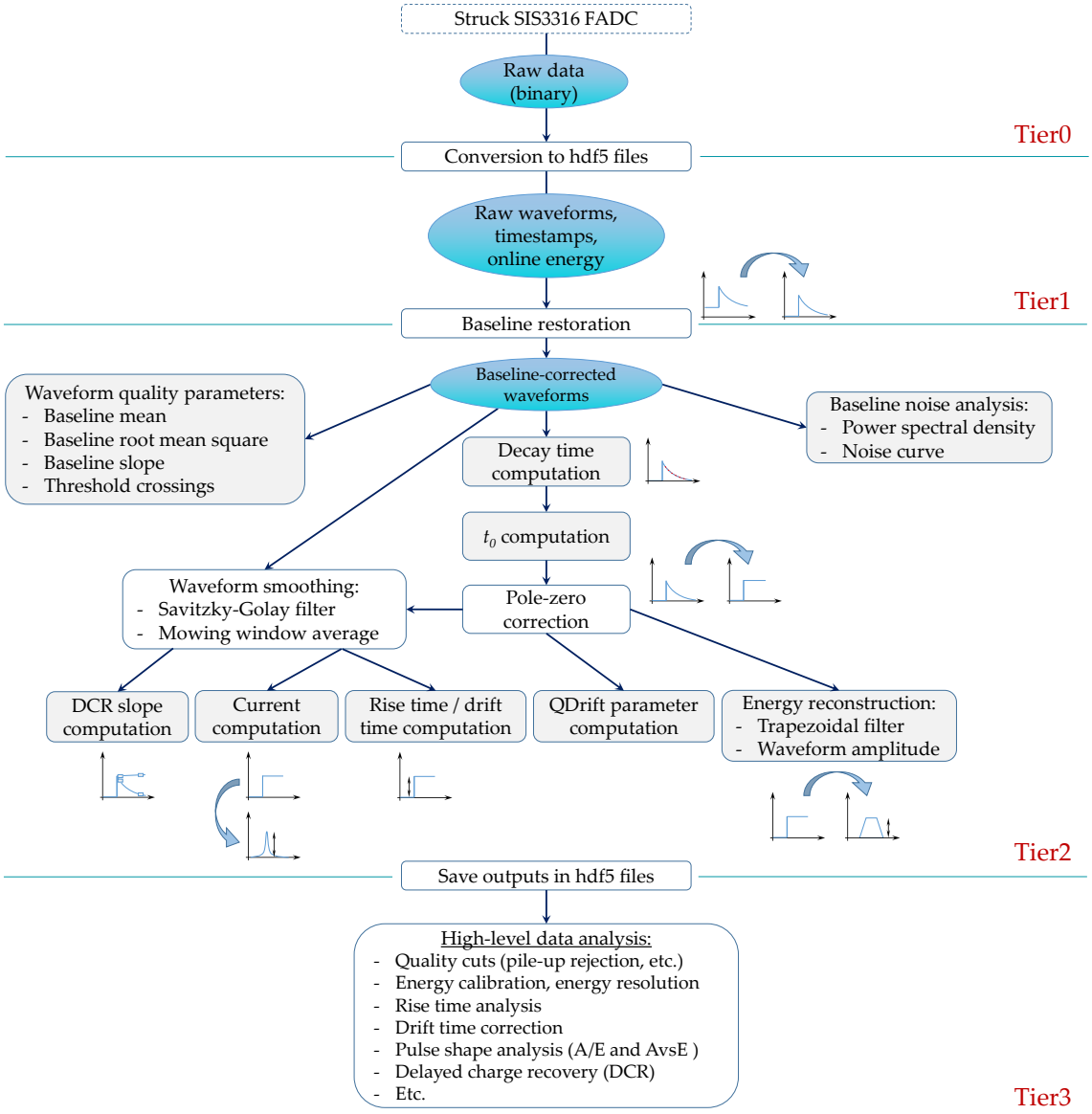

Figure 6.6: Overview of the analysis chain used for processing the data taken with the PONaMa1 detector in the GALATEA test facility. The outputs of the `Tier2` level are indicated by the grey colored boxes. A detailed description of the analysis routines can be found in the text.

BASELINE OPERATIONS AND DATA QUALITY PARAMETERS At the beginning of the `Tier2` analysis level, the baselines[1] of the raw waveforms are restored, i.e. they are corrected for their ADC offset. To this end, the first 1000 samples (corresponding to a trace length of 4 µs) of each waveform are averaged. This offset is then subtracted from each waveform sample resulting in a baseline centered around zero, see **Fig.** 6.7.

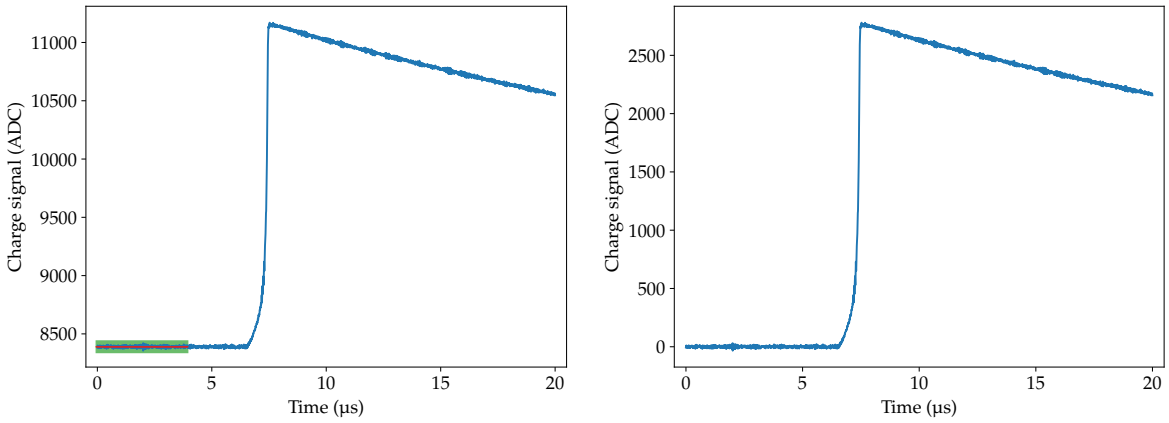

(a) Uncorrected waveform.

(b) Baseline-corrected waveform.

Figure 6.7: Example for the restoration of a waveform baseline. (a) The waveform samples are averaged in the time frame $0 - 4$ µs. The green band indicates the time frame for averaging and the red line the baseline mean. (b) The baseline mean is then subtracted from every waveform sample.

The baseline-corrected waveforms are used as an input for various further computations. To determine the data quality with respect to electronic noise, pile-up, etc., and to be capable of applying quality cuts in the `Tier3` level, several waveform quality parameters are computed: baseline mean, baseline root mean square (RMS), and baseline slope. An example for the distributions of these parameters is shown in **Fig.** 6.8.

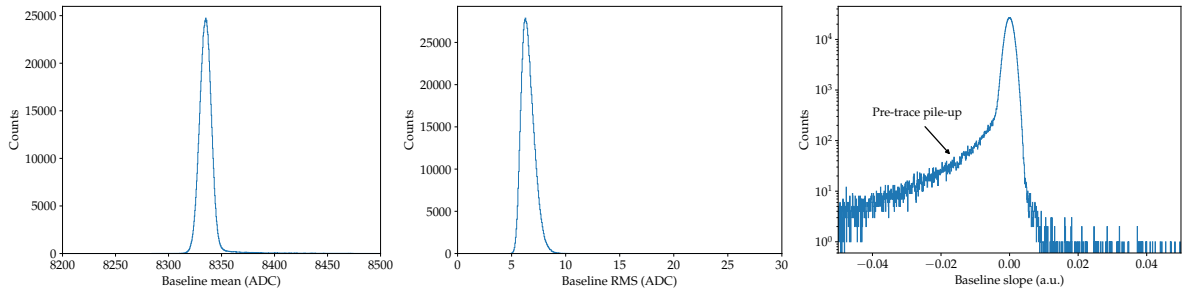

(a) Baseline mean.

(b) Baseline RMS.

(c) Baseline slope.

Figure 6.8: Examples for the distributions of the waveform quality parameters: (a) baseline mean, (b) baseline root mean square, and (c) baseline slope. The quantities were computed based on the first 1000 samples of every waveform (trace length of 4 µs).

While the first two quantities can be used as estimators for the stability of the detector leakage current and the electronic noise, respectively, the baseline slope is a proxy for pre-trace pile-up. This type of pile-up is a superposition of the exponentially decaying tail of the previous event and the baseline of the actual waveform, see **Fig.** 6.9a. The baseline slope is obtained by fitting the first 1000 baseline samples with a first order polynomial[2]. If the absolute baseline slope is higher than a certain value, the event is rejected. The second type of pile-up, in-trace pile-up, is a superposition of two signals within the same trace, see **Fig.** 6.9b. To identify these events, a trapezoidal filter (rise and fall time of 200 ns, flat top time of 1 µs) is applied to the charge signal. The filter times need to be

1 The baseline corresponds to the quiescent output level of the charge sensitive amplifier.

2 An exponential fit to determine the baseline slope would be more accurate (given the exponential decay of the waveform tail). However, since no obvious differences were observed and for the sake of computational simplicity, a linear fit was chosen.

optimized such that in-trace pile-up events are identified properly and MSEs are retained. Energy depositions corresponding to different events are identified by finding the regions where the shaped signal exceeds a specified threshold. If the number of energy depositions in a given trace is higher than one, the event is rejected.

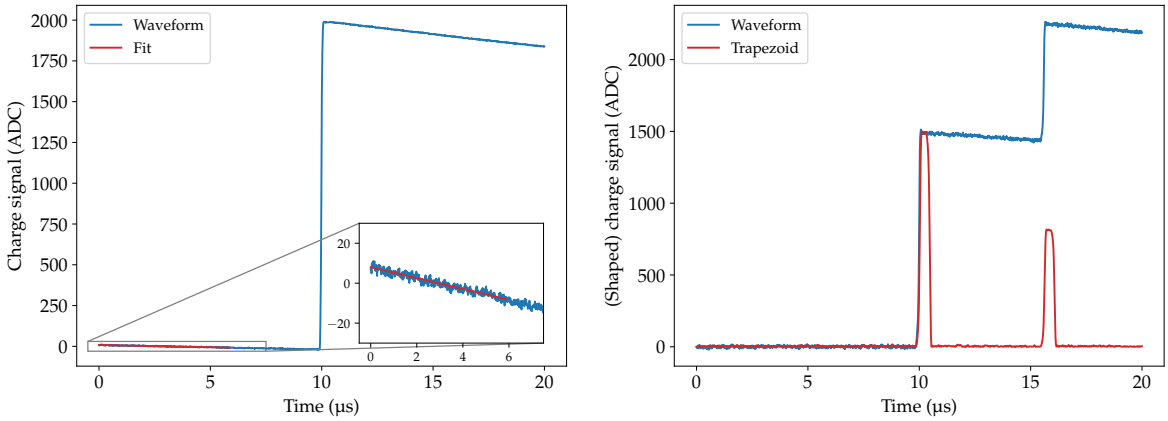

(a) Pre-trace pile-up.

(b) In-trace pile-up.

Figure 6.9: Waveform examples showing (a) pre-trace, and (b) in-trace pile-up events. Pre-trace pile-up events are identified by fitting the baseline with a first order polynomial. In-trace pile-up events are recognized by filtering the trace with a trapezoidal filter and estimating the number of energy depositions above a certain threshold.

DECAY TIME COMPUTATION AND POLE-ZERO CORRECTION To deconvolve the waveform from its exponentially decaying tail induced by resistive-feedback readout electronics, cf. **Ch.** 10.2, a precise value of the decay time (τ) needs to be determined. In a first step, the decay time is computed individually for every event. Assuming that the decaying tail can be described by an exponential of the form

$$y(t) = A \exp(-t/\tau), \tag{6.4}$$

where A denotes the amplitude and t the time, the decay time is obtained by fitting a linear function to the logarithm of $y(t)$, since

$$\log[y(t)] = \log(A) - \frac{1}{\tau} \cdot t. \tag{6.5}$$

For the PPC detector surface characterization measurements in GALATEA, the fit range was constrained to the time frame $12.0\,\mu s \leqslant t \leqslant 19.2\,\mu s$, see **Fig.** 6.10a. In the next step, the decay times of all waveforms (for a given dataset) are histogrammed, see **Fig.** 6.10b. The resulting distribution is approximated with a Lorentzian

$$f(x) = I\left(\frac{\gamma^2}{(x-x_0)^2+\gamma^2}\right), \tag{6.6}$$

where I describes the amplitude of the distribution, x_0 the peak position and γ the half width at half maximum (HWHM). The peak position is extracted from the distribution and used as the decay time for the pole-zero (PZ) correction of all waveforms. For the deconvolution of the exponential decay in the discrete time-domain, an infinite impulse response (IIR) filter of the following recursive form is used [242]:

$$y[n] = y[n-1] + x[n] - \alpha \cdot x[n-1]. \tag{6.7}$$

Here, $y[n]$ is the deconvolution of the signal $x[n]$ at time $n = t$. In addition, $\alpha = \exp(-1/\tau)$ is the deconvolution parameter.

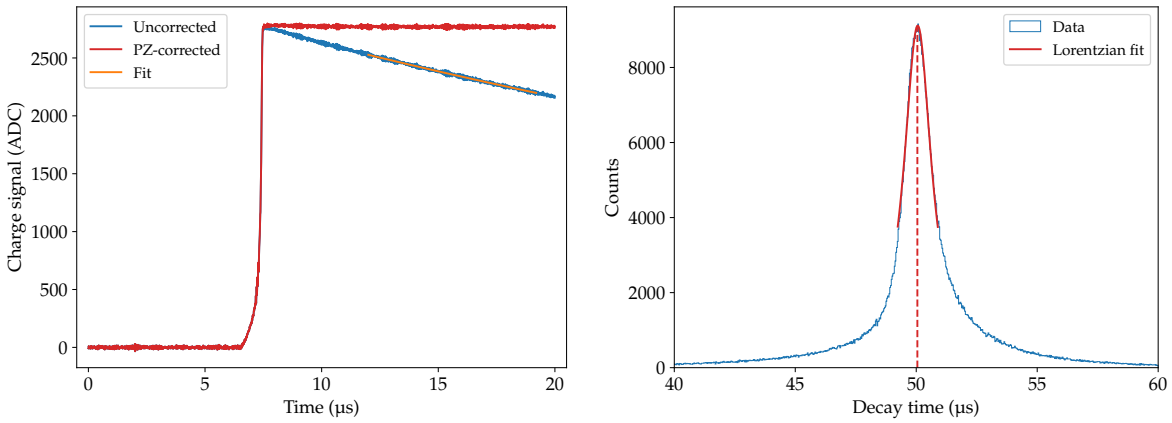

(a) Pole-zero correction.

(b) Decay time distribution.

Figure 6.10: (a) Example for the waveform pole-zero correction. The waveform tail (blue curve) is fit with an exponential function (orange curve). (b) The decay times of all events are histogrammed and the centroid of the distribution (approximated with a Lorentzian) is used to pole-zero correct all waveforms.

WAVEFORM SMOOTHING Since quantities such as the signal rise time, the current amplitude, and the delayed charge recovery (DCR) slope are very sensitive to noise, an appropriate smoothing of the waveforms is required. Therefore, different smoothing filters were implemented in the analysis code. In most cases, the best smoothing performance was achieved with a Savitzky-Golay filter [243]. It was applied to the baseline-corrected waveforms multiple times before extracting quantities such as the signal rise time, etc. **Fig.** 6.11 shows examples of a smoothed low- and high-energy waveform.

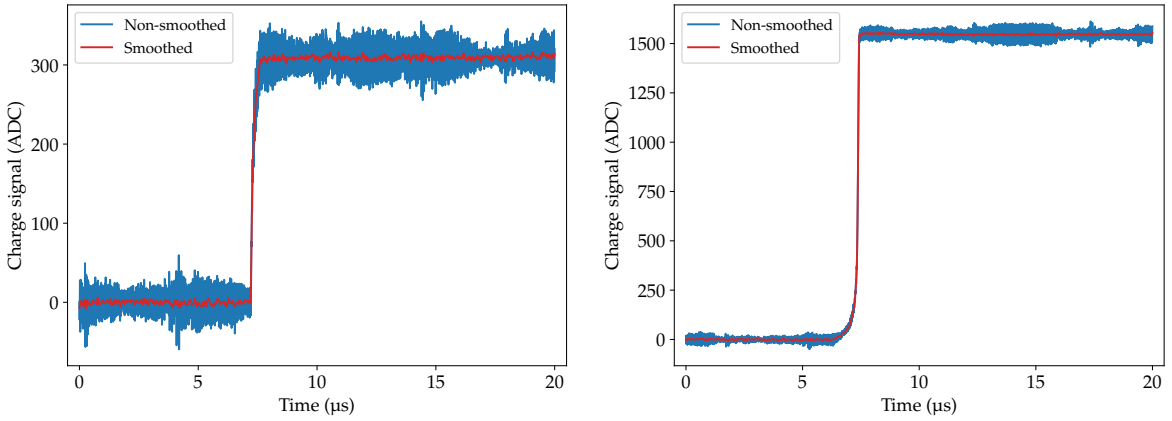

(a) Low-energy event.

(b) High-energy event.

Figure 6.11: Examples for smoothing waveforms (low- and high-energy events) with a Savitzky-Golay filter.

SIGNAL RISE TIME AND DRIFT TIME COMPUTATION The signal rise time is an important waveform parameter providing information on the location of charge production within the HPGe detector. While events in close proximity to the signal readout electrode have short rise times, events farther away have longer rise times. In addition, a precise knowledge of the rise time is important to successfully apply PSD techniques, cf. **Ch.** 4.1.2. Usually, it is defined as the time taken by a signal to change from 10% to 90% of the maximum amplitude of the leading edge. However, other rise time definitions are also frequently used, e.g. 0.5% – 90% [217].

For the PPC detector surface characterization measurements, the rise time was determined based on the PZ-corrected, smoothed waveforms. First, the waveforms were normalized to unity

by dividing them by their energy (pulse height). Then, the time corresponding to 50% of the maximum amplitude of the leading edge was used as a starting point to successively walk backward and forward to estimate the times corresponding to 10% and 90% of the maximum amplitude, respectively. To obtain more precise values, an interpolation between the relevant samples was applied (the leading edge only provides a limited number of samples). An example for the rise time determination is shown in **Fig.** 6.12a.

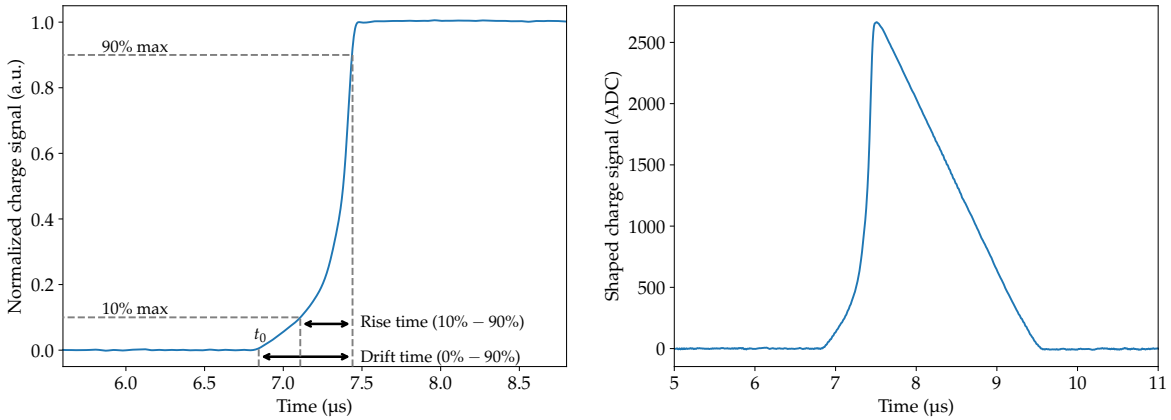

(a) Rise time (10% – 90%) and drift time (0% – 90%).

(b) Shaped signal (asymmetric trapezoid) for t_0 estimation.

Figure 6.12: Example for the determination of the signal rise time (10% – 90%) and drift time (0% – 90%). (a) The rise time is extracted from the PZ-corrected, smoothed and normalized waveform. (b) For the computation of the drift time, a precise time value t_0 corresponding to the onset of the charge collection is required. To this end, an asymmetric trapezoid is applied to the waveform.

Another important waveform parameter is the signal drift time. Typically, it is defined as the time period in which 90% of the total charges are collected [244]. To extract the drift time from the signal, a precise value for the onset of the charge collection is required. This time point t_0 is estimated by finding the point when a fixed threshold on the leading edge is crossed. Depending on the noise situation, it might be difficult to compute a precise t_0 from the raw waveform. Hence, an asymmetric trapezoidal filter with a rise time of 40 ns, a flat top time of 100 ns, and a fall time of 2000 ns is applied to the PZ-corrected waveform. These filter times optimize the signal-to-noise ratio (SNR) for the t_0 estimation. While a short filter rise time is comparable to the threshold crossing time and avoids adding noise, the long fall time gives a good measure of the baseline value [245]. An example for the signal waveform shaped with an asymmetric trapezoid is shown in **Fig.** 6.12b. The t_0 is eventually obtained by computing the maximum of the trapezoid which is then used as a starting point to successively walk backward and estimate the last time point crossing the threshold (for the GALATEA surface characterization measurements, a fixed value of 5 ADC units was used).

CURRENT COMPUTATION For the PPC detector surface characterization measurements, the current trace was computed either by applying a triangular filter (rise and fall time of 80 ns) to the PZ-corrected, smoothed waveform or by taking the temporal derivative across N samples of the waveform. Then, the maximum amplitude A was extracted from the current trace. Examples for the current traces corresponding to a SSE and a MSE are depicted in **Fig.** 4.2. The reduced maximum amplitude of the current trace for the MSE can be clearly observed.

ENERGY RECONSTRUCTION The event energy (in terms of ADC units) was reconstructed based on the PZ-corrected waveforms using two different algorithms.

1) Waveform amplitude: The first energy reconstruction method is based on extracting the energy from the amplitude of the waveform (pulse height). To this end, the last 1000 samples and the first 1000 samples of each PZ-corrected waveform are averaged. The difference of these averages corresponds to the energy, see **Fig.** 6.13a.

2) Trapezoidal filter: The second energy reconstruction method uses a trapezoidal filter with adjustable rise and flat top times to shape the waveform. In most of the GALATEA surface

characterization measurements, the best energy resolution was obtained with a filter rise time of 4 µs and a flat top time of 3 µs. A comparably long flat top time was chosen to ensure a complete charge integration. This is particularly important for events with long drift times, i.e. for those being far away from the readout electrode. In general, the flat top time needs to be at least as long as the the maximum drift time plus the preamplifier rise time. In addition, the filter rise time needs to be long enough to integrate away high-frequency noise. In contrast, it should not be too high to not include too much low-frequency noise. Eletronic noise will be discussed in more detail in **Ch.** 10.3. Finally, the energy is extracted from the shaped signal using a fixed-time-pickoff (ftp), i.e. it is extracted at a fixed time point relative to the onset of the charge collection t_0, e.g. at the center or maximum of the flat top region, see **Fig.** 6.13b.

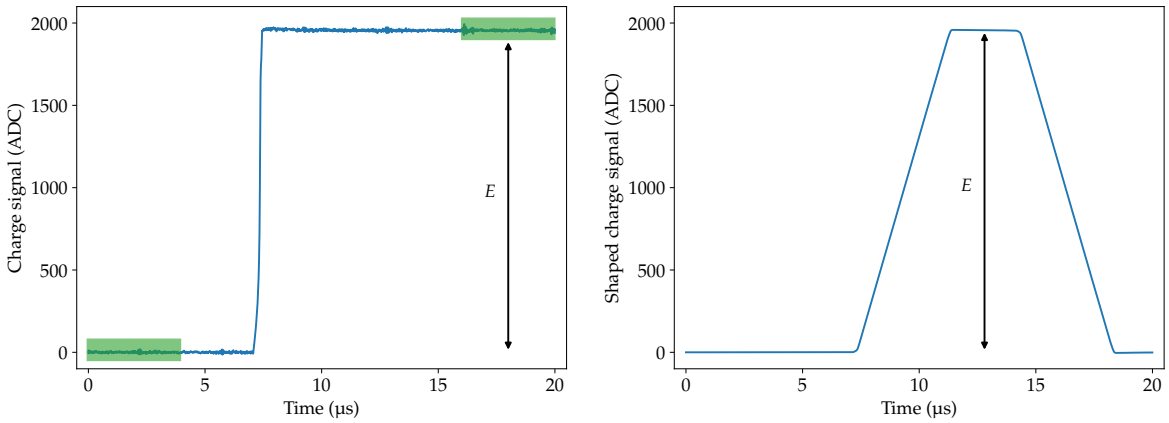

(a) Charge signal.

(b) Shaped charge signal (trapezoid).

Figure 6.13: Examples for the event energy reconstruction. The energy E is extracted from the PZ-corrected waveform by (a) estimating the amplitude or (b) from the shaped signal. For shaping the charge signal, a trapezoidal filter with a certain rise time (= fall time) and flat top time was used.

DRIFT TIME CORRECTION FOR CHARGE TRAPPING Drift path-dependent charge trapping (CT) in HPGe detectors can worsen the energy resolution considerably. Charge trapping can be identified by investigating the correlation of the quantities drift time and energy. **Fig.** 6.14 shows an example for a ^{228}Th calibration measurement with events constrained to the 2.6 MeV ^{208}Tl peak. It can be observed that without any corrections, the quantities are strongly correlated (Pearson correlation coefficient of $\rho \approx -0.5$) indicating a strong amount of CT. To account for this effect, a drift time correction is deployed [245].

In the first step of the correction, the product A_0 of uncollected charge and drift time is estimated based on the PZ-corrected waveforms. This quantity is also referred to as QDrift. It is equal to the area A_0 above the normalized signal trace in the time range between the onset and the end of the charge collection process, see **Fig.** 6.15a. Assuming that $A_0 + A_1 = A_2$ (time intervals of equal length), the QDrift parameter is estimated as follows:

$$A_0 = A_2 - A_1 \tag{6.8}$$

$$= \sum s[t_0 + \xi + \Delta t : t_0 + \xi + 2\Delta t] - \sum s[t_0 : t_0 + \Delta t]. \tag{6.9}$$

Here, $s(t)$ denotes the signal and Δt a time interval chosen such that the charge for different interaction positions in the detector is fully collected within $t_0 + \Delta t$. Moreover, $\xi \geqslant 0$ describes a time separating the intervals corresponding to A_1 and A_2. For the PPC detector surface characterization measurements in GALATEA, a value of $\Delta t = 2.5\,\mu s$ and $\xi = 0$ was chosen (the simulated maximum drift time is slightly higher than 1 µs). The CT-corrected energy E_c is then determined via

$$E_c = E + f_{CT}(E) \cdot A_0, \tag{6.10}$$

where $f_{CT}(E)$ is the energy-dependent CT factor. It is determined by optimizing the energy resolution of various gamma peaks in the energy spectrum. To this end, several peaks are selected and the CT

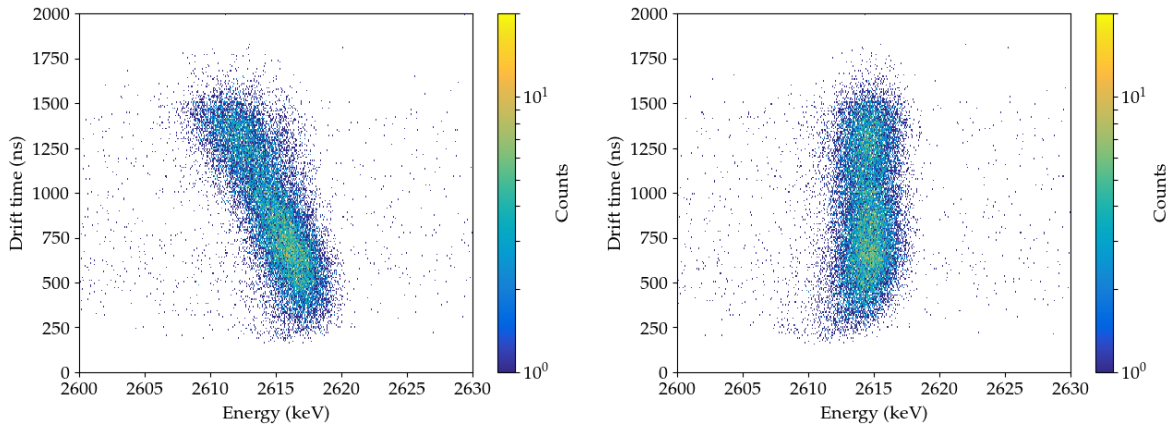

(a) Before charge trapping correction.

(b) After charge trapping correction.

Figure 6.14: Charge trapping in a HPGe detector: (a) The quantities drift time and energy (here constrained to events in the 2.6 MeV ^{208}Tl peak) are clearly correlated ($\rho \approx -0.5$) resulting in a poor energy resolution ($\Delta E \approx 4.99$ keV FWHM). (b) After applying a drift time correction for CT, the quantities are uncorrelated ($\rho \approx 0$) and the energy resolution is improved considerably ($\Delta E \approx 3.05$ keV FWHM).

factor is varied until the resolution is minimal. **Fig.** 6.15b shows an example for the estimation of the optimal CT factor for the 2.6 MeV ^{208}Tl peak. As can be seen, the energy resolution is optimal for a CT factor of $f_{CT}(2.6\,\text{MeV}) = 0.03$. For gamma peaks at smaller energies, the optimal CT factor is smaller. This energy dependence of the CT factor can be typically approximated by a linear relation of the form

$$f_{CT}(E) = a \cdot E + f_{CT,0}. \tag{6.11}$$

The parameters a and $f_{CT,0}$ are determined using a linear fit. It should be noted here that in some cases, higher order corrections might be necessary. Depending on the initial amount of CT in a specific detector, the energy resolution might improve considerably after having applied the drift time correction for CT. An example for the 2.6 MeV ^{208}Tl peak of a ^{228}Th calibration measurement before and after the correction is shown in **Fig.** 6.16. It can be observed that the peak width decreases significantly after the correction. In addition, the peak is much more Gaussian in shape.

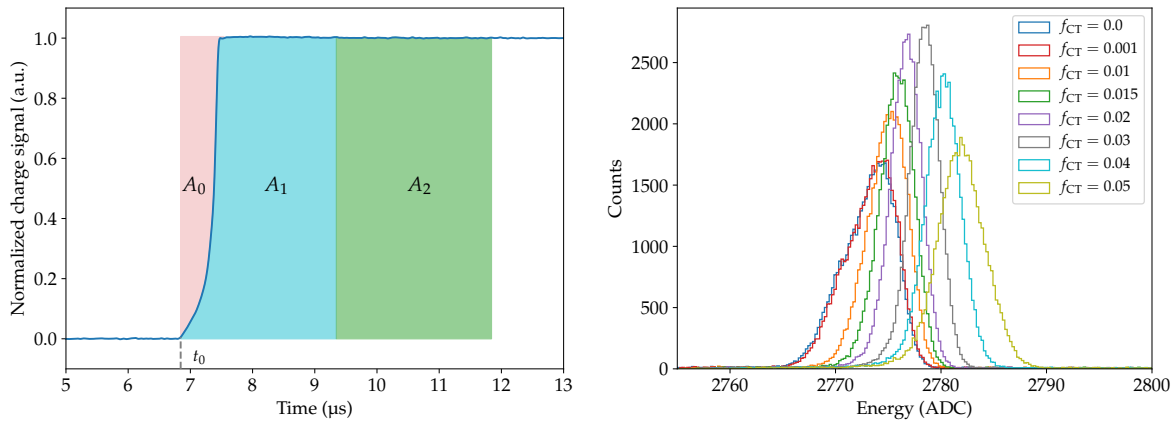

(a) Determination of the QDrift parameter A_0.

(b) Optimization of the charge trapping factor.

Figure 6.15: Drift time correction for charge trapping. (a) The parameter A_0 represents the product of uncollected charge and drift time. It is determined based on the areas A_1 and A_2 via $A_0 = A_2 - A_1$. (b) For the final energy correction, the energy-dependent charge trapping factor f_{CT} is determined by optimizing the energy resolution of various gamma peaks (here shown for the example of the 2.6 MeV ^{208}Tl peak).

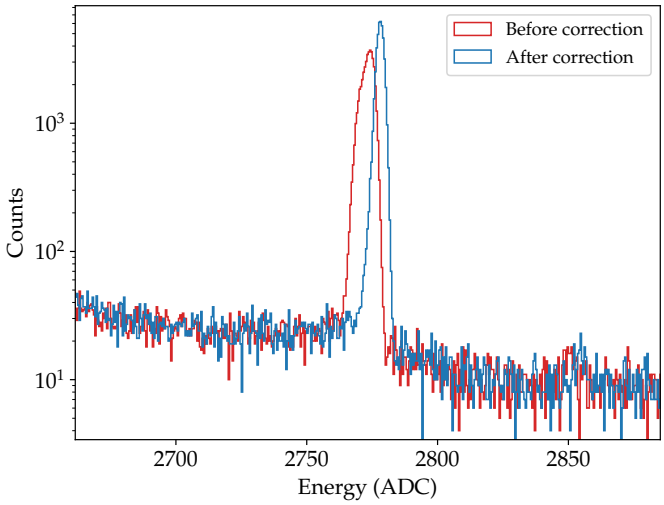

Figure 6.16: Shape of the (uncalibrated) 2.6 MeV ^{208}Tl peak before and after the application of a drift time correction for charge trapping. The correction optimizes the energy resolution and the peak shape.

DELAYED CHARGE RECOVERY (DCR) PARAMETER ESTIMATION As already discussed in **Ch.** 5.3, the delayed charge recovery (DCR) effect is a powerful tool to identify and discriminate surface alpha events. The effect manifests itself as an excess slope in the exponentially decaying waveform tail. This can be exploited to define a tail-based PSD parameter, the DCR parameter. Typically, it is computed as described in the following [142, 228, 235]:

1) First, the slope δ of the waveform tail is computed based on a two-point slope estimation, see **Fig.** 6.17a. To this end, the time point $t_{97\%}$ at which the waveform has reached 97% of its maximum amplitude, as well as the time point t_{last} corresponding to the last sample of the waveform trace are estimated. Then, the charge signal (in terms of ADC units) and the time are averaged in the two time windows[3] [142, 235]

$$\text{I)}\ t_{97\%} + 2\,\mu s \leqslant t \leqslant t_{97\%} + 3\,\mu s, \tag{6.12}$$

$$\text{II)}\ t_{last} - 1\,\mu s \leqslant t \leqslant t_{last}. \tag{6.13}$$

While the first window is located relatively close behind the end of the leading edge (to avoid shaping effects potentially induced by the readout electronics), the second window comprises the last microsecond of the waveform trace. The tail slope δ is then obtained by dividing the difference of the averaged signal values y_1, y_2 by the difference of the averaged time values t_1, t_2 [235]:

$$\delta = \frac{y_1 - y_2}{t_1 - t_2}. \tag{6.14}$$

The slope estimation can be performed for both the PZ-corrected and the uncorrected waveform. It should be noted here that a tail slope estimation based on an exponential fit would be more accurate (given the exponentially decaying waveform tail). However, the two-point slope estimation is preferred since it optimizes the computation time per waveform. In a comparable study, no measurable improvement on the surface alpha rejection efficiency was observed when the waveform tail was fit with an exponential [235].

2) This step only applies if the tail slope in the previous step was computed based on the uncorrected waveform (no PZ correction). The tail slope of every waveform is histogrammed as a function of energy, see **Fig.** 6.17b. It can be observed that the slope shows an energy dependence, i.e. it decreases with increasing energy. To correct for this dependence, the data are fit with a linear function.

3 These time windows have been chosen to enable comparability with the measurement results presented in [142, 228, 235]. However, it should be noted here that this definition introduces a slight dependence on the trigger time in the waveform trace: The second window is not defined relative to t_0 but rather comprises a fixed time window (last microsecond of the waveform trace).

3) For the non PZ-corrected waveforms, the uncorrected DCR parameter is eventually obtained by correcting the tail slopes δ for their linear energy dependence:

$$\mathrm{DCR_u} = \delta - (aE + b), \tag{6.15}$$

where a and b denote the fit parameters. In the case of the PZ-corrected waveforms, the uncorrected DCR parameter is equivalent to the tail slope, i.e. $\mathrm{DCR_u} = \delta$, and no energy correction is needed. The DCR parameter describes the rate of charges re-released into the detector bulk (typically expressed in units ADC/ns). The resulting distribution as a function of energy is shown in **Fig.** 6.17c. Moreover, the distribution of the $\mathrm{DCR_u}$ values is illustrated in **Fig.** 6.17d. While bulk events have DCR values centered around zero, surface alpha events can be identified as events in the high tail of the distribution.

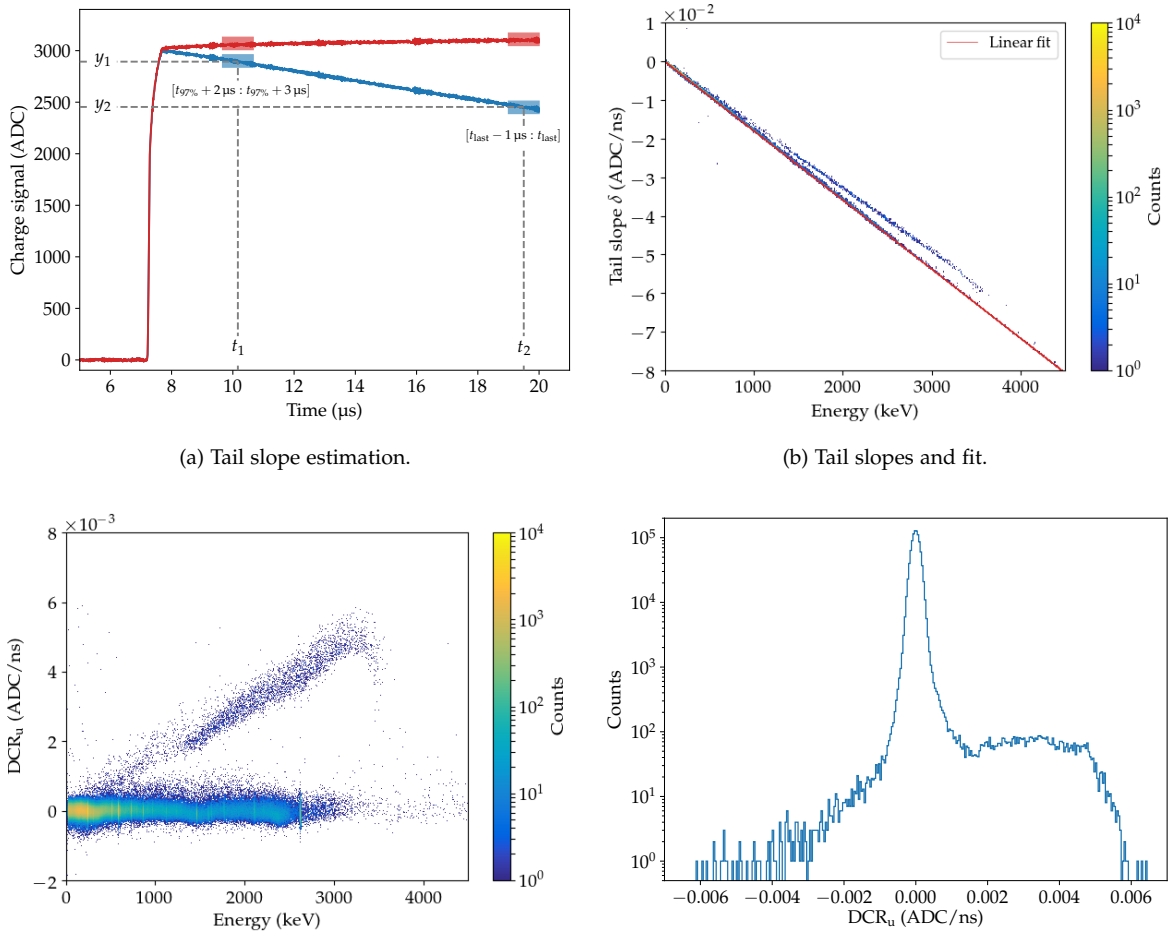

(a) Tail slope estimation.

(b) Tail slopes and fit.

(c) Slope energy correction.

(d) DCR histogram.

Figure 6.17: Determination of the delayed charge recovery (DCR) parameter. (a) First, the tail slope δ of every waveform is computed based on a two-point slope estimation using the average signal and time values in the blue and red marked areas. (b) Then, in the case of the uncorrected waveforms (no PZ correction), the δ values of all waveforms are histogrammed as a function of energy and fit with a linear function. (c) The uncorrected DCR parameter is obtained by correcting the tail slopes for their linear energy dependence. For the PZ-corrected waveforms, no energy correction is necessary, i.e. $\mathrm{DCR_u} = \delta$. (d) When histogramming the DCR values, surface alpha events can be recognized as events in the high tail of the distribution.

4) Typically, when applying DCR PSD cuts to physics data, a normalized version of the DCR parameter is used. To this end, the $\mathrm{DCR_u}$ distribution of ^{228}Th or ^{232}Th calibration events from the Compton continuum in the energy region around the $Q_{\beta\beta}$-value is fit with a Gaussian and

shifted by the centroid μ of the fit. The 99% acceptance value σ_{99} of the shifted distribution is estimated and the corrected DCR parameter is obtained via [235]

$$\mathrm{DCR_c} = \frac{\mu - \mathrm{DCR_u}}{\sigma_{99}}. \tag{6.16}$$

The $\mathrm{DCR_c}$ parameter differs from $\mathrm{DCR_u}$ only by a slight shift and scaling. Since quantitative DCR PSD cuts are not relevant in this work, and due to the additional dependencies of $\mathrm{DCR_c}$, the $\mathrm{DCR_u}$ parameter will be mostly used in the following.

It should be noted here that within this work, waveforms with a trace length of 20 µs were recorded. However, the DCR effect continues beyond the end of this digitization window. Therefore, the measured DCR values are only an approximation of the full amount of re-released charges.

6.6 DETECTOR PERFORMANCE

In the following paragraphs, the performance of the PONaMa1 detector in the GALATEA test facility will be discussed. The detector was first installed in the setup in April 2019. The measurements were conducted in several phases in the time period from June to October 2019. An overview of the measurements can be found in **Tab.** A.1 in the appendix. Between the measurement phases, the cryostat was opened several times to exchange radioactive sources and to fix electronic noise issues.

DEPLETION First, the depletion of the detector was investigated. To this end, the uncollimated ^{228}Th source on top of the IR shield was used. Energy spectra for different bias voltages in the range $500\,\mathrm{V} \leqslant V_B \leqslant 1800\,\mathrm{V}$ in $\Delta V_B = 100\,\mathrm{V}$ steps were recorded. From these spectra, the peak positions and the peak resolutions of the 238.6 keV ^{212}Pb peak were extracted. **Fig.** 6.18 shows the normalized peak position and resolution as a function of the applied bias voltage. For voltages $V_B \gtrsim 1000\,\mathrm{V}$, both quantities remain constant indicating the full depletion of the detector.

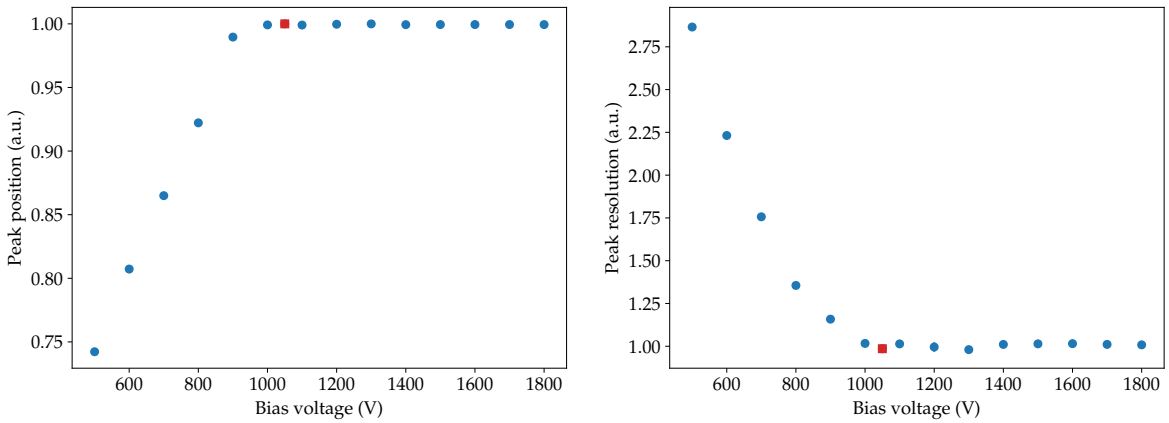

(a) Peak position.

(b) Peak resolution.

Figure 6.18: Bias voltage scan of the PONaMa1 detector with a ^{228}Th source. (a) The normalized peak position and (b) the peak resolution of the 238.6 keV ^{212}Pb line are used to determine the depletion voltage of the detector. The red square measurement point at $V_B = 1050\,\mathrm{V}$ indicates the bias voltage that was used in the surface alpha characterization measurements.

ENERGY CALIBRATION, ENERGY RESOLUTION AND STABILITY A precise energy calibration of the measurement data is important since almost all subsequent analyses depend on it. HPGe detectors are commonly calibrated using gamma sources such as the isotope ^{228}Th, cf. **Ch.** 6.3. In a first step, the event energies are reconstructed in terms of ADC units of the digitizer. Thereupon, depending on the amount of charge trapping present in the detector, a drift time correction for CT is

applied. Several monoenergetic gamma lines in the uncalibrated, CT-corrected energy spectrum are fit using a function of the form [94]

$$f(E) = \underbrace{A\exp\left(-\frac{(E-\mu)^2}{2\sigma^2}\right)}_{\text{Gaussian}} + \underbrace{\frac{B}{2}\operatorname{erfc}\left(\frac{E-\mu}{\sqrt{2}\sigma}\right)}_{\text{Low-energy step}} + \underbrace{C + D(E-\mu)}_{\text{Linear background}} + \underbrace{\frac{F}{2}\exp\left(\frac{E-\mu}{\delta}\right)\operatorname{erfc}\left(\frac{E-\mu}{\sqrt{2}\sigma} + \frac{\sigma}{\sqrt{2}\delta}\right)}_{\text{Low-energy tail}}. \tag{6.17}$$

Here, A, B, C, D and F describe normalization factors, μ the mean (peak position) and σ the standard deviation of a Gaussian distribution, and δ the decay constant of an exponential. The second, third and fourth terms (low-energy step and linear background) describe the background shape of the energy spectrum underlying the gamma peaks. The last term is an exponentially modified low-energy Gaussian tail used to approximate the peak shape distortion due to incomplete charge collection or the residual presence of pile-up events in the energy spectrum [94, 142]. An example for the spectral fit of the 2.6 MeV ^{208}Tl peak is shown in **Fig.** 6.19. The peak positions in terms of ADC units are then associated with the corresponding true energy values of the gamma peaks (usually expressed in keV units). Typically, the relationship can be described by a linear function of the form

$$E\,[\text{keV}] = a \cdot E\,[\text{ADC}] + b, \tag{6.18}$$

where a and b denote the fit parameters. It should be mentioned here that in some cases, higher order relationships might be necessary. After having determined the fit parameters, all ADC values are converted into energy values accordingly. An example of a long-term calibration measurement with a ^{228}Th source in the GALATEA facility is shown in **Fig.** 6.20a.

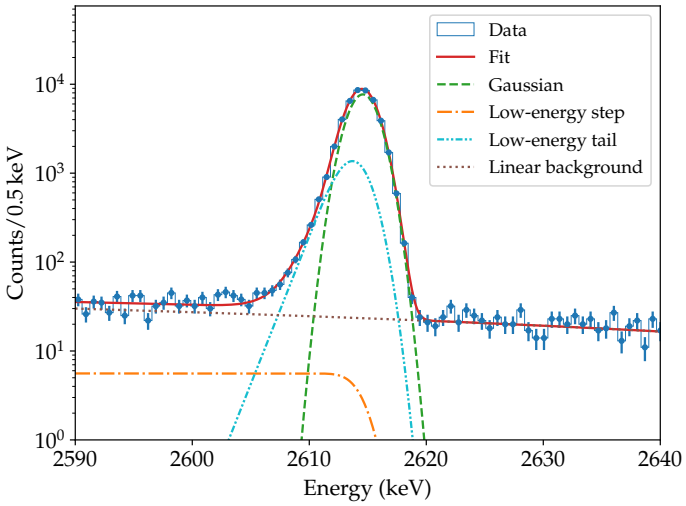

Figure 6.19: Example for the spectral fit (after drift time correction for CT) of the 2.6 MeV ^{208}Tl peak in a ^{228}Th calibration measurement. The peak shape is modeled as the sum of a full-energy Gaussian (green curve), a low-energy step (orange curve), a low-energy tail (cyan curve), and a linear background continuum (brown curve). The error bars correspond to statistical uncertainties assuming Poissonian statistics.

The energy resolution ΔE is described in terms of the FWHM of a given gamma line at energy E, cf. **Ch.** 10.3.5. It is computed by numerically extracting the difference of the two half-maximum points of the fit function. When computing the energy resolution for various peaks in the calibrated ^{228}Th spectrum, the 511 keV annihilation peak and the SEP are not considered since they are Doppler-broadened. This is due to the fact that in the pair production process, cf. **Ch.** 3.1.3, the electron-positron pair has a finite momentum. In the subsequent pair annihilation, the emitted gammas are subject to an opposite Doppler shift by some energy amount $\pm\Delta E$. If only one of these gammas is detected (which holds true for the annihilation peak and the SEP), the corresponding peak has a larger width than a FEP of the same energy. In contrast, the DEP is not affected by

Doppler broadening since if both gammas escape the detector, the excess and deficit energies cancel each other: $(511\,\text{keV} + \Delta E) + (511\,\text{keV} - \Delta E) = 2 \cdot 511\,\text{keV}$ [94].

The relationship between the energy resolution and the energy is finally approximated with the function in **Eq.** (10.21). An example for the estimation of the energy resolution is shown in **Fig.** 6.20b.

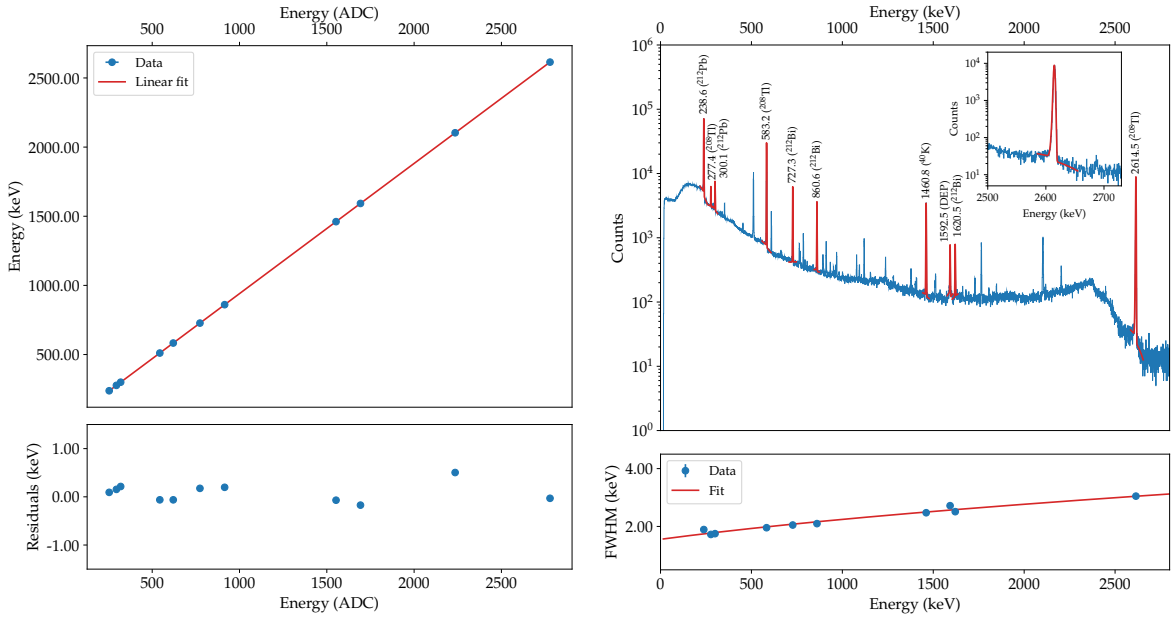

(a) Energy calibration.

(b) Energy resolution.

Figure 6.20: Example for the energy calibration procedure and the energy resolution estimation of a long-term ^{228}Th measurement (20 h). (a) The fitted centroids of the uncalibrated, charge trapping-corrected spectrum are related to the true energy values. (b) The energy resolution in terms of the FWHM is extracted from several gamma lines. The fitted lines are indicated by their energy (in keV) and the corresponding isotope. The inset shows a zoom of the 2.6 MeV ^{208}Tl peak.

The stability of the detector in the measurement facility was investigated by analyzing the temporal evolution of the baseline mean and the energy in the long-term calibration measurement. As can be observed in **Fig.** 6.21, both quantities remained very stable over the measurement period of 20 h. In particular, the stability of the baseline mean (no significant drift) indicates that there were no major changes in the leakage current of the detector during the measurement.

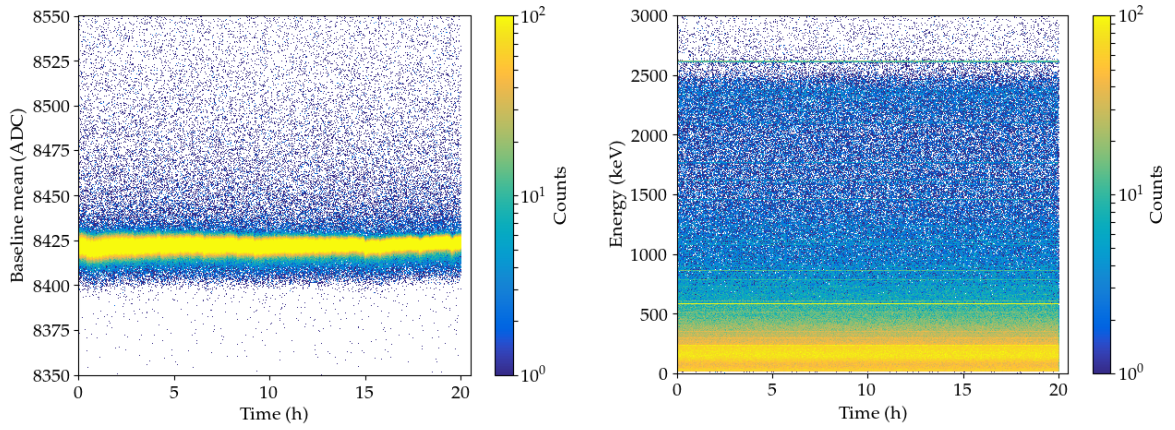

(a) Baseline mean vs time.

(b) Energy vs time.

Figure 6.21: Temporal stability of (a) the baseline mean and (b) the energy in the long-term ^{228}Th calibration measurement.

PULSE SHAPE DISCRIMINATION PERFORMANCE For the PPC detector surface characterization measurements in GALATEA, the PSD performance was validated in a long-term ^{228}Th calibration measurement. The survival efficiencies ε_{PSD} were estimated as described in **Ch.** B.1 in the appendix. The acceptance of MSEs in the SEP is heavily suppressed, i.e. only ~6.7% of these events survive. At the same time, the acceptance of events in the ROI is ~40.4%. The obtained survival efficiencies are in good agreement with the efficiencies obtained with the same detector type in the MAJORANA DEMONSTRATOR experiment [142, 246].

ELECTRONIC NOISE In most of the surface characterization measurements, a strong high-frequency noise component was present. Although several attempts were made to reduce the electronic noise (improvement of the signal readout electronics and of the grounding scheme), it was unfortunately not possible to locate its origin within the experimental setup. To better understand the noise, it was investigated in terms of the power spectral density. This quantity was determined for the waveform baseline of many events and then averaged. Using the example of a background measurement, see **Fig.** 6.22, strong noise components with frequencies below 40 MHz can be observed. In addition, there are two pronounced components with frequencies 65 MHz and 120 MHz, respectively. Due to the noisy measurement environment, a waveform smoothing for estimating different waveform parameters such as the rise time, etc. was indispensable, cf. **Ch.** 6.5.

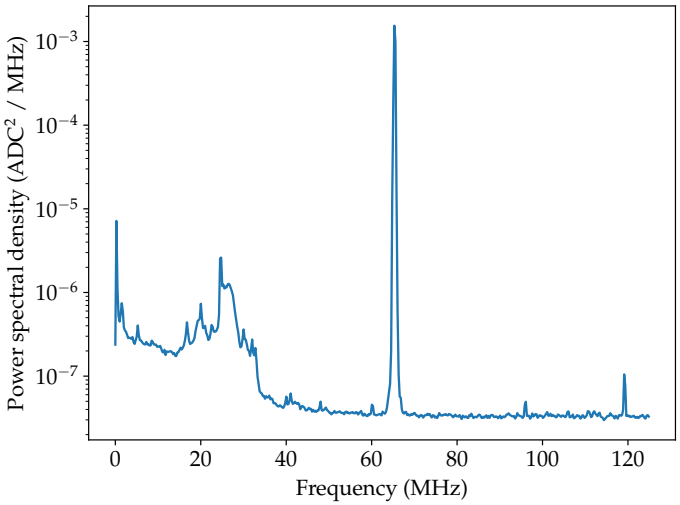

Figure 6.22: Example for the power spectral density of a background measurement with the PONaMa1 detector in the GALATEA facility. Several pronounced noise components can be observed.

BACKGROUND RADIATION A precise knowledge of the radioactive background is important to distinguish it from physics events. Therefore, several background measurements were conducted with the PONaMa1 detector in the GALATEA facility. Typically, the background event rate was on the order of 90 cts/s (detection threshold of ~50 keV). The energy spectrum of a three-hours long background measurement is shown in **Fig.** 6.23. It can be observed that the spectrum shows several characteristic gamma lines superimposed on a background continuum (mostly due to Compton scattering of photons). The most prominent lines are from the isotopes ^{40}K, ^{208}Tl and ^{214}Bi.

Since GALATEA has no active muon veto system, it is important to have a rough estimate of the cosmic ray muon flux ϕ_μ at the detector. Assuming that the average vertical flux of muons with a mean energy of 4 GeV at sea level is about one muon per square centimeter per minute and knowing that the detector has a top surface area of about 37 cm^2, the muon flux at the detector can be estimated as follows: $\phi_\mu = 37 \cdot 60\,\text{muons/hr} = 2220\,\text{muons/hr} = 0.62\,\text{cts/s}$. Hence, the muon flux is rather small compared to the overall background event rate.

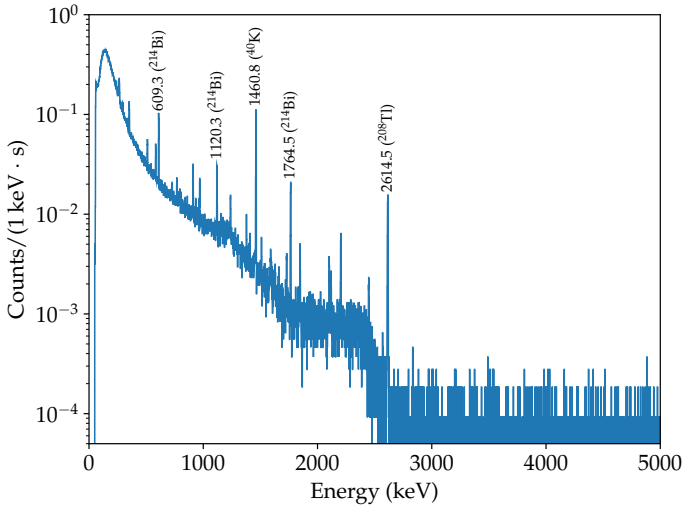

Figure 6.23: Energy spectrum of a three-hours long background measurement with the PONaMa1 detector in GALATEA. The most prominent gamma lines are indicated by their energy (in keV) and the corresponding isotope.

7

CHARACTERIZATION OF SURFACE ALPHA INTERACTIONS

This chapter discusses the PPC detector surface characterization measurements with alpha particles. After an overview of the measurement conditions in **Ch.** 7.1, the measurement results of the radial alpha scans are discussed in **Ch.** 7.2. A comparison to previous measurements and conclusions can be found in **Ch.** 7.3.

7.1 OVERVIEW AND MEASUREMENT CONDITIONS

For the surface characterization measurements with alpha particles, an ^{241}Am source (Eckert & Ziegler) with an activity of $A_0 = 40\,\text{kBq}$ was used. It is an open source, with the radionuclide deposited onto a thin stainless steel disc (active area with a diameter of 7 mm). For the 5.5 MeV alpha peak, the source has an expected FWHM of ~ 19 keV. In the GALATEA test facility, the ^{241}Am source was installed in the top collimator. A collimator configuration based on former GEANT4 studies was used [239]. It consisted of two cylindrical copper (Cu) segments, followed by two cylindrical PTFE segments and four additional Cu segments, see **Fig.** 7.1. The ^{241}Am source was installed between the two PTFE segments. Based on the collimator geometry and the source strength, an alpha rate of ~ 0.7 cts/s was expected at the detector top surface. In all measurements, the ^{241}Am beam spot had an incidence of 90° on the detector surface. Its shape was simulated using GEANT4, see **Fig.** 7.2. To increase statistics of alpha events on the detector surface, collimator segments with a comparably large diameter were used. Therefore, the top slit of the copper IR shield (width of 2.0 mm, cf. **Ch.** 6.1) acted as an additional collimator in the horizontal direction. This explains the oval shape of the ^{241}Am beam spot. In close vicinity to the point contact, the beam spot was shadowed by the PTFE bar. Hence, it was not possible to take data in this region. For energy calibration purposes and to confirm PSD capabilities, an uncollimated ^{228}Th source was additionally mounted on top of the IR shield. The ^{228}Th source with an activity of $A_0 = 100\,\text{kBq}$ was encapsulated in a cylinder made from stainless steel.

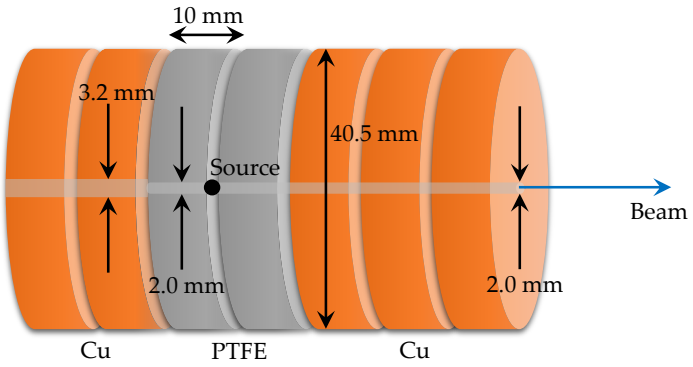

Figure 7.1: Collimator geometry used for the surface alpha characterization measurements in GALATEA. An ^{241}Am source was installed between the two PTFE segments. The figure is not to scale.

Several radial scans at different azimuthal positions, as well as background and stability measurements were conducted. An overview of the surface alpha measurements is listed in **Tab.** A.1 in the appendix. For the radial scans, to acquire sufficiently high statistics, a measurement time of 2 hr at each scan point was chosen. The measurements were performed by splitting the scan directions. First, the collimator was moved from small to high radial positions (from $r_{\text{col.}} = 0\,\text{mm}$ to $r_{\text{col.}} = 36\,\text{mm}$)

in $\Delta r_{col.} = 4\,mm$ steps. Then, the collimator was moved from high to small radial positions (from $r_{col.} = 38\,mm$ to $r_{col.} = 2\,mm$) in $\Delta r_{col.} = 4\,mm$ steps. The detector was operated at a bias voltage of $V_B = 1050\,V$. This voltage was chosen to ensure comparability with the results of previous surface alpha characterization measurements, cf. [228, 235].

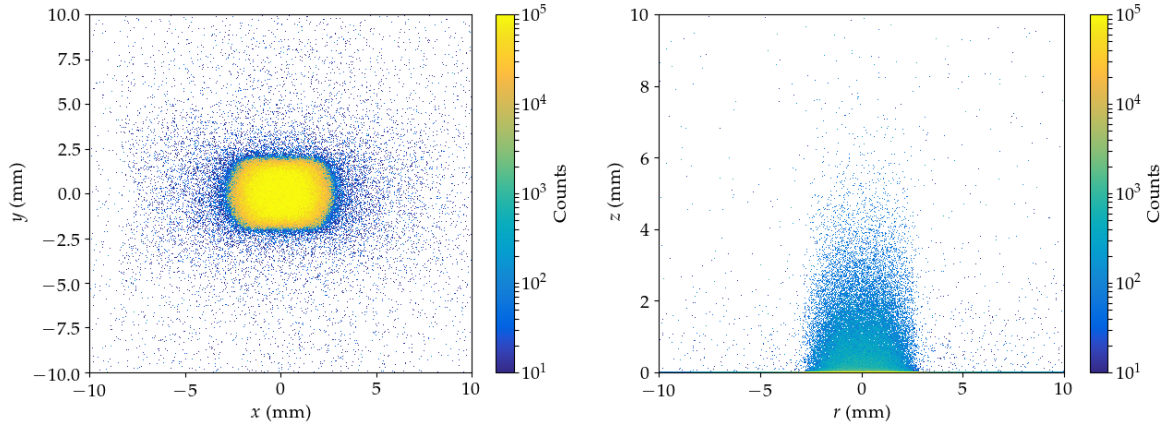

(a) Beam spot in (x, y) plane.

(b) Beam spot in (r, z) plane.

Figure 7.2: Shape of the ^{241}Am beam spot in the (a) (x, y) and (b) (r, z) plane (simulated using GEANT4). For visual purposes, the PTFE bar mounted on top of the detector was excluded here (no shadowing of the beam spot). The origin of the coordinate system is at the top center of the point contact with the z-axis pointing towards the detector bulk.

7.2 MEASUREMENT RESULTS

RADIAL OFFSET In the following paragraphs, the radial response of the PONaMa1 detector with respect to alpha events on the passivated surface will be studied. For the measurements with the ^{241}Am source, all radial positions r are expressed in terms of the radial detector position (origin at the point contact). The data were corrected for a small radial offset between the detector position r_{det} and the position r_{col} of the collimator:

$$r \equiv r_{det} = r_{col} + 3\,mm. \tag{7.1}$$

Here, the offset of 3 mm was determined by comparing the measured alpha event rate to the rate obtained in GEANT4 simulations, see **Fig.** 7.8. The offset could be due to misalignments of the detector and its holding structure in the test facility, and of the collimator on top of the IR shield.

IDENTIFICATION OF ALPHA EVENTS In a first step, the alpha events needed to be identified and distinguished from other events, particularly from those of the ^{228}Th source. The energy spectra of a measurement with the ^{241}Am source (radial position $r = 5\,mm$), and of a measurement in which only the ^{228}Th source was used are shown in **Fig.** 7.3a. The contribution of the ^{228}Th source dominates the energy spectrum for energies up to $\sim 2.6\,MeV$. At higher energies, the measurement with the ^{241}Am source deviates from the ^{228}Th-only measurement. The elevated count rate is attributed to alpha events [229]. A zoom into the low-energy region, see **Fig.** 7.3b, further shows the 59.5 keV gamma peak, the gamma ray byproduct of the alpha decay of ^{241}Am, cf. **Ch.** 6.3.

To investigate the radial response of surface alpha events, the following observables were analyzed as a function of energy: A/E, decay time τ, and rise time ($10\% - 90\%$ and $60\% - 96\%$). Examples for the correlation plots at several radii are shown in **Fig.** 7.4. Just as the energy spectrum, the distributions are dominated by events from the ^{228}Th source. However, in some of the correlation plots at various radial positions, alpha events can be identified. At small radii, alphas are best visible in the decay time and rise time distributions. At higher radii, alpha events can be observed in the A/E and rise time $10\% - 90\%$ distributions. In all cases, the alpha response strongly depends on the radial position of the radioactive ^{241}Am source. While at small radii the alpha population is located at high energies, it moves towards smaller energies with increasing radius. This makes it difficult to distinguish alphas from other events in some of the correlation plots.

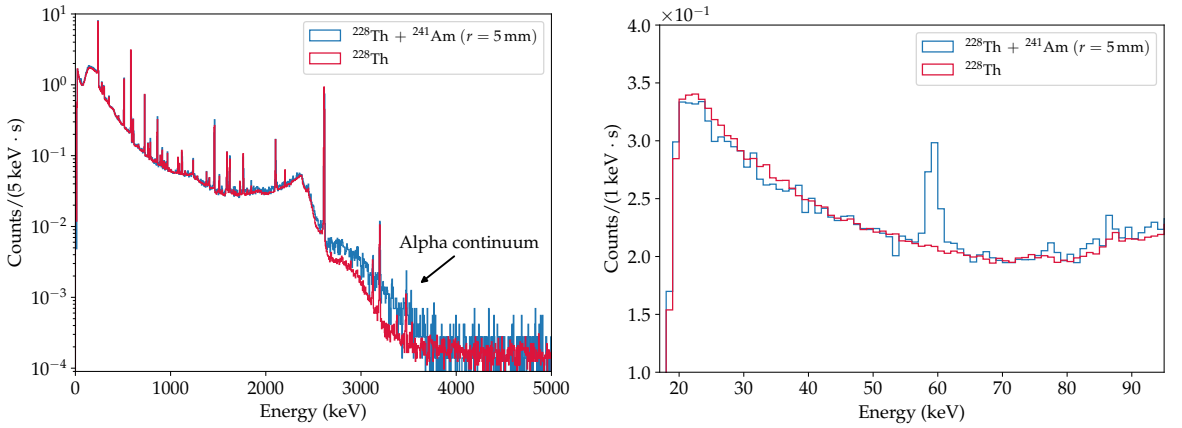

(a) ^{241}Am and ^{228}Th energy spectrum.

(b) 59.5 keV ^{241}Am gamma peak.

Figure 7.3: Energy spectra as measured with the ^{228}Th and ^{241}Am sources at the position $r = 5$ mm (blue curve) and the ^{228}Th source only (red curve). (a) At higher energies, a continuum of alpha events is visible. (b) A zoom into the spectrum at small energies shows the 59.5 keV ^{241}Am gamma peak.

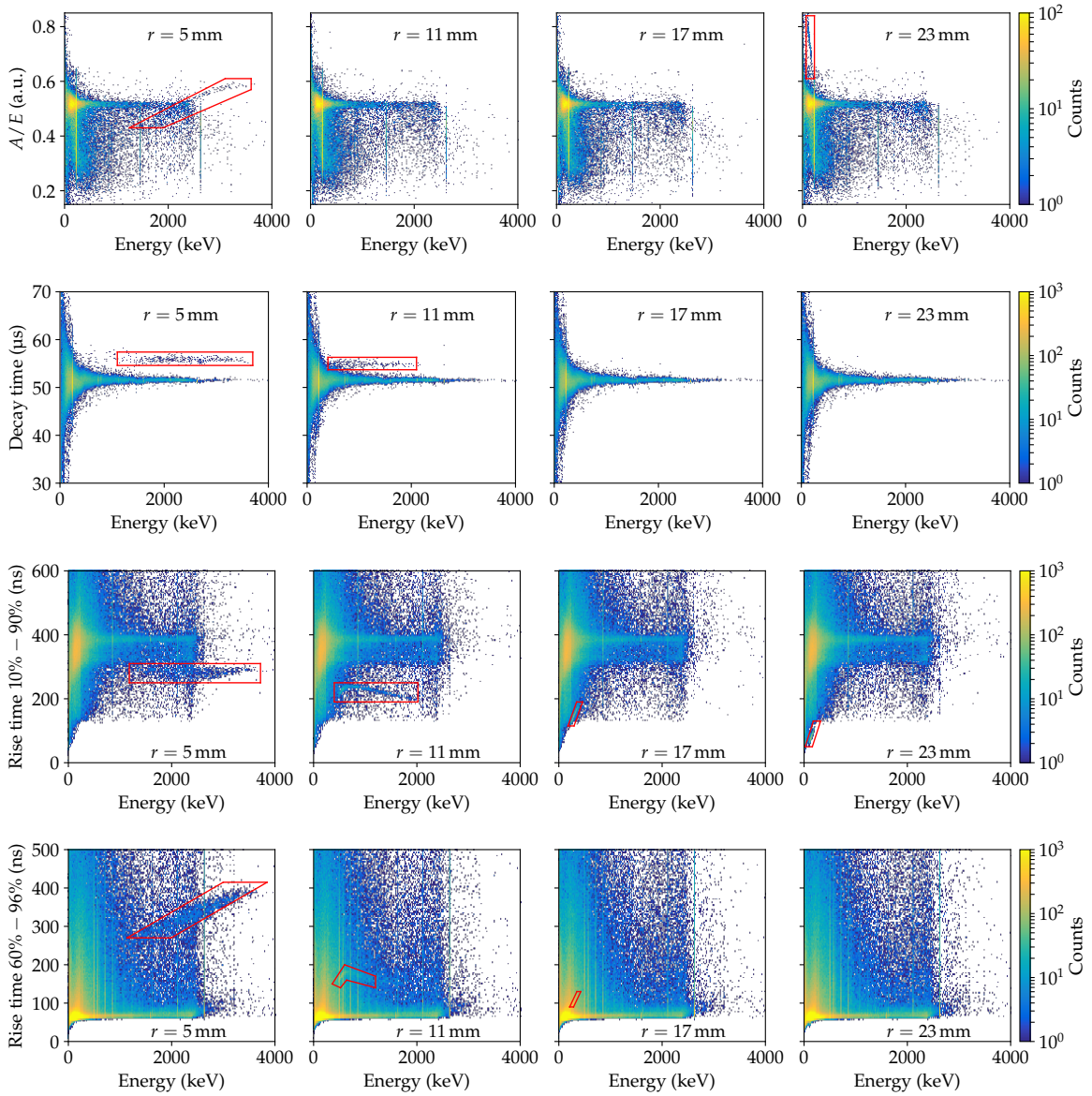

Figure 7.4: Correlation plots of the quantities A/E, decay time τ, and rise time (10% – 90% and 60% – 96%) as a function of energy at selected radial positions (r = 5, 11, 17, 23 mm). In some plots, alpha populations can be identified. For better visibility, they are marked with red boxes.

ISOLATION OF ALPHA EVENTS AND CUT EFFICIENCY To better understand the observed radial dependence, multivariate cuts have been developed to isolate alpha events. To this end, cuts have been applied to the pulse shape parameters A/E, decay time τ, and rise time ($10\% - 90\%$ and $60\% - 96\%$). These cuts exclude regions from the data set, where no alpha events are present, see **Fig.** 7.5. It is important to note that the cuts are radial-independent, i.e. the same cuts were applied at every radial position. Special care was taken to only exclude regions in the parameter space which did not contain alpha events. While for the A/E and the decay time distributions only small regions could be eliminated, a large number of non-alpha events could be excluded by applying cuts to the rise time distributions, particularly in the case of the rise time $10\% - 90\%$ vs E distribution.

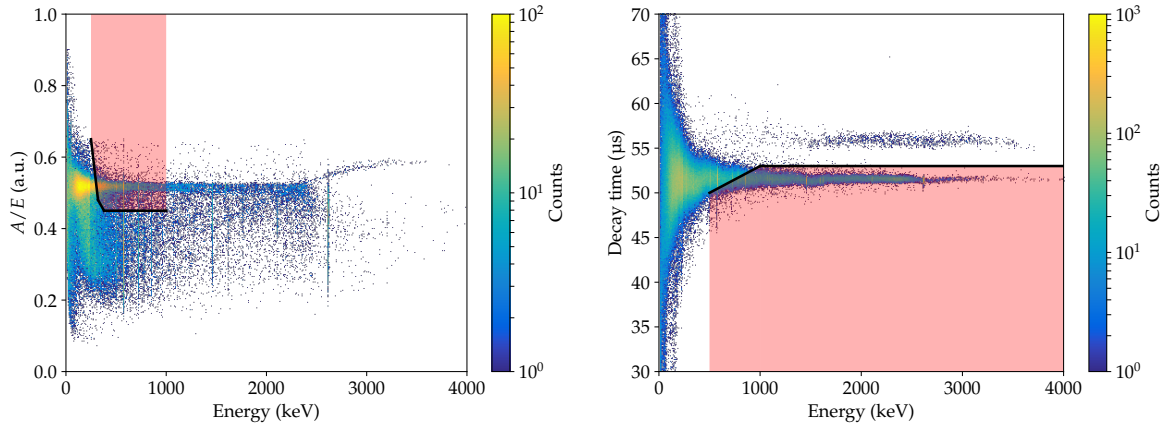

(a) A/E vs E.

(b) Decay time τ vs E.

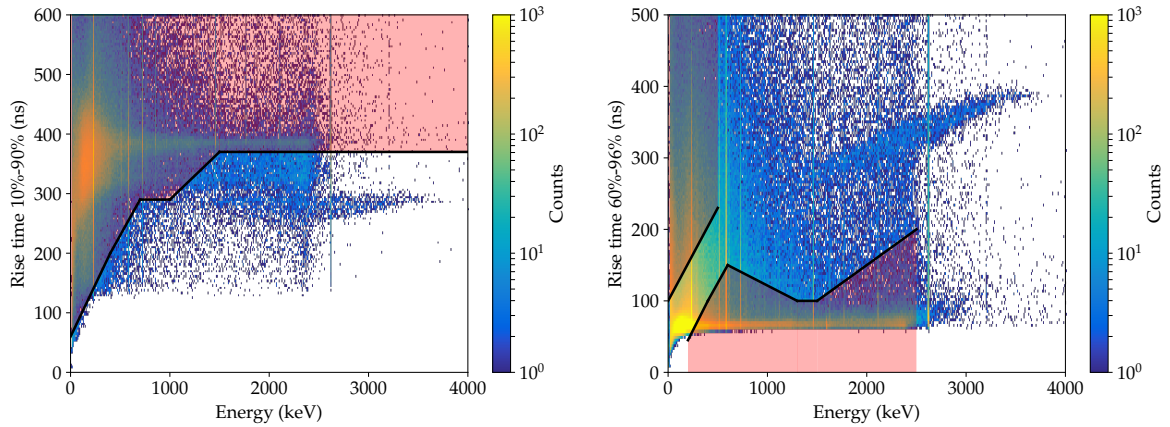

(c) Rise time $10\% - 90\%$ vs E.

(d) Rise time $60\% - 96\%$ vs E.

Figure 7.5: Application of radial-independent multivariate cuts to the quantities A/E, decay time τ, and rise time ($10\% - 90\%$ and $60\% - 96\%$) to isolate alpha events from other events. The quantities are shown with the ^{241}Am source at the radial position $r = 5\,\text{mm}$. The excluded regions are marked red. Most of the non-alpha events can be eliminated by applying cuts to the rise time distributions.

In the end, the cuts on the four different pulse shape parameters were combined, i.e. only those events that survived every cut concurrently were accepted. **Fig.** 7.6 shows the distributions of the observables at various radial positions after having applied the cuts. In any case, it can be observed that the energy of the alpha events degrades with increasing radial position. Moreover, the pulse shape quantities evolve as follows with increasing radius and decreasing energy, respectively: the A/E parameter first decreases, has a turning point at an energy of $E \approx 1000\,\text{keV}$ and then increases again. In contrast, the decay time of the alpha populations remains approximately constant (mean value of $\tau \approx 55\,\mu\text{s}$). The rise time of the alpha events decreases considerably with increasing radius. In all cases, it can be observed that at small radii the alphas have a large spread in energy. This spread gets smaller at higher radii. The spread can be explained by the strongly changing weighting potential at small radii. At small radial positions this results in a large slope dE/dr of energy over radius so that the size of the beam spot has a strong effect on the energy width.

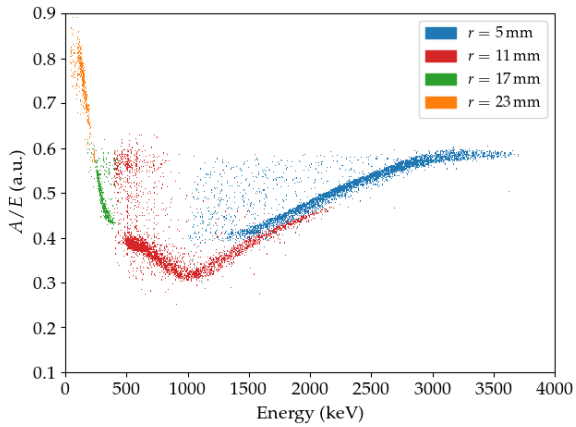

(a) A/E vs E.

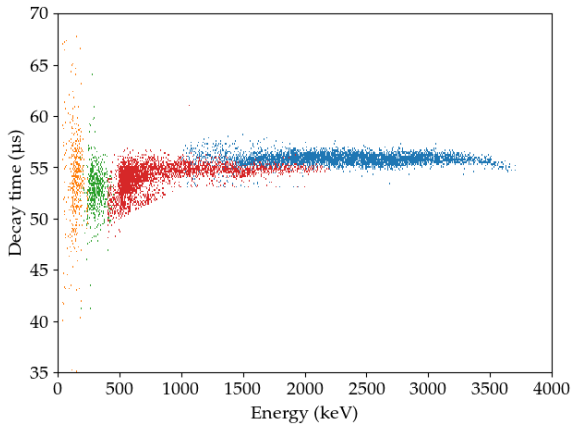

(b) Decay time τ vs E.

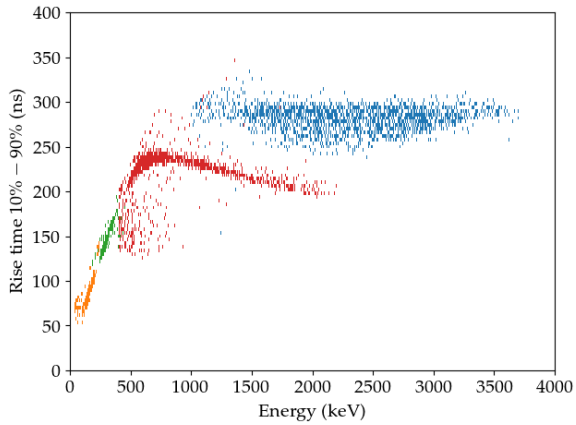

(c) Rise time 10% – 90% vs E.

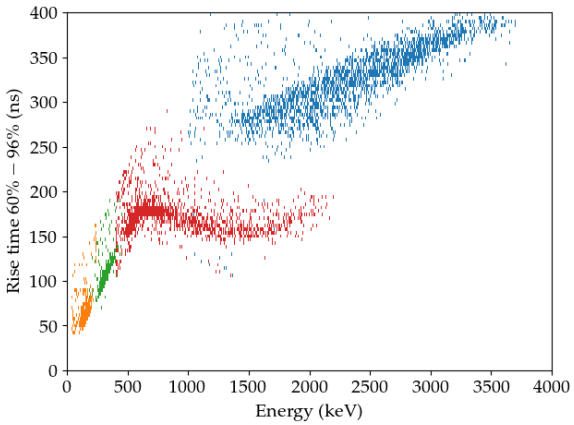

(d) Rise time 60% – 96% vs E.

Figure 7.6: Correlation plots of the quantities A/E, decay time τ, and rise time (10% – 90% and 60% – 96%) as a function of energy at selected radial positions (r = 5, 11, 17, 23 mm) after the application of multivariate cuts to isolate alpha events. It can be observed that the alpha energy decreases with increasing radial position.

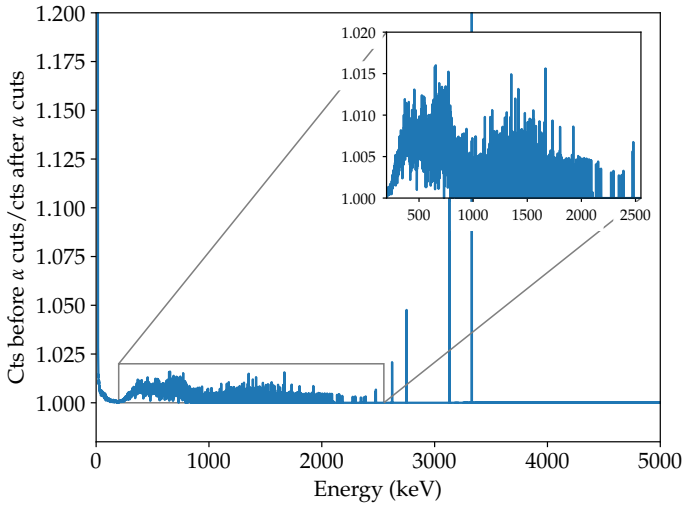

Figure 7.7: Efficiency of the multivariate cuts to maintain non-alpha events. The efficiency was determined by comparing the energy spectra of a ^{228}Th calibration measurement before and after the application of multivariate cuts to isolate alpha events. In the signal ROI, only slight deviations on the sub-percent level can be observed.

The efficiency of maintaining non-alpha events, particularly in the ROI, was investigated by applying the multivariate cuts to a ^{228}Th background measurement. By comparing the number of events before and after the application of multivariate cuts, see **Fig.** 7.7, a global non-alpha event survival fraction of 99.57% was obtained. In addition, in the ROI ($Q_{\beta\beta} \pm 100$ keV), a non-alpha event survival fraction of 99.98% was obtained. Therefore, the developed cuts are very efficient at isolating alpha events and maintaining other events at the same time.

ALPHA COUNTS The evolution of the total number of alpha events as a function of radius is shown in **Fig.** 7.8. The plot shows that in almost the entire radial range, the number of alphas remained constant at a value of about 5000 events/scan position. For a measurement time of 2 h/position, this translates into an alpha count rate of about 0.7 cts/s. The deviation at small radii is most likely due to a partial shadowing of the ^{241}Am beam spot by the PTFE bar, cf. **Ch.** 6.2. Moreover, the decreasing alpha rate at the outer radii might be explained by the fact that the alphas hit the lithiated layer of the taper which they cannot penetrate. The plot also shows a comparison of the normalized alpha counts and the alpha counts as predicted by GEANT4 simulations, cf. **Ch.** 9.3.1. The simulations were used to correct the measurement data for a slight offset of 3 mm between the radial detector position and the position of the collimator. To this end, the radial detector position was shifted so that the increasing and falling edges of the alpha counts at small and large radii match, respectively [229].

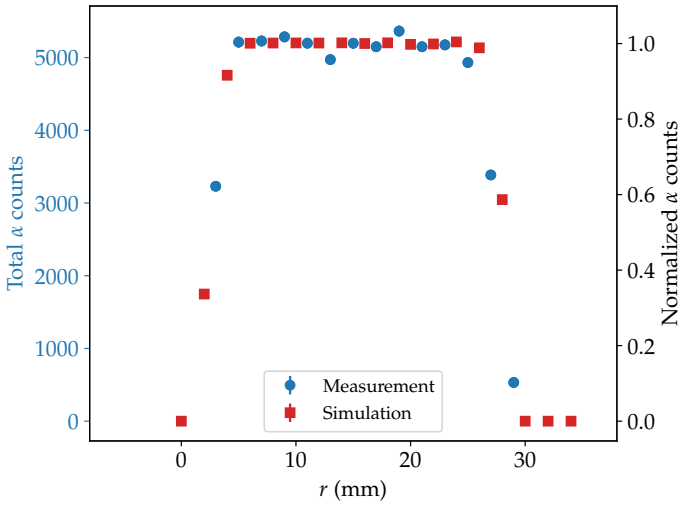

Figure 7.8: Radial dependence of the number of recorded alpha events and comparison to simulation. Except for the innermost and outermost radial positions, the alpha counts remained nearly constant. Published in [229].

STABILITY OF ALPHA RESPONSE To investigate the stability of the detector response to surface alpha events, a long-term stability measurement was carried out. The measurement with a total duration of 8 h was equally-divided into four sub-runs. During the measurement, the radioactive ^{241}Am source was positioned at a fixed azimuthal and radial position (r = 7 mm). The detector was operated at a bias voltage of $V_B = 1050$ V. The stability was analyzed in terms of the mean alpha energy and the total alpha counts during the individual sub-runs. **Fig.** 7.9 shows that both quantities remained quite stable over the measurement duration. It should be noted here that also during the sub-runs, the quantities showed a high temporal stability.

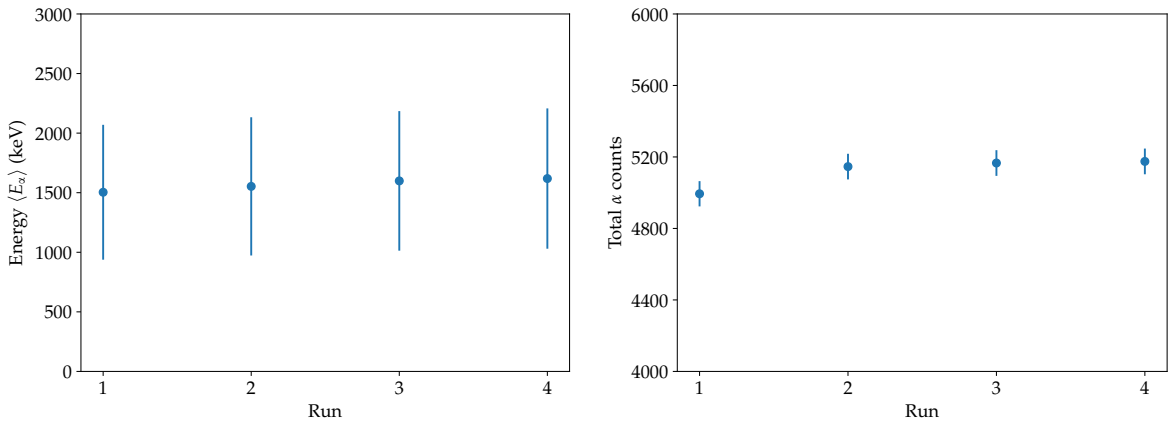

(a) Alpha energy stability.

(b) Alpha counts stability.

Figure 7.9: Stability of the detector response to surface alpha events in terms of (a) the mean alpha energy and (b) the total alpha counts. Each run corresponds to a measurement duration of 2 h. The measurement was carried out with the ^{241}Am source at a fixed azimuthal and radial position (r = 7 mm).

RADIAL ENERGY DEPENDENCE To quantify the energy degradation observed for the surface alpha events, the energy values of the alpha populations were histogrammed and corrected for background events, see **Fig.** 7.10a. Just as in the correlation plots in **Fig.** 7.6, a strong radial-dependent degradation can be observed. A quantitative description was obtained by extracting the mean alpha energies $\langle E_\alpha \rangle$ from the distributions. The alpha energy ranges were constrained manually to reject remaining background events and to get a more precise estimate of the mean alpha energies. **Fig.** 7.10b shows the mean energy as a function of radius for two radial ^{241}Am scans at different azimuthal positions. Between the two scans, the detector was unbiased and the cryostat was re-evacuated. Error bars represent the standard deviations of the constrained alpha energy distributions. At small radial positions, due to the width of the distributions, the error bars are large. It can be observed that at the outermost radii, the mean alpha energy is strongly reduced, i.e. almost no charges are collected anymore. In contrast, at small radial positions, the alphas have a mean energy of $E_\alpha > 2500$ keV. The plot also shows that the results of the two measurements are in good agreement [229].

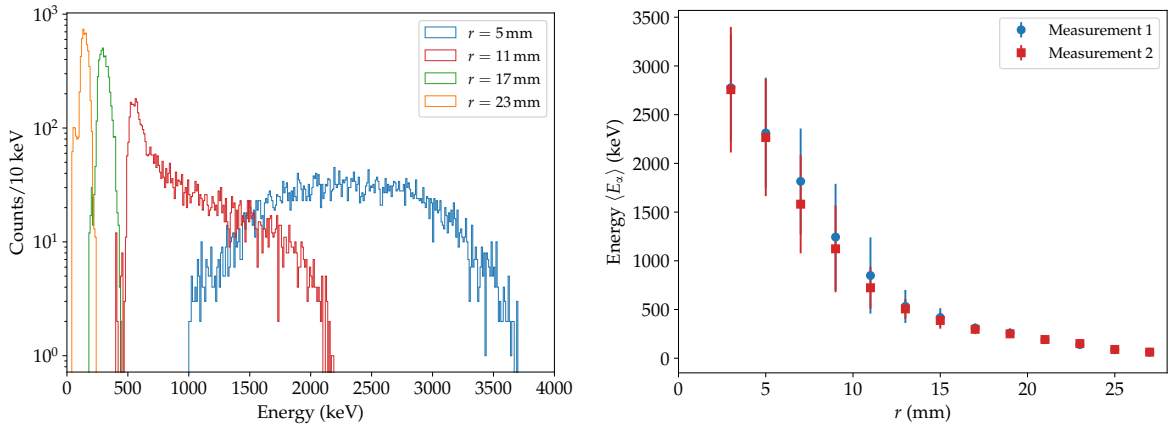

(a) Energy histograms of alpha events.

(b) Radial energy dependence of alpha energies.

Figure 7.10: Measured radial energy dependence of the surface alpha events: (a) Energy spectra of the alpha populations at selected radial positions after the application of multivariate cuts. (b) Mean alpha energy $\langle E_\alpha \rangle$ as a function of radius r for two radial ^{241}Am scans at different azimuthal positions. Published in [229].

The observed radial-dependent energy degradation is consistent with the presence of negative surface charges at the passivation layer, cf. **Ch.** 5.2. The holes created during a particle interaction are attracted to the surface, whereas the electrons are repelled. After having arrived at the passivation layer, the holes slowly drift along it in the direction of the point contact and can get trapped. Conse-

quently, the signal development is primarily due to the collection of electrons resulting in reduced signal amplitudes. The radial dependence can be attributed to the proportionality of the total electron charge to the weighting potential, cf. **Eq.** (5.4), which itself shows a radial dependence. In the vicinity of the point contact, the weighting potential is close to unity and falls off sharply with increasing radial position. It should be noted that unbiasing the detector and re-evacuating the vacuum cryostat did not affect the observations significantly [229].

ALPHA SUPERPULSE WAVEFORMS In the next step, the pulse shape of the surface alpha events was studied. Since single waveforms are very sensitive to noise, alpha superpulses were computed. To this end, at a given radius, all waveforms corresponding to events in the range $\langle E_\alpha \rangle \pm 5\,\mathrm{keV}$ around the mean alpha energy were selected. After a t_0 time alignment of every pulse, they were combined into a superpulse, see **Fig.** 7.11. At small radial positions, the signals first have a sharply rising component followed by a very slowly rising one. The fast component is due to the collection of holes which are close to the detector point contact. In this region the weighting potential is very high resulting in a fast drift. In contrast, the slow component is due to the collection of electrons. They must drift all the way to the n^+ electrode in a strongly decreasing weighting field. At higher radial positions, the hole component is reduced and the slowly rising electron component gets faster. In general, the signal rise time ($10\% - 90\%$) decreases with increasing radius. This is due to the fact that at higher radii, the electrons have a much shorter drift path to the n^+ contact. **Fig.** 7.11a also shows that the surface alpha events feature a slowly rising waveform tail, especially at small radial positions. This is a clear indication for the delayed charge recovery (DCR) effect that will be analyzed in more detail in the next paragraph.

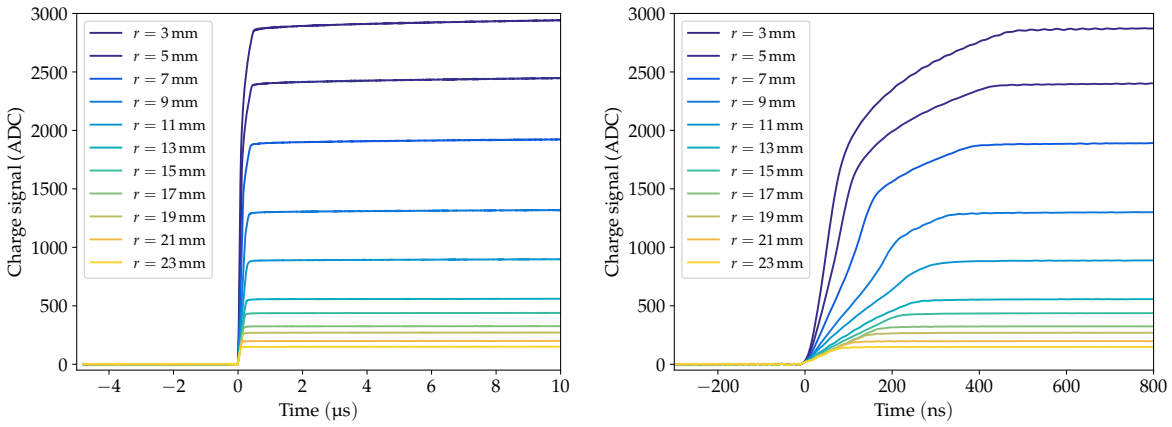

(a) Alpha superpulses (full waveforms).

(b) Alpha superpulses (zoom of leading edge).

Figure 7.11: Superpulses of the surface alpha events at selected radial positions. For the computation of the pulses, alpha waveforms in the range $\langle E_\alpha \rangle \pm 5\,\mathrm{keV}$ were selected. After a time alignment of the pulses, they were averaged to a superpulse. (a) The left plot shows the full waveforms, whereas the right one (b) shows a zoom of the leading edge.

RADIAL DCR DEPENDENCE As discussed in **Ch.** 5.3, the DCR parameter is a powerful variable to discriminate surface alpha events. To investigate its radial dependence in the surface characterization measurements, the $\mathrm{DCR_u}$ parameter[1] was computed for every event as described in **Ch.** 6.5. Its correlation with the alpha energy after the application of multivariate cuts is shown in **Fig.** 7.12a. It can be observed that at small radii, the surface alpha events have comparably high DCR values. With increasing radial position and decreasing energy, respectively, their DCR rate decreases. To quantify this dependence, the DCR rates were histogrammed and corrected for background events, see **Fig.** 7.12b. In the next step, the mean DCR rates $\langle \mathrm{DCR_r} \rangle$ were extracted from the distributions. **Fig.** 7.13a shows the mean DCR rate as a function of radius for two radial ^{241}Am scans at different azimuthal positions. Just as the mean alpha energy, the mean DCR rate decreases considerably with increasing radius. At higher radial positions, the DCR rate of surface alpha events is close to zero. Therefore, in this region, they are no longer distinguishable from normal bulk events. The

1 Similar results (slighty shifted and scaled) were obtained for the $\mathrm{DCR_c}$ parameter, but are not discussed here.

radial dependence can be explained in analogy to the radial energy dependence (the DCR rate is proportional to the energy). The observations are consistent with the presence of negative surfaces charges at the passivation layer. In particular, the results indicate that the DCR effect is caused by the trapping of charges in a region close to the passivated surface, their subsequent slow re-release into the detector bulk, and their drift to the corresponding electrode (here delayed arrival of electrons at the n^+ contact). This will be investigated in more detail by means of pulse shape simulations in **Ch.** 9.

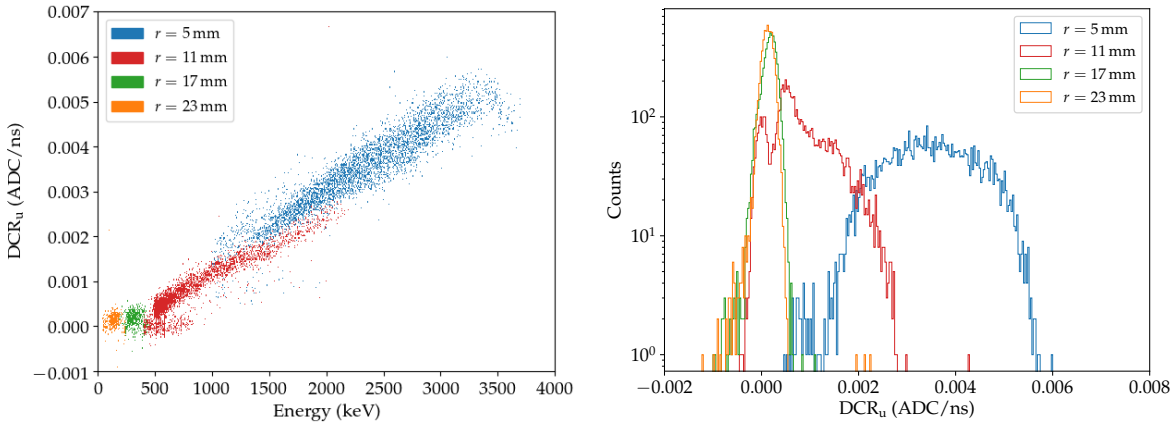

(a) DCR rate vs E.

(b) DCR histograms of alpha events.

Figure 7.12: (a) Correlation plot of the DCR rate with the alpha energy and (b) DCR histograms at selected radial positions.

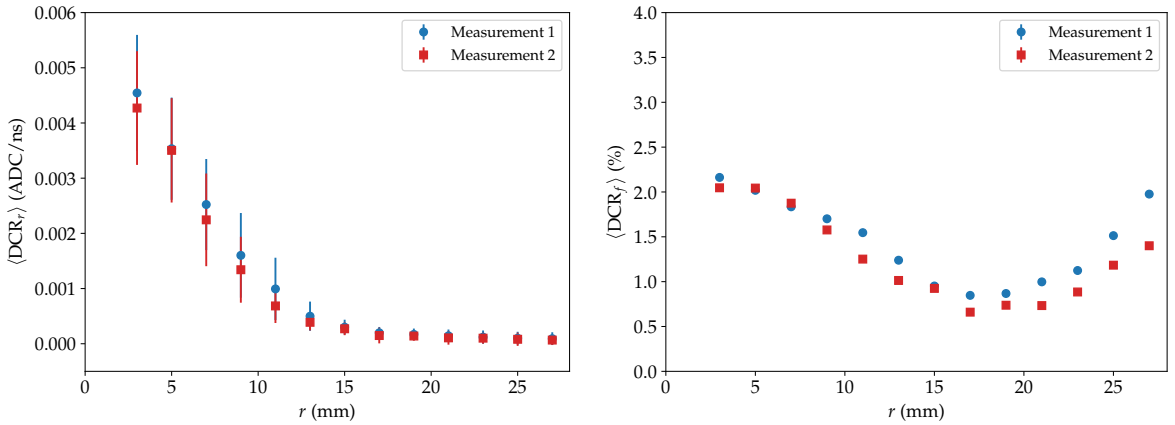

(a) Mean DCR rate.

(b) Mean DCR fraction.

Figure 7.13: Measured radial dependences of (a) the mean DCR rate and (b) of the mean DCR fraction for two radial ^{241}Am scans at different azimuthal positions. The DCR rate shows a strong radial dependence. The fraction of charges re-released into the detector bulk is on the order of $0.5 - 2.5\%$ of the total detected alpha event energy and is slightly dependent on the radius. Published in [229].

Another way of quantifying the DCR effect is in terms of the mean DCR fraction $\langle \mathrm{DCR_f} \rangle$. The fraction is defined as the ratio between the amount of delayed charges that are re-released into the detector bulk during a certain integration time window and the mean alpha energy. More specifically, the parameter is obtained by converting the DCR rate from ADC/ns to keV/ns units using the linear energy calibration constant a from **Eq.** (6.18), integrating over the length of the waveform tail t_t (here $t_t \approx 14\,\mu\mathrm{s}$), and finally dividing by the detected mean alpha energy $\langle E_\alpha \rangle$:

$$\langle \mathrm{DCR_f} \rangle = a \cdot t_t \cdot \frac{\langle \mathrm{DCR_r} \rangle}{\langle E_\alpha \rangle}. \tag{7.2}$$

The mean DCR fraction as a function of radius for the two radial scans is shown in **Fig.** 7.13b. The fraction of re-released charges varies in the range $0.5 \lesssim \langle \mathrm{DCR_f} \rangle \lesssim 2.5\%$ and shows a slight radial dependence. At higher radial positions, $\langle \mathrm{DCR_f} \rangle$ seems to increase again. However, it should be noted that these fractions are numerically problematic as also $\langle E_\alpha \rangle$ is close to zero [229].

Finally, the correlation between the mean DCR rate and the mean alpha energy was investigated, see **Fig.** 7.14. For event energies $\langle E_\alpha \rangle \gtrsim 500\,\text{keV}$, the variables show a strong linear correlation. At smaller energies, a deviation from this behavior can be observed. Most importantly, in the signal ROI at the $Q_{\beta\beta}$-value of ^{76}Ge, the DCR rate for surface alpha events clearly deviates from zero, and thus from the DCR rate of normal bulk events. Therefore, even if the passivated surface is charged-up negatively, surface alpha events ending up in the signal ROI can be rejected efficiently by applying a DCR cut. As discussed above, in the presence of negative surface charges, the discrimination of surface alpha events at high radial positions based on the DCR parameter is not feasible. However, these events feature such a strongly degraded energy that they do not contribute as a background source in the ROI.

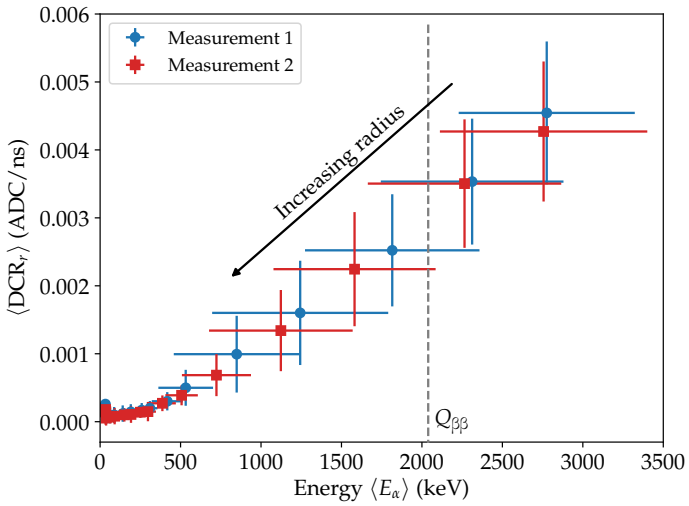

Figure 7.14: Correlation between the mean DCR rate and the mean alpha energy for two radial ^{241}Am scans at different azimuthal positions. The grey dashed line indicates the $Q_{\beta\beta}$-value of ^{76}Ge.

7.3 COMPARISON TO PREVIOUS MEASUREMENTS AND CONCLUSIONS

An extensive measurement campaign was carried out to study the impact of alpha events on the passivated surface of a PPC HPGe detector. The characterization measurements in a vacuum test facility validated that the detector surface is prone to effects such as charge build-up. A radial-dependent energy degradation of the surface alpha events was observed, i.e. a decreasing alpha energy with increasing radial distance from the point contact. This could be explained with the presence of negative surface charges and the intrinsic radial dependence of the weighting potential. The measurements also demonstrated that surface alpha events exhibit a DCR effect which can be exploited to powerfully reject them. Comparable to the alpha energy, a radial dependence was observed for the DCR parameter. The reproducibility of the results was verified in several measurements. Moreover, the detector response to surface alpha events showed a high stability over an extended measurement period.

The measurement results obtained in this work are highly complementary to previous surface alpha characterization measurements with the same detector in another measurement facility, the TUM Upside-down BEGe (TUBE) scanning system [228, 235]. In those measurements, a positive charge build-up on the passivated detector surface was observed. In accordance with the theoretical descriptions in **Ch.** 5.2, a radial dependence of the alpha energy and the DCR parameter of the opposite behavior was measured (quantities increasing with increasing distance from the point contact) [235]. **Fig.** 7.15 shows a comparison of the radial dependence of the alpha energy in both measurement facilities. The different results decisively proof that the passivated surface of one and the same detector can accumulate either positive or negative charges. Unfortunately, it was not possible to figure out conclusively what led to the different behaviors in the two test facilities. Possible explanations are based on differences in the experimental setups, e.g. different

grounding schemes close to the passivated detector surface (vacuum conductance), differences in the PTFE holding structure, etc. Consequently, to enable an efficient rejection of alpha backgrounds in LEGEND-200, measurements to determine the surface charge polarity in a LAr environment are indispensable.

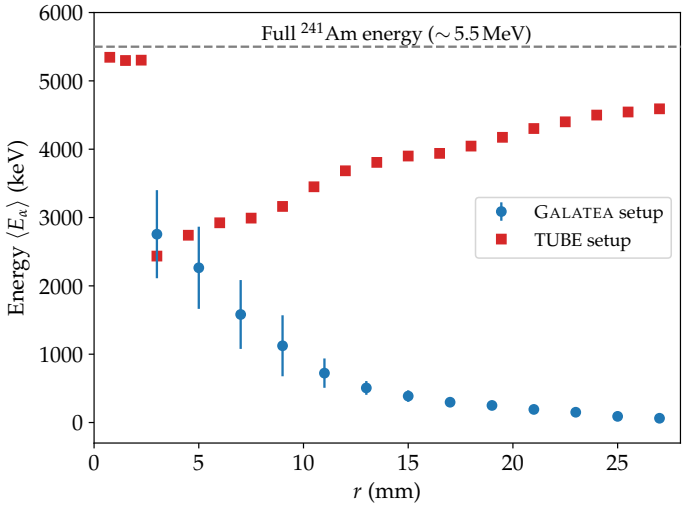

Figure 7.15: Comparison of the radial dependence of the alpha energy in the GALATEA and TUBE facilities. Measurements were performed with the same PPC detector. While in GALATEA a negative charge build-up on the passivated detector surface was observed, the measurements in TUBE showed positive surface charges. This results in the opposite radial dependence of the alpha energy. TUBE data provided by J. Gruszko [228, 235].

8

CHARACTERIZATION OF SURFACE BETA INTERACTIONS

In this chapter, the PPC detector surface characterization measurements with beta particles are presented. An overview of the measurement conditions can be found in **Ch.** 8.1. The measurement results of the radial beta scans are discussed in detail in **Ch.** 8.2. **Ch.** 8.3 briefly summarizes the results.

8.1 OVERVIEW AND MEASUREMENT CONDITIONS

For the surface characterization measurements with beta particles, two different ^{90}Sr sources and collimator configurations were used within two measurement campaigns. In the first campaign, a relatively weak source ($A_0 = 1.6\,\mathrm{MBq}$) with a comparably large beam spot on the detector surface was used. Based on the experience gained in the first campaign, the collimator geometry was slightly modified and a source with a higher activity ($A_0 = 5.0\,\mathrm{MBq}$) was used in the second phase. In the following, we will focus our discussion on the results obtained in the second phase. In the GALATEA test facility, the ^{90}Sr source was installed in the top collimator. A collimator consisting of seven cylindrical tungsten (W) segments was used, see **Fig.** 8.1. The radioactive source was installed in the third segment. Based on the collimator geometry and the source strength, a beta electron rate of $\sim 300\,\mathrm{cts/s}$ was expected at the detector surface. In all measurements, the ^{90}Sr beam spot had an incidence of 90° on the detector surface. Its shape was simulated using GEANT4, see **Fig.** 8.2.

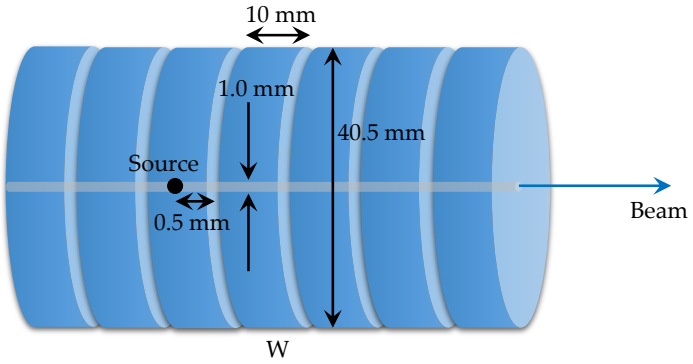

Figure 8.1: Collimator geometry used for the surface beta characterization measurements in GALATEA. A ^{90}Sr source was installed in the third segment. The figure is not to scale.

As for the surface characterization measurements with alpha particles, several radial scans at different azimuthal positions, as well as background and stability measurements were conducted. An overview of the measurements is listed in **Tab.** A.1 in the appendix. Typically, a measurement time of 0.5 hr at each scan point was chosen. Most of the scans were performed by moving the collimator from high to small radial positions (from $r_{col.} = 36\,\mathrm{mm}$ to $r_{col.} = 0\,\mathrm{mm}$) in $\Delta r_{col.} = 2\,\mathrm{mm}$ steps. The measurements were conducted with the detector operated either at the bias voltage of $V_B = 1050\,\mathrm{V}$ or at $V_B = 2000\,\mathrm{V}$. Here, we will focus our analysis on the measurements conducted at the higher bias voltage (comparable, but less pronounced results were obtained for the data taken at the lower bias voltage). The observed small dependence on the bias voltage is not yet fully understood.

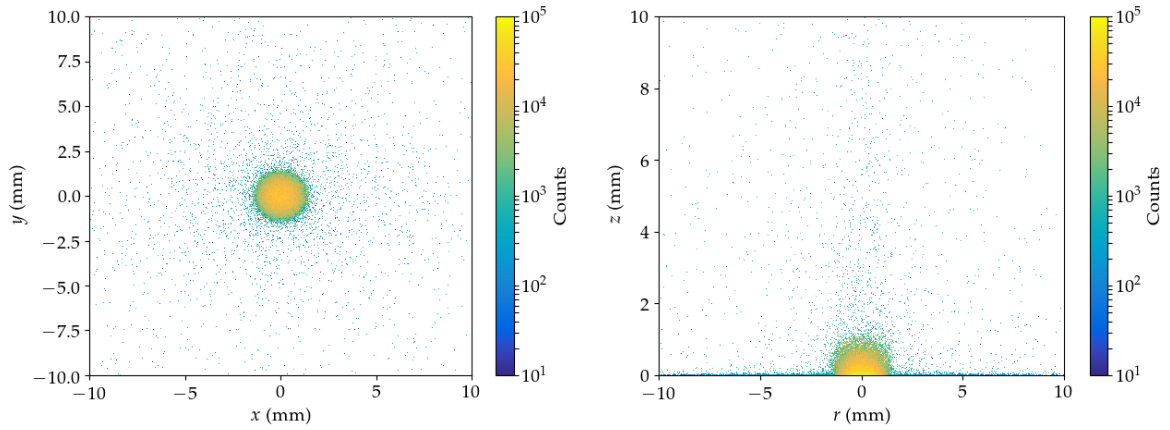

(a) Beam spot in (x, y) plane.

(b) Beam spot in (r, z) plane.

Figure 8.2: Shape of the ^{90}Sr beam spot in the (a) (x, y) and (b) (r, z) plane (simulated using GEANT4). For visual purposes, the PTFE bar mounted on top of the detector was excluded here (no shadowing of the beam spot). The origin of the coordinate system is at the top center of the point contact with the z-axis pointing towards the detector bulk.

8.2 MEASUREMENT RESULTS

RADIAL ENERGY DEPENDENCE In the following paragraphs, the radial response of the PONaMa1 detector to beta events on the passivated surface will be investigated. In contrast to the surface alpha characterization measurements with the ^{241}Am source, no radial offset between the detector and the collimator position was measured (the detector holding structure and the collimator were readjusted between the measurement campaigns). Hence, in the following, all radial positions are expressed in terms of $r = r_{det} = r_{col}$.

The energy spectra of a measurement with the ^{90}Sr source (radial position $r = 4\,mm$), and of a background measurement are shown in **Fig.** 8.3a. Compared to the energy spectrum of the background measurement, the ^{90}Sr energy spectrum features a strong beta continuum for energies up to $\sim 2.2\,MeV$. This can be mainly attributed to the beta decay of ^{90}Y, cf. **Ch.** 6.3. However, at smaller energies, the pure ^{90}Sr beta contribution is also visible.

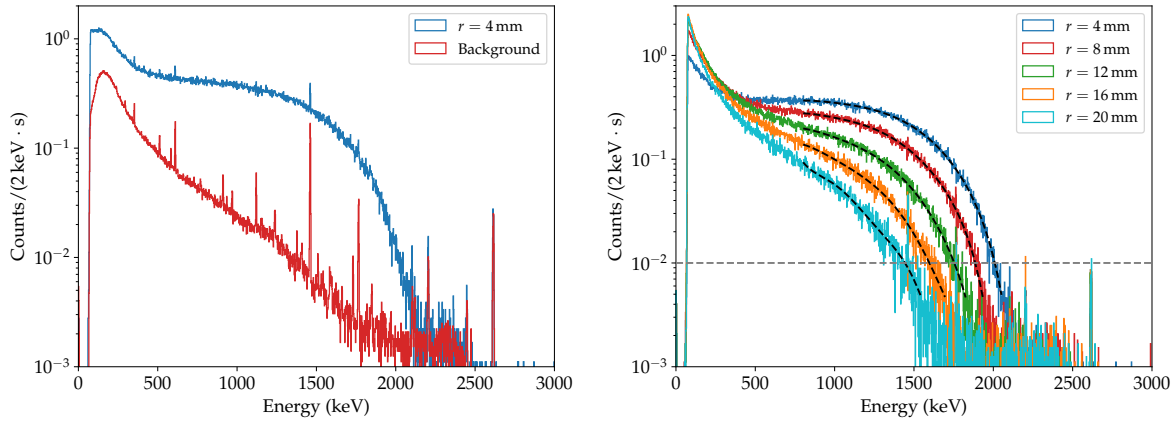

(a) ^{90}Sr and background energy spectra.

(b) Background-subtracted ^{90}Sr energy spectra.

Figure 8.3: (a) Energy spectra of a measurement with the ^{90}Sr source (position $r = 4\,mm$) (blue curve), and of a background measurement (red curve). (b) Background-subtracted ^{90}Sr energy spectra at selected radial positions. The black dashed lines correspond to polynomial fits of the spectra. The endpoint was approximated by finding the intersection of the fits with a fixed value (grey dashed line). Published in [229].

To quantify the radial energy dependence, the ^{90}Sr energy spectra at different radial positions were first corrected for background events, see **Fig.** 8.3b. The following two effects can be observed [229]:

1) The total number of events decreases with increasing radial position.

2) The energy continuum shifts to lower energies with increasing radial position. This is especially pronounced around the endpoint of the distribution.

The first effect was quantified by investigating the evolution of the total count rate (integrated over the entire energy range $0-3\,\mathrm{MeV}$) as a function of radius, see **Fig.** 8.4a. The plot shows that the count rate first increases and then decreases with radius. The reduced rate at small radii can be related to a partial shadowing of the ^{90}Sr beam spot by the PTFE bar, cf. **Ch.** 6.2. Compared to the surface characterization measurements with alpha particles, where the total number of alpha events stayed nearly constant, cf. **Ch.** 7.2, the number of beta electrons clearly decreases at larger radii in the case of the ^{90}Sr measurements. This can be explained by the fact that surface events with a small energy deposition (small penetration depth) were affected so severely by the energy degradation that they fell below the detection threshold of the DAQ system. Compared to the measurements with the ^{241}Am source, the threshold was increased by a factor of ~3 (from ~16 keV to ~50 keV) for the measurements with the ^{90}Sr source. This was necessary due to the much stronger activity of the beta source (to avoid too high count rates) [229].

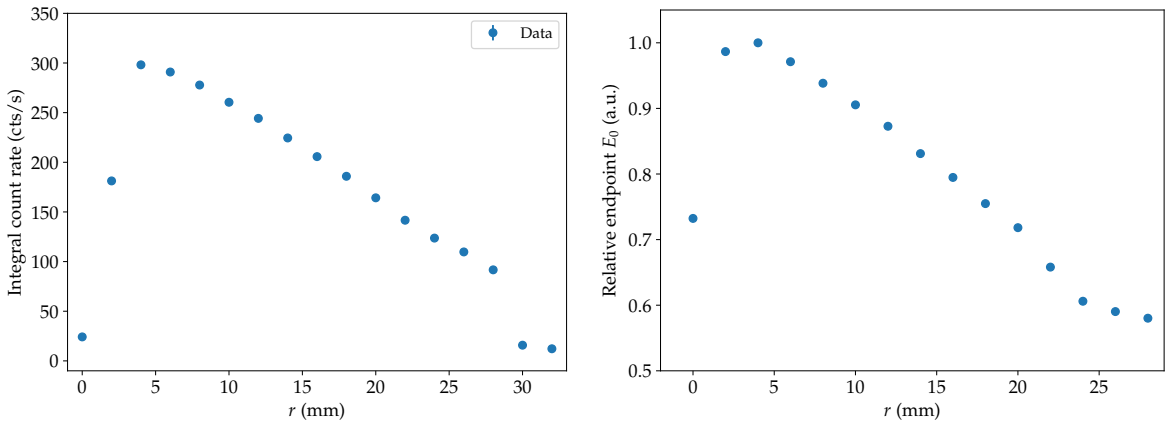

(a) Integral count rate.

(b) Relative endpoints.

Figure 8.4: (a) Evolution of the integral count rate in the energy range $0-3\,\mathrm{MeV}$, and (b) of the relative endpoint as a function of radius in a ^{90}Sr scan. The quantities have been determined based on the background-subtracted ^{90}Sr energy spectra. Published in [229].

To also quantify the radial-dependent degradation of the beta continuum, the background-subtracted energy spectra were fit with a seventh-order polynomial. To achieve convergence, the fits were constrained to certain energy ranges (depending on the radial position). The endpoint E_0 was approximated by estimating the intersection of the fit functions with a fixed value of the energy spectra, i.e. $10^{-2}\,\mathrm{cts}/(2\,\mathrm{keV}\cdot\mathrm{s})$. This value was chosen to avoid statistical fluctuations at smaller count rates which result in poor fits. **Fig.** 8.3b shows an example for the endpoint determination. Due to the rough estimate of the endpoint and keeping in mind that this method is slightly subject to binning effects, the endpoint was expressed as a relative endpoint (normalized to the maximum value), see **Fig.** 8.4b. Just as the integral count rate, the spectral endpoint decreases considerably with increasing radial position [229].

The observed radial-dependent energy degradation, i.e. a decreasing beta electron energy with increasing radial distance from the point contact, is in qualitative agreement with the results obtained in the surface alpha characterization measurements, cf. **Ch.** 7.2. In particular, the results are again consistent with the presence of negative charges at the passivated detector surface.

RADIAL DEPENDENCE OF OTHER PULSE SHAPE PARAMETERS Analogous to the surface alpha characterization measurements, the radial response of surface beta events was investigated in terms of various pulse shape parameters. Examples for the correlation plots of the quantities A/E, decay

time τ, drift time (0% − 90%), and DCR rate with energy at selected radii are shown in **Fig.** 8.5. It can be observed that at small radial positions, most of the beta events have decreasing A/E values. At higher radial positions, their A/E values increase again. In contrast, the decay time distributions do not change considerably with increasing radius. In the drift time distributions, two event populations can be observed. One population is located at small energies and its drift time decreases with increasing radial position. The second population is located at higher energies and has an increasing drift time with radius. With the help of pulse shape simulations, cf. **Ch.** 9.3.3, it will be validated that the first population corresponds to events with a small penetration depth which are sensitive to surface effects. For the observed negative charge build-up on the passivated detector surface, the signal formation is driven by the collection of electrons, cf. **Ch.** 5.2. Since at higher radii the electrons are closer to the n^+ contact, their drift time decreases. The second population corresponds to events with higher penetration depths which are less sensitive to surface effects. These interactions are subject to the usual charge collection behavior, in which the signal formation is mainly driven by the collection of holes. Since at higher radii the holes have a longer drift path to the p^+ readout contact, the drift time increases with radius. These separated two event populations show that, unlike alphas, not all beta electrons are affected significantly by surface charges, i.e. mostly those with small penetration depths are affected.

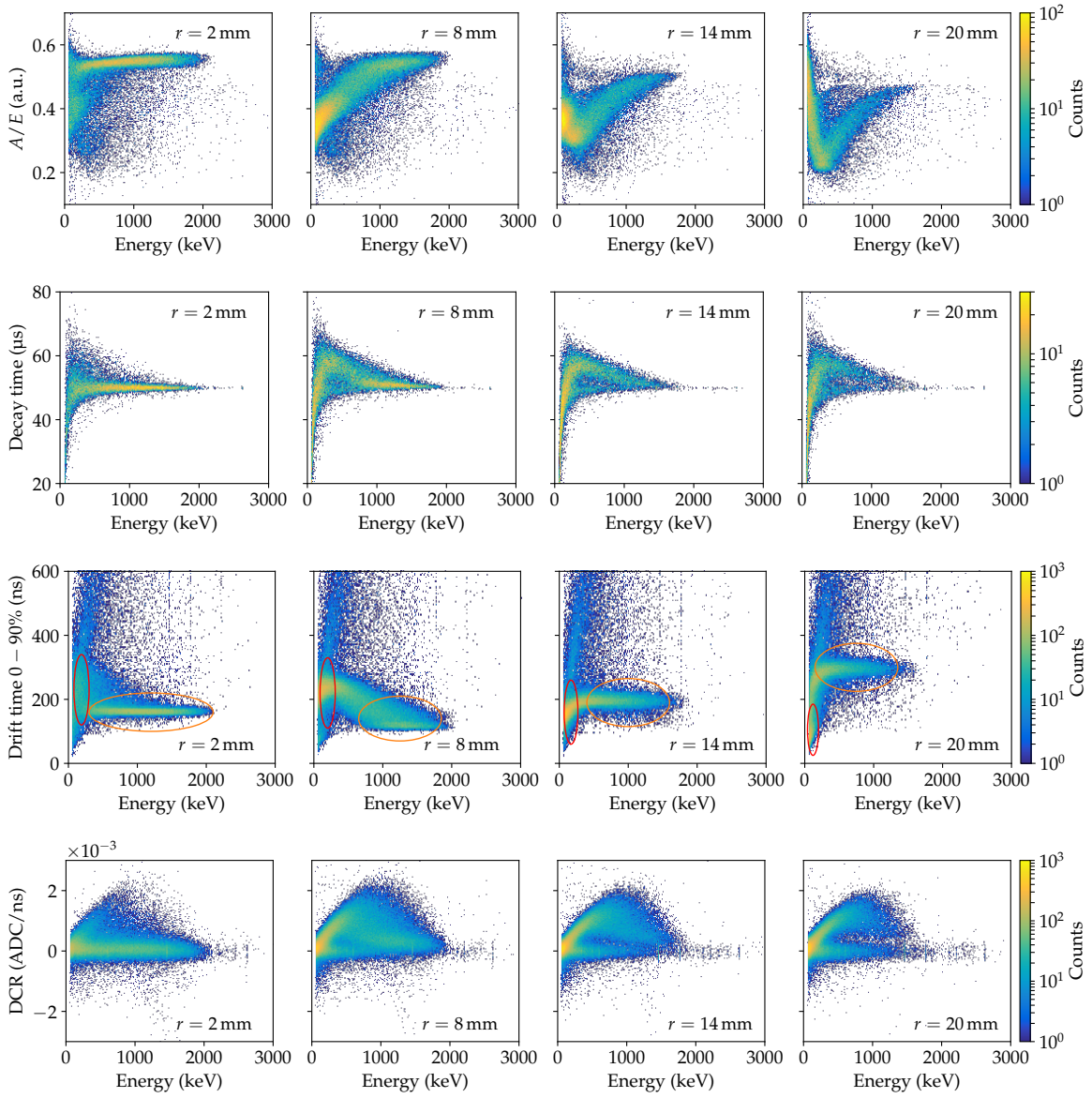

Figure 8.5: Correlation plots of the quantities A/E, decay time τ, drift time (0 − 90%), and DCR rate as a function of energy at selected radial positions (r = 2, 8, 14, 20 mm). The red vertical and orange horizontal ellipses in the drift time distributions indicate two event populations.

The DCR effect for surface beta events is much less pronounced than for surface alpha events. The DCR rate distributions in **Fig.** 8.5 show that some of the events - most likely those being sensitive to surface effects - have increased DCR values. However, these events cannot be clearly separated from those having a zero DCR value, i.e. the distributions are smeared. It is worth mentioning that in the surface beta characterization measurements, the DCR effect was only observed when the detector was operated at a bias voltage of $V_B = 2000\,V$. For the measurements carried out at a lower bias voltage ($V_B = 1050\,V$), the DCR values of all events are smeared around zero, see **Fig.** 8.6. Therefore, in the case of surface beta interactions, the DCR parameter is less suitable for the rejection of surface backgrounds.

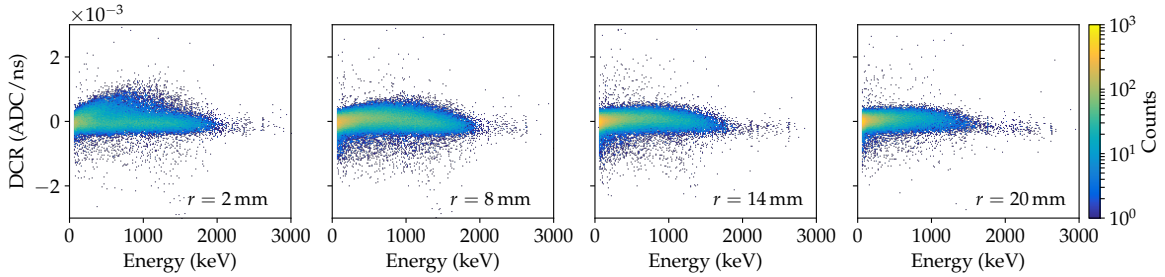

Figure 8.6: Correlation plots of the DCR rate as a function of energy at selected radial positions (r = 2, 8, 14, 20 mm) and at a bias voltage of $V_B = 1050\,V$.

8.3 CONCLUSIONS

The PPC detector surface characterization measurements with beta particles showed a negative charge build-up on the passivated surface. The observations are in qualitative agreement with the surface alpha characterization measurements, i.e. a similar radial energy dependence was observed. By analyzing the drift time distributions, two event populations could be identified: One being affected by surface effects, the other one being mostly insensitive. This is in good agreement with the theoretical expectation, i.e. only beta particles interacting close to the detector surface are being affected. The measurements also demonstrated that surface beta events exhibit a DCR effect that is much less pronounced than for surface alpha events. In addition, a bias voltage dependence of the DCR effect was observed.

As no strong manifestation of the DCR effect was present for surface beta events, and since their signal shape did not show obvious differences to those of normal bulk events, their discrimination at the passivated surface of PPC detectors is expected to be challenging. Further investigations in a realistic measurement environment in LAr are indispensable to better predict these backgrounds, and to develop discrimination techniques. A dedicated scanning facility is currently being constructed at Lawrence Berkeley National Laboratory (LBNL).

9

SURFACE EVENT SIMULATIONS

To better understand the results of the surface characterization measurements with alpha and beta particles discussed in **Chs.** 7 and 8, dedicated surface event simulations were performed. For the pulse shape simulations (PSS), the package `Siggen` consisting of the two programs `mjd_fieldgen` and `mjd_siggen` was used [234].

This chapter is organized as follows: Fist, a brief overview of the simulation framework is presented in **Ch.** 9.1. In **Ch.** 9.2, to gain a comprehensive understanding of surface effects and to understand their impact on various pulse shape parameters, charge collection efficiency maps are analyzed. The results of ^{241}Am and ^{90}Sr Monte Carlo simulations are presented and compared to the measurement results in **Ch.** 9.3. Finally, conclusions can be found in **Ch.** 9.4.

9.1 OVERVIEW

ELECTRIC FIELD AND WEIGHTING POTENTIAL The stand-alone program `mjd_fieldgen` calculates the electric potential, the electric field, and the weighting potential inside the detector. In addition, it calculates the detector capacitance. The computation is based on a numerical relaxation algorithm with an automatic adaptive grid. For PPC detectors, due to their cylindrical symmetry, the computation can be performed on a two-dimensional grid (coordinates: r and z). At the passivated detector surface, a reflective symmetry is used as a boundary condition for the relaxation algorithm. This is in accordance with the requirement that for zero surface charge at the passivation layer, the field lines close to the surface are parallel to that surface, such that no charges intersect the surface [229]. When computing the electric potential, `mjd_fieldgen` identifies and handles undepleted volumes in the detector by setting the local net impurity of the corresponding voxels to zero. This allows for realistic PSS even if the detector is not fully depleted [247]. **Fig.** 9.1 shows an example of the electric potential and electric field of the PONaMa1 detector simulated with `mjd_fieldgen`. It can be observed that the electric field is very high close to the point contact and low elsewhere.

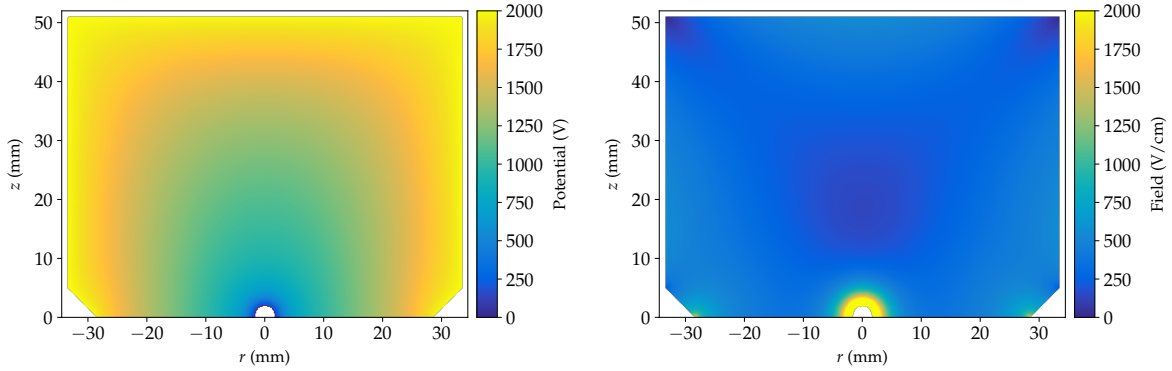

(a) Electric potential.

(b) Electric field.

Figure 9.1: (a) Simulated electric potential and (b) electric field in the PONaMa1 detector without surface charges. The potential in the detector is determined by the bias voltage (here $V_B = 2000\,V$). The electric field is high in the vicinity of the point contact and relatively low elsewhere. Simulations were performed using `mjd_fieldgen`.

SIGNAL FORMATION The signals corresponding to energy depositions at specific positions in the detector can be simulated with `mjd_siggen`. The program combines the field maps generated with `mjd_fieldgen` with a charge drift model [248] containing information on the electron and hole mobilities to compute the charge drift path. Furthermore, the corresponding signal is calculated by solving the Shockley-Ramo theorem numerically, cf. **Ch.** 3.3.1. The output is a normalized, PZ-corrected signal waveform starting at $t_0 = 0$. `mjd_siggen` takes into account the temperature and crystal axis dependence of the drift velocities [247].

Both programs, `mjd_fieldgen` and `mjd_siggen`, require a number of user inputs that are read from a common configuration file. These inputs include the detector geometry and configuration (bias voltage, temperature), the impurity profile, and other settings (grid size, charge cloud size and diffusion, electronics response, etc.). Most importantly for this work, a (homogeneously distributed) surface charge can be added to the passivated detector surface. The surface charge is expressed in units of e/cm^2 and is added as an impurity at every grid point on the surface [229].

9.2 CHARGE COLLECTION EFFICIENCY MAPS

In a first step, charge collection efficiency maps of the PONaMa1 detector were calculated to study the impact of surface effects on important pulse shape parameters such as the energy, A/E, drift time, etc. To this end, point charges with starting positions arranged in a finely meshed grid in the (r, z) plane were simulated using `Siggen`. The effects of diffusion and self-repulsion were not included in the simulations. This will be discussed further in **Ch.** 9.3.4. The grid size was adjusted dynamically in the z-axis direction to better visualize surface effects in the vicinity of the passivated detector surface. **Fig.** 9.2 shows the charge collection efficiency maps for negative and positive surface charges ($\sigma = \pm 0.3 \cdot 10^{10}\,e/cm^2$) for the quantities energy fraction, A/E, and drift time ($0-90\%$). Here, the energy fraction is defined as the amount of energy that an event still has after signal propagation in the presence of surface charges.

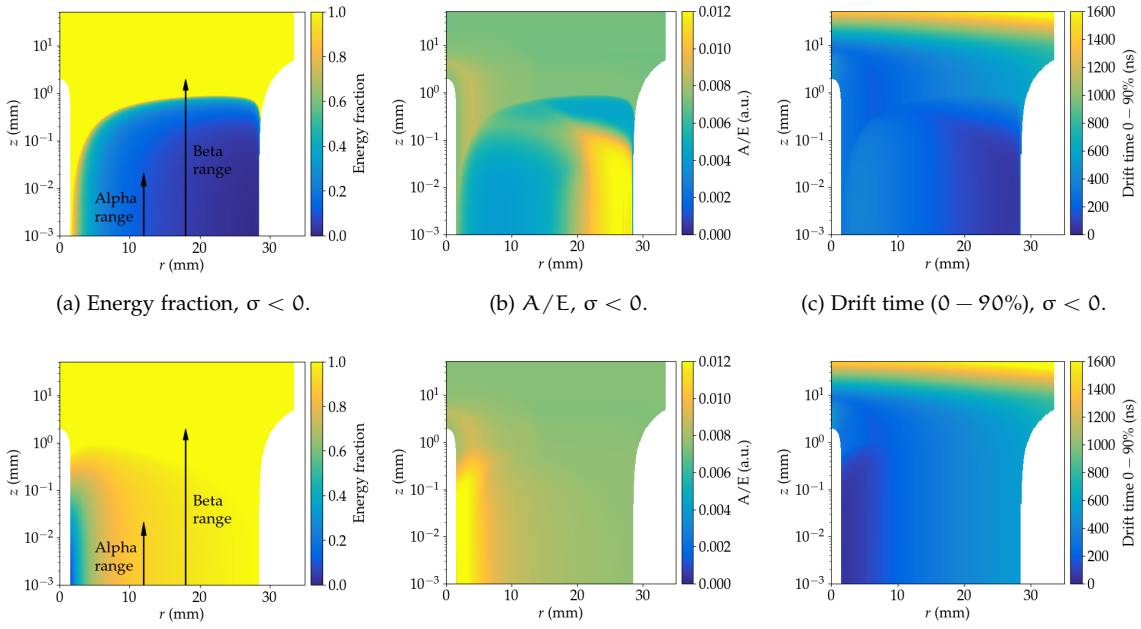

(a) Energy fraction, $\sigma < 0$. (b) A/E, $\sigma < 0$. (c) Drift time ($0-90\%$), $\sigma < 0$.

(d) Energy fraction, $\sigma > 0$. (e) A/E, $\sigma > 0$. (f) Drift time ($0-90\%$), $\sigma > 0$.

Figure 9.2: Charge collection efficiency maps of the quantities energy fraction, A/E, and drift time ($0-90\%$) for negative surface charges ($\sigma = -0.3 \cdot 10^{10}\,e/cm^2$, top row), and for positive surface charges ($\sigma = +0.3 \cdot 10^{10}\,e/cm^2$, bottom row) at a bias voltage of $V_B = 1050\,V$. The distributions are shown with a logarithmic scale in z to highlight surface effects at the passivation layer. The typical ranges of alpha and beta particles within the active detection volume are indicated by the arrows. Published in [229].

The energy fraction maps for negative and positive surface charges, see **Figs.** 9.2a and 9.2d, show that in most of the active detection volume, the full event energy is obtained. However, for $\sigma < 0$,

there is a strong charge loss in the region close to the passivated surface that extends to depths of $z \lesssim 1\,\text{mm}$. This can be also seen in **Fig.** 9.3a showing the energy fraction as a function of depth for various radial slices. Moreover, **Fig.** 9.3b shows the boundary between the charge loss region and the region in which charges are fully collected. In the charge loss region, holes created during an interaction are attracted to the passivated surface and do not contribute to the signal development. The signal formation is driven by the collection of electrons to the n^+ contact, cf. **Ch.** 5.2. The efficiency map in **Fig.** 9.2a shows that at a given depth $z \lesssim 1\,\text{mm}$, with increasing radial position the energy fraction decreases, i.e. the energy degradation gets stronger. The boundary of full charge collection further indicates that at high radial positions, even alpha particles with high penetration depths are affected by surface charges. With typical ranges of several tens of micrometers in germanium, cf. **Ch.** 3.1.1, surface alpha events are completely subject to the charge loss region. In contrast, surface beta events with higher penetration depths up to a few millimeters are only partially affected [229].

In the case of positive surface charges, $\sigma > 0$, there is only a small region in the vicinity of the point contact where events have a strongly degraded energy. Here, electrons created during an interaction are attracted to the passivated surface and do not contribute to the signal development, i.e. the signal formation is driven by the collection of holes. At a given depth $z \lesssim 1\,\text{mm}$, with increasing radius, the energy degradation gets less severe. Compared to a negative surface charge build-up, the degradation is much less pronounced. This is due to the fact that for $\sigma < 0$, holes are not collected. In general, electrons do contribute less to the signal formation process since they drift through a low weighting field to the n^+ contact [229].

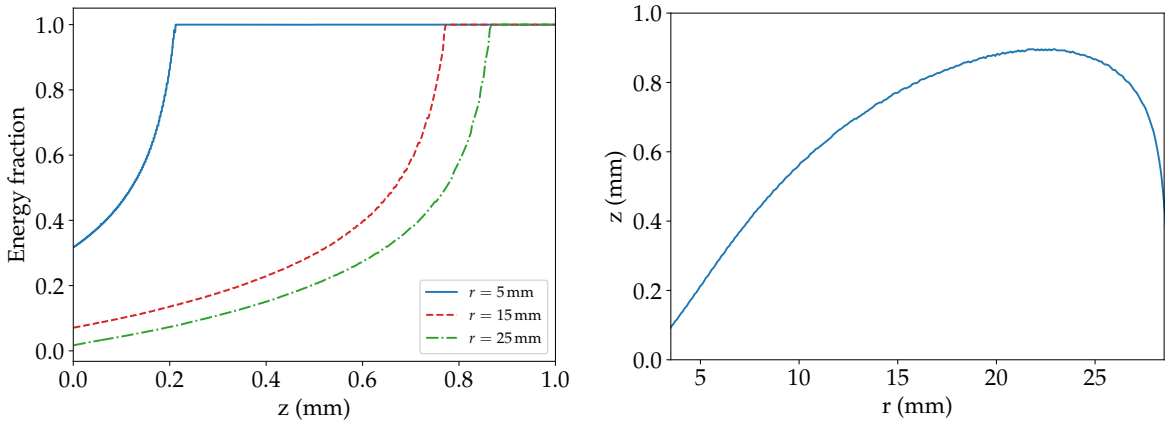

(a) Energy fraction for various r slices.

(b) Boundary of full charge collection.

Figure 9.3: (a) Energy fraction as a function of depth z for selected slices along a fixed radial position. (b) Boundary indicating the full charge collection, i.e. the z-value above which the full event energy is obtained. Simulation results are shown for negative surface charges ($\sigma = -0.3 \cdot 10^{10}\,\text{e/cm}^2$) at a bias voltage of $V_B = 1050\,\text{V}$.

For an increasing absolute amount of surface charges $|\sigma|$ (at a fixed bias voltage) or a decreasing bias voltage (at a fixed amount of surface charges), the charge loss region extends towards higher depths z, see **Fig.** 9.4. It can be also observed that at higher bias voltages, events near the point contact are less affected by energy degradation.

Finally, the impact of the detector temperature on the charge loss region was investigated. The boundary of full charge collection for different temperatures (at a fixed amount of surface charges and bias voltage) is shown in **Fig.** 9.5. The plot shows that with increasing detector temperature, the charge loss region extends slightly towards higher depths z. However, compared to the results at varying surface charge or bias voltage, the effect is rather small.

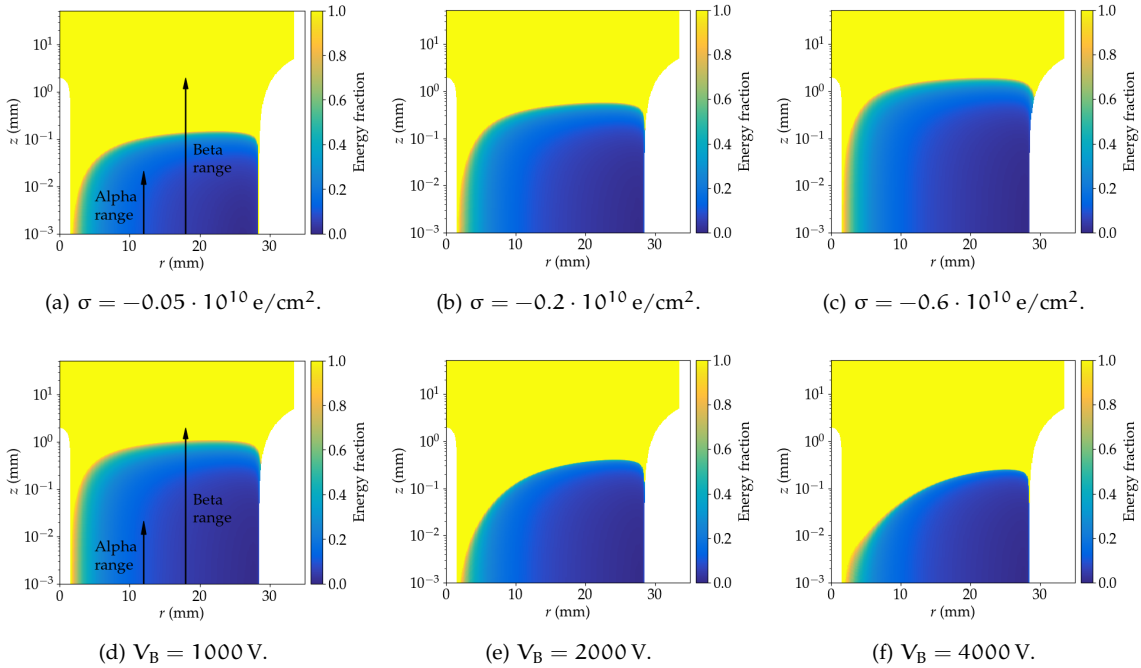

(a) $\sigma = -0.05 \cdot 10^{10}\,\mathrm{e/cm^2}$. (b) $\sigma = -0.2 \cdot 10^{10}\,\mathrm{e/cm^2}$. (c) $\sigma = -0.6 \cdot 10^{10}\,\mathrm{e/cm^2}$.

(d) $V_B = 1000\,\mathrm{V}$. (e) $V_B = 2000\,\mathrm{V}$. (f) $V_B = 4000\,\mathrm{V}$.

Figure 9.4: Charge collection efficiency maps showing the energy fraction for selected negative surface charges (upper row, $V_B = 1050\,\mathrm{V}$) and bias voltages (lower row, $\sigma = -0.3 \cdot 10^{10}\,\mathrm{e/cm^2}$). For higher absolute surface charges or lower bias voltages, the charge loss region extends further into the detector bulk.

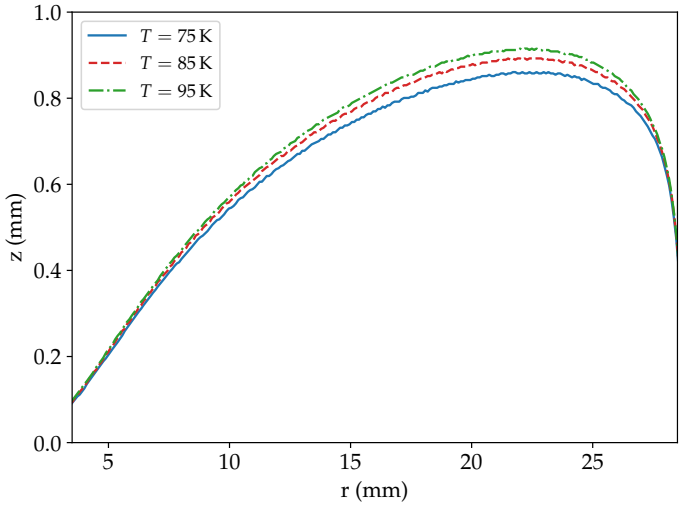

Figure 9.5: Boundaries indicating the full charge collection for selected detector temperatures. Simulation results are shown for negative surface charges ($\sigma = -0.3 \cdot 10^{10}\,\mathrm{e/cm^2}$) at a bias voltage of $V_B = 1050\,\mathrm{V}$.

The A/E map for a negative surface charge build-up, see **Fig.** 9.2b, shows that at a given depth $z \lesssim 1\,\mathrm{mm}$, the A/E values first slightly decrease and then strongly increase with increasing radius. This can be explained by the fact that at higher radial positions, the electrons drift in a slowly changing weighting field with a short drift time which results in fast signals and thus high A/E values. For positive surface charges, see **Fig.** 9.2e, high A/E values are encountered in the region close to the point contact. Here, the holes drift in a rapidly changing weighting field with a short drift time which also results in fast signals [229].

The drift time of events in the charge loss region for $\sigma < 0$ decreases with increasing radial position (at a given depth $z \lesssim 1\,\mathrm{mm}$), see **Fig.** 9.2c. This is due to the closer proximity of the electrons to the n^+ electrode at higher radii so they are collected faster. The drift time map also

shows that at higher penetration depths outside of the charge loss region ($z \gtrsim 1\,\mathrm{mm}$), the drift time increases with increasing radial position. Here, the holes drive the signal formation. At larger radii, they have a longer drift path to the p^+ contact and therefore a longer drift time. Likewise, for positive surface charges, see **Fig.** 9.2f, where the signal formation in the charge loss region is driven by the collection of holes, the drift time increases with radius [229].

9.3 COMPARISON OF MEASUREMENT TO SIMULATION

9.3.1 *Monte Carlo and pulse shape simulations*

Extensive simulations were carried out to better understand and validate the results obtained in the surface characterization measurements with alpha and beta particles. First, realistic energy deposition distributions in the PPC detector were simulated using the toolkit GEANT4. Second, the corresponding signals were simulated using `Siggen`. Third, various pulse shape parameters (A/E, DCR, rise time, etc.) were computed and analyzed in post-processing routines. This three-step procedure, illustrated schematically in **Fig.** 9.6a, will be discussed in more detail in the following paragraphs.

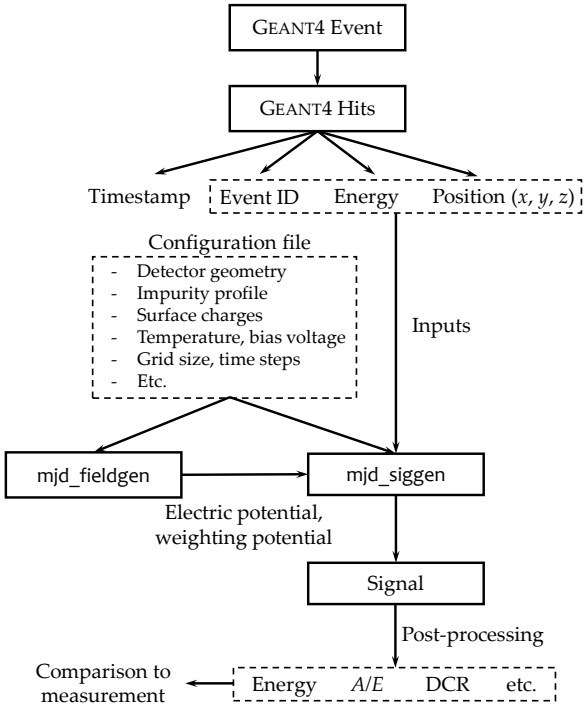

(a) Simulation structure.

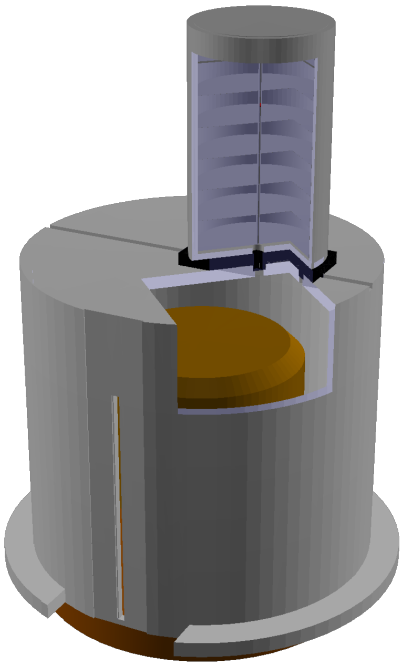

(b) GEANT4 geometry.

Figure 9.6: (a) Structure of the PPC detector surface event simulations. (b) Three-dimensional rendering of the GEANT4 geometry of the surface characterization measurements in GALATEA. Rendering provided by L. Hauertmann. Published in [229].

1) GEANT4 SIMULATIONS In the first step, the interaction positions (x, y, z) and energy depositions (E) of surface alpha and beta events in a PPC detector were simulated using GEANT4. To this end, a simplified geometry of the GALATEA scanning facility was implemented (work by L. Hauertmann). **Fig.** 9.6b shows a rendering of the simulation geometry. Special care was taken to model the measurement setup as realistically as possible. The geometry includes the vacuum cryostat, the PONaMa1 detector, the PTFE support structure, the IR shield, the collimator geometry, and the slider support structure. Depending on the measurement conditions (^{241}Am vs ^{90}Sr), the collimator geometry was adjusted accordingly. To acquire sufficiently high statistics, several million events were simulated. For every simulated event, the parameters timestamp, event ID, energy, and interaction position were stored for every charge deposition (hit) in the detector [229].

2) PULSE SHAPE SIMULATIONS The outputs of the GEANT4 simulations (event ID, energy, and position) were used as an input for pulse shape simulations (PSS) with `Siggen`. For a given event, the signals corresponding to the individual hits were simulated and finally summed into one signal (weighted with the individual energy depositions). For most of the PSS, the following settings were used in the `Siggen` configuration file: The computation was performed on a grid with a size of 50 µm × 50 µm (smallest possible size). For simplicity, a linear impurity profile was used, with a net impurity concentration at the detector top surface of $\rho_0 = 0.372 \cdot 10^{10}\,e/cm^3$ and a net impurity gradient of $0.025 \cdot 10^{10}\,e/cm^4$. The parameters surface charge (surface impurity), surface drift velocity, detector bias voltage, detector temperature, and preamplifier time constant were adjusted based on the specific measurement conditions. The evolution of the charge cloud size due to diffusion and self-repulsion was neglected in all simulations. This will be discussed in more detail in **Ch.** 9.3.4. Moreover, the implementation of a sophisticated electronic response model (e.g. modeling the electronic noise) was omitted. The simulated waveform of every event was stored for a time period of 1500 ns (starting at $t = t_0 = 0$ ns) with a time step length of $\Delta t = 1$ ns. This trace length was chosen to minimize the computing time and to ensure a full charge collection of events close to the passivated detector surface [229].

3) POST-PROCESSING In post-processing, several pulse shape parameters were extracted from the simulated waveforms. These include the signal energy, the maximum current amplitude to estimate A/E, the signal drift and rise time, and the DCR slope. Most of the parameters were determined as described in **Ch.** 6.5. The DCR effect for surface alpha events was modeled by convolving the current signal with an exponential, followed by a re-integration to obtain the convolved charge signal $\hat{s}(t)$:

$$\hat{s}(t) = C \sum_{t,t'=t+1} [s(t) - s(t-1)] \left(1 - \exp\left(\frac{t-t'}{\tau}\right)\right). \tag{9.1}$$

Here, C denotes a factor containing the fraction of charges re-released into the detector bulk, $s(t)$ the original (non-convolved) signal, and τ an exponential time constant describing the time scale of charge re-release. The equation accounts for the fact that the delayed charges are released starting from when the alpha particle penetrates the surface, and then decaying away. The DCR rate defined in this equation is proportional to the energy of the signal, in agreement with the measurement results, cf. **Ch.** 7.2. It should be noted here that the DCR model in **Eq.** (9.1) was tuned to match the measurement results obtained within this work. Alpha or beta surface events with another topology, e.g. different incidence and/or energy, may not be described well [229].

9.3.2 *Surface alpha events*

OVERVIEW In the following paragraphs, the results of the ^{241}Am surface alpha event simulations will be discussed and compared to the measurements. Events were simulated for different radial positions (0 mm ⩽ r ⩽ 36 mm) in $\Delta r = 1$ mm steps. **Fig.** 9.7 shows an example for the event distribution of the beam spot weighted with the event energy. While alpha events are located directly at the passivated surface, other events, particularly gamma radiation (e.g. 59.5 keV gammas), have higher penetration depths up to several cm. It is worth noting that almost all alphas are deposited at a fixed depth ($z \approx 16$ µm) which is closely related to the fact they are mostly monoenergetic.

NEGATIVE SURFACE CHARGES Typical alpha event waveforms obtained in the PSS with negative surface charges ($\sigma < 0$) at various radial positions are shown in **Fig.** 9.8a. Qualitatively, the simulated waveforms reproduce the behavior observed in the ^{241}Am measurements very well, cf. **Fig.** 7.11, i.e. the signal amplitude and thus the alpha energy decreases with increasing radial position. At the highest radii, the signal energy is strongly degraded. It can be also observed that with increasing radius, the drift time decreases, i.e. the electrons have a shorter drift path to the n^+ contact.

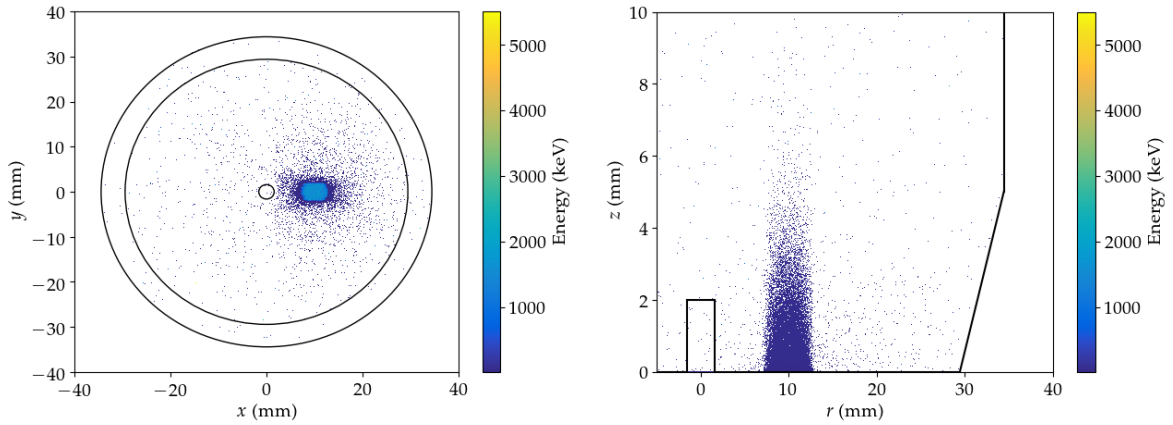

(a) Beam spot in (x, y) plane.

(b) Beam spot in (r, z) plane.

Figure 9.7: Event distribution of the ^{241}Am beam spot in the (a) (x, y) and (b) (r, z) plane weighted with the event energy (simulated using GEANT4). The oval shape of the beam spot in the (x, y) plane is due to shadowing of the spot by the slit in the IR shield. Alpha events are in close proximity to the passivated surface (mean depth of $z \approx 16\,\mu m$). Events with higher penetration depths are mainly gamma events (particularly from the 59.5 keV gamma peak).

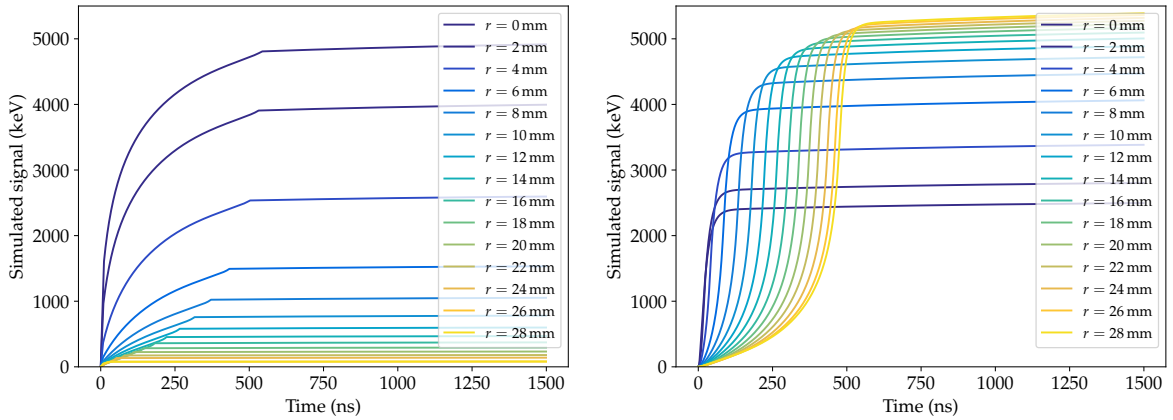

(a) Negative surface charges, $\sigma < 0$.

(b) Positive surface charges, $\sigma > 0$.

Figure 9.8: Alpha waveform examples simulated with `Siggen` for (a) negative and (b) positive surface charges at selected radial positions. With increasing radius, for negative (positive) surface charges, the signal amplitude decreases (increases). To emulate the DCR effect, the waveforms were convolved with an exponential, cf. **Eq.** (9.1). Therefore, the waveform tails slightly increase with time.

The reconstructed energies and DCR rates of all simulated ^{241}Am events were histogrammed before and after the signal propagation with negative surface charges ($\sigma = -0.1, -0.3 \cdot 10^{10}\,e/cm^2$), see **Fig** 9.9. The histograms show that with increasing radius, the alpha population moves towards smaller energies/DCR rates and gets narrower, in good qualitative agreement with the measurements, cf. **Fig.** 7.10a. However, it should be noted here that there are differences between the spectral shapes of the measured and simulated ^{241}Am spectra, cf. **Ch.** 7.2. This is most likely due to the fact that the simulation framework does not fully cover all relevant effects, e.g. diffusion and self-repulsion of the charge cloud evolution were neglected. Moreover, the simplified simulation settings (e.g. simplified geometry of the experimental setup, homogeneous distribution of the surface charges, discrete simulation grid, no sophisticated electronics response, etc.) could also have an impact [229].

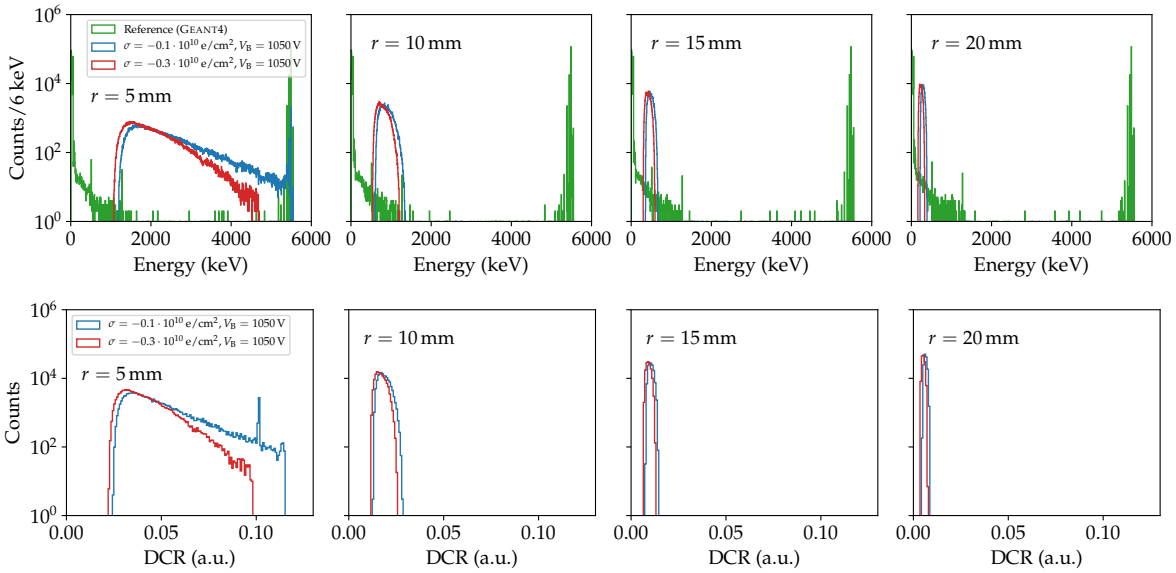

Figure 9.9: Energy (upper row) and DCR histograms (lower row) of the simulated ^{241}Am events at selected radial positions. The energy spectra are shown for the cases of no signal propagation (GEANT4 reference, green curve), and for the signal propagation with negative surface charges ($\sigma = -0.1, -0.3 \cdot 10^{10}$ e/cm^2) (blue and red curves). Published in [229].

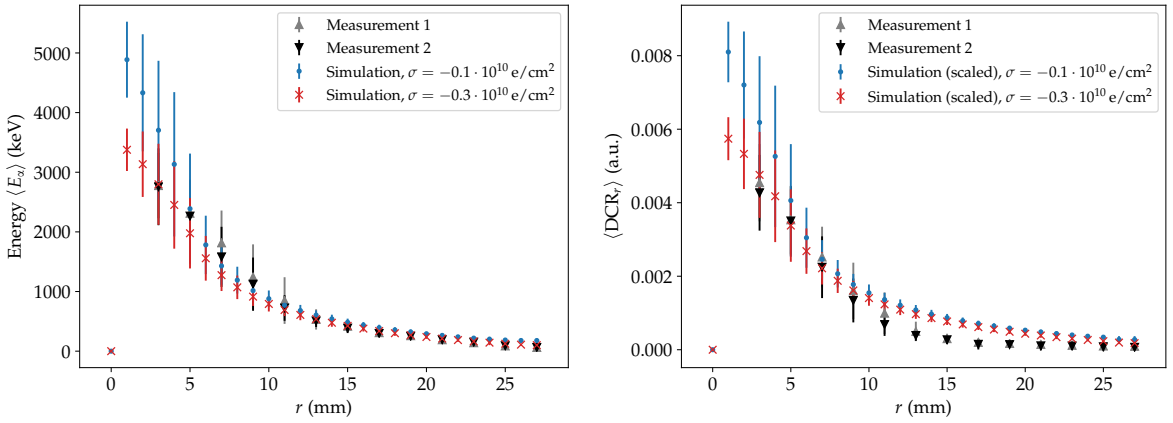

(a) Mean alpha energy.

(b) Mean DCR rate.

Figure 9.10: Comparison of measurement to simulation: (a) mean alpha energy and (b) mean DCR rate as a function of radius. Simulation results are shown for negative surface charges ($\sigma = -0.1, -0.3 \cdot 10^{10}$ e/cm^2). For both the radial dependence of the mean energy and the DCR rate, a good agreement with the simulation was obtained for $\sigma = -0.3 \cdot 10^{10}$ e/cm^2. For reasons of better comparability, the simulated DCR rates were scaled with a constant factor. Published in [229].

To quantify the radial dependence observed in the PSS, the mean alpha energies and the mean DCR rates were extracted from the distributions, see **Fig.** 9.10. To eliminate background events (particularly the gamma ray byproduct at 59.5 keV), only alpha events with an initial energy of > 5.3 MeV were selected. As for the measurements, the error bars represent the standard deviations of the distributions. It can be observed that for a higher absolute amount of surface charges, the energy and DCR rate degradation is stronger, particularly at small radii. The values extracted from the simulations are also compared to the measurement results. For better comparability, the simulated DCR rates were scaled with a constant factor (a comparison of the absolute DCR values is not meaningful, since they depend on the trace length which is different for measurement and simulation). The plots show that the measurement and simulation results qualitatively agree well, i.e. they have the same radial dependence. The measured and simulated mean alpha energies further show a good quantitative agreement for a moderate surface charge of $\sigma = -0.3 \cdot 10^{10}$ e/cm^2. In contrast, the measured mean DCR rates slightly deviate from the simulated ones, particularly for radial positions $r \gtrsim 10$ mm. This might be due to the simplicity of the applied DCR model, cf. **Eq.** (9.1) [229].

POSITIVE SURFACE CHARGES Alpha waveform examples obtained in the PSS with positive surface charges ($\sigma > 0$) at various radial positions are shown in **Fig.** 9.8b. It can be observed that the signal amplitude and thus the alpha energy increases with increasing radial position. At the highest radii, the full signal energy of about 5.5 MeV is retained. In addition, the drift time increases with increasing radius. This can be explained by the fact that at higher radial positions, the holes have a longer drift path to the p^+ contact.

As in the case of negative surface charges, the energies and DCR values of all simulated ^{241}Am events were histogrammed before and after the signal propagation with positive surface charges ($\sigma = +0.3, +3.0 \cdot 10^{10}$ e/cm^2), see **Fig.** 9.11. Subsequently, the mean alpha energies and DCR rates were extracted from the distributions. The plots show that the alpha energy degradation for positive surface charges is much less pronounced than for negative surface charges. Moreover, increasing the amount of surface charges only has a slight impact on the degradation level. In contrast, the DCR effect is slightly enhanced at higher radii for higher surface charges. The simulation results are in qualitative agreement with the TUBE measurement results, cf. **Ch.** 7.3 [228, 235].

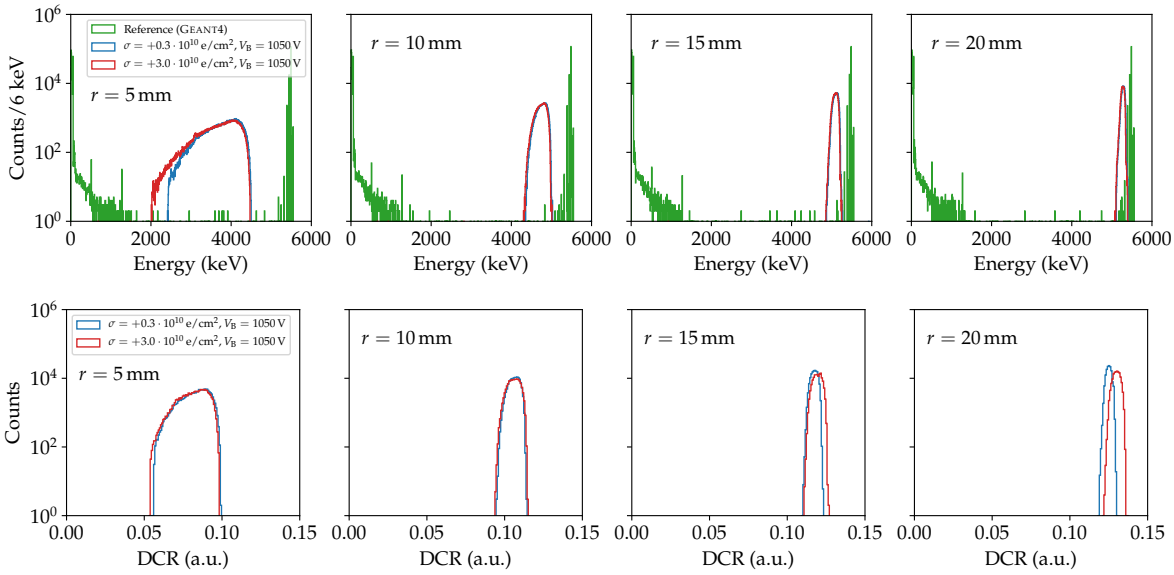

Figure 9.11: Energy (upper row) and DCR histograms (lower row) of the simulated ^{241}Am events at selected radial positions. The energy spectra are shown for the cases of no signal propagation (GEANT4 reference, green curve), and for the signal propagation with positive surface charges ($\sigma = +0.3, +3.0 \cdot 10^{10}$ e/cm^2) (blue and red curves).

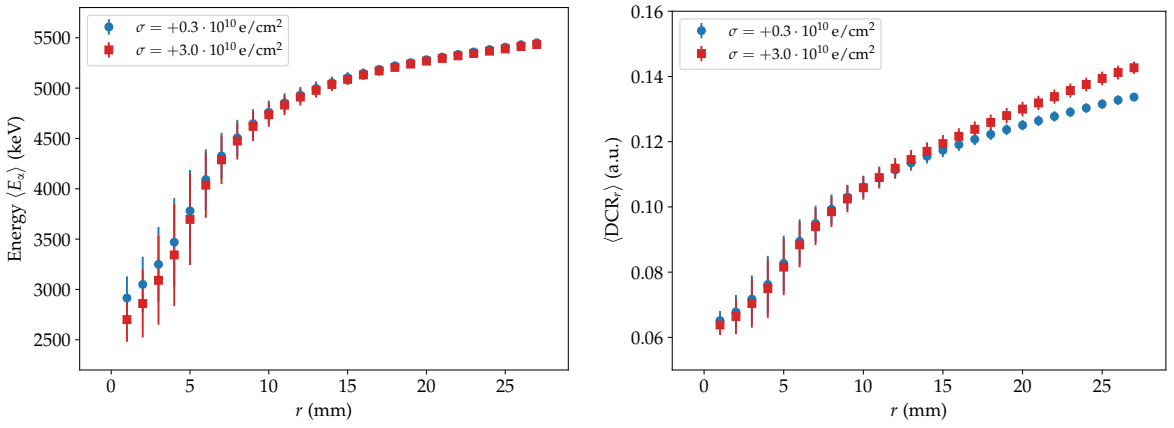

(a) Mean alpha energy.

(b) Mean DCR rate.

Figure 9.12: (a) Mean alpha energy and (b) mean DCR rate as a function of radius. Simulation results are shown for positive surface charges ($\sigma = +0.3, +3.0 \cdot 10^{10}$ e/cm^2).

COMPLEMENTARITY OF PULSE SHAPE DISCRIMINATION PARAMETERS In the previous TUBE PPC detector surface characterization measurements with alpha particles, the leading edge-based A/E and the tail-based DCR PSD parameters were found to be highly complementary [228, 235]. For the observed positive surface charge build-up, alpha events close to the point contact have high A/E values but small DCR values. With increasing radius, the DCR value increases, while the A/E value decreases. This can be seen in **Fig.** 9.13a showing the correlation between the A/E and DCR parameters for the TUBE measurement. By applying a combined cut on the two variables (indicated by the dashed lines in the plot), almost all alpha events can be rejected efficiently [235].

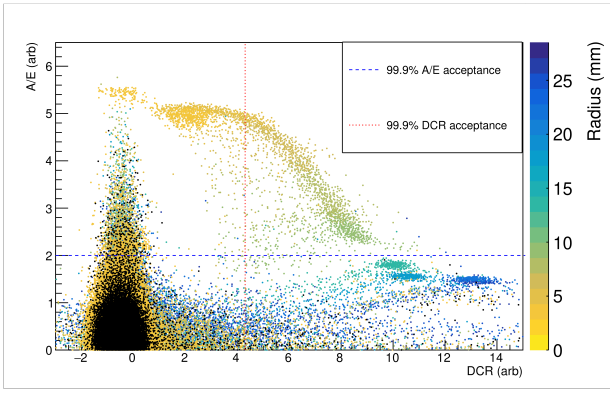

(a) Measurement ($\sigma > 0$). Source: [235].

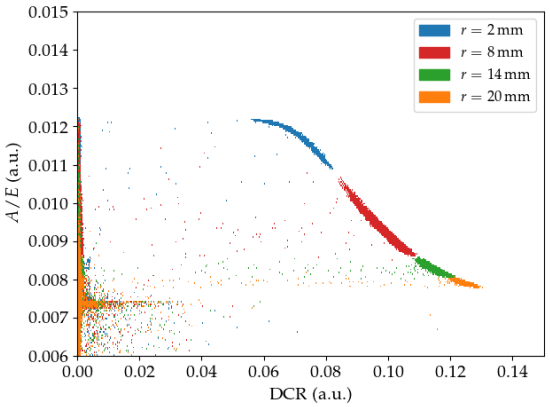

(b) Simulation ($\sigma > 0$).

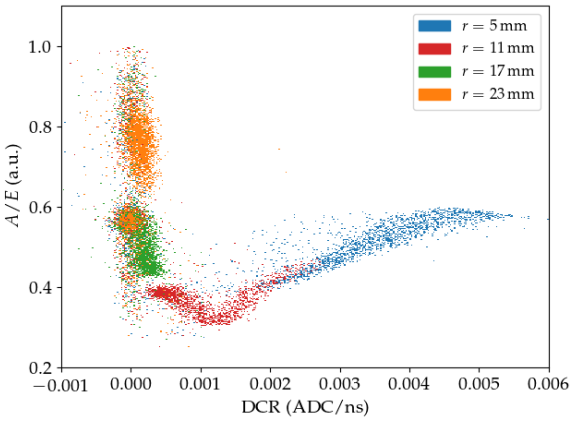

(c) Measurement ($\sigma < 0$).

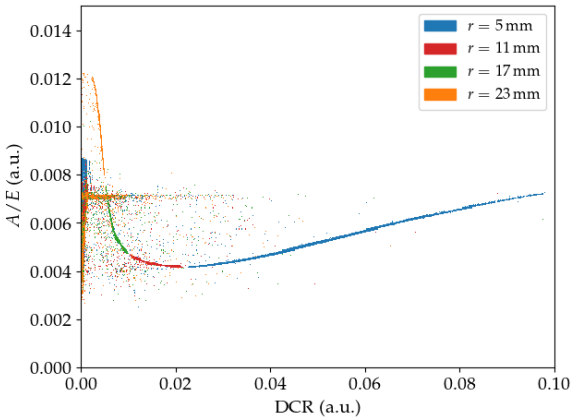

(d) Simulation ($\sigma < 0$).

Figure 9.13: Comparison of the correlation plots (measurement and simulation) of the A/E and DCR pulse shape parameters for (a, b) positive and (c, d) negative surface charges at selected radial positions. Since the quantities are uncalibrated, the absolute scales between measurement and simulation differ.

In the case of a negative charge build-up on the passivated detector surface, as observed in the surface characterization measurements in GALATEA, the correlation between the two PSD parameters is quite different. **Fig.** 9.13c shows that alpha events in close vicinity to the point contact have moderate A/E values and high DCR values. With increasing radius, the A/E values first decrease and then increase again, while the DCR values are falling steadily. At higher radial positions, a substantial amount of the alpha events has an overlap with non-alpha events which are distributed around DCR = 0 and A/E ≈ 0.5 (not visible in the plot due to the alpha selection using multivariate cuts). Therefore, in the case of negative surface charges, the two PSD parameters are less complementary. In particular, a combined cut cannot be used to reject all alpha events. However, at larger radii, the energy is already degraded to such an extent that they do not constitute a background in the signal ROI at the $Q_{\beta\beta}$-value of ^{76}Ge, cf. **Ch.** 7.2.

It is remarkable that the measurement results for both positive and negative surface charges are in very good qualitative agreement with the simulation results, see **Figs.** 9.13b and 9.13d. This strongly supports the validity of the surface charge model to explain the measurement results.

9.3.3 *Surface beta events*

OVERVIEW In the following paragraphs, the results of the ^{90}Sr surface beta event simulations will be discussed and compared to the measurements. Events were simulated for different radial positions ($0\,\text{mm} \leqslant r \leqslant 36\,\text{mm}$) in $\Delta r = 1\,\text{mm}$ steps. **Fig.** 9.14 shows an example for the event distribution of the beam spot weighted with the event energy. While beta events with small energies (small penetration depths) are located close to the passivated surface, those with higher energies have higher penetration depths. In general, beta events can be observed up to depths of $z \approx 1\,\text{mm}$. Therefore, compared to alpha events, the maximum penetration depth of beta events is much higher.

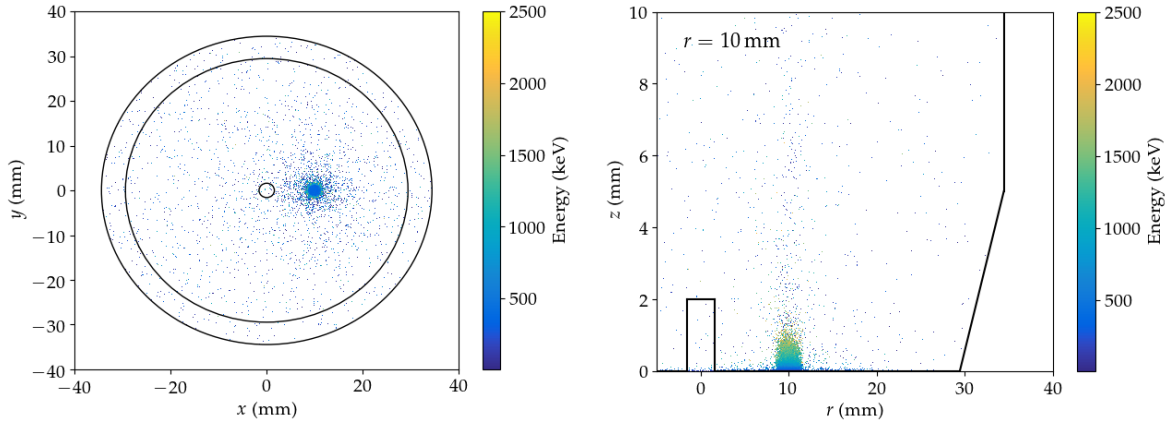

(a) Beam spot in (x, y) plane.

(b) Beam spot in (r, z) plane.

Figure 9.14: Event distribution of the ^{90}Sr beam spot in the (a) (x, y) and (b) (r, z) plane weighted with the event energy (simulated using GEANT4). Most events have penetration depths up to about 1 mm.

NEGATIVE SURFACE CHARGES As for the ^{241}Am simulations, the energy values of all simulated ^{90}Sr events were histogrammed before and after the signal propagation with negative surface charges ($\sigma = -0.3, -0.7 \cdot 10^{10}\,\text{e/cm}^2$), see **Fig.** 9.15. The histograms show that with increasing radial position, the beta event energy degrades, in good qualitative agreement with the measurements, cf. **Ch.** 8.2. For higher absolute surface charges, the degradation is stronger. It should be noted here that there are slight differences in the spectral shape of the measured and the simulated ^{90}Sr energy spectra, particularly at smaller energies. As for the ^{241}Am simulations, this is most likely due to the simplified simulation environment.

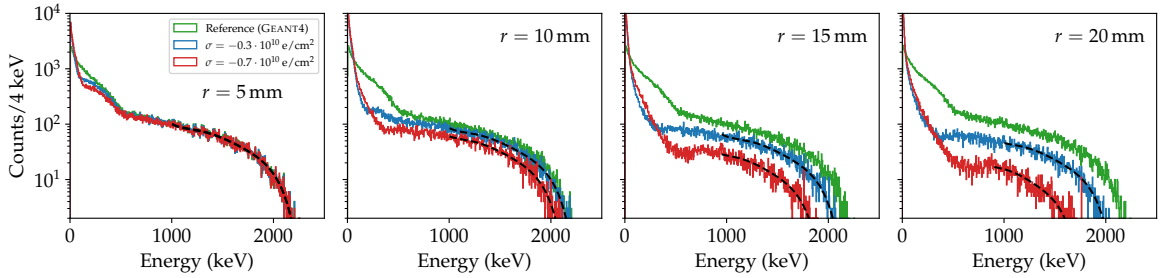

Figure 9.15: Energy histograms of the simulated ^{90}Sr events at selected radial positions. The energy spectra are shown for the cases of no signal propagation (GEANT4 reference, green curve), and for the signal propagation with negative surface charges ($\sigma = -0.3, -0.7 \cdot 10^{10}\,\text{e/cm}^2$) (blue and red curves). To quantify the energy degradation, the spectra were fit with a seventh-order polynomial (black dashed lines). Published in [229].

To quantify the radial dependence, the integral count rate was investigated, see **Fig.** 9.16a. The energy threshold used in the simulation had to be adjusted such that the count rate of the simulation roughly matches the measured rate. Due to the spectral differences and the negligence of effects such as charge diffusion and self-repulsion, a quantitative comparison is not feasible. Instead,

only qualitative statements are derived. As in the measurement, the simulated count rate at small radii first increases (partial shadowing of the beam spot by the PTFE bar) and then decreases. The energy degradation was also quantified in terms of the endpoint degradation of the ^{90}Sr spectra, see **Fig.** 9.16b. To this end, the spectra were fit with a seventh-order polynomial and the endpoint was approximated in a comparable way as for the measurements. Larger deviations between measurement and simulation can be observed at higher radial positions. This might be explained by the fact that at higher radii, the endpoint estimation is rather inaccurate due to large statistical fluctuations in the region of the spectral endpoint [229].

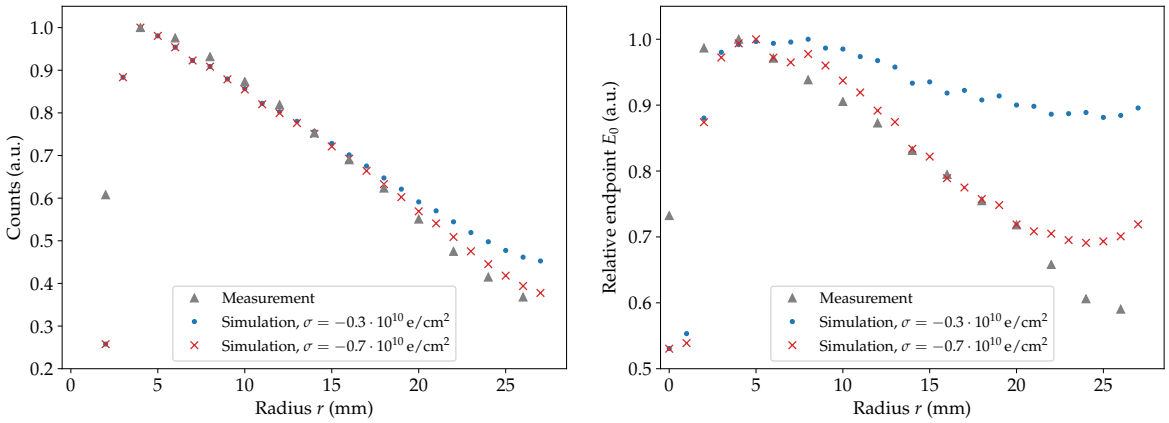

(a) Integral count rate.

(b) Relative endpoints.

Figure 9.16: Comparison of measurement to simulation: (a) integral count rate and (b) relative endpoints of the ^{90}Sr energy spectra. Simulation results are shown for negative surface charges ($\sigma = -0.3, -0.7 \cdot 10^{10}$ e/cm^2). Published in [229].

In the radial ^{90}Sr measurements, two event populations were observed, cf. **Ch.** 8.2. The first population consists of low-energy events which have a decreasing drift time with radius. In contrast, the second population consists of events with higher energies, whose drift time increases with radius, see **Fig.** 8.5. The observed behavior is validated by the ^{90}Sr simulations, see **Fig.** 9.17, and can be explained as follows: Events with a small energy deposition E_{dep} have a small penetration depth z_0, see **Fig.** 9.18. As discussed in **Ch.** 9.2, depending on the actual depth and the amount of surface charges, these events are sensitive to surface effects, particularly to an energy degradation. In contrast, events with a high energy deposition generally have a higher penetration depth. These events are less sensitive to surface effects and most of the charges are collected in the usual behavior, i.e. mainly driven by the collection of holes to the p^+ contact [229].

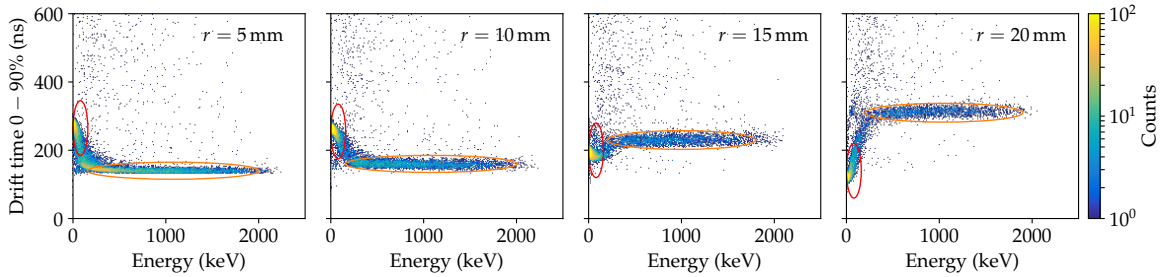

Figure 9.17: Correlation plots of the quantities drift time and energy at selected radial positions of the simulated ^{90}Sr events. Simulation results are shown for negative surface charges ($\sigma = -0.3 \cdot 10^{10}$ e/cm^2). The red vertical and orange horizontal ellipses in the distributions indicate two event populations. Published in [229].

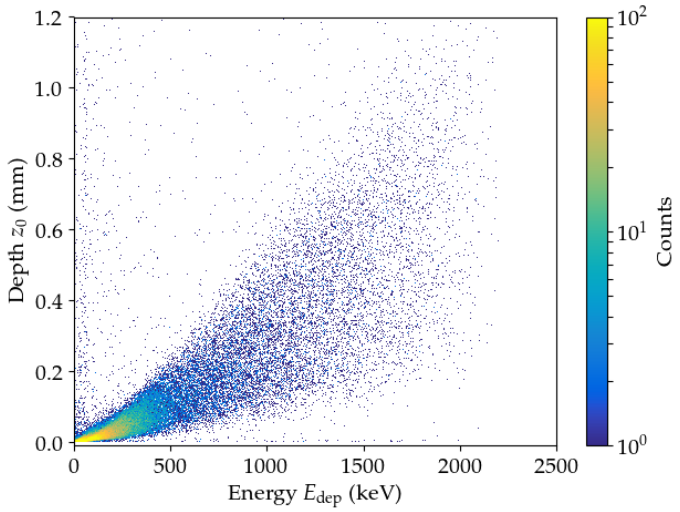

Figure 9.18: Correlation between the deposited energy E_{dep} and the penetration depth z_0 of the simulated ^{90}Sr events (before the signal propagation with surface charges). Most events with a high energy deposition have a high penetration depth. The penetration depth corresponds to the average depth of the different hits for a given event weighted with the hit energies.

POSITIVE SURFACE CHARGES Finally, the impact of positive surface charges on the simulated ^{90}Sr events was investigated. The histogrammed energy values of all simulated events before and after the signal propagation with positive surface charges ($\sigma = +1.0, +3.0 \cdot 10^{10}$ e/cm^2) are shown in **Fig.** 9.19. The histograms show that with decreasing radial position, the beta event energy only degrades slightly. However, compared to a negative charge build-up on the passivated detector surface, the effect is much less pronounced, in good agreement with the observations in the charge collection efficiency maps, cf. **Ch.** 9.2. In particular, higher absolute surface charges are required to be capable of observing the energy degradation.

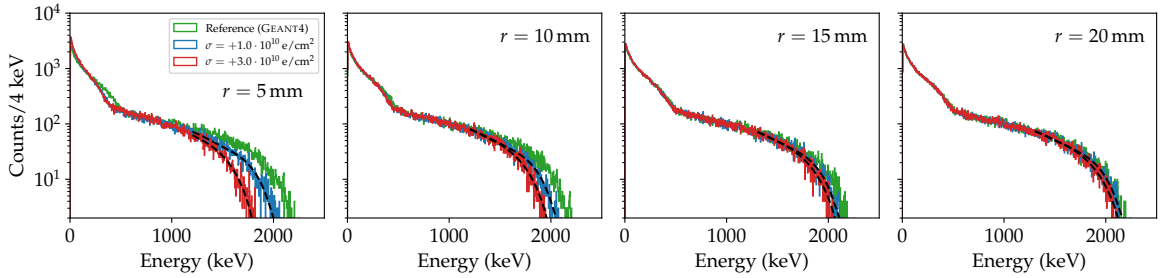

Figure 9.19: Energy histograms of the simulated ^{90}Sr events at selected radial positions. The energy spectra are shown for the cases of no signal propagation (GEANT4 reference, green curve), and for the signal propagation with positive surface charges ($\sigma = +1.0, +3.0 \cdot 10^{10}$ e/cm^2) (blue and red curves). To quantify the energy degradation, the spectra were fit with a seventh-order polynomial (black dashed lines) and the intersection with a fixed value was determined.

The radial dependence was again characterized in terms of the integral count rate (in the energy range up to 3 MeV, excluding zero-energy events) and the degradation of the spectral endpoint, see **Fig.** 9.20. At small radial positions, due to a partial shadowing of the beam spot by the PTFE bar, the count rate increases. At higher radii, the count rate remains approximately constant. The energy degradation can be best observed in the region of the spectral endpoint. With increasing radial position, the endpoint energy increases. For higher absolute surface charges, the effect is slightly stronger, particularly at smaller radii.

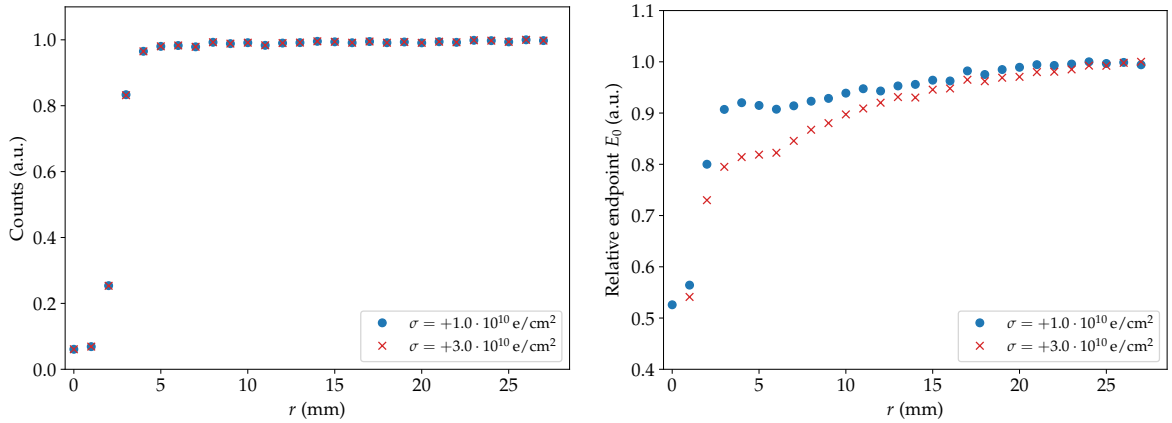

(a) Integral count rate.

(b) Relative endpoints.

Figure 9.20: (a) Integral count rate and (b) relative endpoints of the simulated ^{90}Sr energy spectra. Simulation results are shown for positive surface charges ($\sigma = +1.0, +3.0 \cdot 10^{10}$ e/cm^2).

9.3.4 *Impact of diffusion and self-repulsion*

For the surface event simulations carried out in the scope of this work single point charges were used to model surface alpha and beta effects. Estimates of energy degradation, and of other pulse shape parameters such as drift time, A/E, etc. were extracted and could reproduce the measurement results qualitatively very well. However, when trying to reproduce the measured alpha superpulse waveforms [249], cf. **Ch.** 7.2, it was realized that thermal diffusion and Coulomb self-repulsion effects between charge carriers could have a significant impact [237]. Since these processes lead to an increase of the charge cloud size during its evolution, they are of particular importance for the investigation of detector surface effects. In the case of diffusion, the size of the charge cloud can be described in terms of a Gaussian width σ_D [217]:

$$\sigma_D = \sqrt{2Dt}, \tag{9.2}$$

where D denotes the diffusion coefficient, and t the time. In general, the coefficient D has a transverse and a longitudinal component, i.e. the charge cloud has a different diffusion coefficient perpendicular to the drift than it does along the drift. The charge cloud size evolution due to self-repulsion can be described in terms of the width σ_R [217]:

$$\sigma_R = \sqrt[3]{\frac{3\mu e}{4\pi\epsilon} Nt}. \tag{9.3}$$

Here, μ describes the charge carrier mobility, ϵ the permittivity in germanium, and N the number of charge carriers. For interactions close to the (passivated) detector surface, the transverse diffusion component together with self-repulsion has an important impact. Depending on the deposited energy, the transverse charge cloud size grows very quickly (faster for higher interaction energies). In contrast, the longitudinal component has a smaller impact (the longitudinal diffusivity is low at a high electric field) [250]. Therefore, the charge cloud size essentially spreads out in two of the three directions leading to a disc-like charge cloud. If the charges are now drifting parallel to the surface, the diffusion component perpendicular to the drift at some point pushes the upper half of the charge cloud onto the surface. Due to the disc-like structure, this will result in a smear of charges on the surface that are trapped. The lower half of the charge cloud first moves away from the surface and drifts further before being collected or trapped. This results in a modified charge collection behavior compared to the case of point charges neglecting the effects of diffusion and self-repulsion [229].

First attempts have been made to include these effects in PSS [237]. However, for several reasons this is very challenging. The (three-dimensional) charge density distributions for both electrons and holes, need to be evolved simultaneously. At each time step, a self-consistent electric field has to be recalculated. Moreover, a fine computational grid ($\mathcal{O}(20\,\mu m)$) and short simulation time

steps ($\mathcal{O}(0.2\,\mathrm{ns})$) are required. From the computational point of view, these requirements are very challenging and serious approximations, e.g. two-dimensional calculations, are needed to make the simulations tractable [229, 237].

9.4 CONCLUSIONS

An extensive simulation campaign was conducted to better understand the results obtained in the PPC detector surface characterization measurements with alpha and beta particles. In a first step, charge collection efficiency maps were simulated. They comprehensively illustrated the impact of a charge build-up on the passivated detector surface on various pulse shape parameters. One of the main results was that 1) for a higher absolute amount of surface charges, 2) for a lower detector bias voltage, and 3) for a higher detector temperature, the charge collection loss region extends further into the detector bulk. While alpha particles with small penetration depths are always sensitive to this region and thus to surface effects, beta particles with high penetration depths are only partially affected. It was also shown that the surface effects are much less pronounced in the case of positive surface charges.

In the next step, Monte Carlo simulations in combination with pulse shape simulations were performed. The radial-dependent behavior of the energy and the DCR parameter observed in surface alpha characterization measurements for both negative and positive surface charges, could be reproduced in dedicated ^{241}Am simulations. Moreover, a good qualitative agreement between measurement and simulation was obtained for the A/E vs DCR distributions. This supports the validity of the surface charge model to explain the measurement results. In the scope of ^{90}Sr simulations, the radial energy dependence observed in the surface beta characterization measurements could be reproduced. Furthermore, the existence of two distinct event populations could be validated: one being sensitive to surface effects, the other one being subject to the normal charge collection behavior.

Part III

DEVELOPMENT OF SIGNAL READOUT ELECTRONICS FOR LEGEND

Signal readout electronics in close proximity to the germanium detectors plays a major role in maximizing the experiment's discovery sensitivity by reducing electronic noise and improving pulse shape analysis (PSA) capabilities for the rejection of backgrounds. However, the proximity also poses unique challenges for the radiopurity of the electronics. One of the main goals of this work is the development and characterization of readout electronics for LEGEND. In LEGEND-200, a novel readout scheme based on former implementations will be used. Within this work, calibration and physics data of a first full chain integration test are analyzed. It is shown that the novel readout system features an excellent performance. For LEGEND-1000, backgrounds must be decreased even further. To reduce the component originating from the readout electronics, the use of an application-specific integrated circuit (ASIC) amplifier is foreseen. In this work, the properties and electronic performance of a commercially available ASIC together with a PPC detector are investigated. It is shown that low noise levels and excellent energy resolutions can be obtained. In addition, the viability of PSA techniques is demonstrated.

10

SIGNAL READOUT ELECTRONICS

This chapter discusses the basics of signal readout electronics for HPGe detectors. In **Ch.** 10.1, the readout architecture typically used in ^{76}Ge-based $0\nu\beta\beta$ decay searches will be presented. **Ch.** 10.2 focuses on the operating principle of a charge sensitive amplifier. Finally, electronic noise will be discussed in detail in **Ch.** 10.3. This includes the description of various noise sources, their mitigation, and a mathematical framework for noise analyses.

10.1 SIGNAL READOUT ARCHITECTURE

The typical readout chain of radiation measurements with HPGe detectors is illustrated in **Fig.** 10.1. The detector, operated as a diode with a reverse bias voltage applied, is followed by a charge sensitive amplifier (CSA). In ^{76}Ge-based $0\nu\beta\beta$ decay searches, the detector and (parts[1] of) the CSA are typically operated in a cryogenic environment (LAr or LN_2 temperature). The amplified signals are then acquired through analog or digital signal processing. In the analog chain, the output signals of the amplifier are first shaped and then processed, for example by means of a multichannel analyzer (MCA). Usually, the shaping options (filters, shaping times) are rather limited. In contrast, in the digital chain, the raw signals are recorded with an FADC. The digitized waveforms can then be post-processed offline. A major advantage of digital signal processing is its enormous flexibility. In particular, it allows to analyze the data with a wide variety of shaping filters. In addition, PSD techniques can be applied which is important to effectively reject backgrounds, cf. **Ch.** 4.1.2.

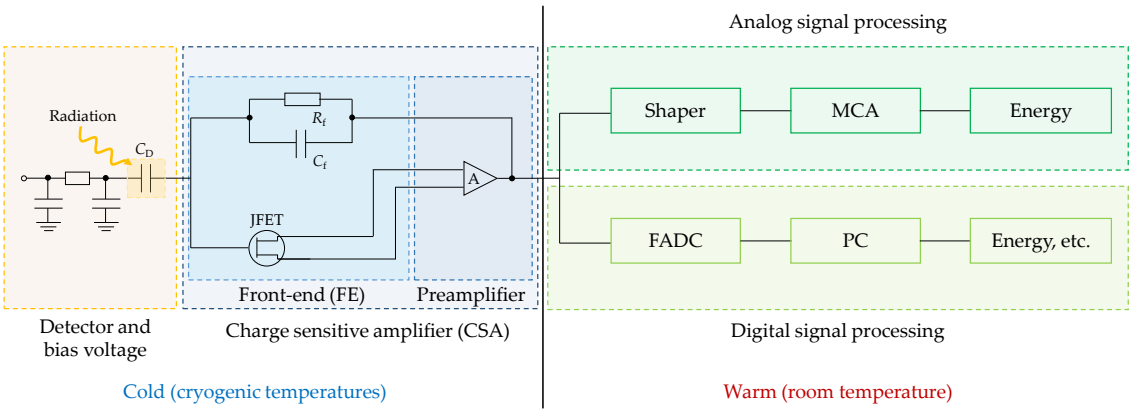

Figure 10.1: Typical readout chain of radiation measurements with a HPGe detector. The detector and bias voltage section is followed by the charge sensitive amplifier. In $0\nu\beta\beta$ decay searches, it typically consists of a front-end stage located close to the detector, and of a second-stage preamplifier farther away. The amplified signal is acquired through an analog or a digital signal processing.

10.2 CHARGE SENSITIVE AMPLIFIERS

Since the charge liberated by the incident radiation in a HPGe detector is usually very small, it needs to be amplified before it can be processed further by analog or digital circuits. In ^{76}Ge-based $0\nu\beta\beta$ decay searches, the CSA is typically divided into two stages: a first stage located close to

1 In the MAJORANA DEMONSTRATOR, the second-stage preamplifier was operated at room temperature.

the detector, the front-end (FE) electronics stage, and further amplification stages farther away. The front-end electronics stage improves the noise performance of the setup due to the minimization of stray input capacitance which mainly originates from interconnections and increases with cable length. In practice, the stage consists of a junction gate field-effect transistor (JFET) coupled to a feedback circuit, see **Fig.** 10.1. The feedback circuit in turn consists of a feedback capacitor C_f between the input and output integrating the charge from the detector. Moreover, a feedback resistor R_f in parallel to the capacitor is typically used to continuously reset the amplifier (a second type of reset mechanism will be discussed in **Ch.** 10.2.4). This is necessary to avoid a saturation of the dynamic range of the readout electronics. As a result, after full charge collection, the preamplifier output waveform is characterized by an exponential decay back to the baseline with a time constant of

$$\tau \approx R_f C_f. \tag{10.1}$$

10.2.1 *Requirements for 0νββ decay experiments*

Amplifiers deployed in 0νββ decay searches have to fulfill stringent requirements. First, the CSA should be located as close as possible to the detector. This reduces the capacitive load on the amplifier as well as the pickup noise and is necessary to keep the electronic noise of the system low. High noise levels increase the energy threshold and degrade the energy resolution, thereby decreasing the experimental sensitivity, cf. **Ch.** 2.4.3. Another advantage of close proximity of the CSA to the detector is the enhanced bandwidth of the system, i.e. faster signal rise times, which are important for the successful application of PSD techniques. These noise and rise time requirements are in conflict with the radiopurity requirements. The components close to the detectors contribute to the radioactive background budget and thus decrease the experimental sensitivity. It is therefore desirable to have as little material as possible close to the detectors. Consequently, the material mass and the volume of the CSA must be very small. In addition, the selected components must be very radiopure. In conclusion, one has to find a good compromise between low noise levels and fast rise times on the one hand, and low radioactivity of the components close to the detectors on the other [16]. To be capable of detecting signal events over a wide energy range (up to 10 MeV), the CSA needs to have a large dynamic range. In addition, it must be capable of driving (differential) output signals into a large capacitance (long cables). Another requirement in ^{76}Ge-based 0νββ decay searches is that the CSA must be compatible with a range of different detectors (different capacitances).

In LEGEND-200, the CSAs together with the detectors will be operated at cryogenic temperatures in LAr, cf. **Ch.** 4.3.1. There are several commercially available amplifiers that fulfill the stringent noise and bandwidth requirements discussed above. However, only few CSAs can be operated at cryogenic temperatures. The main challenge of designing an amplifier working at these temperatures is that typically the electronic behavior of components below temperatures of $T \lesssim 230\,K$ is not specified. The components need to have a high reliability, i.e. they need to withstand many thermal cycles from room to cryogenic temperature and vice versa. In addition, they need to be robust against electrostatic discharges, particularly when the electronics is connected to the detectors. Consequently, the mechanical component integrity and the electrical performance have to be tested thoroughly. Operation at cryogenic temperatures also requires a relatively low power consumption of the CSA. This is necessary to avoid bubble formation due to local boiling of the cryogenic liquid which could lead to microphonic noise. Further details of the signal readout electronics for LEGEND-200 will be discussed in **Ch.** 11.

10.2.2 *Junction gate field effect transistors*

In LEGEND-200, a junction gate field-effect transistor (JFET) will be used as an amplification device in the front-end electronics stage. The JFET is a voltage-controlled electronic device manufactured from semiconductor materials. It has three terminals: gate, source, and drain. The path between the source and drain terminals is called channel and is made from n-type or p-type semiconducting material[2]. By applying a reverse bias voltage to the input terminal (gate), the channel is pinched. Thereby, the current flowing through the channel (drain-source current) can be controlled. The

2 Typically, n-channel JFETs have a higher conductivity since electrons have a higher mobility than holes [192].

possibility of changing the electrical conductivity with the applied voltage can be exploited to amplify or switch electronic signals.

A JFET as an amplification device has several advantages. Due to the high input impedance of the gate terminal (ensuring that all charge is collected on the feedback capacitance), the device draws very little current on its inputs. Consequently, JFETs have a low power consumption and dissipate little heat which makes them amenable to miniaturization and dense packing in integrated circuits (ICs) [251]. Moreover, when cooled, JFETs have a low electronic noise ($1/f$ noise and series noise, cf. **Ch.** 10.3) [252]. Finally, due to the possibility of in-die production (no additional chip packaging), they can have a high radiopurity.

10.2.3 *Application-specific integrated circuit (ASIC) technology*

In ^{76}Ge-based $0\nu\beta\beta$ decay searches, the JFET amplifier has been the traditional choice for front-end electronics [225, 252–254]. Metal-oxide semiconductor field effect transistors (MOSFETs) have a similar operating principle as JFETs but allow for the integration of the complete CSA and additional signal processing stages into a single chip [252]. Compared to JFETs, MOSFETs have a gate that is insulated electrically from the drain-source channel by a thin layer of metal-oxide. This makes their input impedance even higher compared to JFETs. In contrast, they tend to have higher $1/f$ noise factors, cf. **Ch.** 10.3.2, than their JFET counterparts [252, 255]. MOSFET circuits are typically custom-designed and realized using CMOS processes.

CMOS TECHNOLOGY The term complementary metal-oxide semiconductor (CMOS) describes a technology for the fabrication of ICs. It is characterized by the complementary use of n-type and p-type MOSFETs (nMOSFET and pMOSFET) in a single substrate. Usually, CMOS technology is used in digital electronics. However, due to its convenience, it is gaining more importance in analog electronics as well. CMOS devices are characterized by low electronic noise levels, a low power consumption, and high speeds. The production process is commonly specified in terms of the size of the smallest component (transistor) in a chip. Common sizes such as 250 nm, 180 nm, and 65 nm are widely available and cheap. The smaller the components, the less is the power consumption, the higher is the speed (circuit delays decrease), and the less space is required. On the other hand, decreasing the component size also decreases the maximum supply voltage and hence the dynamic range. Furthermore, the production costs increase as the component sizes decrease. The noise performance of the device remains unaffected by changing the size [192].

ASIC TECHNOLOGY The term application-specific integrated circuit (ASIC) refers to an IC customized for a particular use, rather than intended for general-purpose use. Commonly, ASICs are designed and produced using CMOS technology. The development of a specialized ASIC is often costly and time-consuming. The chip design is mainly based on circuit simulations in which several design rules have to be obeyed. Several design cycles (including prototype productions) are typically needed before a final version of the chip is obtained. After every cycle, the performance is reviewed and the reliability, as well as the robustness are optimized. There are three different types of ASICs: 1) digital, 2) analog, and 3) mixed-signal:

1) Digital ASICs are usually programmable and allow for an external control of various electronic parameters. Nowadays, they are the most commonly used ASICs.

2) The electronic parameters of analog ASICs, on the other hand, cannot be controlled externally. Due to their limited flexibility, they can only be found in very few specific applications, e.g. for CSAs. Their advantages are the absence of digital noise (e.g. switching noise from electronic clocks), and a high reliability.

3) In mixed-signal ASICs, digital and analog circuitry is coexisting in the same chip.

In the context of $0\nu\beta\beta$ decay searches, ASIC technology as signal readout electronics provides the unique possibility to further reduce the radioactive mass close to the detectors, while maintaining or even improving the spectral and noise performance achieved with conventional amplifiers. The electronics baseline design of LEGEND-1000 envisages the use of a custom-designed analog ASIC readout scheme [136].

10.2.4 *Preamplifier reset technologies*

In order to avoid saturation and a reduction of the dynamic range of the CSA, it needs to be reset appropriately. While traditional signal readout electronics devices are commonly reset via a continuous reset, ASICs are often reset via a pulsed reset, see **Fig.** 10.2. In the continuous reset mode, the reset of the preamplifier is realized by a feedback resistor (R_f) in parallel with the feedback capacitor (C_f). As discussed in **Ch.** 10.2, this results in an exponential decay of every signal pulse with a time constant $\tau \approx R_f C_f$. In contrast, in the pulsed reset mode, the preamplifier is reset externally, see **Fig.** 10.2. Commonly, an external logic signal (rectangular pulse) is used to control a CMOS transistor to discharge the feedback capacitor. The reset rate strongly depends on the count rate, and on the leakage current of the detector. Waveform examples for both reset modes are shown in **Fig.** 10.3.

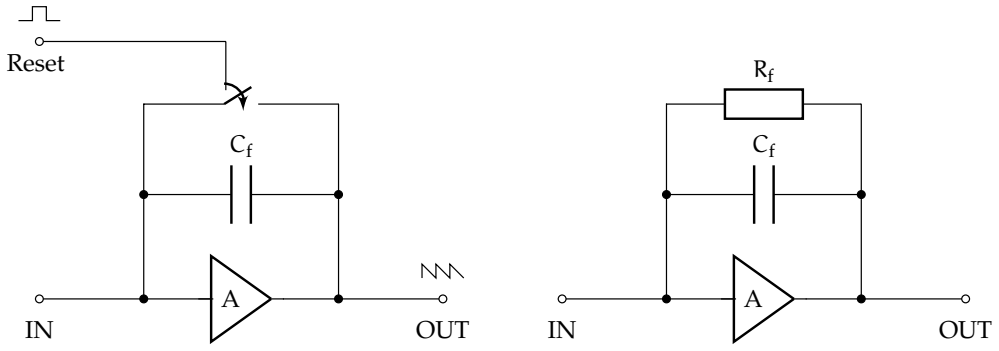

(a) Pulsed reset. (b) Continuous reset.

Figure 10.2: Preamplifier reset via (a) pulsed reset and (b) continuous reset. In the pulsed reset mode, the feedback capacitor is discharged by an external logic signal. In contrast, in the continuous reset mode, a feedback resistor in parallel to the feedback capacitor resets the preamplifier.

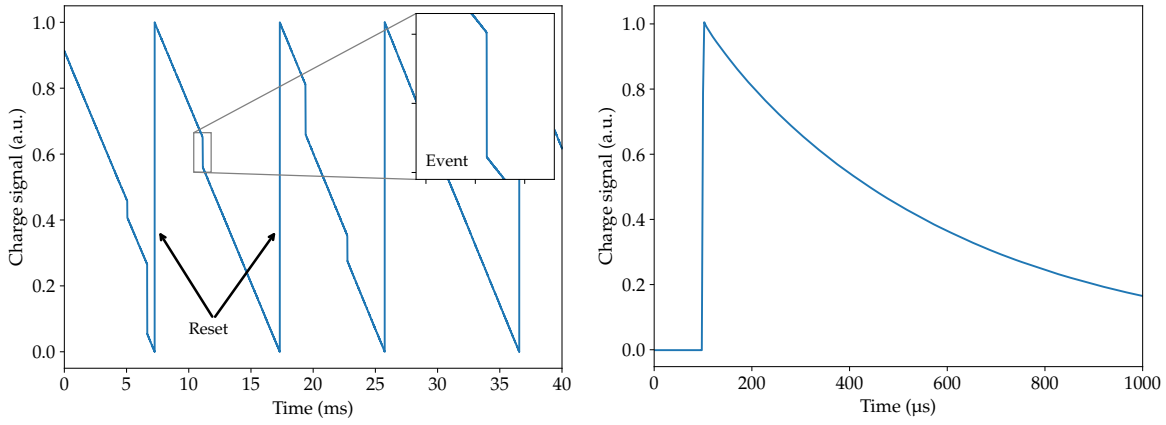

(a) Pulsed reset. (b) Continuous reset.

Figure 10.3: Waveform examples of (a) the pulsed reset mode and (b) the continuous reset mode. Events in the pulsed reset mode can be identified as steps in the linearly decreasing ramps (see inset). Since there is no feedback resistor removing the charges from the feedback capacitance, every event decreases the preamplifier output to a lower voltage. As soon as the dynamic range of the CSA is reached, it is reset back to the starting value by an external device. The reset events can be identified as the large positive steps between the decreasing ramps. In the continuous reset mode, the reset is realized by a feedback resistor resulting in an exponentially decaying pulse with a certain decay time.

Advantages of the pulsed reset mode encompass the absence of exponentially decaying waveforms (no pole-zero correction required), a better noise performance (no parallel noise from the feedback

resistor), and a higher radiopurity (no feedback resistor). On the other hand, every reset is accompanied by a recovery time of typically a few µs increasing the dead time of the measurement system. In addition, synchronizing resets in systems consisting of many detectors might be problematic.

At the time of writing of this thesis, only a few DAQ systems were compatible with the pulsed reset mode. For measurements conducted in the pulsed reset mode in this work, this aspect was bypassed by using an AC (capacitive) coupling element interconnected between the preamplifier output and the DAQ system input, see **Fig.** 10.4. The AC coupling acts as an RC high-pass filter. Effectively, it differentiates the pulsed reset signals with a certain time constant, thereby transforming them into continuous reset-like signals.

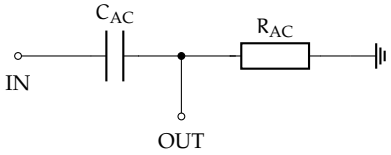

Figure 10.4: AC coupling to transform pulsed reset events into continuous reset-like events. The capacitive coupling filters out the DC component of a signal. It is realized by inserting a capacitor C_{AC} in series with the signal. The resistor R_{AC} is realized by 50 Ω termination of the transmission line.

10.3 ELECTRONIC NOISE

10.3.1 *Overview*

Electronic noise describes unwanted random fluctuations superimposed upon electrical signals. It is present to some extent in all electronic systems. In the context of readout electronics, noise leads to a degradation of the information carried by the signals. In particular, it worsens the energy resolution and hence the ability of the system to distinguish signal from background events. Two mechanisms contribute to the total noise [256]:

1) Random fluctuations of the charge carrier velocities due to thermal motion (e.g. thermal noise).
2) Random fluctuations of the charge carrier number (e.g. 1/f noise, shot noise).

For CSAs, electronic noise is commonly expressed in terms of the root mean square (RMS) voltage of the signal baseline. Due to the randomness of noise, its distribution is typically Gaussian. The critical parameter is the total capacitance in parallel with the input of the amplifier. By reducing the input capacitance of the CSA, the signal-to-noise ratio can be enhanced.

10.3.2 *Noise sources*

THERMAL NOISE One of the main noise sources in detector electronics is thermal noise (also called Johnson or Nyquist noise). It is caused by the random thermal motion (Brownian motion) of free charge carries and is intrinsic to all conductors, even if no voltage is applied. At microwave frequencies and lower, thermal noise is Gaussian and its amplitude in terms of RMS can be described by the Rayleigh-Jeans approximation [251]:

$$V_n = \sqrt{4 k_B T R}, \tag{10.2}$$

where k_B denotes the Boltzmann constant, T the temperature, and R the resistance of the conductor. Thermal noise power is independent of the frequency and is thus also called white or broadband noise. White noise is characterized by equal contributions from the whole frequency range. The noise in **Eq.** (10.2) is expressed in units of $V/\sqrt{Hz}$. This means that the amplitude of the fluctuations depends on the range of frequencies the system is sensitive to, the so-called bandwidth. The RMS noise fluctuations in terms of volts are obtained by assuming a finite bandwidth B of the considered system so that [251]

$$V_{RMS} = V_n \cdot \sqrt{B}. \tag{10.3}$$

As can be seen from **Eq.** (10.3), thermal noise increases with the square root of bandwidth. Hence, by decreasing the bandwidth of the considered system, thermal noise can be reduced. In a HPGe detection system, various thermal noise sources can be encountered, e.g. Johnson noise in the feedback resistor.

1/f NOISE Many dynamical systems (not limited to electrical ones) exhibit noise that decreases with frequency f according to a power law:

$$P(f) \propto f^{-k}, \tag{10.4}$$

with k typically being close to unity. This low-frequency noise is called $1/f$ noise (also Flicker or pink noise). It is often characterized by a corner frequency denoting the frequency for which it becomes comparable to the white noise in the system [251].

SHOT NOISE The electrical current I is quantized in units of electron charge e. At a given node of a circuit, current fluctuations are expected since the charge carriers arrive at random times. These statistical fluctuations of the number of charge carriers are referred to as shot noise. Just as thermal noise, shot noise is broadband noise that can be described by a Gaussian distribution. The amplitude ΔI_{RMS} of the current fluctuations in terms of RMS can be approximated as [251]

$$\Delta I_{RMS} = \sqrt{2eIB} \tag{10.5}$$

which is valid for frequencies up to I/e. **Eq.** (10.5) shows that the relative contribution of shot noise increases with decreasing current:

$$\frac{\Delta I_{RMS}}{I} \propto \frac{1}{\sqrt{I}}. \tag{10.6}$$

This means that at small currents shot noise can become the dominant source of noise. In signal readout electronics, shot noise is only relevant in the first stages of a CSA, where small signals are amplified [251]. An example in HPGe detection systems is the JFET in the front-end stage.

ELECTROMAGNETIC INTERFERENCE Noise originating from external sources outside the circuit can be attributed to electromagnetic interference (EMI). Cables and circuit components act like antennas and can pick up noise from stray electromagnetic fields around them. An important example of EMI is 50 Hz mainline noise (60 Hz in the USA) which can also show up at harmonics (100 Hz, 150 Hz, etc.). Another example is the noise introduced by modern power supplies converting AC to DC via rapid switching of voltages. This can be mitigated by using linear power supplies [251].

10.3.3 *Mathematical formalism*

The electronic noise measured at the output of a CSA is commonly expressed in terms of the equivalent noise charge (ENC). The quantity describes the amount of charge (number of electrons) that injected by a delta-like pulse leads to a signal at the amplifier output whose amplitude equals the RMS noise, i.e. the amount of charge that makes the signal-to-noise ratio equal to one. The ENC is composed of three uncorrelated quantities that include the noise sources described in **Ch.** 10.3.2. More specifically, it is a sum of the parallel, series, and $1/f$ noise [224]:

$$ENC^2 = ENC_p^2 + ENC_s^2 + ENC_{1/f}^2. \tag{10.7}$$

In the context of a HPGe detection system, the signal and noise sources can be modeled as depicted in **Fig.** 10.5. While the detector is modeled as a capacitor with capacitance C_D, the current signal is modeled as a delta-like charge pulse $I(t) = Q\delta(t)$. The charge is delivered to the detector capacitance, as well as to the input capacitance C_i of the CSA. The output signal transmitted to the digitizer can be interpreted as the output of a noiseless preamplifier with gain A in parallel to a current noise generator, and in series to a voltage noise generator [94, 224].

PARALLEL NOISE The parallel noise ENC_p^2 is associated with noise currents flowing into the input circuit. It is dominated by the detector leakage current and the thermal noise induced by the feedback resistor and can be expressed as [256]

$$ENC_p^2 \propto \left(2eI_T + \frac{4k_BT}{R_f}\right)\tau_s. \tag{10.8}$$

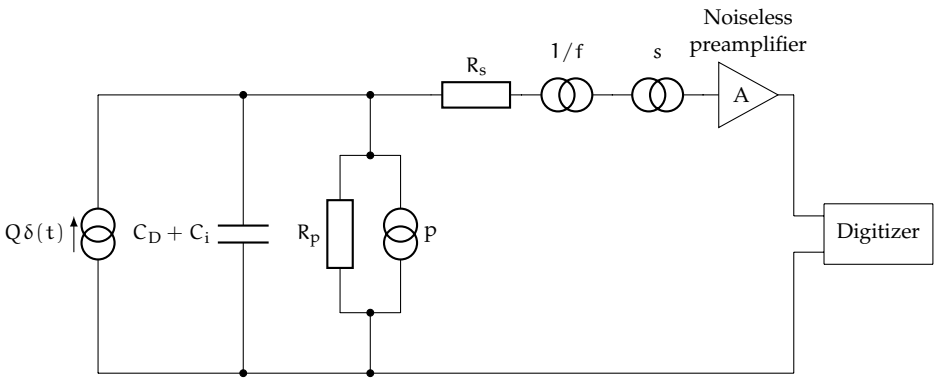

Figure 10.5: Signal and noise sources in the readout system of a HPGe detector. The output signal transmitted to the digitizer is modeled as the output of a noiseless preamplifier, connected to a detector with capacitance C_D, a series voltage generator (index s), and a parallel current generator (index p). The current signal is modeled as a delta-like charge pulse $Q\delta(t)$, and the CSA input capacitance is denoted as C_i. Plot idea from [224, 257].

Here, I_T denotes the total current, k_B the Boltzmann constant, T the operational temperature of the feedback resistor, R_f the feedback resistance, and τ_s a characteristic shaping time of the selected shaping filter. The total current is proportional to the sum of the detector leakage current I_L and the gate current I_G of the JFET in the input stage of the CSA [192, 224]. While the latter component is usually negligible, the leakage current component can be minimized by reducing the operating temperature of the detector, cf. **Ch.** 3.2. The parallel noise can be also reduced by using a resistor with a high feedback resistance. On the other hand, too high a feedback resistance results in a long decay time of the signal pulse, cf. **Eq.** (10.1), which can lead to pile-up. Consequently, a compromise between reasonably low parallel noise and a moderate decay time has to be found.

SERIES NOISE The series noise ENC_s^2 originates from sources in series with the detector signal. The dominant contribution is due to shot noise in the JFET. It can be expressed as [256]

$$ENC_s^2 \propto \frac{4k_BT}{g_m}\frac{C_T^2}{\tau_s}, \tag{10.9}$$

where g_m is the transconductance of the JFET, and C_T the total capacitance. The transconductance is the ratio of the drain current fluctuation and the gate-source voltage fluctuation. The total capacitance is the sum of the detector capacitance C_D, the input capacitance C_i of the CSA, and the feedback capacitance C_f [224]:

$$C_T = C_D + C_i + C_f. \tag{10.10}$$

Typically, the detector capacitance is the dominating term [251]. As can be seen from **Eq.** (10.9), the series noise can be minimized by reducing the total capacitance. This is the reason why detectors with a low capacitance are used preferentially. Moreover, the series noise component can be reduced by choosing a JFET with a high transconductance, and operating it at low temperatures.

1/f NOISE The 1/f noise is independent of the shaping time and is typically subdominant [251]. It can be expressed as [256]

$$ENC_{1/f}^2 \propto A_f C_T^2. \tag{10.11}$$

Here, A_f is a 1/f noise factor depending on the dielectric properties and the fabrication process of the specific JFET [252].

OPTIMAL SHAPING TIME As can be seen from **Eqs.** (10.8) and (10.9), the electronic noise strongly depends on the chosen shaping time. While the parallel noise is proportional to it ($ENC_p^2 \propto \tau_s$), the series noise is inversely proportional to it ($ENC_s^2 \propto 1/\tau_s$). Consequently, the shaping time can

be optimized such that the sum of the parallel and series noise components is minimal. This is applicable to any chosen shaping filter [251]. If we define the pre-factors as

$$A := \frac{4k_B T}{g_m} C_T^2 \quad \text{and} \quad B := 2eI_T + \frac{4k_B T}{R_f}, \tag{10.12}$$

then the optimal shaping time τ_s^* is given by

$$\tau_s^* \propto \sqrt{\frac{A}{B}}. \tag{10.13}$$

In practice, the optimal shaping time is obtained by investigating the ENC as a function of shaping time. This procedure is commonly referred to as noise sweep and results in a noise curve. An example of a typical noise curve is shown in **Fig.** 10.6.

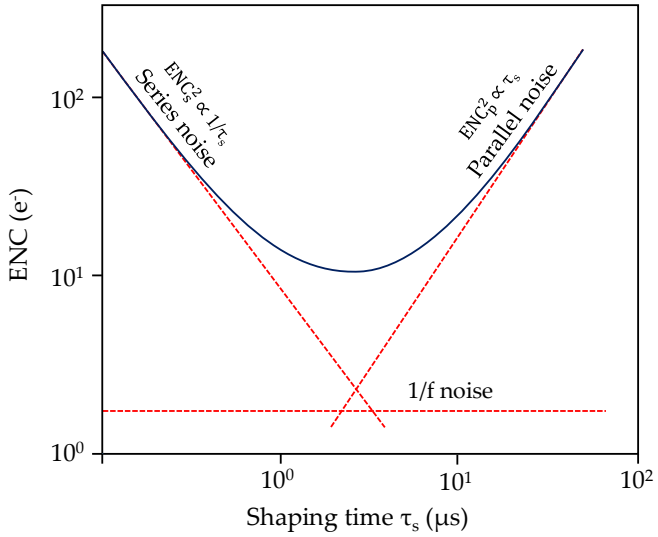

Figure 10.6: Noise curve example showing the equivalent noise charge (ENC) as a function of the shaping time. To minimize the electronic noise, the shaping time of the shaping filter needs to be optimized. For too short (long) a shaping time, the series (parallel) noise term dominates. Plot idea from [94, 251].

10.3.4 *Noise mitigation*

To reduce the electronic noise sources discussed in the previous sections and to enhance the signal detection efficiency in a radiation detection system, appropriate noise mitigation and reduction strategies are of major importance. Many noise sources can be eliminated by deploying proper grounding and shielding. The ground defines the reference potential for all voltages in an electronic circuit. In complex circuits, grounding noise can arise from potential differences between different ground connections, i.e. ground loops. They can be mitigated by bringing all ground connections to the same potential to a single common node (star grounding). Another effective means of reducing noise is to use shielded cables such as coaxial cables. The shielding acts as a Faraday cage and isolates the circuit from external noise sources such as electromagnetic interference.

10.3.5 *Energy resolution*

The energy resolution of a HPGe detection system depends on the electronic noise of the signal readout electronics, on statistical fluctuations in the charge production process, and on the efficiency of the charge collection process in the crystal. Moreover, the data analysis procedures in post-processing have an impact (e.g. shaping filter and settings, quality cuts, calibration procedure, etc.). From the theoretical point of view, the energy resolution ΔE is defined in terms of the FWHM of a given

gamma line in the energy spectrum. The contribution of the electronic noise to the line width (in units of keV) is a constant that is independent of the energy [94]:

$$w_{\mathrm{ENC}} = 2\sqrt{2\log 2} \cdot \frac{\epsilon}{e} \cdot \mathrm{ENC}. \tag{10.14}$$

Here, ϵ denotes the average energy necessary to create an electron-hole pair in germanium. A second contribution to the energy resolution is given by the charge production process in the crystal which is characterized by statistical fluctuations in the number of produced electron-hole pairs [94]. The average number N of electron-hole pairs created in a particle interaction is given by the ratio of the absorbed energy E and the average energy ϵ:

$$N = \frac{E}{\epsilon}. \tag{10.15}$$

Assuming Poissonian statistics, the uncertainty σ_N on the average number N can be expressed as:

$$\sigma_N = \sqrt{N} = \sqrt{\frac{E}{\epsilon}}. \tag{10.16}$$

This implies that the uncertainty σ_E of the absorbed energy is given by

$$\sigma_E = \sigma_N \epsilon = \sqrt{\epsilon E}. \tag{10.17}$$

If we further consider a material-dependent Fano factor F to account for the not purely Poissonian nature [258], the charge production process contributes with a width of [94]

$$w_{\mathrm{CP}} = 2\sqrt{2\log 2} \cdot \sqrt{\epsilon F E}. \tag{10.18}$$

Although various measurements have been conducted, the Fano factor for germanium is not yet known precisely. Recently published values lie in the range $0.05 \leqslant F \leqslant 0.11$ [259–262]. The last component contributing to the spectral line width is the charge collection efficiency of the detector and readout system, and the charge integration properties of the shaping filter. The charge collection and integration term can be described by the empirical formula [94]

$$w_{\mathrm{CC}} = 2\sqrt{2\log 2} \cdot c \cdot E, \tag{10.19}$$

where c is a constant factor. Summing the terms $w_{\mathrm{ENC}}, w_{\mathrm{CP}}$ and w_{CC} in quadrature (they are statistically uncorrelated), the following expression is obtained for the energy resolution:

$$\mathrm{FWHM}(E) = \sqrt{w_{\mathrm{ENC}}^2 + w_{\mathrm{CP}}^2 + w_{\mathrm{CC}}^2} \tag{10.20}$$

$$= 2\sqrt{2\log 2}\sqrt{\frac{\epsilon^2}{e^2}\mathrm{ENC}^2 + \epsilon F E + c^2 E^2}. \tag{10.21}$$

While at low energies the electronic noise dominates, the charge collection term takes over at higher energies. This implies that minimizing the electronic noise is crucial when measuring at low energies. The three terms in **Eq.** (10.21) represent a lower limit on the energy resolution and give rise to a purely Gaussian peak. Sources of resolution loss and a deviation from the Gaussian peak shape include imperfect charge collection in the crystal, ballistic deficit, etc.

11

SIGNAL READOUT ELECTRONICS FOR LEGEND-200

In this chapter, the signal readout electronics for LEGEND-200 will be discussed. An overview of the readout architecture is given in **Ch.** 11.1. First results of the Post-GERDA Test are presented in **Ch.** 11.2. **Ch.** 11.3 focuses on the characterization of a backup CSA for LEGEND-200. Finally, the main measurement results are summarized in **Ch.** 11.4.

11.1 OVERVIEW

For the signal readout electronics in LEGEND-200, the expertise gained in implementations by the predecessor experiments, GERDA and MAJORANA DEMONSTRATOR, was channeled to develop a novel, fully custom-designed readout system. **Fig.** 11.1 shows a simplified illustration of the LEGEND-200 readout scheme. To optimize the noise performance and to obtain low detection thresholds, the CSA is divided into two stages. A first stage very close to the detectors (several cm) is based on the radiopure low-noise, low-mass front-end (LMFE) readout electronics of the MAJORANA DEMONSTRATOR [263]. It is a resistive-feedback device consisting of a JFET amplifier, a feedback capacitor (C_f), and a feedback resistor (R_f). A second stage farther away ($\sim 0.3 - 1.5$ m

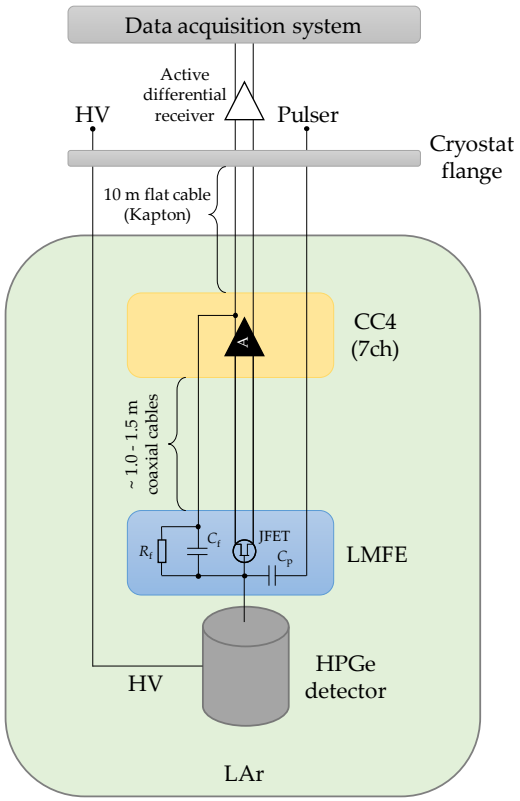

Figure 11.1: Simplified illustration of the readout scheme in LEGEND-200. The HPGe detectors together with the signal readout electronics are operated in LAr. The electronics consists of a first-stage low-noise, low-mass front-end (LMFE), and of a second-stage CC4 preamplifier. In addition, the readout system comprises an active receiver and a DAQ system outside of the cryostat.

above the detector array), the CC4 preamplifier, has been developed based on the preamplifier of the GERDA experiment [19, 20]. Finally, the LEGEND-200 readout electronics includes a novel active receiver and a DAQ system to read out up to 200 HPGe detectors. In the following sections, the signal readout electronics for LEGEND-200 will be described in more detail.

11.1.1 *Low-mass front-end (LMFE) electronics*

The first amplification stage of the readout electronics in LEGEND-200, the low-mass front-end (LMFE) electronics, is located in close proximity to the HPGe detectors (close to the p^+ readout contact). This puts very stringent constraints on the radiopurity of the components, i.e. the contribution to the background budget needs to be as small as possible. LEGEND-200 will use a custom-designed and fabricated, modified version of the LMFE that has been developed for the MAJORANA DEMONSTRATOR and meets these requirements. In particular, it has been adapted for the operation in LAr. The physical layout and a photograph of the LMFE are shown in **Fig.** 11.2.

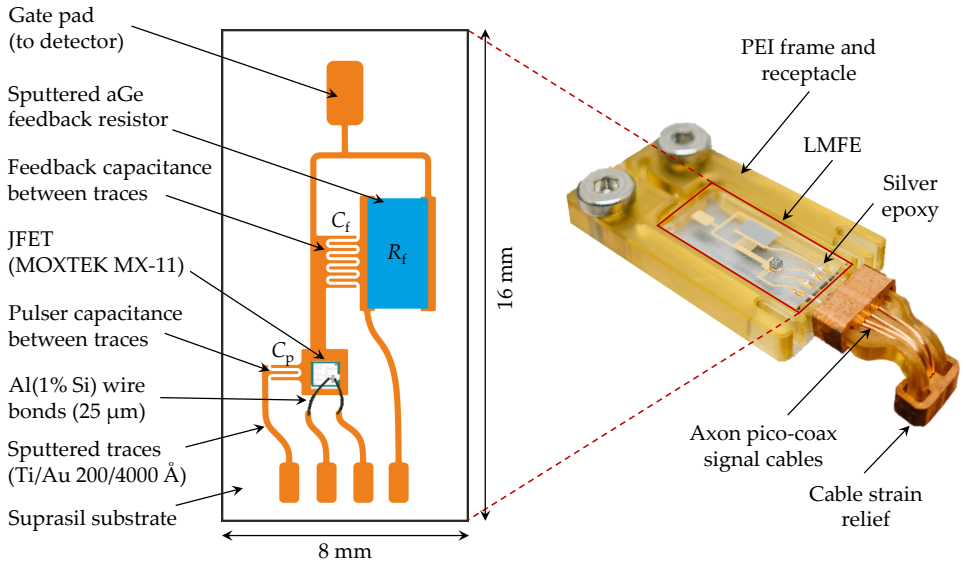

Figure 11.2: Physical layout (left) and photograph (right) of the custom-designed LEGEND-200 LMFE. It consists of an MX11 JFET, a resistive-feedback circuit (feedback resistor R_f, feedback capacitance C_f), and a pulser capacitance C_p. The components are hosted on a Suprasil substrate which is mounted in a low-mass PEI frame.

The electronics components are hosted on a 8 mm × 16 mm and 500 µm-thick Suprasil substrate. The amplification device is a three-terminal MOXTEK MX11 n-channel ultra-low noise JFET [264]. It is commercially available as bare die (no housing) with small dimensions (900 µm × 900 µm × 510 µm) ensuring a minimum amount of material (pure silicon). The JFET has a low input capacitance (C_{GS} = 2.6 pF) and a high transconductance (g_m = 10 mS at 110 K) making it a suitable electronic device for low-noise readout electronics [264]. Its optimal operating temperature is in the range 100 – 200 K. Even though the JFET is located in a cryogenic environment (LAr temperature), the constant current flow through the chip results in localized heating [15, 225].

Traces on the Suprasil substrate are sputtered in an ultra-high vacuum system and patterned via photolithography and chemical wet etching [225]. They consist of two layers: The first layer is made from titanium with a thickness of ~200 Å and is required for an appropriate adhesion. On top of the first layer, a ~4000 Å-thick gold layer is used for routing. The feedback resistor is a sputtered thin film amorphous germanium (aGe) resistor with a resistance of $R_f \approx 1\,G\Omega$ at a temperature of ~87 K. The feedback capacitance ($C_f \approx 400$ fF) and the pulser capacitance ($C_p \approx 100$ fF) are realized by the stray capacitances between the traces on the substrate. The JFET is epoxied to the board with low-stress, low-outgassing conductive silver epoxy. Its terminals are connected to the pads on the Suprasil substrate via Al(1%Si) wire bonds. An additional wire bond together with a bronze spring connects the p^+ contact of the detector with the gate pad of the JFET. The LMFE

is mounted in a low-mass frame made from polyetherimide (PEI) material. It is connected to a second-stage preamplifier via 0.45 mm diameter Axon pico-coaxial signal cables [265]. The cables with lengths of ~ 1.0 – 1.5 m are connected to the LMFE with conductive silver epoxy. A cable strain relief is provided by a clamp made from electro-formed copper. **Fig.** 11.3 shows the assembly of the LMFE on top of a HPGe detector.

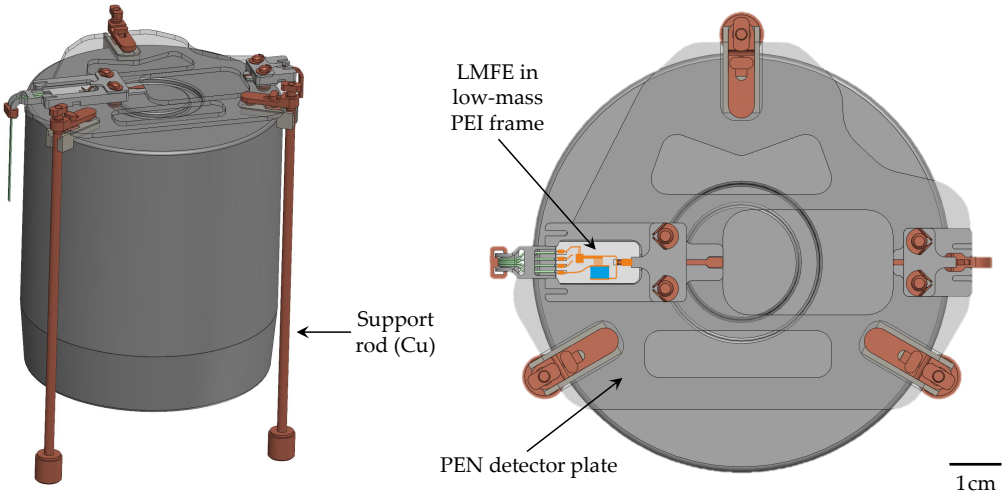

Figure 11.3: Assembly of the LMFE on top of a detector in LEGEND-200 (side and top view). The LMFE is mounted in a low-mass frame made from PEI material. The figure also shows the detector holding plate (made from PEN) and the corresponding support rods made from ultra-pure copper. The scale only applies to the top view. Renderings provided by M. Busch.

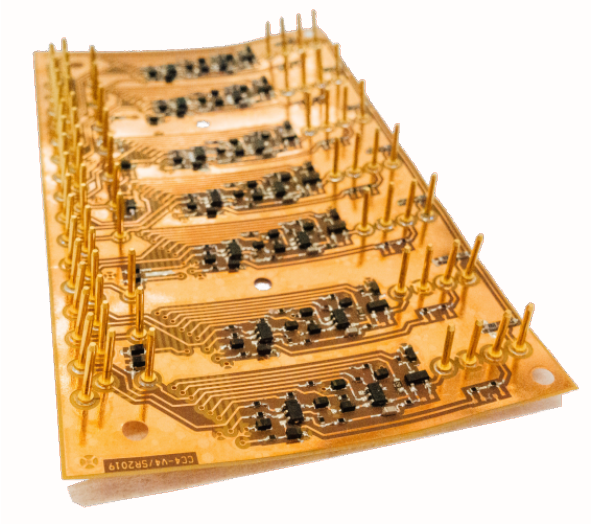

Figure 11.4: Photograph of the CC4 preamplifier consisting of seven identical channels. The printed circuit board is made from low-mass Kapton material. Image courtesy of M. Willers.

11.1.2 *CC4 preamplifier*

The stringent requirements on CSAs in $0\nu\beta\beta$ decay experiments, particularly the operation in LAr, cf. **Ch.** 10.2.1, led to the development of a CSA specifically designed to meet the demands of the GERDA experiment [19, 20]. The CC4 preamplifier for LEGEND-200 takes advantage of this existing design. It will be placed at a distance ranging from 0.3 m to 1.5 m from the detectors (depending on their actual position in the string), where the radiopurity requirements are less stringent. The printed circuit board (PCB) is based on low-mass Kapton material, see **Fig.** 11.4. Each CC4 preamplifier consists of seven channels, i.e. there will be up to 28 CC4 preamplifiers operated in LEGEND-200. The board is populated with small-footprint surface-mount device (SMD) components that have shown

a stable long-term operation in the GERDA experiment. For a given channel, the CC4 preamplifier provides a differential signal output via two operational amplifiers (LMH6654) to reduce potential noise and crosstalk on the transmission line to the cryostat flange. To this end, two complementary signals (opposite in polarity) are driven to the top of the croystat in two different conductors (10 m-long Kapton flat cables). By subtracting the signals from each other, the common mode noise, i.e. noise that is present in both signals with the same polarity, can be eliminated. Details on the implementation of the electronic circuit can be found in [266].

11.1.3 *Active receiver and DAQ system*

LEGEND-200 will use an active receiver at the flange level of the LAr cryostat, also denoted as cryostat head electronics. The purpose of the receiver is to provide a termination for the differential signals coming from the CC4 preamplifiers. It actively reduces the power consumption by compensating for the offset voltage of the MX11 JFET (±2.7 V). In addition, the receiver buffers the signals so that they can be driven to the DAQ system. Finally, the head electronics provides the supply voltages for the preamplifier and monitors the leakage current of the HPGe detectors.

The DAQ system in LEGEND-200 will be based on the FlashCam FADC that has been originally developed for the Cherenkov Telescope Array (CTA) [267]. A major advantage of the system is its modular design that allows for easy scalability. Each channel will be digitized with a sampling frequency of 250 MHz by four ADCs. The FADC will finally deliver 16-bit effective waveforms sampled at 62.5 MHz by combining the four ADCs and downsampling.

11.2 POST-GERDA TEST

11.2.1 *Overview*

The Post-GERDA Test (PGT) was carried out in the time period from February to August 2020 at LNGS. The purpose was to test all components newly developed for LEGEND-200 and the functionality of PPC detectors in LAr. The full experimental chain including improved signal readout electronics, new detector mounts, PEN plates, as well as the new DAQ and calibration system, cf. **Ch.** 11.1, was tested under realistic conditions. In the final PGT configuration, seventeen enriched HPGe detectors were installed in four strings (S1-S4) using the GERDA infrastructure. An overview of the detectors and their properties is listed in **Tab.** 11.1. In addition, a photograph of one of the detector strings and a graphic overview of the array configuration (string arrangement) can be found in **Figs.** 11.5 and 11.6. Four detectors were PPC detectors that had been previously operated in the MAJORANA DEMONSTRATOR experiment. Moreover, five detectors were BEGe detectors, and two detectors were ICPC detectors that had been previously operated in the GERDA experiment. Finally, four novel LEGEND-200 ICPC detectors were installed. Out of the seventeen installed detectors, thirteen were working properly (some detectors were not connected due to broken wire bonds, or had other issues), corresponding to a detector mass of about 18 kg. Some of the detectors were equipped with a shielded HV cable, while others used an unshielded one (for testing purposes). Unshielded cables offer the advantage of lower mass (lower background), and simplified cable management. Finally, some detectors were equipped with silicon plates and others with scintillating PEN plates.

Figure 11.5: Photograph of a detector string in the Post-GERDA Test. Image courtesy of M. Willers.

Table 11.1: Overview of the detectors installed in the PGT. The bias voltage is denoted as V_B. For testing purposes, slightly different implementations of the active receivers were used: Genius refers to an active receiver based on the Genius shaper used in the GERDA experiment, whereas MPIK/LBNL denote implementations developed at Max Planck Institute for Nuclear Physics and Lawrence Berkeley National Laboratory, respectively. While for some of the detectors a shielded (S) HV cable was used, an unshielded (U) one was used for other detectors. Detectors marked in red were not functional.

No	Str	Detector	Type	Mass (kg)	V_B (V)	Ch	Active receiver	HV cable	Detector plate	Comments
1	1	B00091D	BEGe	0.693	4500	24	Genius	U	Si	
2	1	B00002A	BEGe	0.545	2500	25	Genius	S	PEN	
3	1	P00749B	PPC	0.922	1500	26	Genius	U	PEN	reduced V_B
4	1	P00909A	PPC	0.600	-	-	-	-	Si	not connected
5	2	V01240A	ICPC	2.100	-	-	-	-	Si	not connected
6	2	B00079B	BEGe	0.736	3500	28	MPIK	U	PEN	
7	2	P00853A	PPC	1.029	3000	29	MPIK	S	Si	
8	2	P00712B	PPC	1.034	2800	30	MPIK	S	PEN	low gain
9	2	P01239A	ICPC	1.838	0	31	MPIK	U	Si	no HV
10	3	V00048A	ICPC	1.919	3700	32	MPIK	S	PEN	
11	3	V00050B	ICPC	1.929	4000	33	MPIK	U	Si	
12	3	B00076C	BEGe	0.824	3500	34	LBNL	S	Si	
13	3	B00035B	BEGe	0.810	4000	35	LBNL	U	Si	
14	4	V02160A	ICPC	1.750	4000	37	LBNL	U	Si	
15	4	V02160B	ICPC	1.719	4500	38	LBNL	U	Si	
16	4	V02162B	ICPC	2.480	4500	39	LBNL	S	PEN	
17	4	V02166B	ICPC	2.634	4500	40	Genius	S	PEN	

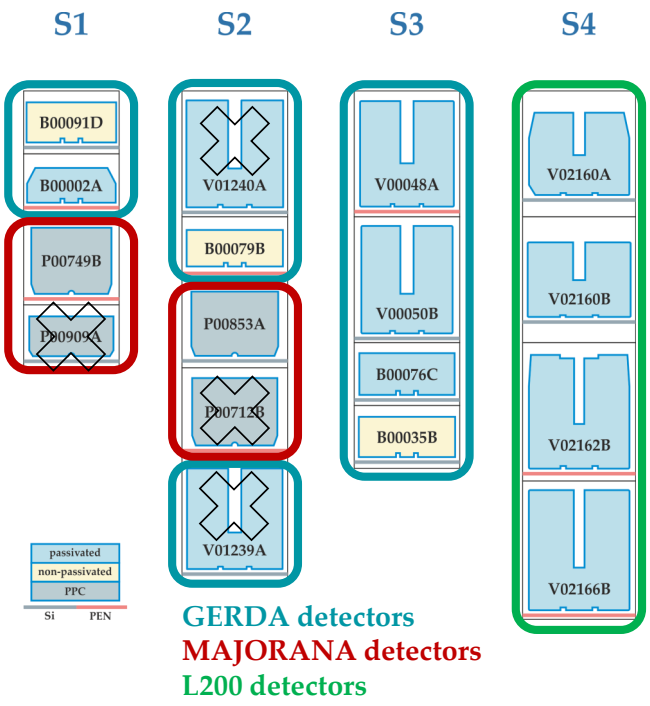

Figure 11.6: Detector array configuration (string arrangement) in the PGT in the final configuration. Out of the 17 installed detectors, 13 were working. Some detectors have previously been operated in the GERDA and MAJORANA DEMONSTRATOR experiments. The last string S4 contained four novel LEGEND-200 ICPC detectors. Si and PEN detector plates are illustrated in grey and red, respectively. Sketch provided by K. Gusev.

Data were acquired using the FlashCam system with a sampling frequency of 62.5 MHz. Every recorded waveform consists of 3404 samples and has a total trace length of 54.464 µs. Consequently, one sample represents a time interval of 16 ns. The acquisition window was divided into about one half of pre-trigger and one half of post-trigger region, with the start time t_0 of the waveform located at $t_0 \approx 27$ µs. All waveform traces were stored on disk for offline data analysis.

In the PGT, several runs with various measurement conditions and settings were performed. This work focuses on the analysis of an extended calibration run (Run0033) with a ^{228}Th source, and on a long-term physics run (Run0030). In the calibration run, roughly 17 h of data were acquired. In the physics run, data were recorded for a period of about 27 days (> 600 h) corresponding to a live time of ~ 0.072 yr. In both runs, an external pulser was used for testing purposes (e.g. non-linearity investigations, etc.).

Data were analyzed using a modified version of the software developed for the analysis of the PPC detector surface characterization measurements carried out in the GALATEA test facility, cf. **Ch.** 6.5.

11.2.2 *Analysis of calibration data*

For the calibration measurements in the PGT, several ^{228}Th calibration sources were inserted from three ports on top of the cryostat lock system, each of them operated by an independent source insertion system (SIS). All sources had activities up to ~ 18 kBq.

DATA QUALITY In a first step, the quality of the recorded data in the PGT was investigated. To this end, the distribution of the baseline mean of all events was analyzed, see **Fig.** 11.7. It can be observed that for most of the detectors, a narrow distribution consisting of a single peak is obtained. However, some detectors show a distorted peak shape (e.g. PPC detectors on Ch26, Ch29). In addition, the BEGe detector on Ch28 shows a strong double peak structure. These features are an indication for a drifting baseline which can be validated by analyzing the temporal stability of the baseline mean, see **Fig.** 11.8. The time evolution plots indicate that most of the detectors show a stable performance within the calibration run, especially the ICPC detectors. However, the PPC detectors (Ch26, Ch29) and some of the BEGe detectors (Ch28, Ch34) show baseline mean drifts on the order of $5 - 10\%$. In particular, the BEGe detector on Ch28 exhibits a strong baseline mean jump after $\sim$8 h of data taking leading to the observed double peak structure. The drifts might be explained by strongly changing leakage currents in the affected detectors. It should be noted here that the observed drifts cannot be associated in an obvious manner neither with the HV cable (shielded vs unshielded) nor with the detector plate (Si vs PEN). Fortunately, the baseline mean instability has little impact on subsequent analyses since the baseline restoration is done on an event-by-event basis. In **Fig.** 11.8 it can be further observed that for some detectors several events strongly deviate from the centroid of the baseline mean. These events are unphysical and mostly correspond to discharges.

DATA CLEANING To reject unphysical events as well as background events, several data quality and analysis cuts were deployed. First, pre-trace and in-trace pile-up events were eliminated in a similar way as described in **Ch.** 6.5. Second, a detector anti-coincidence (AC) cut was deployed, i.e. only multiplicity-1 events were accepted. Third, PSD cuts were applied: a low A/E cut and a high A/E cut.

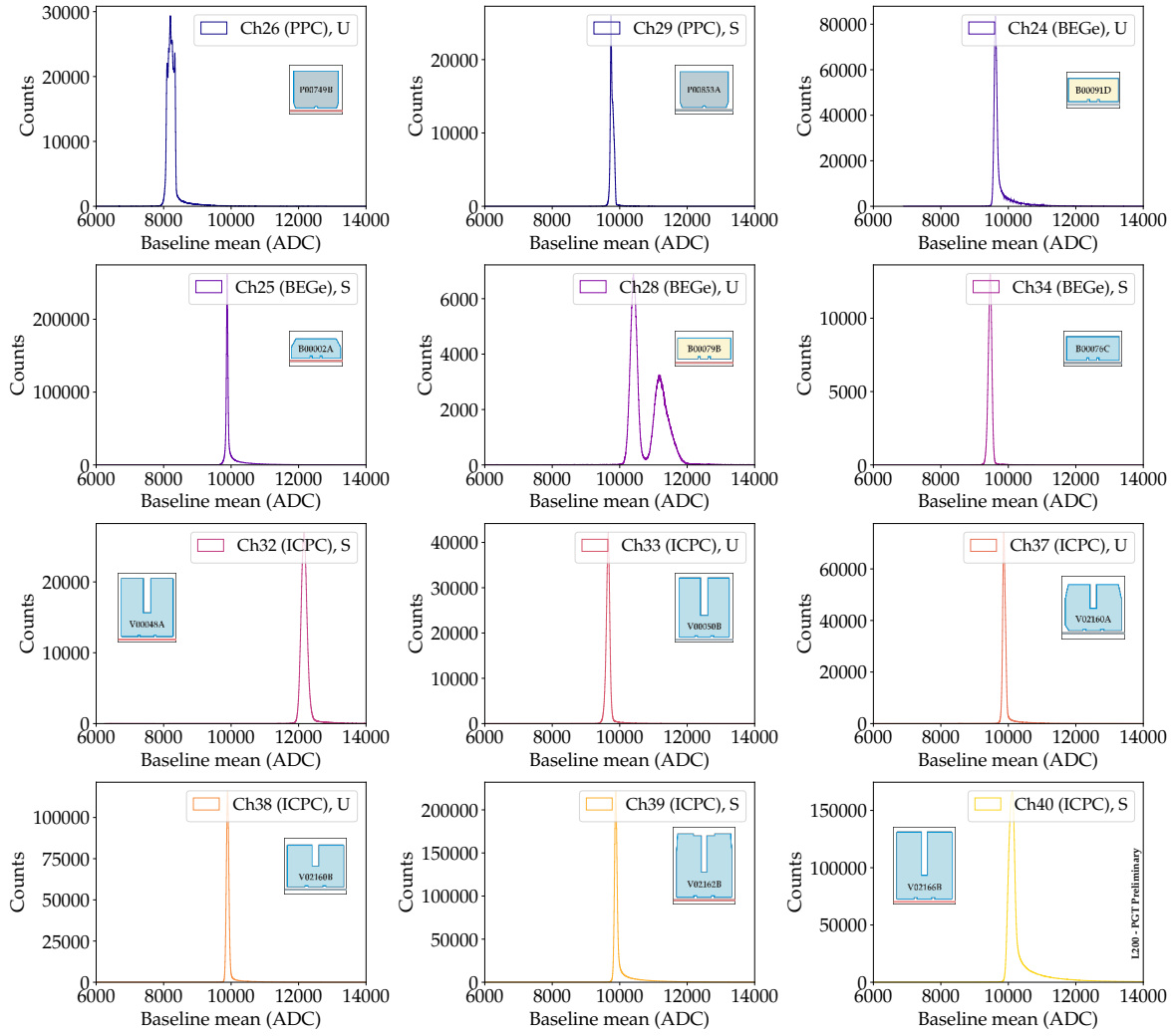

Figure 11.7: Baseline mean distributions of the detectors in the PGT (^{228}Th calibration data). The mean is computed based on the first 1000 samples of every waveform. For reasons of visual clarity, the distribution for the BEGe detector on channel 35 is not illustrated. The legends indicate the detector channel, detector type, and the HV cable type (shielded: S, unshielded: U).

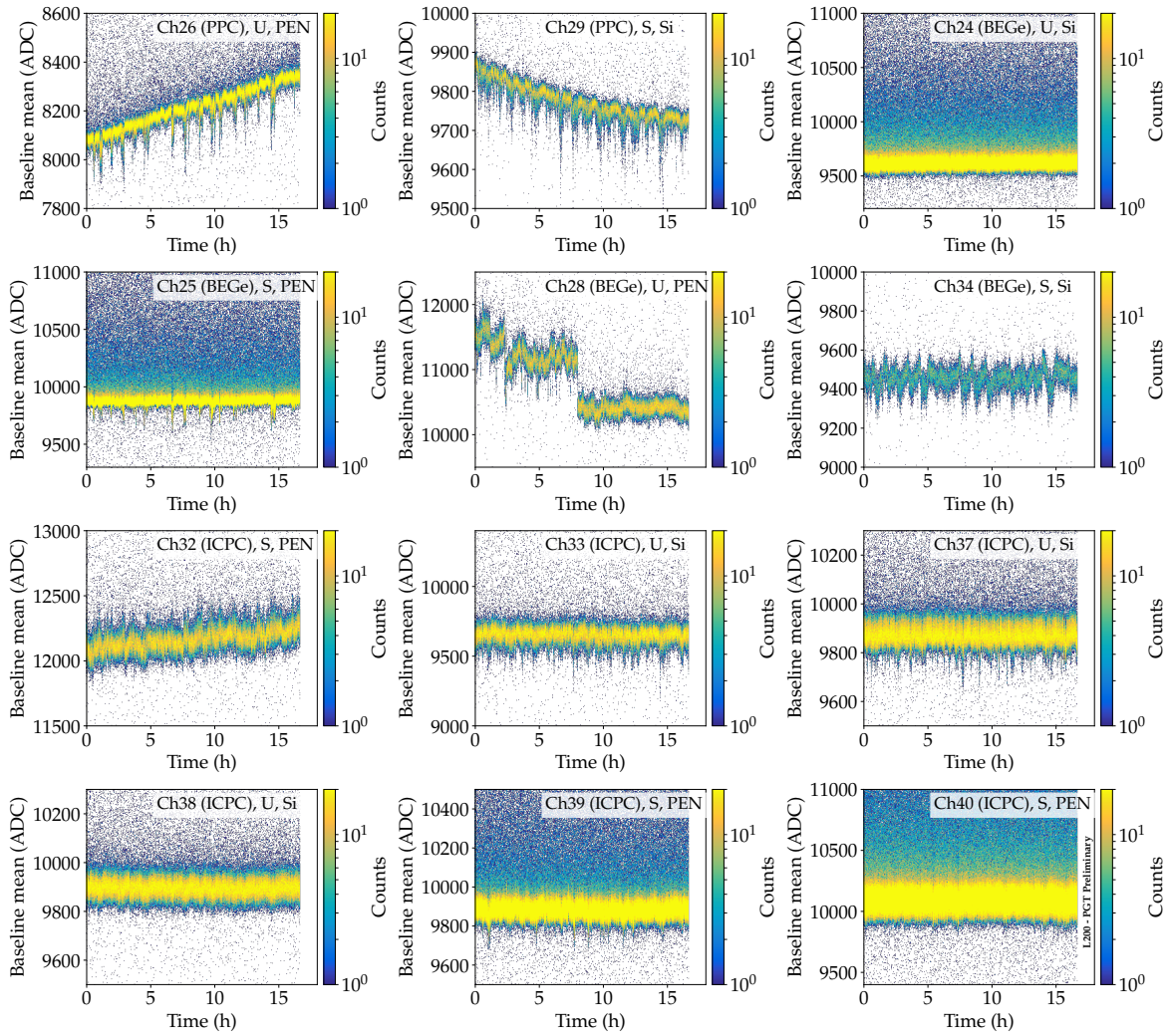

Figure 11.8: Time evolution of the baseline mean of the detectors in the PGT (^{228}Th calibration data). While some of the detectors were equipped with a silicon plate (Si), others used scintillating PEN plates (PEN). The labels also indicate the HV cable type (shielded: S, unshielded: U).

CHARGE TRAPPING To reconstruct the event energy, different estimators were used (fixed-time-pickoff (ftp) trapezoid, amplitude energy, FADC online energy). In most cases, the best energy resolution was obtained with an ftp trapezoid with a rise and fall time of 10 µs, and a flat top time of 4 µs. To determine the amount of charge trapping within the different detectors, the correlation between the drift time and the energy for events constrained to the 2.6 MeV ^{208}Tl peak was investigated. Examples for several detectors are shown in **Fig.** 11.9. It can be observed that the ICPC detector on Ch39 shows a strong correlation between drift time and energy and thus features a considerable amount of CT. The plots also show that the ICPC detectors comprise two distinct event populations (double peak structure), one with shorter and the other one with higher drift times. The first population corresponds to events close to the signal readout electrode, where the weighting potential is high, cf. **Ch.** 3.3.2. In contrast, the second population with higher drift times corresponds to events in the bottom part of the detector, where the weighting potential is relatively small. Independent of the amount of CT in a particular detector in the PGT, a drift time correction is applied to correct for this effect. The correction follows the procedures described in **Ch.** 6.5. It should be noted here that for a successful application of the correction, low-noise readout electronics are required (to get a precise value for the onset t_0 of the charge collection and the drift time). For LEGEND-200, an energy resolution of 2.5 keV FWHM at the $Q_{\beta\beta}$-value is targeted. This criterion is fulfilled in the PGT.

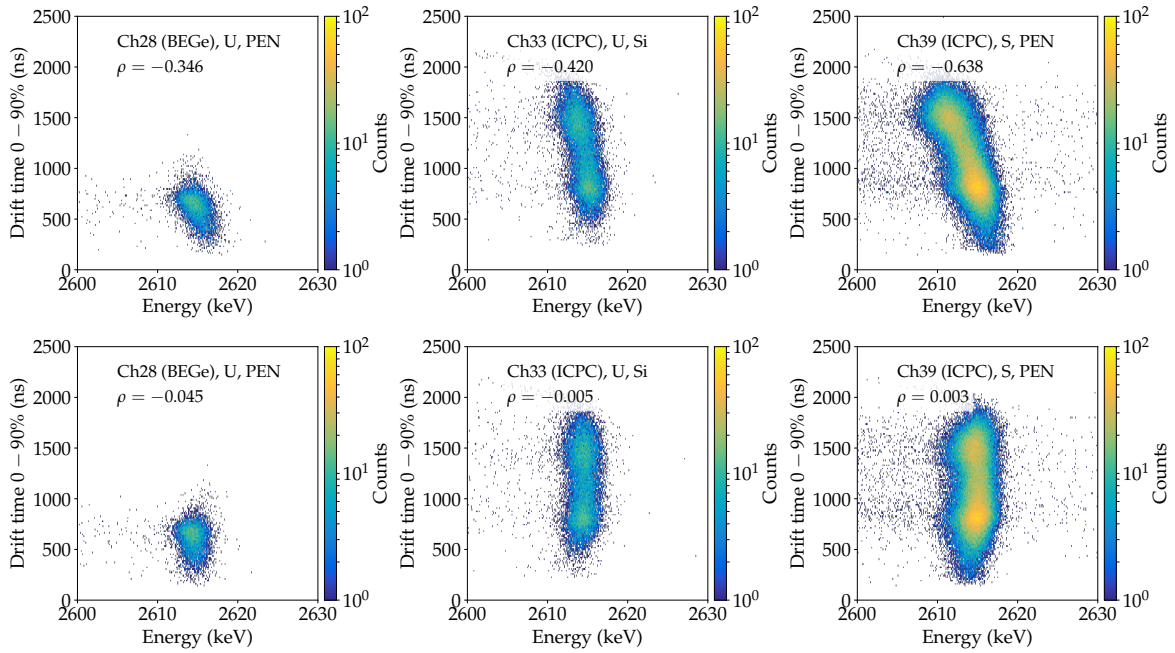

Figure 11.9: Investigation of charge trapping in the PGT: Correlation between drift time and energy for events constrained to the 2.6 MeV ^{208}Tl peak for several detectors. The higher the correlation between the two quantities (expressed in terms of the Pearson correlation coefficient ρ), the stronger the amount of charge trapping. The upper row shows the correlation before the application of a drift time correction for charge trapping. After the correction (bottom row), the quantities have a much smaller correlation. For detectors with a considerable amount of charge trapping, this leads to a significant improvement of the energy resolution.

After having applied the data quality cuts and the drift time correction for CT, the energy was calibrated independently for every detector in a similar way as described in **Ch.** 6.6. The calibrated energy spectra before and after the application of quality cuts are shown in **Fig.** 11.10. It can be observed that the cuts efficiently remove, inter alia, low-energy tails. For most of the channels, the peak located at energies $\gtrsim$ 3 MeV corresponds to pulser events.

ENERGY RESOLUTION The energy resolution curve of the detectors was determined by extracting the FWHM of several gamma lines as described in **Ch.** 6.6. **Fig.** 11.11 shows an example of the resolution estimation for an ICPC detector. Moreover, a summary of the energy resolution of all functional detectors at the $Q_{\beta\beta}$-value at 2039 keV, as well as at the 2.6 MeV ^{208}Tl peak can be found in **Fig.** 11.12. It can be observed that most of the BEGe and ICPC detectors performed very well, i.e. they exceeded the targeted energy resolution of 2.5 keV FWHM at the $Q_{\beta\beta}$-value. When comparing to the

average energy resolution at the 2.6 MeV ^{208}Tl peak obtained in the GERDA experiment, most BEGe and ICPC detectors even show a better performance in the PGT. This can be attributed to the fact that the noise situation in the PGT was better. This in turn might be due to the use of improved signal readout electronics, particularly the separation of the CSA into a first amplification stage very close to the detectors and a second stage farther away, see **Ch.** 11.1. The two functional PPC detectors (Ch26, Ch29) show a rather poor performance in terms of energy resolution ($\Delta E > 3$ keV FWHM at the $Q_{\beta\beta}$-value). However, the detector on Ch26 was operated at a bias voltage of only $V_B = 1500$ V, far below the recommended operating voltage of $V_B = 3000$ V. Therefore, the poor performance is most likely due to a not fully depleted detection volume. The PPC detector on Ch29 already showed a poor performance in the detector characterization measurements initially carried out by its manufacturer ORTEC ($\Delta E = 2.51$ keV FWHM at the 1.3 MeV ^{60}Co peak). Furthermore, the BEGe detector on Ch34 shows a comparably poor performance ($\Delta E \approx 4$ keV FWHM at the $Q_{\beta\beta}$-value). This can be explained by the fact that the signals were based on a single-ended output resulting in a low gain and thus in a poor energy resolution. Finally, even though the BEGe detector on Ch35 has an acceptable performance in terms of energy resolution, it showed strong instabilities in the PGT (unstable baseline, many discharge events, etc.). For the reasons mentioned above, the subsequent analyses will focus on the following nine well-performing detectors: BEGe's on Ch24, Ch25, Ch28, and ICPC's on Ch32, Ch33, Ch37-40. For these detectors (total mass of 14.405 kg), an excellent average energy resolution of $\langle \Delta E \rangle \approx 2.20$ keV FWHM at the $Q_{\beta\beta}$-value was obtained.

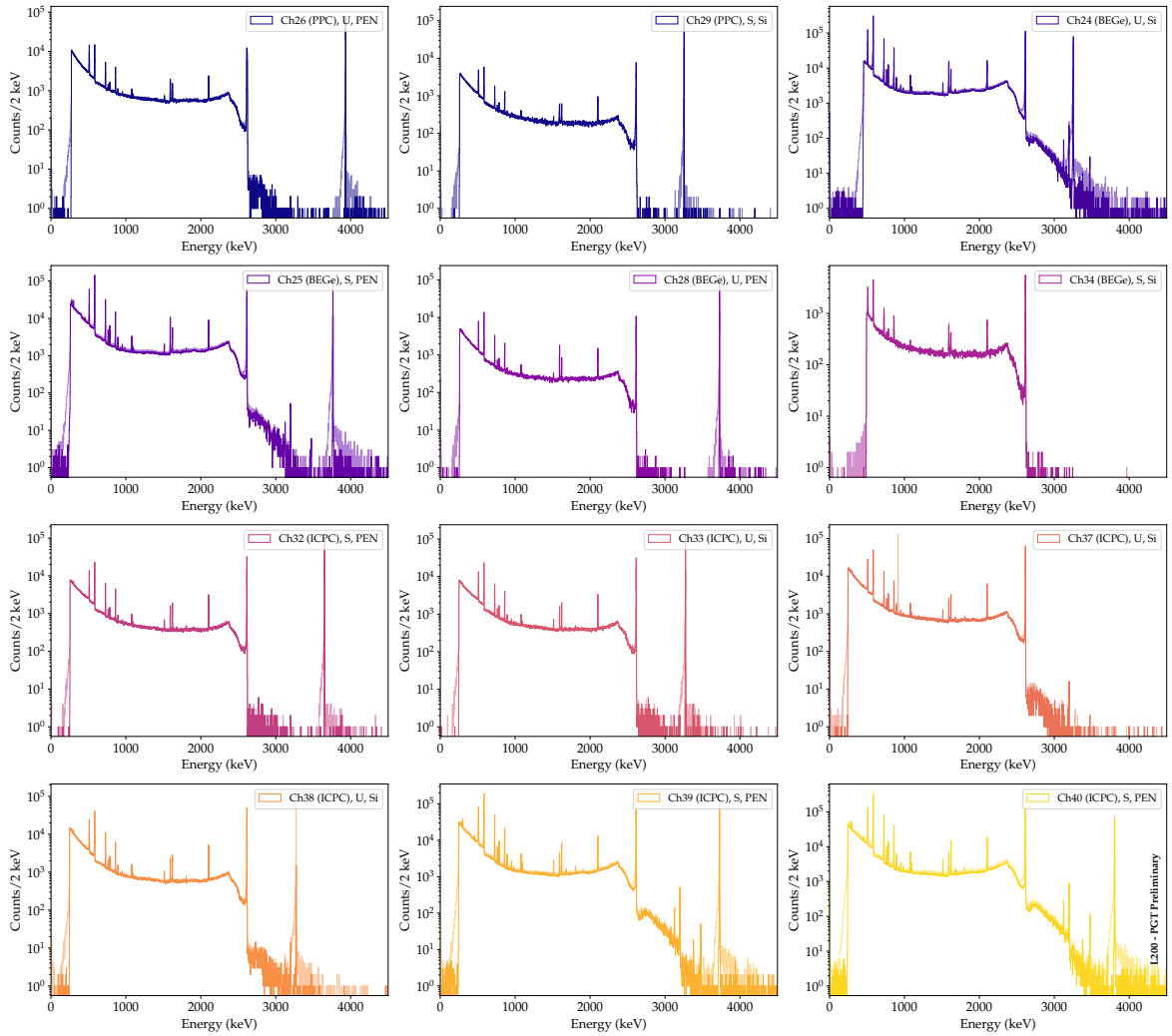

Figure 11.10: PGT energy spectra in the ^{228}Th calibration run. The faint curves correspond to the spectra before quality cuts, the solid lines to those after the application of cuts.

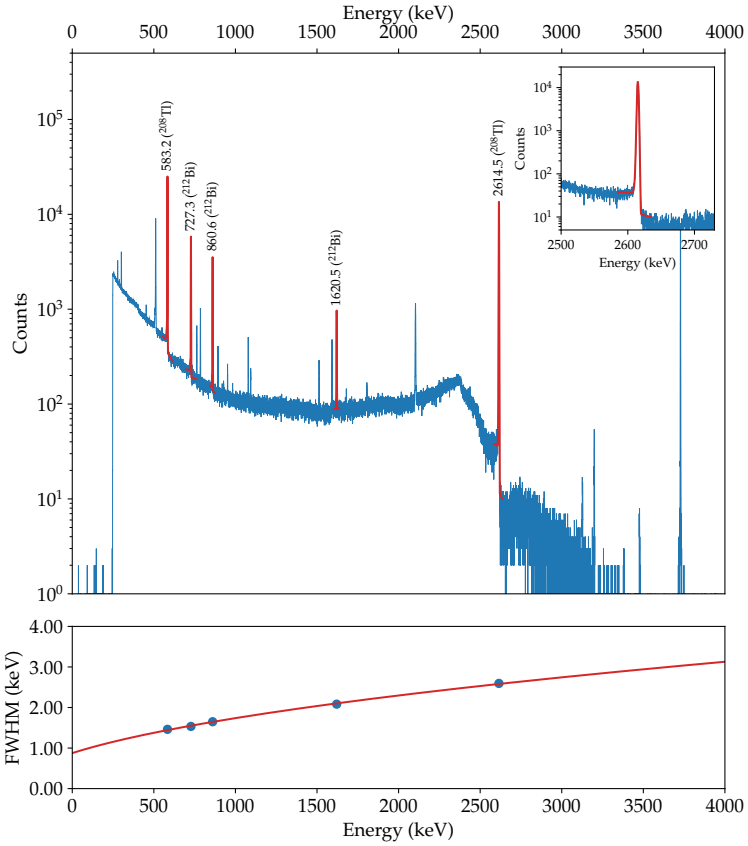

Figure 11.11: Example for the determination of the energy resolution in the ^{228}Th calibration run in the PGT (ICPC detector on Ch39). The red lines in the upper plot correspond to spectral fits of several gamma lines. The inset shows a zoom of the 2.6 MeV ^{208}Tl peak. The bottom plot shows the energy resolution curve.

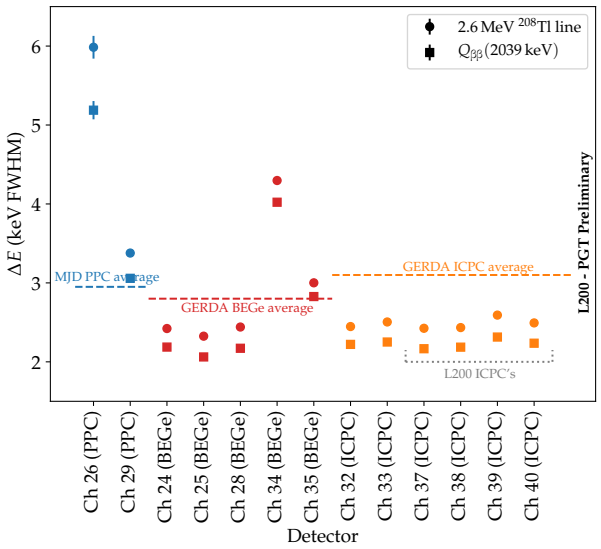

Detector	Type	Ch	ΔE (keV)	
			$Q_{\beta\beta}$	2.6 MeV
P00749B	PPC	26	5.21	5.91
P00853A	PPC	29	3.05	3.40
B00091D	BEGe	24	2.17	2.43
B00002A	BEGe	25	2.08	2.36
B00079B	BEGe	28	2.21	2.50
B00076C	BEGe	34	4.00	4.31
B00035B	BEGe	35	2.77	2.91
V00048A	ICPC	32	2.16	2.46
V00050B	ICPC	33	2.31	2.52
V02160A	ICPC	37	2.17	2.43
V02160B	ICPC	38	2.21	2.45
V02162B	ICPC	39	2.33	2.61
V02166B	ICPC	40	2.20	2.50

Figure 11.12: Energy resolution ΔE of the detectors in the ^{228}Th calibration run in the PGT. The resolution is shown for the $Q_{\beta\beta}$-value at 2039 keV (squares), as well as for the 2.6 MeV ^{208}Tl peak (circles). The dashed lines correspond to the average energy resolution of the 2.6 MeV ^{208}Tl peak obtained in the GERDA and MAJORANA DEMONSTRATOR experiments [142, 268]. In the following analyses, a focus will be put on the nine well-performing detectors marked in green in the table.

PSD PERFORMANCE In the next step, the PSD performance of the detectors in the PGT was investigated in terms of the A/E parameter, cf. **Ch.** 4.1.2. The A/E vs E distributions for the nine well-performing detectors in an extended ^{228}Th calibration run are shown in **Fig.** 11.13. The distributions were corrected for a slight linear energy dependence. It can be observed that the distributions are as expected. The bands corresponding to SSEs centered around A/E = 1 can be clearly identified. Events below these bands mainly correspond to MSEs and n^+ surface events, whereas events above these bands can be mainly attributed to p^+ events. They can be suppressed by applying low and high A/E cuts to the data, respectively. For a quantitative PSA, the A/E cut was tuned to accept

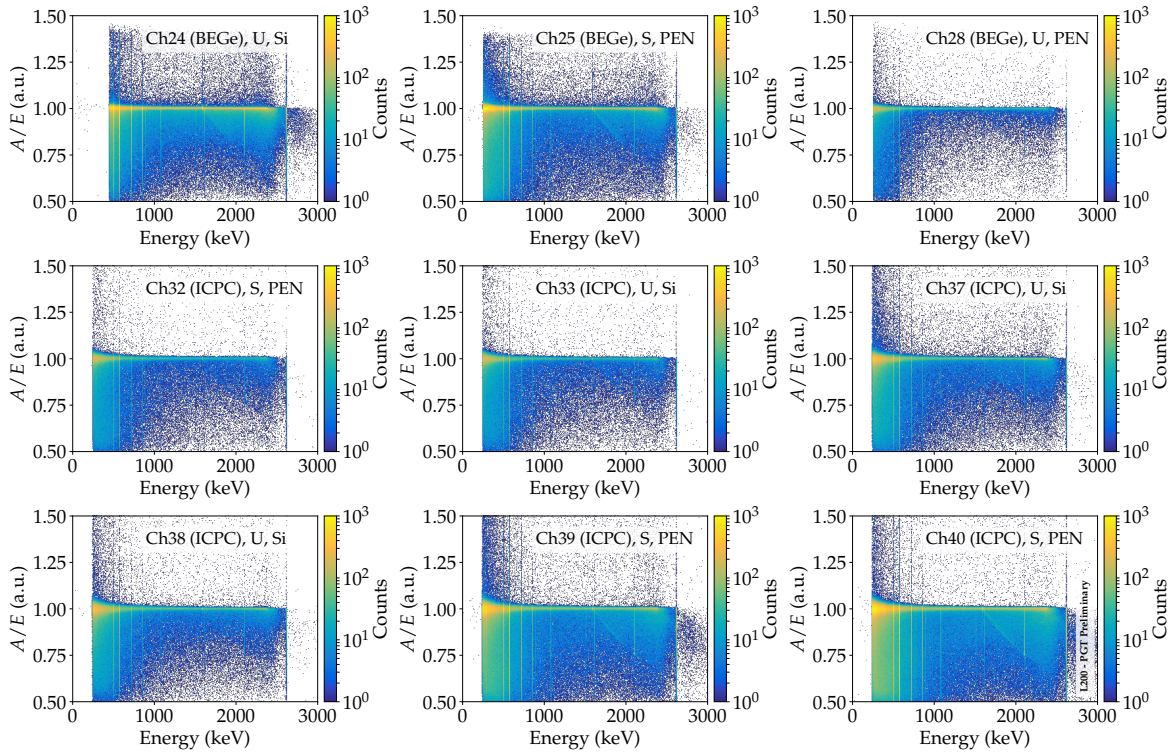

Figure 11.13: Normalized A/E distributions as a function of energy in a ^{228}Th calibration measurement in the PGT. While SSEs are located along A/E = 1, MSEs and n^+ surface events are characterized by A/E < 1. Events in close proximity to the p^+ readout contact feature values of A/E > 1.

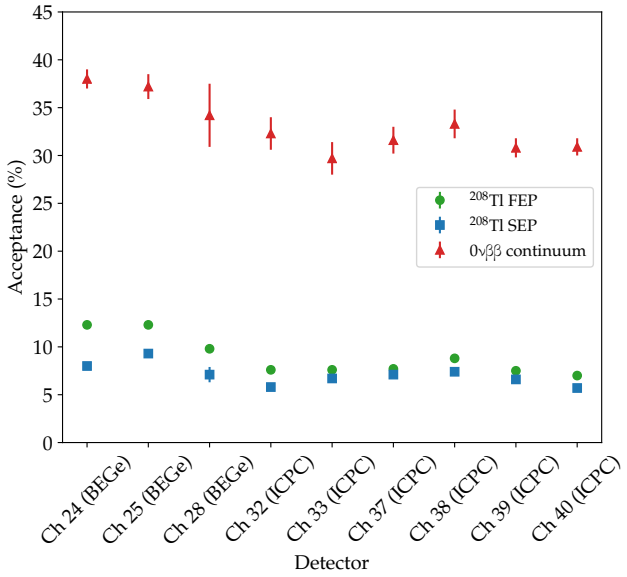

Figure 11.14: PSD performance of the detectors in the PGT. The estimation of the survival efficiencies is based on the A/E pulse shape discriminator. The acceptance of events in the DEP is tuned to 90%. The plot shows the corresponding survival efficiencies of events in the ^{208}Tl FEP, the ^{208}Tl SEP, as well as in the 0νββ continuum at the $Q_{\beta\beta}$-value.

90% of the events in the ^{208}Tl DEP. Further details on the A/E PSA technique can be found in **Ch.** B.1 in the appendix. The computed survival efficiencies for the various detectors are illustrated in **Fig.** 11.14. The acceptance of background events (MSEs) in the ^{208}Tl SEP is heavily suppressed, i.e. only ~6-9% of these events survive. At the same time, the acceptance of events in the signal ROI is ~32-41%. The survival efficiencies obtained in the PGT are in good agreement with those obtained in the GERDA and MJD experiments [142, 215, 246].

DECAY TIME The decay time τ is an important pulse shape parameter since it provides information on the stability of the first stage of the readout electronics, i.e. the LMFE. Since τ is approximately given by the product of the feedback resistance R_f and the feedback capacitance C_f, $\tau \approx R_f C_f$, any instability in these quantities directly translates into an instability in the decay time. A stable decay time is further needed to be capable of rejecting surface alpha events using the DCR parameter, cf. **Ch.** 5.3. In the PGT, the decay time was estimated on an event-by-event basis in a similar way as described in **Ch.** 6.5. The decay time distributions for the different detectors are shown in **Fig.** 11.15. The centroid of each distribution was fitted with a Lorentzian. The peak position of the Lorentzian was then used for the PZ-correction of all events (for a given channel). It can be observed that for most of the detectors, a mean decay time of $\langle\tau\rangle \lesssim 400\,\mu s$ was obtained. This is in good agreement with the expectation from the readout electronics: The LMFE uses a feedback resistor with $R_f \approx 0.4\,pF$ and a feedback capacitor with $C_f \approx 1\,G\Omega$. The tails at lower and higher decay times mostly correspond to low-energy events, for which an accurate fit is challenging (due to noise). In some channels, a multi-peak structure can be observed. The peak marked in red corresponds to pulser events and does not coincide with the peak marked in blue corresponding to physics events. The reason for this are issues with the pulsers in some channels leading to degraded waveforms and thus an inappropriate fit of the decay time. The time evolution of the decay time is illustrated in **Fig.** 11.16. The plots show that within the calibration run, the decay time of the detectors was stable, i.e. no drift was observed. This implies that also the feedback resistor and the feedback capacitor remained stable during the measurement.

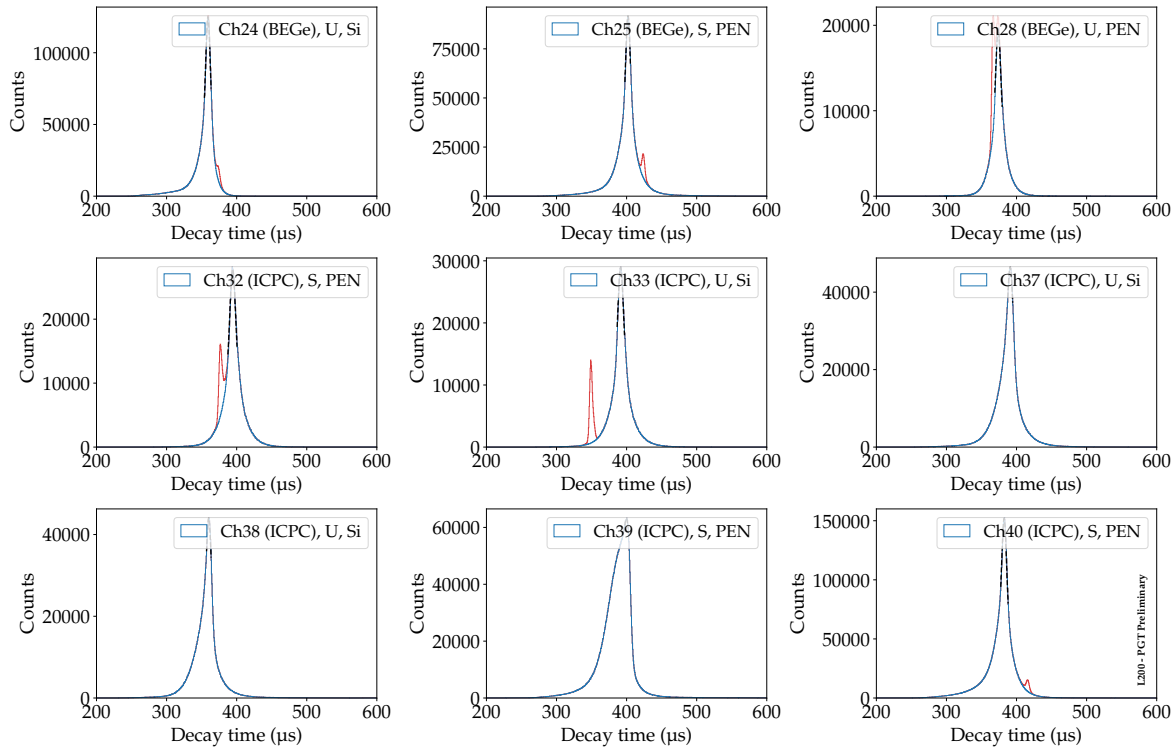

Figure 11.15: Decay time distributions of the detectors in the PGT (^{228}Th calibration data). The blues curves correspond to physics events, while the red curves are pulser events. The centroids of the physics event distributions are approximated with a Lorentzian (dashed black curves) and are then used for the PZ-correction of all events (for a given channel).

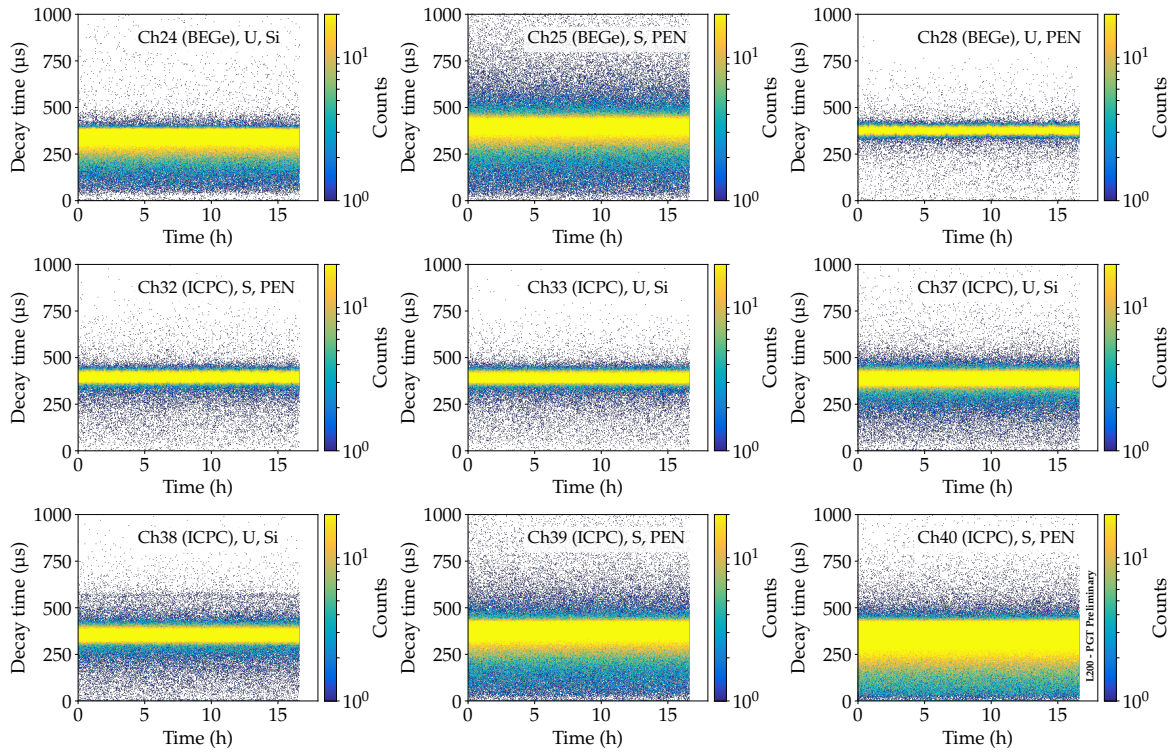

Figure 11.16: Time evolution of the decay time of the detectors in the PGT (^{228}Th calibration data). For reasons of visual clarity, pulser events have been excluded here. The temporal stability of the decay time indicates that also the feedback resistor and the feedback capacitor of the LMFE remained stable during the measurement.

11.2.3 *Analysis of physics data*

In the following paragraphs, data of the long-term background measurement (Run0030, $>$ 600 h of data) will be analyzed.

DATA QUALITY In a first step, as for the PGT calibration measurements, the data quality of the physics measurements was investigated. The distribution of the baseline mean and its time evolution is shown in **Figs.** 11.17 and 11.18, respectively. In the baseline mean distributions, a strong multi-peak structure can be observed for some detectors, e.g. ICPC detectors on Ch32 and Ch33. These features are reflected in the time evolution plots. Most of the detectors have a slightly drifting baseline indicating a changing leakage current. The strongest instabilities can be observed for the ICPC detector on Ch32 with drifts up to 10%. The drift of physics and pulser events behaves in the same way. It is worth mentioning that the trends of the drift (upward or downward trend) are usually not compatible with the trends observed in the calibration measurements.

In the next step, the distributions of the baseline root mean square (RMS, computed based on the first 1000 samples of every waveform) were investigated, see **Fig.** 11.19. While the peak at small RMS values is populated with non-degraded (physics) events, the continuum and the second peak at higher RMS values are composed of unphysical events: discharges, false trigger events, zero-energy events, noise, etc. Fortunately, these events can be identified and rejected by the quality cuts discussed in the **Ch.** 11.2.2.

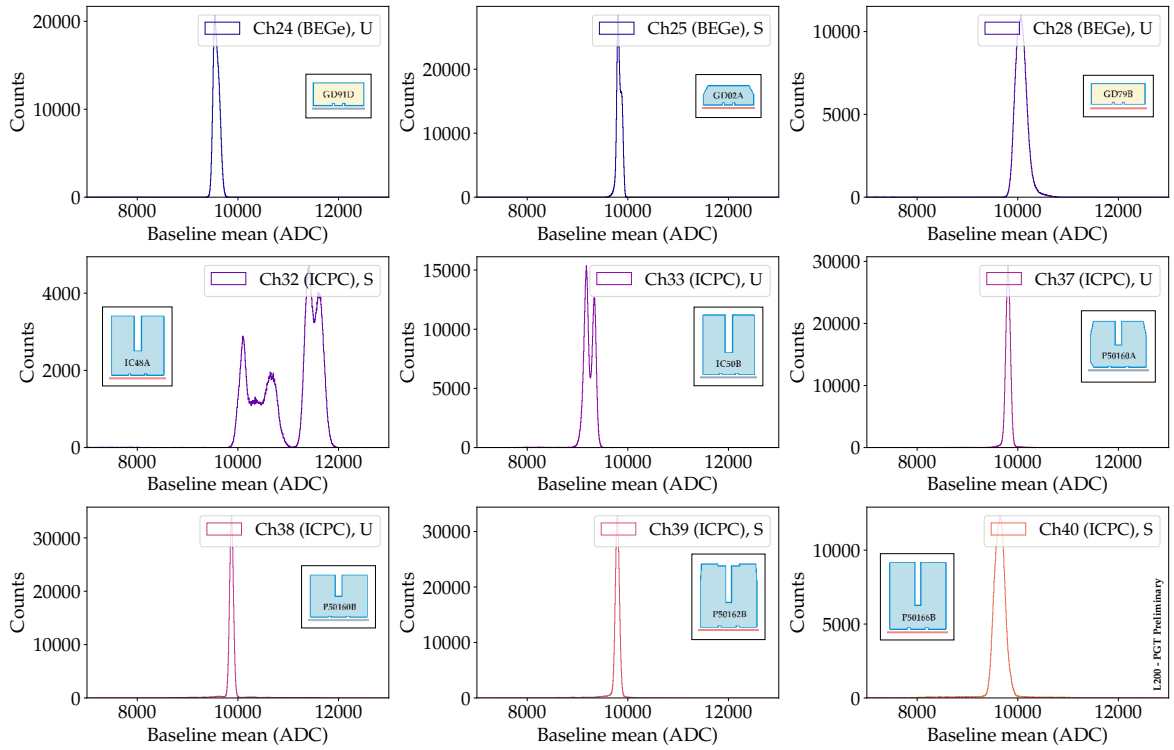

Figure 11.17: Baseline mean distributions of the detectors in the PGT (physics data). The mean is computed based on the first 1000 samples of every waveform. The legends indicate the detector channel, detector type, and the HV cable type (shielded: S, unshielded: U).

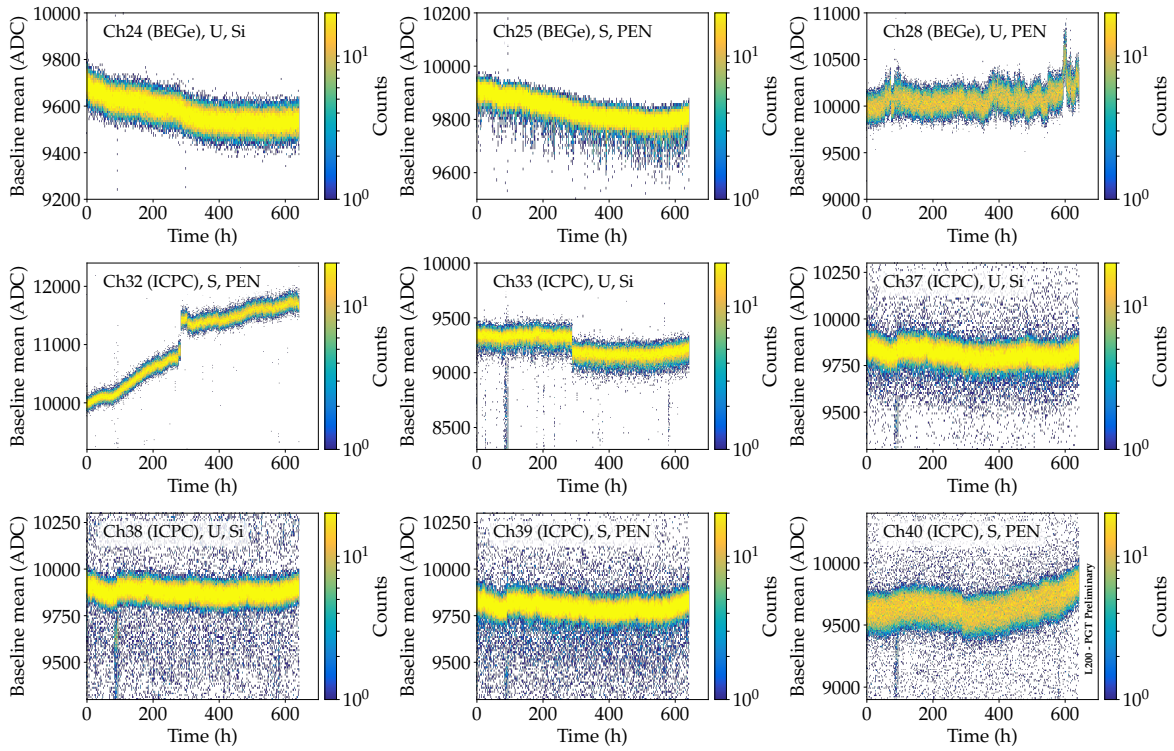

Figure 11.18: Time evolution of the baseline mean of the detectors in the PGT (physics data). Several detectors show a drifting baseline indicating a changing leakage current.

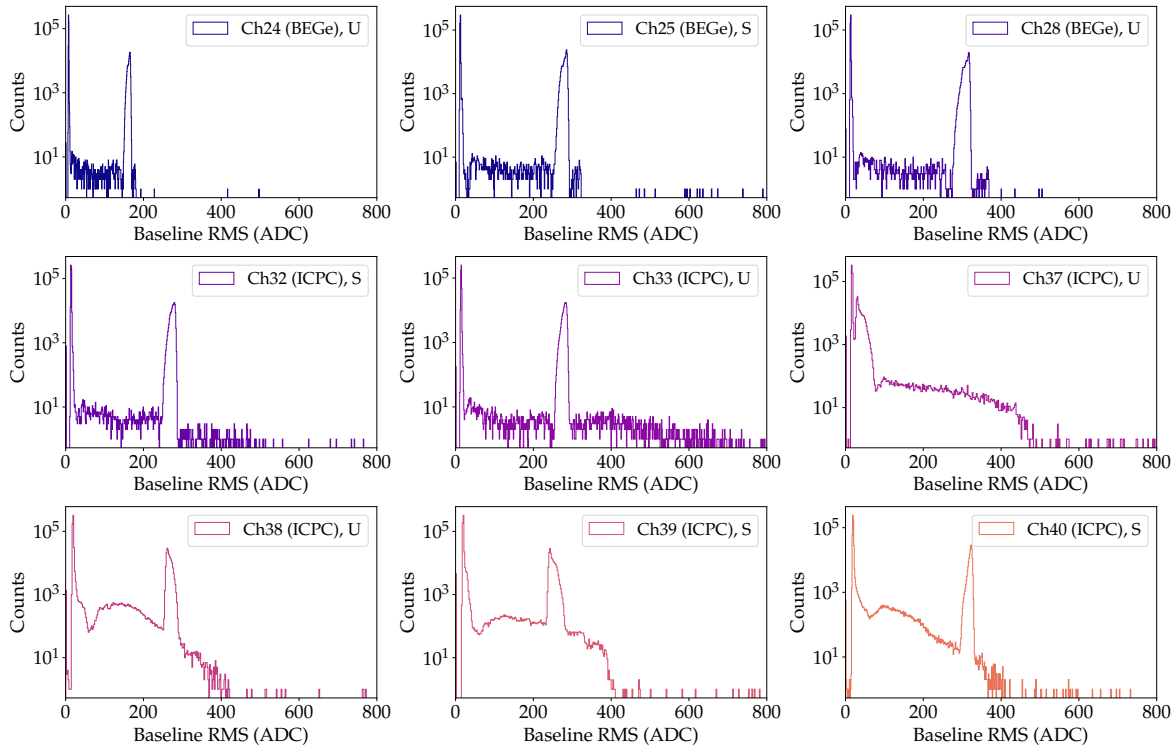

Figure 11.19: Baseline RMS distributions of the detectors in the PGT (physics data). The continuum and the peak at higher values are populated with unphysical events (discharges, zero-energy events, etc.).

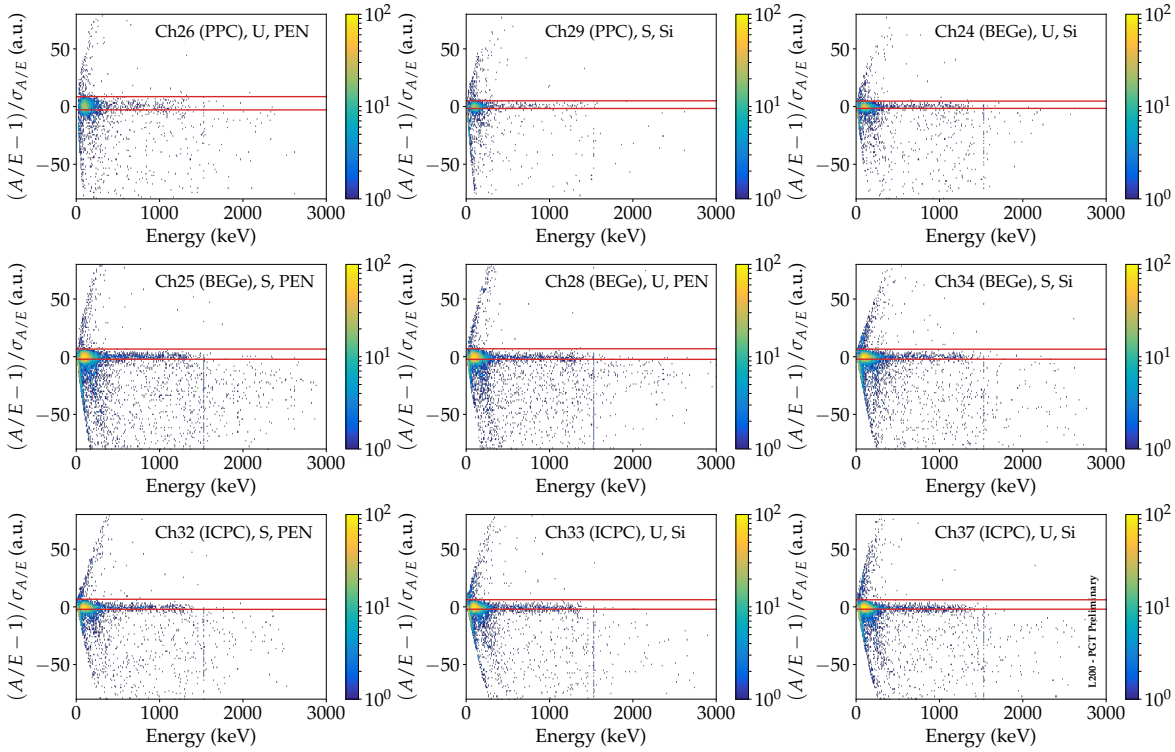

Figure 11.20: Normalized A/E distributions as a function of energy in the physics run in the PGT. The red lines indicate the low and high A/E cut values.

ENERGY SPECTRA One of the main goals of the physics run in the PGT was to obtain a background energy spectrum that can be used for further data analyses, e.g. event count analysis in the ROI, etc. To this end, after a basic data cleaning (rejection of pile-up and coincidence events), PSD cuts were applied to the data. A low A/E cut to reject MSEs and n^+ surface events is based on the results obtained in the ^{228}Th calibration run, cf. **Ch.** 11.2.2. Moreover, a high A/E cut to reject p^+ events (volume cut around the p^+ contact) is determined by multiplying the low A/E cut value by a factor of −3. The A/E vs E distributions in terms of the PSD parameter [133, 186, 269]

$$\zeta = \frac{A/E - 1}{\sigma_{A/E}}, \tag{11.1}$$

where $\sigma_{A/E}$ denotes the resolution of the A/E SSE band distributions, are shown in **Fig.** 11.20. Furthermore, the plots indicate the low and high A/E cuts.

In the next step, the PSD cuts were applied to the energy spectra. **Fig.** 11.21 shows the spectra before the application of any cuts, after the application of basic quality cuts (including an AC cut), and after the additional application of A/E PSD cuts. Slight differences in the spectral shape between the different detectors can be explained by differences in the detector geometries [270].

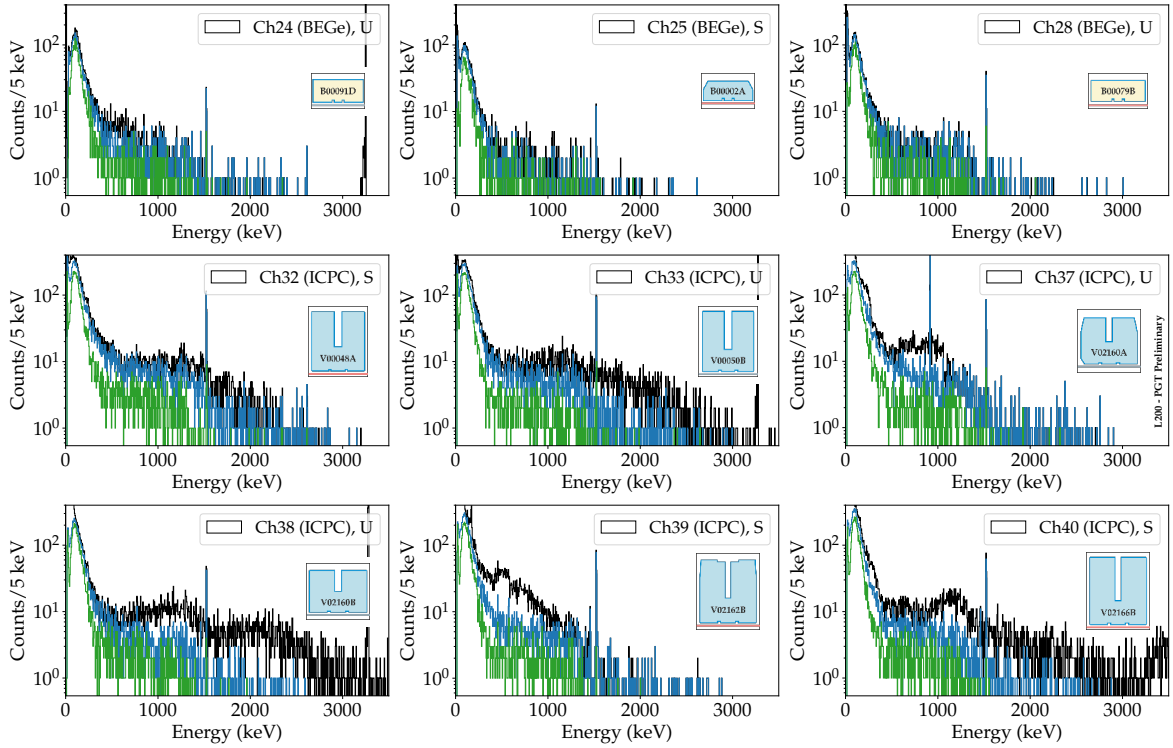

Figure 11.21: Energy spectra in the long-term background measurement in the PGT. The black curves correspond to the energy spectra before cuts, the blue curves to the spectra after basic quality cuts (rejection of pile-up and coincidence events), and the green curves to the spectra after the additional application of PSD cuts.

To better recognize the spectral features, the energy spectra of the nine well-performing detectors were combined into a single spectrum, see **Fig.** 11.22. The energy spectrum before cuts is dominated by pulser events, noise events, and zero-energy events. After having applied basic quality cuts, most of these events are removed and some prominent spectral features become visible. The low-energy part up to energies of 565 keV is dominated by beta decay of cosmogenic ^{39}Ar. Moreover, the 1.5 MeV ^{42}K gamma line, and the 2.6 MeV ^{208}Tl peak can be clearly identified. After the additional application of the A/E PSD cuts, backgrounds are further reduced. It should be noted here that the PSD results are only valid for energies $E \gtrsim 500$ keV (at smaller energies, no accurate PSD calibration was possible with the ^{228}Th data). Around the $Q_{\beta\beta}$-value in the energy window 1930 − 2190 keV, a background index of BI $\approx 0.04\,\mathrm{cts/(keV \cdot kg \cdot yr)}$ is obtained. This corresponds to a PSD suppression factor of ∼ 19. The observed background in the energy window around the ROI is higher by a factor of $\gtrsim 50$ compared to the one in the GERDA experiment. This might be due to the following reasons:

1) Since in the PGT the detectors were not surrounded by nylon cylinders (mini shroud) limiting the drift of charged ions to the detector surfaces, enhanced ^{42}K backgrounds are expected.

2) Above the detector array, non-radiopure materials were used, e.g. CC4 preamplifier boards made from FR4 material, CC4 holding structures made from aluminum, additional LMFE shipping containers and copper boxes (to spool cables) installed in cryostat, etc. This could have led to enhanced ^{232}Th backgrounds. This hypothesis is supported by the fact that the background for the detectors with a higher position in a given detector string is typically higher, see **Fig.** 11.23.

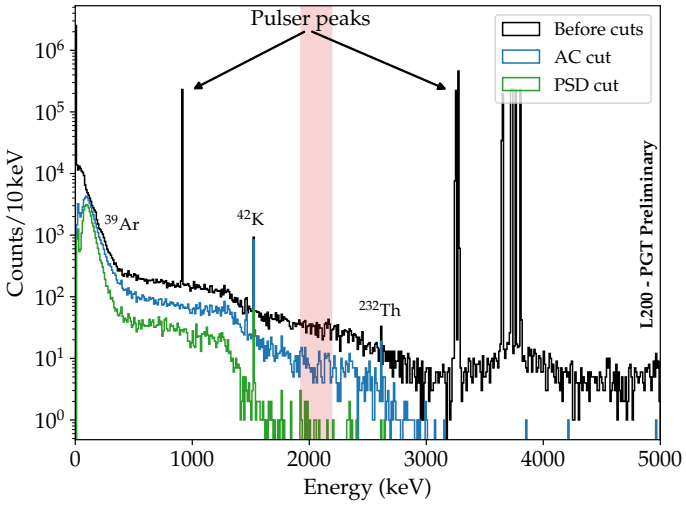

Figure 11.22: Combined energy spectrum of the long-term background measurement in the PGT before (black curve) and after the application of AC and PSD cuts (blue and green curves). The spectrum is based on the nine well-performing detectors. The data correspond to a total exposure of $M \cdot t = 1.038\,\mathrm{kg} \cdot \mathrm{yr}$. The red band indicates the energy window around the ROI ($1930 - 2190\,\mathrm{keV}$).

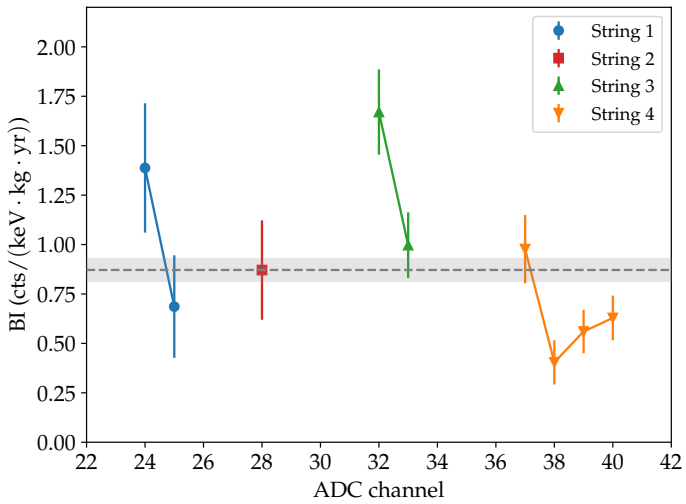

Figure 11.23: Background indices in the energy window $1930 - 2190\,\mathrm{keV}$ of the detectors in the PGT after the application of basic quality cuts. The grey dashed line and the band indicate the mean background index and its uncertainty, respectively. For a given detector string, detectors with a lower ADC channel number have a higher position in the array.

DECAY TIME As for the calibration measurements, the stability of the decay time was investigated for the background data. The time evolution of the decay time for a period of $> 600\,\mathrm{h}$ is shown in **Fig.** 11.24. It can be observed that even for the extended time period, the decay time was stable,

i.e. no drift was observed. This can be translated into a stable operation of the feedback resistor and the feedback capacitor on the LMFE. It should be also noted, that the centroids of the distributions are in good agreement with those obtained in the calibration measurements.

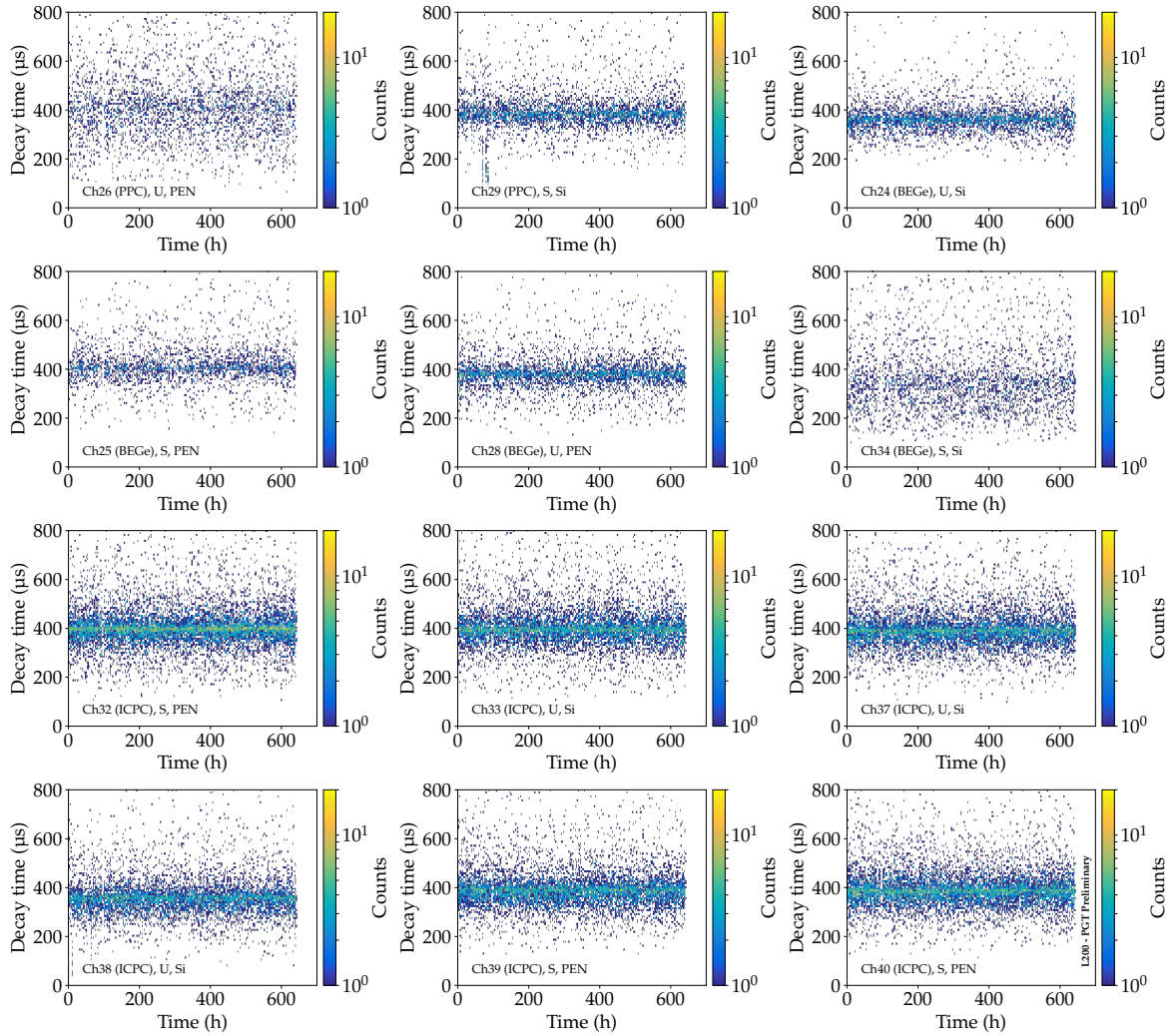

Figure 11.24: Time evolution of the decay time of the detectors in the PGT (physics data). The temporal stability of the decay time indicates that also the feedback resistor and the feedback capacitor of the LMFE remained stable during the measurement.

11.3 BACKUP PREAMPLIFIER FOR LEGEND-200

11.3.1 *Electronic circuit*

The qAMP CSA is a backup solution for LEGEND-200 that was developed at LBNL. The preamplifier encompasses a simple electronic circuit optimized for the operation at cryogenic temperatures in LAr or LN_2. It is based on a fully differential operational amplifier (Analog Devices LTC6363) that features a low input noise (2.9 $nV/\sqrt{Hz}$), a low power consumption (2 mA maximum supply current) and a large bandwidth (35 MHz-3 dB) [271]. A simplified schematic of the electronic circuit is shown in **Fig.** 11.25.

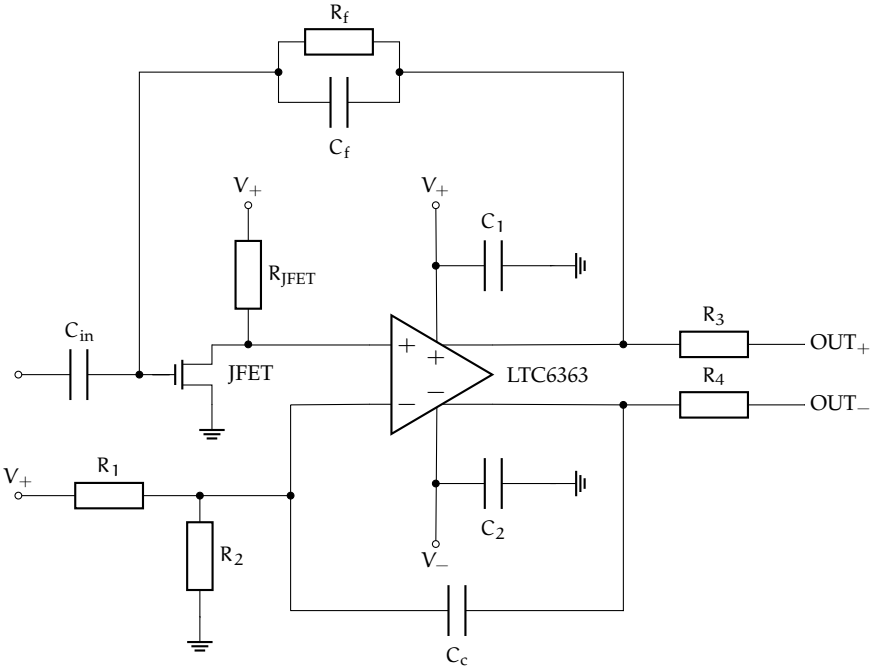

Figure 11.25: Simplified electronic circuit of the qAMP CSA. It is based on the fully differential operational amplifier LTC6363. The front-end circuit consists of a JFET and a resistive-feedback circuit (R_f, C_f).

The front-end circuit and the preamplifier circuit are separated spatially. The front-end circuit consists of an injection capacitor C_{in} (detector or test pulser), a JFET, and a resistive-feedback circuit (R_f and C_f). The signal input is connected to the gate of the JFET. The JFET is powered with a positive voltage V_+ that is connected to the drain via a resistor R_{JFET}. This resistor determines the drain current I_D and can be adjusted to optimize the noise performance and the power consumption of the CSA. For a given voltage V_+, decreasing the resistance R_{JFET} increases the drain current I_D. Up to a certain current I_D, the electronic noise decreases. On the other hand, increasing the drain current results in a higher power consumption. The operational amplifier is powered via the positive and negative voltages V_+ and V_-, respectively. Both voltage supplies are filtered with bypass capacitors (C_1, C_2). The capacitor C_C is used to compensate for the capacitance induced by the use of (long) cables. In particular, it can be used to adjust the bandwidth of the circuit and thus the signal rise time. The higher the compensating capacitance, the slower the circuit. Slowing the circuit down is required when the leading edge of the signal waveform shows an overshoot or even ringing, i.e. a damped oscillation (e.g. due to the use of long cables). The voltage divider consisting of the resistors R_1 and R_2 adjusts the offset between the positive and negative input voltages.

11.3.2 *Measurement results*

OVERVIEW In the framework of this work, the qAMP preamplifier has been characterized and optimized at LBNL in March and April 2019. The optimization work was performed based on the electronic requirements for LEGEND-200, i.e. short signal rise time, low power consumption, large dynamic range, low electronic noise and functionality at cryogenic temperatures. For the characteri-

zation measurements, a dedicated front-end board was used, see **Fig.** 11.26. On the board, the JFET (MOXTEK MX11 or Semefab SF291) is epoxied to a floating pad and the source and drain contacts are ultrasonically wedge-bonded to the traces. The feedback resistor is a discrete SMD resistor with $R_f = 1\,G\Omega$. Its stability was measured with a source meter (Keithley 2450). While at room temperature only small tolerances of the resistance were measured (few percent), at cryogenic temperatures fluctuations of up to 10% were observed. The feedback capacitance C_f and the pulser capacitance C_p are realized as stray capacitances between the traces on the board. For most of the characterization measurements, a compensating capacitance of $C_C = 7\,fF$ was used. Moreover, an arbitrary waveform generator (Agilent 33500B) was used for the generation of input signals. Power for the CSA was provided by a standard power supply (Agilent 3631A). The waveforms were acquired with an oscilloscope (Agilent MSO X 3054A). For the noise measurements, analog (Canberra Spectroscopy Amplifier 2026-X, Ortec Easy-MCA 8k) and digital digitizers (labZY nano MCA) were used.

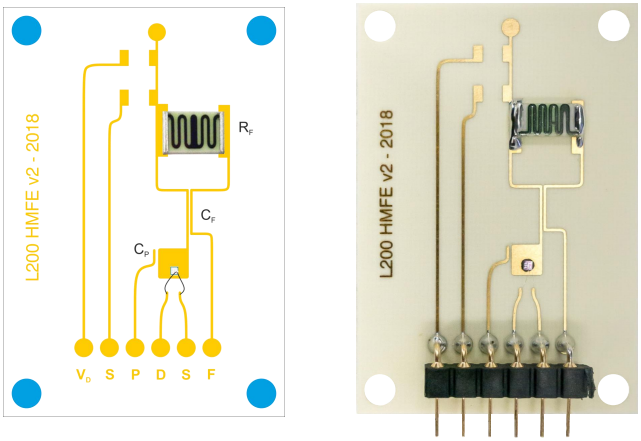

Figure 11.26: Schematic (left) and photograph (right) of the front-end board used for the qAMP CSA characterization measurements. The feedback and pulser capacitances C_f and C_p are realized by the stray capacitances between the traces. The feedback resistance R_f is based on a discrete SMD resistor. Images provided by M. Willers.

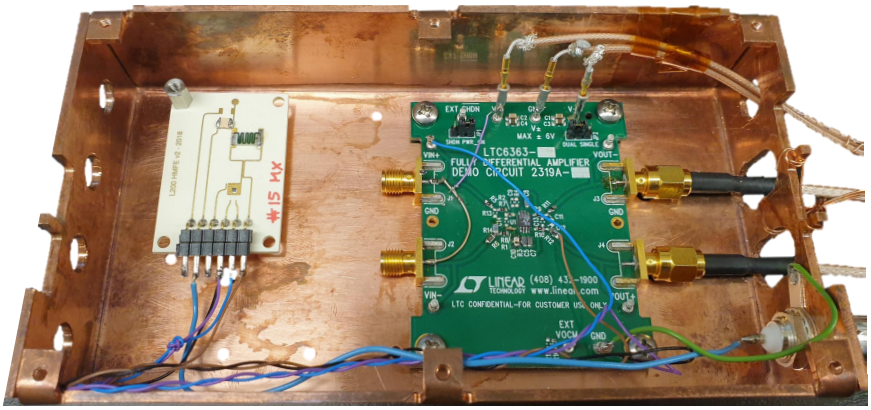

Figure 11.27: Photograph showing the qAMP CSA (green board) together with the front-end board (white board) assembled in a copper box.

To reduce the electronic noise in the system, several noise mitigation techniques were applied, cf. **Ch.** 10.3.4. Most importantly, the front-end and preamplifier boards were installed in a copper box. A photograph of the assembly is shown in **Fig.** 11.27. This not only reduced the 60 Hz power line pickup noise but also the sensitivity of the JFET to ambient light (the cable feedthroughs were covered with aluminum foil). Since the MX11 and the SF291 are bare die JFETs, their gates are directly exposed to light. As a consequence, they behave as phototransistors which are highly

sensitive to light[1]. To account for an appropriate grounding scheme, all ground connections were brought to the same potential to a common ground bus. Moreover, all measurement devices were connected to the same power socket.

The qAMP preamplifier together with the MX11 JFET was characterized at room temperature and at cryogenic temperatures. Unless indicated otherwise, measurement results are presented for the case of cryogenic temperatures. To this end, the copper box including the electronics was submerged in a dewar filled with LN_2. First measurements were carried out to test the functionality of the CSA. For these tests, short cables between the front-end board and the preamplifier, and between the preamplifier and the DAQ system were used. In subsequent measurements, to reflect the conditions encountered in LEGEND-200, the cable lengths were increased ($\sim 80\,\text{cm}$ between the front-end board and the preamplifier, $\sim 2\,\text{m}$ between the preamplifier and the DAQ system).

RISE TIME AND DECAY TIME First, the signal rise time ($10\% - 90\%$) of the differential output signal was measured. Fast signal rise times are crucial for the efficient rejection of background events using PSD techniques, cf. **Ch.** 4.1.2. Depending on the actual test conditions (operating temperature, value of the compensating capacitance C_C, cable lengths, etc.), signal rise times of $80 - 200\,\text{ns}$ were measured. Usually, for measurements at cryogenic temperatures, rise times were faster than at room temperature. **Fig.** 11.28a shows a measurement example.

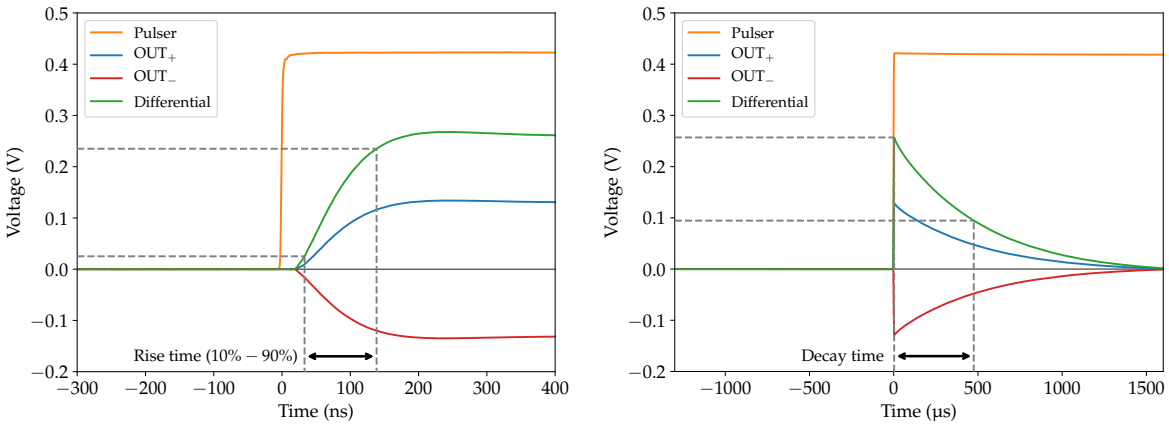

(a) Signal rise time.

(b) Decay time.

Figure 11.28: (a) Measurement of the qAMP CSA signal rise time and (b) decay time. The red and blue traces show the differential outputs of the amplifier (OUT_+, OUT_-). The orange trace indicates the pulser signal, whereas the green trace is the differential signal (difference between OUT_+ and OUT_-). The time window for the estimation of the rise time and decay time is indicated by the vertical dashed grey lines. For reasons of visual clarity, the pulser signal has been scaled by a factor of 1/4. The measurement was conducted at cryogenic temperatures in LN_2. Waveforms were acquired with an oscilloscope.

The decay time τ of the differential output signal was determined with an oscilloscope by measuring the fall time to $1/e \approx 37\%$ of the maximum signal amplitude. Since τ is approximately given by the product of the feedback capacitance C_f and the feedback resistance R_f, cf. **Eq.** (10.1), the feedback capacitance can be derived from the measurement (for a given feedback resistance) via $C_f \approx \tau/R_f$. For most of the measurements, decay times on the order of $\tau = 450 - 550\,\mu\text{s}$ for $R_f = 1\,\text{G}\Omega$ and hence feedback capacitances of $C_f = 450 - 550\,\text{fF}$ were obtained. Usually, for measurements at cryogenic temperatures, decay times were slightly higher than for measurements at room temperature. An example for the decay time determination is shown in **Fig.** 11.28b. It is important to mention that the value of the feedback capacitance (which is based on the stray capacitance between the traces) strongly depends on the environment (temperature, distance to grounding plane, etc.). This also holds true for the pulser capacitance C_p.

1 Light penetrating the JFET induces a leakage current due to the photoelectric effect.

POWER CONSUMPTION Operation at cryogenic temperatures requires a low power consumption of the CSA to avoid bubble formation, i.e. the evaporation of cryogenic liquid due to elevated temperatures. To determine the power consumption of the amplifier, the voltage and the current were monitored. In most of the measurements, depending on the specific conditions, a power consumption of $P \approx 80 - 240\,\text{mW}$ was obtained. At cryogenic temperatures, the power consumption was slightly higher than at room temperature. Furthermore, it turned out that the bulk of the power consumption is required for the operation of the JFET. The qAMP CSA itself only consumes very little power on the order of a few mW. A dedicated measurement was carried out to investigate the phenomenon of bubble formation. To this end, the front-end board and the CSA were dunked into a dewar filled with LN_2. Then, the voltages V_+ and V_- were increased incrementally. Even at the maximum operating voltage of the amplifier ($V = |V_+ + V_-| = 15\,\text{V}$), no bubble formation was observed, neither at the JFET nor at the operational amplifier. In contrast, some bubble formation was present in the region around the connector. This can be explained by the pulser line connection acting as a heat sink: The cable ends were at different temperatures (room temperature versus cryogenic temperatures) resulting in a continuous heat transfer into the cryogenic liquid.

DYNAMIC RANGE In the next step, the dynamic range of the qAMP CSA was investigated. A fixed amount of charge (measured in terms of the input voltage V_{IN}) provided by the pulse generator was injected via the pulser capacitance into the circuit and the corresponding output voltage V_{OUT} was measured. **Fig.** 11.29 shows the amplifier output (both in terms of voltage and energy) as a function of the input voltage. The measurements at room temperature and at cryogenic temperatures show a high linearity over a large input voltage range. However, for input voltages $V_{IN} \gtrsim 1800\,\text{mV}$ at cryogenic temperatures, the leading edge of the waveform started to degrade. Therefore, at cryogenic temperatures the maximum dynamic range was on the order of 10 MeV, while at room temperature the dynamic range went up to 17 MeV.

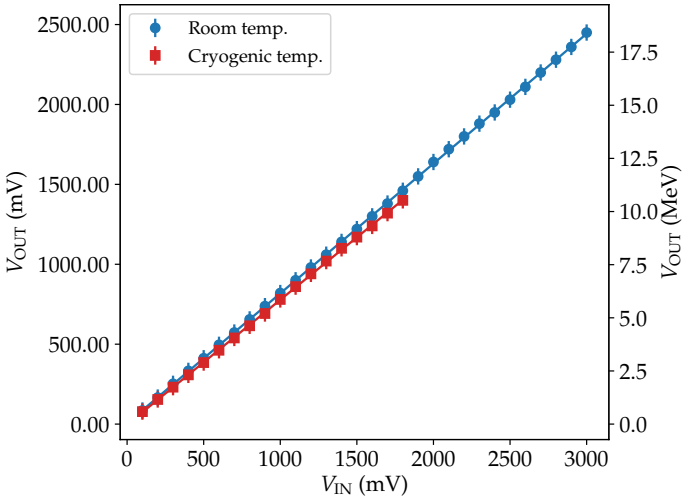

Figure 11.29: Dynamic range of the qAMP CSA at room temperature and at cryogenic temperatures.

NOISE PERFORMANCE The noise performance of the signal readout electronics plays an important role for the energy resolution and for background rejection capabilities via PSD techniques, cf. **Chs.** 4.1.2 and 10.3.5. Several measurements were carried out to investigate the electronic noise of the qAMP CSA. As discussed in **Ch.** 11.3.1, with increasing JFET drain current I_D, the noise first decreases and above a certain value increases again. To determine the optimal drain current for the operation of the MX11 JFET, an additional voltage supply line was temporarily added to the amplifier. In particular, the V_+ power rail normally connected to the JFET drain terminal was replaced by a separate voltage line V_{JFET}. The electronic baseline noise at cryogenic temperatures was determined for various drain currents $I_D = V_{JFET}/R_{JFET}$ at a fixed filter rise time of 15 µs. To this end, the voltage V_{JFET} was increased incrementally and the drain current, as well as the electronic noise were determined for each applied voltage. As can be observed in **Fig.** 11.30, the noise minimum is reached for $I_D \approx 10\,\text{mA}$. Therefore, in the subsequent measurements, the voltages V_+ and V_- were chosen such that the drain current was close to this value.

In the next step, the noise performance at cryogenic temperatures was investigated for different input voltages and filter shaping times (analog shaping). A minimum noise level of about 760 eV FWHM was obtained for the voltages $V_+ = 10.0\,V$, $V_- = -4.0\,V$, and a shaping time of 12 µs, see **Fig.** 11.31a. It can be also observed that for a lower voltage V_+ (being equivalent to a reduced JFET drain current), the noise level increases.

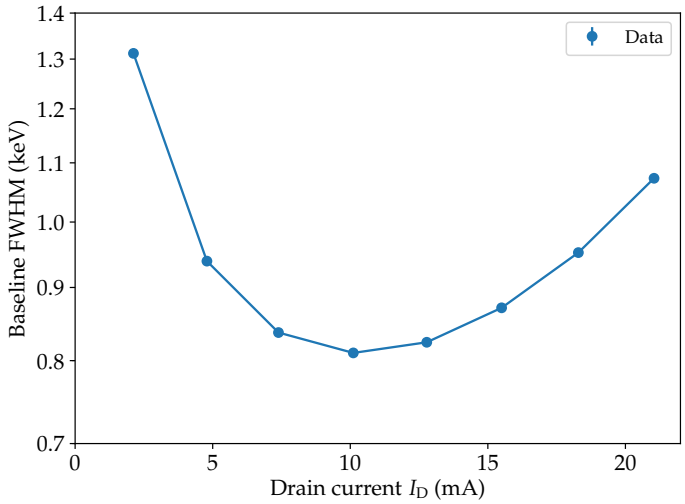

Figure 11.30: Baseline noise performance of the qAMP CSA as a function of the JFET drain current (normalized to the first measurement point). A minimum noise is obtained for a drain current of $I_D \approx 10\,mA$. Data were acquired with a labZY nanoMCA.

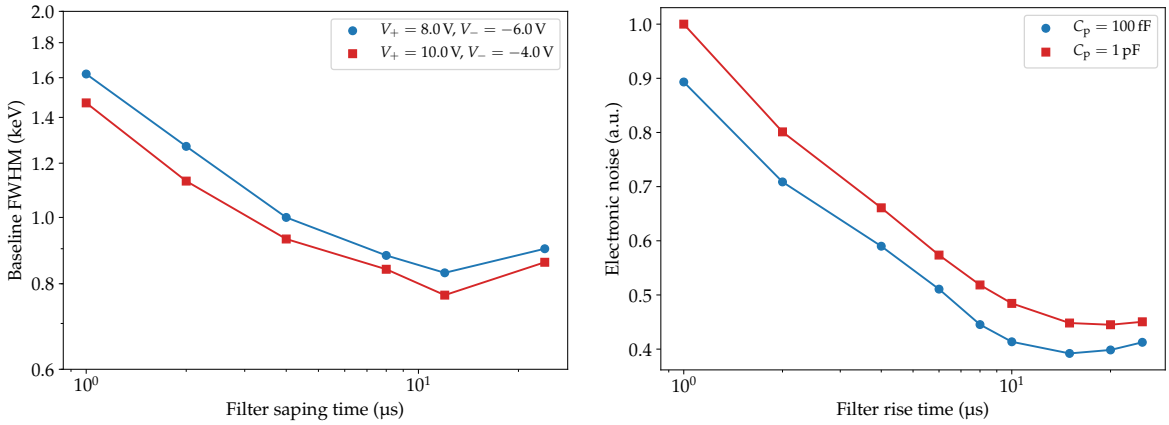

(a) Impact of supply voltage on noise.

(b) Impact of input (pulser) capacitance on noise.

Figure 11.31: (a) Noise performance of the qAMP CSA at different operating voltages, and (b) for different input (pulser) capacitances. In the latter case, noise levels were normalized to account for the strong environmental dependence of the input capacitance. The performance improves for higher voltages V_+, and for smaller pulser capacitances C_P.

The electronic noise of signal readout electronics is proportional to the CSA input capacitance, cf. **Ch.** 10.3.3. Consequently, any change in the input capacitance directly affects the noise. In the qAMP CSA characterization measurements it was observed that the input (pulser) and feedback stray capacitances on the front-end board are highly sensitive to their environment (operating temperature, distance to grounding plane, etc.). Depending on the actual environment, the decay time and hence the feedback capacitance varied[2] by up to 30%. The environmental dependence of the in-

2 The strong dependence of the stray capacitance on the measurement environment was verified by measuring the decay time in two different scenarios. In the first case, the front-end board was mounted freely (no bottom coverage), whereas in the second case it was mounted on an aluminum plate. In the latter case, the capacitance decreased by about 29% compared to the first one.

put capacitance makes the energy calibration for the noise determination prone to large uncertainties. Therefore, for the ease of comparability, some of the measurement results are expressed in terms of relative noise values (normalized by the maximum value). The dependence of the noise on the input capacitance was examined in a dedicated measurement, in which two different pulser capacitances were used, see **Fig.** 11.31b. It can be observed that for higher pulser (input) capacitances, electronic noise levels are higher.

COMPATIBILITY WITH OTHER DEVICES The simple and modular design of the electronic circuit makes it possible to easily test the compatibility and performance of the qAMP CSA with other devices. First, the MOXTEK MX11 JFET was replaced by a Semefab SF291 JFET. Similar characterization measurements as described above were carried out. For the quantities signal rise time, power consumption and dynamic range comparable results were obtained. The noise performance of the qAMP CSA with the SF291 JFET was slightly better, see **Fig.** 11.32.

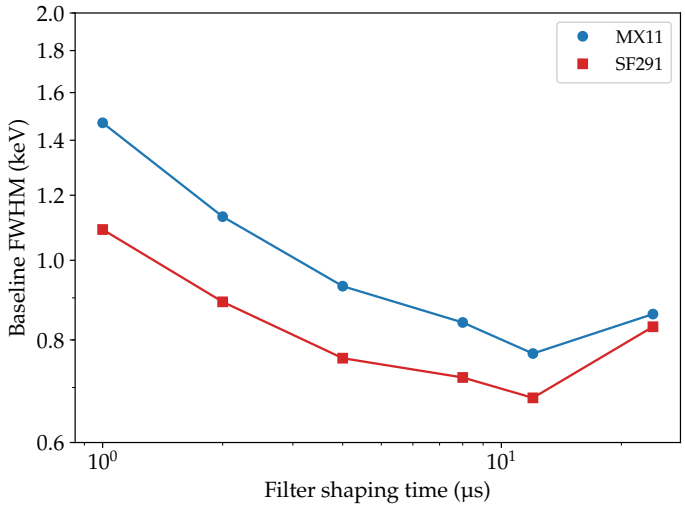

Figure 11.32: Comparison of the qAMP CSA noise performance for different JFETs (MOXTEK MX11 and a Semefab SF291) at cryogenic temperatures.

Furthermore, the qAMP CSA was tested with other operational amplifiers (Texas Instruments THS4150 and THS4130) having similar electronic properties as the LTC6363 device. These devices have a higher maximum operating voltage ($V = |V_+ + V_-| = 30\,V$) enhancing the flexibility of operating the CSA. However, the characterization measurements revealed that the performance of the qAMP CSA equipped with the THS4150 device was slightly worse. In particular, the signal rise time and noise levels were higher.

11.3.3 *Comparison to LEGEND-200 baseline preamplifier*

Performance metrics of the qAMP CSA were compared in detail to those of the LEGEND-200 baseline CSA, the CC4 preamplifier, cf. **Ch.** 11.1.2. The characterization measurements of the CC4 preamplifier were performed in the same way and under the same conditions as those of the qAMP amplifier. In particular, the same front-end board and the same electronic devices (power supply, pulse generator, etc.) were used. In addition, the preamplifiers were installed in the same copper shielding box. A summary of the measurement results at cryogenic temperatures can be found in **Tab.** 11.2. Furthermore, a comparison of the electronic noise levels (analog shaping) is shown in **Fig.** 11.33. The decay time, the dynamic range, as well as the noise performance of both amplifiers are comparable. Signal rise times of the qAMP CSA are slightly higher. In contrast, it features a lower power consumption.

Table 11.2: Comparison of the electronic properties of the qAMP and CC4 amplifiers at cryogenic temperatures. Decay times are predetermined by the front-end circuit (feedback capacitor and resistor). The power consumption values are given for the case of the absence of an active receiver.

Property	qAMP	CC4
Rise time (10% – 90%)	80 – 200 ns	50 – 70 ns
Decay time	450 – 550 µs	400 – 500 µs
Dynamic range	~ 10 MeV	~ 9 MeV
Minimum noise		
⋆ Analog shaper ($\tau_s = 12\,\mu s$)	760 eV FWHM	680 eV FWHM
⋆ Digital shaper ($\tau_r = 15\,\mu s$)	1080 eV FWHM	1100 eV FWHM
Power consumption	80 – 240 mW/ch	300 mW/ch

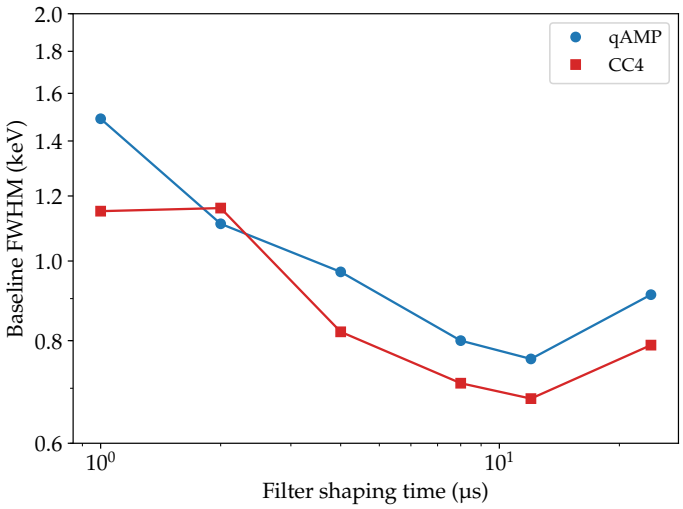

Figure 11.33: Comparison of the noise performance of the qAMP and CC4 CSAs at cryogenic temperatures.

11.4 CONCLUSIONS

Within the scope of this work, two important contributions have been made to the development of signal readout electronics for LEGEND-200: 1) The analysis of the Post-GERDA test calibration and physics data, and 2) the comparison of performance metrics of the CC4 preamplifier to those of a backup CSA.

The PGT data analysis revealed that most of the detectors showed a very good performance. This includes a high stability of parameters such as the decay time, an excellent energy resolution, and a reasonable PSD performance. Of particular relevance is the improved noise situation compared to the GERDA experiment. Most likely, this can be associated with the use of improved signal readout electronics consisting of two spatially separated amplification stages. A low-noise environment is especially important for the ICPC detectors so that a drift time correction for charge trapping can be applied (due to their specific geometry, ICPC detectors are particularly subject to CT). While this was not possible in the case of GERDA, the feasibility of applying the correction was validated for the PGT data. The analysis of the calibration and physics data further indicated a very stable operation of the LMFE (stable feedback resistor and feedback capacitor). In contrast, some issues with the test pulsers were identified. Finally, a background analysis of the physics data in the signal ROI showed enhanced background levels compared to those observed in GERDA, as expected.

The backup amplifier for LEGEND-200, the qAMP CSA, was characterized extensively in bench tests at LBNL. The measurements showed that the amplifier features a comparably low electronic noise, fast signal rise times, a large dynamic range, and a low power consumption. The simplicity and modular design of the electronic circuit also enabled the investigation of slightly modified versions of the amplifier (qAMP equipped with different JFETs, operational amplifiers). Finally, the qAMP CSA was compared to the LEGEND-200 baseline design amplifier, the CC4 preamplifier. A similar performance was obtained.

12

SIGNAL READOUT ELECTRONICS FOR LEGEND-1000

To achieve the ambitious sensitivity on the $0\nu\beta\beta$ decay half-life targeted by LEGEND-1000, the background in the signal ROI has to be decreased even further with respect to LEGEND-200. To reduce the background originating from the signal readout electronics, the collaboration is actively developing an ASIC-based readout scheme. An overview of the technology is given in **Ch.** 12.1. The investigation of a commercially available ASIC together with a PPC germanium detector is presented in **Ch.** 12.2. The results of characterization measurements of a first prototype ASIC for LEGEND-1000 developed at LBNL are reported in **Ch.** 12.3. Finally, a brief summary of the main results can be found in **Ch.** 12.4.

12.1 READOUT ASIC FOR LEGEND-1000

One of the main challenges when scaling up a ^{76}Ge-based $0\nu\beta\beta$ decay experiment is the increased number of individual detectors, resulting in an increase of instrumentation components, such as amplifiers, cables, and connectors. All these components are potential background sources and hence need to be of ultra-high purity and low mass [14]. In LEGEND-1000, the baseline design is to use a readout scheme based on state-of-the-art ASIC technology. The technology enables the integration and miniaturization of the readout electronics components into a single low-mass chip. The main advantage for $0\nu\beta\beta$ decay searches compared to conventional amplification solutions is a potentially higher per-channel radiopurity (e.g. ideally no RC-feedback components, fewer supply voltages, etc.). In principle, clean materials can be used for the production of the chip which allows for an installation of the readout electronics very close to the detectors. Consequently, lower electronic noise levels can be achieved since a high amplification gain is possible before sending the analog signal over a long distance to the DAQ system [16]. Moreover, the technology alleviates the need for a second-stage preamplifier and hence the spatial separation of the CSA. This leads to lower background levels and enhanced electronics properties (faster signal rise times, etc.). A preliminary design study of the ASIC assembled on top of a detector in LEGEND-1000 is shown in **Fig.** 12.1.

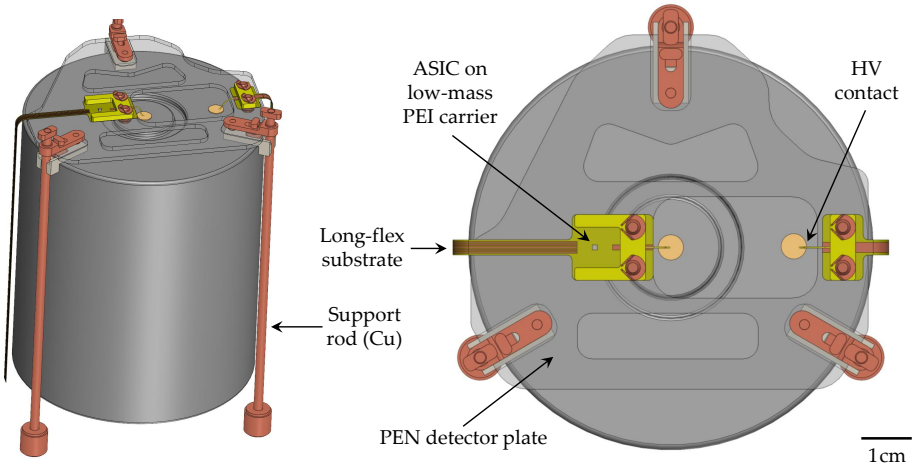

Figure 12.1: Preliminary design study of the ASIC assembled on top of an ICPC detector (side and top view). The ASIC is located on a long-flex substrate. It is connected to the readout electrode of the detector via a wire bond. The figure also shows the detector holding plate (made from PEN) and the corresponding support rods made from ultra-pure copper. The scale only applies to the top view. Renderings provided by M. Busch.

DESIGN REQUIREMENTS For the deployment of a readout ASIC in LEGEND-1000, several requirements have to be fulfilled. Most of the aspects already discussed in **Ch.** 10.2.1 also apply in the ASIC case. This includes low electronic noise levels, a low threshold, a large dynamic range, a low input and feedback capacitance, a sufficient bandwidth, small dimensions and mass, radiopure material and a clean production process, a differential signal output, functionality at cryogenic temperatures, robustness to electrostatic discharges, and a low power consumption. One of the main challenges of designing an ASIC for LEGEND-1000 is to avoid additional external components. Typically, ASICs require external bypass capacitors to reduce the voltage supply noise and to provide a low-impedance supply whenever transient voltage spikes occur [272]. The effectiveness of these capacitors decreases with increasing distance to the ASIC. Therefore, they need to be mounted as close as possible to the CSA. Unfortunately, the bypass capacitors also increase the amount of radioactive material close to the detectors. Usually, they are not clean enough to fulfill the stringent radiopurity requirements [14, 16]. Therefore, it is planned to design an ASIC that is intrinsically stable against power supply noise. To this end, the use of on-chip low-dropout (LDO) regulators is intended to generate stable voltages within the device. Another challenge in the ASIC design arises from the requirement to integrate the reset mechanism into the chip, cf. **Ch.** 10.2.4. In particular, the corresponding stage needs to be designed carefully to avoid additional electronic noise.

12.2 CUBE ASIC

12.2.1 *Overview*

To test the performance of ASIC-based signal readout electronics for ^{76}Ge-based $0\nu\beta\beta$ decay searches, the PONaMa1 HPGe detector was instrumented with a commercially available CUBE ASIC obtained from the company XGLab SRL. The CUBE ASIC is a single-channel low-noise CSA based on CMOS technology, cf. **Ch.** 10.2.3. It was initially designed for low-capacitance (several pF) silicon drift detectors [22]. In a first study of the CUBE ASIC (revision `PRE_024`) with a low-capacitance mini PPC detector ($C_D = 0.26\,\text{pF}$), a noise performance of $5.6\,e^-$ RMS was obtained [252]. With no capacitive load at the input, the ASIC investigated in this work (revision `PRE_042`) has a noise performance of $35.5\,e^-$ RMS at room temperature and is optimized for operation with detectors having higher capacitances [23]. An image of the chip and an annotated illustration of its wire bonding pads is shown in **Fig.** 12.2.

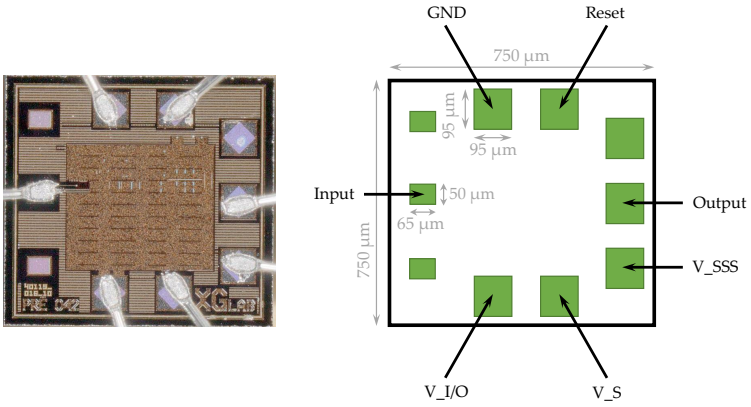

Figure 12.2: The left figure shows a close-up of the CUBE ASIC. The chip is connected to the traces on a printed circuit board via several wire bonds. The right figure shows the dimensions of the ASIC and the bond pad assignment. The dimensions of the input pad ($50\,\mu\text{m} \times 65\,\mu\text{m}$) are smaller than those of the other pads ($95\,\mu\text{m} \times 95\,\mu\text{m}$) to reduce the input capacitance as much as possible. Published in [16].

The CUBE ASIC is an electrostatic discharge sensitive device (ESD) and all bonding pads except for the input pad have a built-in ESD protection. This is due to the fact that an input protection circuit would add electronic noise. The chip measures $750\,\mu\text{m} \times 750\,\mu\text{m} \times 250\,\mu\text{m}$ and has a mass of $\sim 0.33\,\text{mg}$. It has an input capacitance which is optimized for the operation of detectors with

capacitances in the range $0.5 \leqslant C_D \leqslant 3.0\,\text{pF}$. The device is functional at cryogenic temperatures down to 50 K and has a maximum power consumption of 60 mW [23]. The internal feedback capacitance of $C_f = 500\,\text{fF} \pm 10\%$ translates into a large dynamic range which can be calculated according to

$$E_{DR} = V_{DR} \cdot C_f \cdot \frac{\epsilon}{e}. \tag{12.1}$$

Here, V_{DR} denotes the dynamic range in terms of voltage, ϵ the average energy necessary for the creation of an electron-hole pair, cf. **Ch.** 3.2, and e the elementary charge. With $V_{DR} \approx 2.2\,\text{V}$ and $\epsilon(T = 77\,\text{K}) = 2.96\,\text{eV}$, a dynamic range of $E_{DR} \gtrsim 10\,\text{MeV}$ is obtained, in good agreement with the LEGEND requirements.

The CUBE ASIC requires three supply voltages: a core supply voltage (`V_S`), a voltage supply for the input current source (`V_SSS`), and one supply for the input and output sections (`V_I/O`). Each of these supplies needs at least one external bypass capacitor to reduce the voltage supply noise, the one for V_S being the most important one. By default, the CUBE ASIC is operated in a pulsed reset mode, cf. **Ch.** 10.2.4. However, in combination with a suitable vacuum-compatible feedback resistor, the chip can be also operated in a continuous reset mode.

For our measurements, a customized printed circuit board (PCB) accommodating the CUBE ASIC was designed in close collaboration with XGLab SRL. **Fig.** 12.3 shows a drawing and the dimensions of the ASIC PCB, as well as its mounting on top of the PPC HPGe detector. The board is made-up of four different layers. On top of the FR4 substrate, there are 35 µm-thick copper traces for routing. These traces are covered by an electroless nickel immersion gold (ENIG) surface finish. It consists of a 5 µm-thick electroless nickel plating covered with a layer of immersion gold with a thickness of 100 nm. Finally, there are layers of soldermask (thickness: ~10 µm) and silkscreen (thickness: ~10 µm) on top of the ENIG finish. The ASIC is epoxied with a non-conductive glue to a floating pad on the PCB. Pads on the ASIC are ultrasonically wedge-bonded to bond pads on the PCB with 25 µm Al(1% Si) wire.

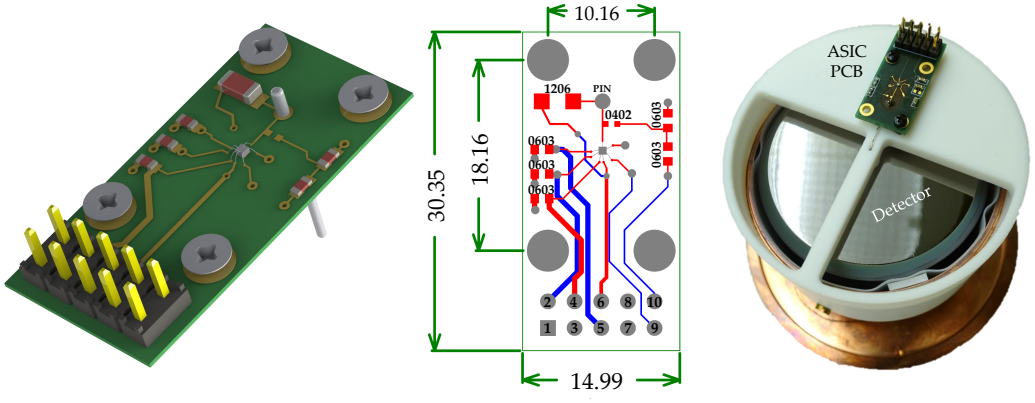

Figure 12.3: Printed circuit board hosting the CUBE ASIC. The left figure shows a three-dimensional rendering of the board. The figure in the center shows the dimensions of the board (in mm), and the footprints for the electronic components (in inch). Traces on the top and bottom surface are indicated by the red and blue solid lines, respectively. The right figure shows the ASIC board mounted on a PTFE structure above the PPC HPGe detector. Published in [16].

The electronic circuit of the PCB hosting the ASIC is illustrated schematically in **Fig.** 12.4. To filter the three supply voltages, it encompasses the bypass capacitors C_1, C_2 and C_3, for which standard ceramic capacitors (footprint[1] 0603, dielectric material X5R) with a capacitance of $10\,\mu\text{F} \pm 10\%$ are used. Moreover, the two resistors R_1 and R_2 (footprint 0603) can be used as a voltage divider for testing the functionality of the ASIC with an external pulse generator. The pulser signal is coupled into the input track of the preamplifier via the voltage divider and the parasitic capacitance $C_4 \approx 30 - 50\,\text{fF}$ between the pads of an 0402 footprint. The supply voltages ($\pm 9\,\text{V}$) for the CUBE ASIC are provided by an external biasing board. The board (revision `Rev9`) also filters the supply voltages, provides reset logic for the ASIC, and buffers the output signal with a certain gain (factor ~4).

1 Within this work, footprints are given in units inch (imperial system).

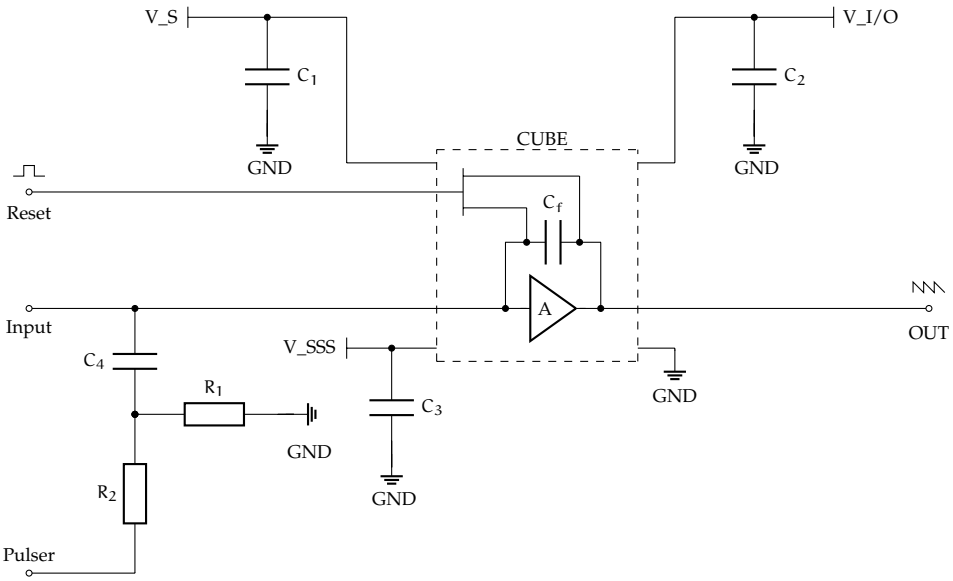

Figure 12.4: Electronic circuit of the PCB hosting the CUBE ASIC. The amplifier requires three supply voltages (`V_S`, `V_SSS`, `V_I/O`). Each of those is filtered with a bypass capacitor (C_1, C_2, C_3). For functionality tests, the input of the ASIC is connected to a pulser input via a voltage divider (R_1, R_2). By default, the chip is operated in a pulsed reset mode, i.e. the feedback capacitor (C_f) is discharged by an external logic signal.

12.2.2 *Measurement setup*

For the investigation of signal readout electronics for LEGEND, a dedicated test stand was designed and built, the CUBE^3 test facility at Technical University of Munich (TUM). Photographs of the experimental setup are shown in **Figs.** 12.5 and 12.6.

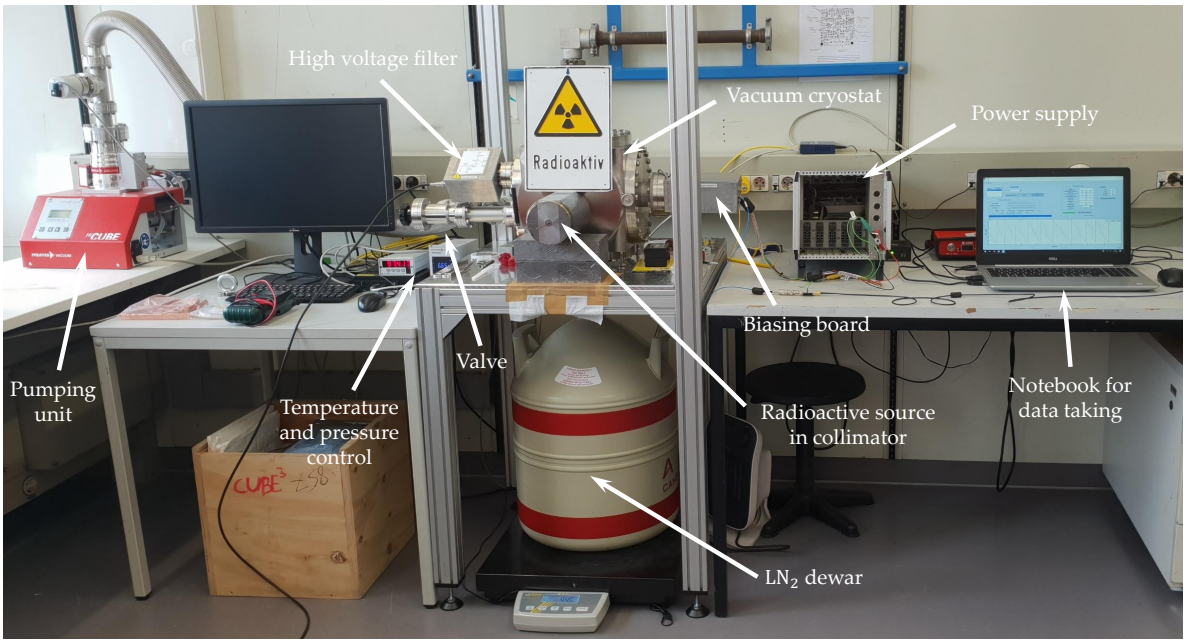

Figure 12.5: Overview of the CUBE^3 test facility used for the investigation of signal readout electronics for LEGEND. The HPGe detector is mounted in a vacuum cryostat and cooled via a copper holding structure connected to a dewar filled with liquid nitrogen (LN_2). The cryostat is evacuated using a pumping unit. Several flanges provide access to its interior.

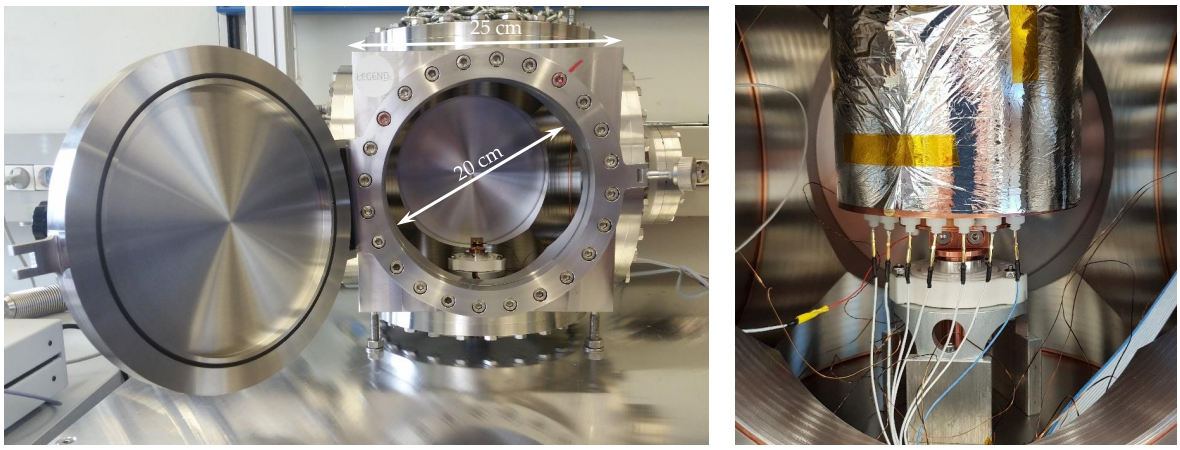

Figure 12.6: Photographs showing details of the CUBE^3 test facility. The left photograph shows an overview of the vacuum cryostat (no detector mounted), whereas the right photograph shows a zoom of its interior with the detector installed. It is surrounded by a copper IR shield and superinsulation foil.

VACUUM CRYOSTAT The core of the setup is a vacuum cryostat that can accommodate a HPGe detector and the signal readout electronics, see **Fig.** 12.7. It is made from stainless steel and provides experimental access via several flanges. Two of the flanges are used as feedthroughs for the detector bias voltage and the signal readout connections. In addition, one of the flanges hosts a feedthrough connected to a vacuum pump. The front side flange is equipped with a quick lock door for easy and fast access to the interior of the cryostat. The germanium detector is cooled via its surrounding copper holding structure which is thermally anchored to a copper cold finger. The cold finger is inserted into a dewar filled with LN_2. The temperature inside the cryostat is measured with three silicon diodes (Lake Shore DT-670). They are installed on the cold finger, on the inner bottom and on the outer top surface of the infrared shield, see **Fig.** 12.7. During the CUBE ASIC characterization measurements, the temperature of the detector support structure was stable at a level of ~98 K (measured with a silicon temperature diode at the bottom of the IR shield). The cryostat is evacuated using a pumping unit (Pfeiffer HiCUBE 80) consisting of a diaphragm forepump and a turbomolecular pump (TMP). After several hours of pumping, a vacuum on the order of 10^{-7} mbar can be obtained. The pressure inside the system is measured with two pressure gauges. One of the gauges is installed above the TMP, while the other gauge is mounted in close proximity to the cryostat. The cryostat and the pumping unit are separated by a vacuum valve. To avoid microphonic noise during the measurements, the valve can be closed which enables to turn off the vacuum pump during data taking.

DETECTOR The CUBE ASIC was characterized together with the PONaMa1 detector, cf. **Ch.** 6.2. In the CUBE^3 test facility, the detector was installed with the point contact facing up in a customized detector mount. Its side walls were insulated from the copper cylinder through a thin sheet of PTFE insulation around the perimeter. The detector was shielded against IR radiation (emitted mainly by the vacuum cryostat walls) by a thin cylindrical copper hat surrounding the holding structure, see **Fig.** 12.7. Moreover, a cryogenic superinsulation foil wrapped around the IR shield acted as thermal insulation, see **Fig.** 12.6. The n^+ electrode of the detector was connected to the HV module (iseg NHQ 204M) via a spring-loaded pin (Fixtest series 29) located at the detector bottom surface. To reduce high-frequency voltage fluctuations introduced by the bias voltage power supply, an RC low-pass filter (100 MΩ, 10 nF) was used. It was assembled in an aluminum box and directly attached to one of the side flanges, see **Fig.** 12.8.

DATA ACQUISITION Data from the detector were acquired using a Struck SIS3301 FADC 14-bit digitizer, the same FADC that was also used for data acquisition in the GERDA experiment [215]. The digitizer samples data with a frequency up to 100 MHz. For the ASIC characterization measurements, two kinds of waveforms were acquired at the same time: a low-frequency waveform (25 MHz) in the time interval $0 - 163.84$ µs (corresponding to 4096 samples), and a high-frequency waveform (100 MHz) around the leading edge in the time interval $76.415 - 86.415$ µs (correspond-

ing to 1000 samples). In both cases, the acquisition window was divided into about one half of pre-trigger and one half of post-trigger region, with the start time t_0 of the waveform located at $t_0 \approx 81\,\mu s$. All waveform traces were stored on disk for offline data analysis.

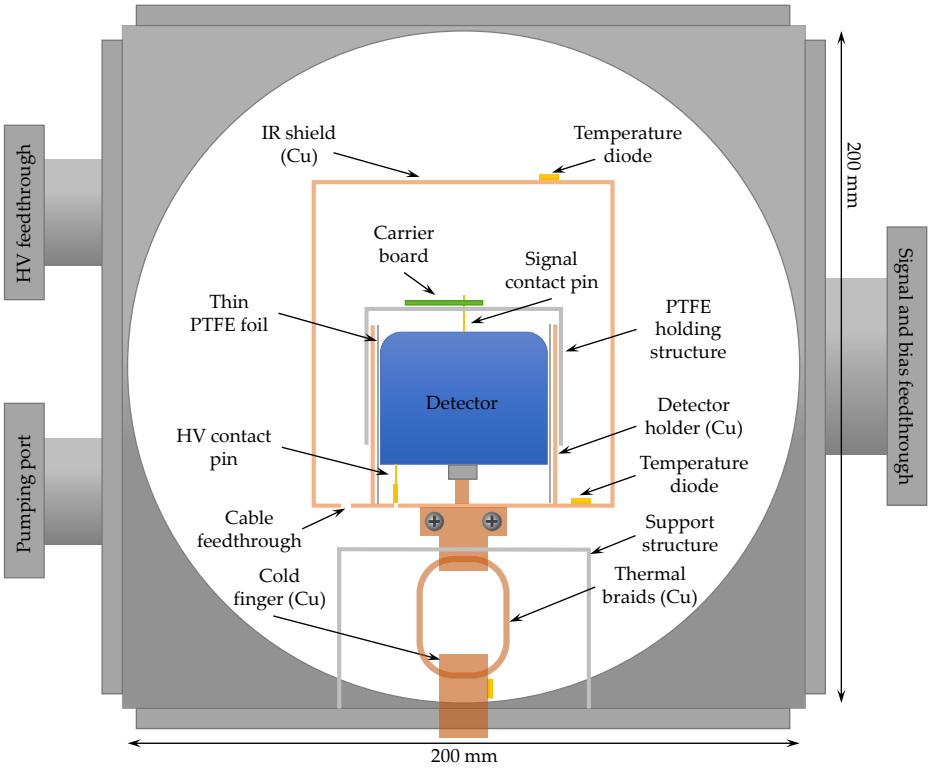

Figure 12.7: Simplified sectional view of the CUBE^3 cryostat. For visual clarity, details of the detector holding structure, readout electronics, and of the cold finger are not shown. Published in [16].

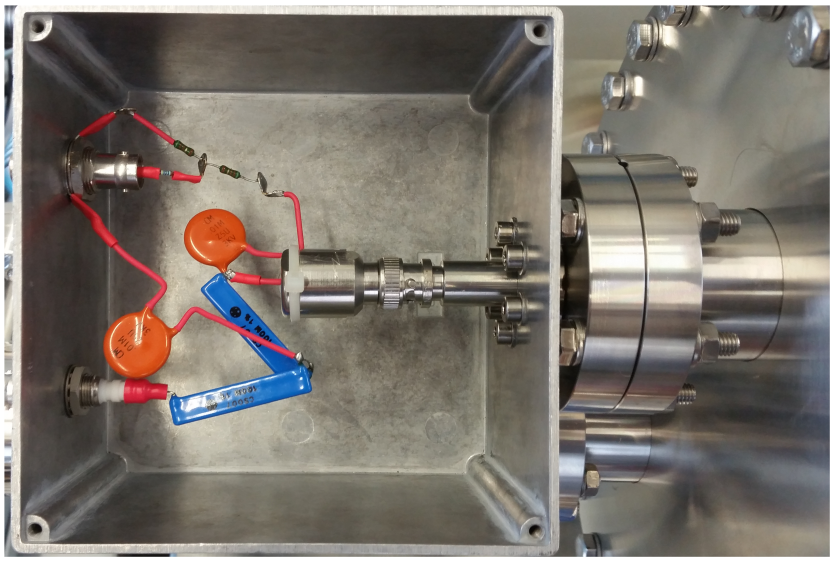

Figure 12.8: Photograph of the high voltage filter used to reduce voltage fluctuations induced by the power supply. To ensure an appropriate grounding connection, the box containing the filter is directly connected to one of the feedthroughs of the CUBE^3 cryostat.

12.2.3 *Measurement results*

In the following paragraphs, the measurement results obtained with the CUBE ASIC operated together with the PONaMa1 HPGe detector are discussed in detail. For the data analysis, the GERDA layout for input output (GELATIO) framework has been used. GELATIO is a ROOT-based software package that has been developed for the GERDA experiment [241]. A standard analysis chain with one channel and a slightly adapted GERDA initialization file has been used. The analysis procedures are similar to those described in **Ch.** 6.5.

LEAKAGE CURRENT The leakage current I_L has an important impact on the electronic noise, with higher leakage currents resulting in higher noise levels, cf. **Ch.** 10.3.3. Hence, dedicated measurements were performed to determine the leakage current of the experimental setup. Several pulsed reset waveforms were acquired with an oscilloscope (Wavesurfer 3024 Teledyne LeCroy) and the slope dV/dt (V: voltage, t: time) of the linearly decreasing waveform ramps (corresponding to the constant collection of holes) was estimated, see **Fig.** 12.9a. The leakage current was then calculated using the equation

$$I_L = C_f \cdot \frac{dV}{dt} \cdot \frac{1}{G}, \tag{12.2}$$

where $G = 4.03 \pm 0.47$ denotes an additional gain introduced by the biasing board of the ASIC readout, cf. **Ch.** 12.2.1. The dependence of the leakage current on the bias voltage is shown in **Fig.** 12.9b. When the detector is not yet fully depleted, the leakage current increases with increasing bias voltage. Thereupon, for bias voltages up to $V_B \approx 1600\,V$, the leakage current stays approximately constant. For higher bias voltages, an increasing backward leakage current can be observed. For the measurement results presented in the following, the detector was operated at a bias voltage of $V_B = 1500\,V$. At this voltage, the leakage current was at a reasonably low level of $I_L \approx 15\,pA$. At the time when the energy resolution measurements were carried out, see below, the leakage current was stable at a level of $10 - 20\,pA$.

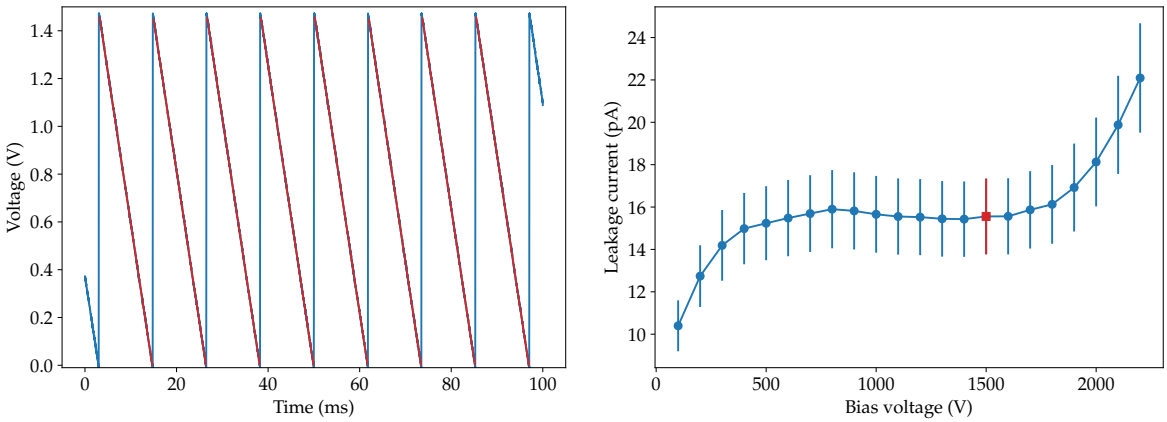

(a) Fit of waveform slope.

(b) Leakage current vs bias voltage.

Figure 12.9: (a) Determination of the leakage current by estimating the slope of the waveform ramps via linear fits. (b) Leakage current as a function of the detector bias voltage. Error bars result from the uncertainties of the feedback capacitance, waveform slope, and gain. For the measurements discussed in the following, the detector was operated at a bias voltage of $V_B = 1500\,V$ (indicated by the red square measurement point). Published in [16].

SIGNAL RISE TIME One of the key parameters for a successful application of PSD techniques is the signal rise time, cf. **Ch.** 4.1.2. Typically, this quantity is defined as the time taken by a signal to change from 10% to 90% of the maximum amplitude of the leading edge. For efficient PSD capabilities, the rise time needs to be fast enough such that MSEs (background events) can be resolved in the time domain (for rise times of several µs, the double peak structure of these events in the current signal smears out). The specification for the first phase of LEGEND foresees rise times ($10\% - 90\%$) faster

than 100 ns with potential for improvements in future phases. A dedicated measurement without a detector was carried out to measure the rise time of the CUBE ASIC, see **Fig.** 12.10. Rise times as low as 15 ns were obtained.

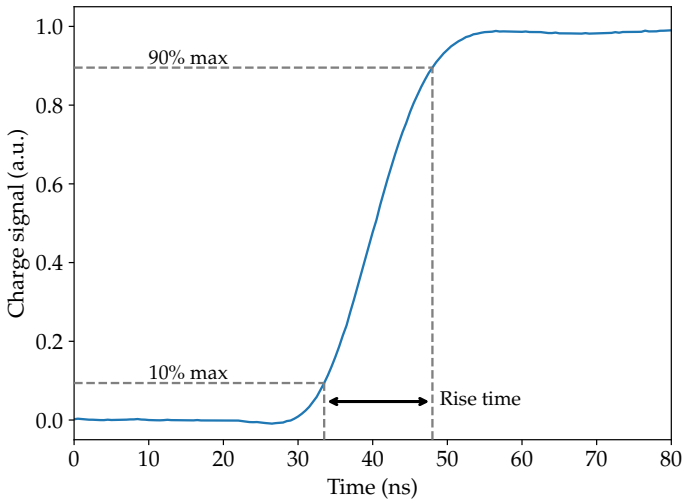

Figure 12.10: Signal rise time (10% – 90%) of the CUBE ASIC (no detector connected). Values as low as 15 ns were measured. Published in [16].

ELECTRONIC NOISE Low electronic noise of signal readout electronics is of major importance for optimizing the energy resolution and the detection threshold of the measurement system, cf. **Ch.** 10.3.5. Furthermore, along with the signal rise time the electronic noise is a key parameter for efficient PSD capabilities. While low-frequency noise ($\mathcal{O}$(kHz)) mainly influences the energy resolution, high-frequency noise ($\mathcal{O}$(MHz)) has an impact on the PSD performance. The relevant frequency range for the application of PSD techniques is given by the necessity of resolving the temporal separation of MSE charge clouds with values in the range 150 – 500 ns, which translates into a frequency range of 2.0 – 6.5 MHz [273].

The noise performance of the CUBE ASIC together with the PONaMa1 detector was determined in terms of the baseline noise. To this end, a trapezoidal filter with varying filter rise times and a fixed flat top time was applied to the waveform baselines. The obtained baseline noise curve is shown in **Fig.** 12.11. At a filter rise time of 4 µs, a minimum baseline noise of 655 eV FWHM was obtained. Moreover, at the reference filter rise time of 1 µs, a baseline noise of about 820 eV FWHM (corresponding to 118 e^- RMS) was measured. Keeping in mind the presence of the additional detector and bonding capacitance, this value is in good agreement with the specified preamplifier noise performance. In summary, fast signal rise times and low noise levels make the CUBE ASIC a well-suited device for the application of PSD techniques [16].

ENERGY RESOLUTION The excellent energy resolution of HPGe detectors is one of the main advantages of ^{76}Ge-based $0\nu\beta\beta$ decay searches, cf. **Ch.** 2.4.4.2. The energy resolution is closely related to the noise performance of the signal readout electronics, i.e. high noise levels directly translate into poor energy resolutions, cf. **Ch.** 10.3.5. Therefore, dedicated measurements were carried out to investigate the energy resolution of the PONaMa1 detector together with the CUBE ASIC. To this end, the detector was irradiated with a strong (A_0 = 250 kBq), collimated ^{228}Th calibration source. The source was positioned outside the vacuum cryostat in front of one of the side flanges. The signal rate was on the order of 350 cts/s. An example of the energy spectrum measured during a typical ^{228}Th calibration run is shown in **Fig.** 12.12a.

The energy was calibrated in a similar way as described in **Ch.** 6.6. Moreover, the energy resolution was determined by numerically extracting the FWHM from several given gamma lines in the spectrum. The relationship between the energy resolution and the energy was finally approximated with the function in **Eq.** (10.21). As can be seen from **Fig.** 12.12b, an excellent energy

resolution over a wide energy range was obtained. In the signal ROI at the $Q_{\beta\beta}$-value and at the 2.6 MeV ^{208}Tl gamma peak, energy resolutions of about 2.3 keV FWHM and 2.6 keV FWHM were obtained, respectively. These values match the design specifications of LEGEND-1000, with a targeted energy resolution of 2.5 keV FWHM at the $Q_{\beta\beta}$-value.

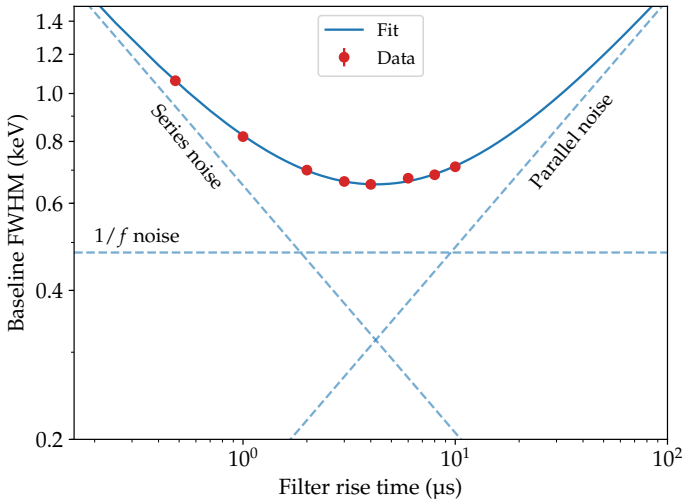

Figure 12.11: Baseline noise performance of the CUBE ASIC with the PONaMa1 HPGe detector. A minimum baseline noise of 655 eV FWHM was obtained at a filter rise time of 4 µs. The dashed lines in the plot correspond to the series (down-sloping), parallel (up-sloping), and 1/f (horizontal) noise contributions. Published in [16].

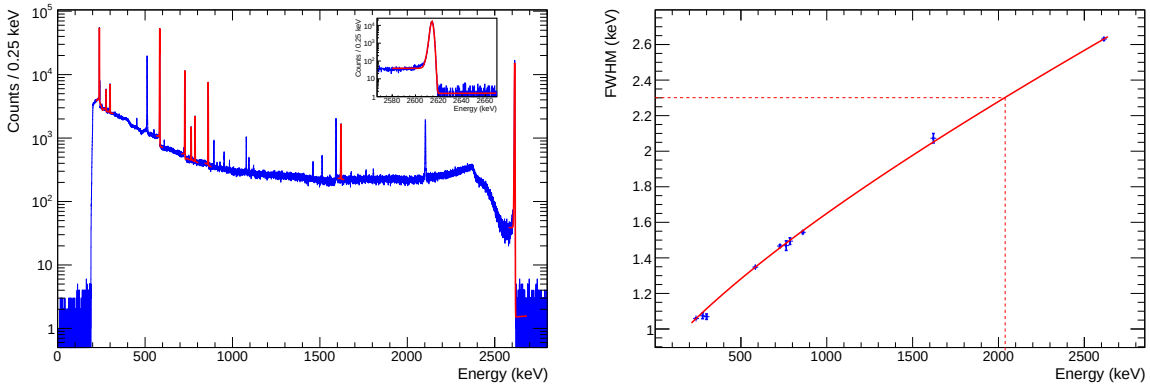

(a) ^{228}Th energy spectrum.

(b) Energy resolution.

Figure 12.12: (a) Energy spectrum and (b) resolution curve acquired during a ^{228}Th calibration run with the PONaMa1 detector and the CUBE ASIC. The energy resolution of about 2.3 keV FWHM in the ROI at $Q_{\beta\beta}$ = 2039 keV is indicated by the dashed lines. At the 2.6 MeV ^{208}Tl gamma line (see inset), an energy resolution of about 2.6 keV FWHM was obtained. Error bars correspond to the fit uncertainties of the standard deviations. Published in [16].

PULSE SHAPE DISCRIMINATION PERFORMANCE The PSD performance of the PONaMa1 HPGe detector together with the CUBE ASIC was validated in a ^{228}Th calibration measurement. The normalized A/E distribution, corrected for a slight linear energy dependence, is shown in **Fig.** 12.13a. The band corresponding to SSEs at A/E = 1 can be clearly identified. Events below this band mainly correspond to MSEs and can be suppressed by applying A/E cuts to the data. The survival efficiencies ε_{PSD} were estimated as described in **Ch.** B.1 in the appendix and are listed in **Tab.** 12.1. The acceptance of background events (MSEs) in the SEP is heavily suppressed, i.e. only 6.0% of these events survive. At the same time, the acceptance of events in the signal ROI is 42% [16].

The PSD performance was also investigated in terms of the AvsE pulse shape parameter. In general, the AvsE parameter is very similar to the A/E parameter. However, the width of the A/E distribution increases significantly at lower energies which reduces the efficiency for SSEs [246]. In the MAJORANA DEMONSTRATOR, the AvsE parameter has demonstrated performance down to 100 keV and is thus also suitable for spectral analyses in the low-energy domain. The uncorrected AvsE parameter is defined as [246]

$$\mathrm{AvsE_u} = A \cdot \frac{E}{E_u}, \tag{12.3}$$

where A denotes the maximum amplitude of the current pulse, E the calibrated energy, and E_u the uncalibrated energy. The linear energy dependence of the A/E parameter translates into a quadratic one in the uncorrected AvsE parameter (it is mostly linear with a small quadratic component). The correction for this dependence is done as described in **Ch.** B.2 in the appendix. The uncorrected and corrected AvsE distributions as a function of energy of a ^{228}Th calibration measurement are shown in **Fig.** 12.14. Moreover, the estimated survival efficiencies ε_{PSD} are listed in **Tab.** 12.1. The efficiencies obtained using the AvsE cut are slightly lower than those obtained with the A/E cut, in good agreement with the results presented in [246]. In general, the survival efficiencies obtained in this work are in good agreement with the efficiencies obtained with the same detector type in the MAJORANA DEMONSTRATOR experiment [142, 246]. The effect of the PSD cuts on the energy spectrum is shown in **Figs.** 12.13b-12.13d.

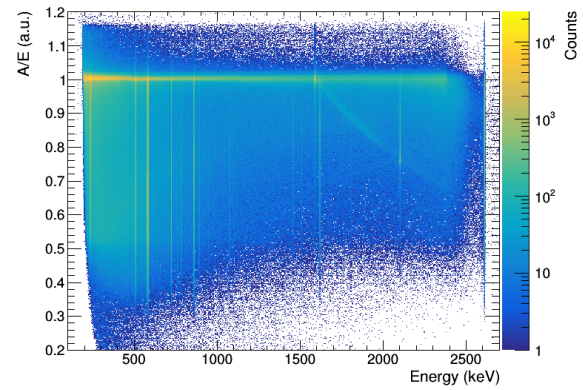

(a) A/E scatter plot.

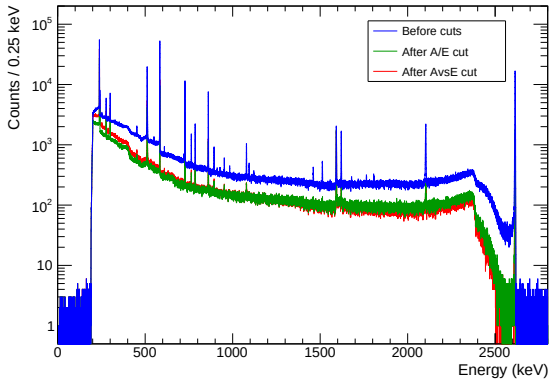

(b) Energy spectra before and after cut.

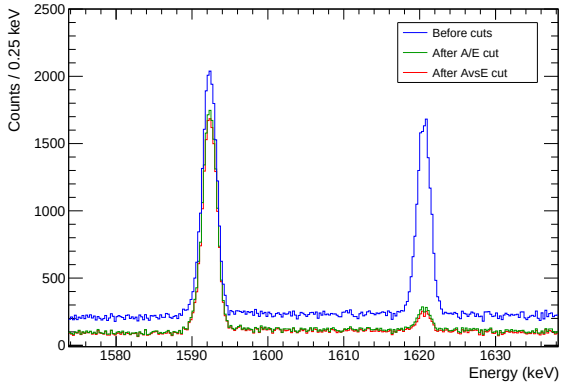

(c) DEP before and after cut.

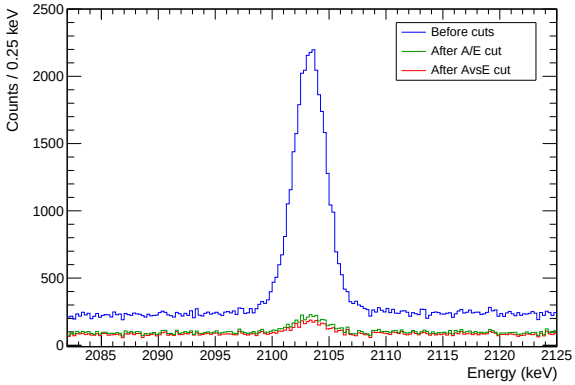

(d) SEP before and after cut.

Figure 12.13: A/E PSD performance of the PONaMa1 detector with the CUBE ASIC: (a) Normalized A/E distribution as a function of energy, and (b) energy spectra before and after the application of the A/E cut for a ^{228}Th calibration run. (c) While the cut is tuned such that 90% of the SSEs (signal-like events) in the DEP survive, (d) the number of MSEs (background events) in the SEP is significantly reduced. Published in [16].

Table 12.1: PSD performance of the PONaMa1 detector together with the CUBE ASIC. The estimation of the survival efficiencies ε_{PSD} is based on the A/E and AvsE pulse shape parameters. The acceptance of events in the double escape peak (DEP, mostly single-site events) is tuned to 90%. The survival efficiencies of (mostly multi-site) events in the single escape peak (SEP), full energy peak (FEP), as well as in the region of interest at the $Q_{\beta\beta}$-value can then be evaluated. The uncertainties of the survival efficiencies correspond to statistical uncertainties.

Peak	Survival efficiency ε_{PSD}	
	A/E	AvsE
^{208}Tl DEP	0.900 ± 0.007	0.900 ± 0.004
^{208}Tl SEP	0.060 ± 0.004	0.054 ± 0.003
^{208}Tl FEP	0.106 ± 0.001	0.085 ± 0.002
$Q_{\beta\beta}$	0.420 ± 0.002	0.371 ± 0.003

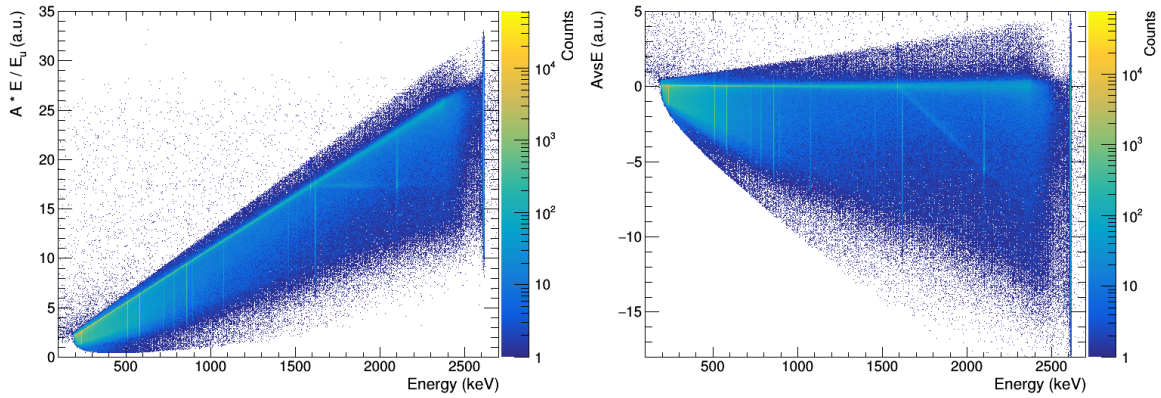

(a) AvsE scatter plot (uncorrected).

(b) AvsE scatter plot (corrected).

Figure 12.14: AvsE PSD performance of the PONaMa1 detector with the CUBE ASIC: (a) Uncorrected and (b) corrected AvsE distributions as a function of energy for a ^{228}Th calibration run.

RADIOPURITY A high radiopurity of the components used in a low-background physics experiment like LEGEND is crucial. In order to predict the background rate that would be induced by the CUBE ASIC in future phases of LEGEND, it has been assayed. These assay measurements were performed at the low-background screening facilities at LNGS in Italy and at Jagiellonian University in Poland by means of direct gamma ray counting, mass spectroscopy, and radon emanation techniques, respectively. All assay results are listed in **Tab.** 12.2.

First, the contamination of 35.3 g ASIC material (leftover production material) in the isotopes ^{232}Th, ^{238}U, as well as ^{40}K was analyzed via gamma ray counting. To this end, the radioactivity of the material was measured with a HPGe detector at LNGS for a time period of about 23.5 days. In the measurement, only upper limits were obtained for the contaminations, see **Tab.** 12.2. At the same time, the ^{232}Th and ^{238}U impurities in the ASIC were investigated via high-resolution inductively-coupled plasma mass spectrometry (ICP-MS). To accomplish this, 17 mg of sample material were dissolved in HF, HNO_3 and HCl. Finally, the radon contamination of the ASIC was investigated. A cryogenic radon detector at Jagiellonian University was used to determine the contaminations in 25 g sample material in both radon isotopes, i.e. ^{222}Rn and the short-lived ^{220}Rn. Just as for the other radiopurity measurements, only upper limits were obtained, see **Tab.** 12.2.

Based on the gamma counting measurement results and the efficiencies obtained with GEANT4 simulations of the LEGEND-200 detector array (used as an approximation for the LEGEND-1000 detector array) [14], the background contribution of the CUBE ASIC can be estimated. For the determination of the efficiencies p_{ROI} (cts/decay/keV) in the signal ROI, a detector AC cut was

Table 12.2: Results of the CUBE ASIC radiopurity assay conducted at LNGS and Jagiellonian University by means of direct gamma counting, ICP-MS, and radon emanation techniques. All values are upper limits. Published in [16].

Method	Radionuclide		Purity	
			mBq/kg	g/g
γ counting	^{232}Th:	^{228}Ra	< 4.9	$< 1.2 \cdot 10^{-9}$
		^{228}Th	< 4.1	$< 1.0 \cdot 10^{-9}$
	^{238}U:	^{234}Th	< 24	$< 1.9 \cdot 10^{-9}$
		^{234m}Pa	< 200	$< 1.6 \cdot 10^{-8}$
		^{226}Ra	< 3.5	$< 2.8 \cdot 10^{-10}$
	^{40}K		< 52	$< 1.7 \cdot 10^{-6}$
ICP-MS	^{232}Th			$< 2.0 \cdot 10^{-9}$
	^{238}U			$< 1.0 \cdot 10^{-9}$
Rn emanation	^{220}Rn		< 0.8	
	^{222}Rn		< 0.9	

Table 12.3: Efficiencies (p_{ROI}) and background indices (BI) of the CUBE ASIC for the radionuclides ^{232}Th and ^{238}U. Upper limits correspond to 90% confidence level. The efficiency values are based on GEANT4 simulations of the LEGEND-200 detector array and are used as an approximation for the LEGEND-1000 detector array [14]. Published in [16].

Radionuclide	p_{ROI} (cts/(decay $\cdot$ keV))	BI (cts/(keV $\cdot$ kg $\cdot$ yr))
^{232}Th	$1.92 \cdot 10^{-5}$	$< 4.1 \cdot 10^{-7}$
^{238}U	$9.62 \cdot 10^{-6}$	$< 1.8 \cdot 10^{-7}$

applied. The simulation results are listed in **Tab.** 12.3. Usually, the radioactive background is expressed in terms of the background index (BI) [16]:

$$\mathrm{BI} = \frac{p_{ROI} \cdot m_{ASIC} \cdot a}{m_{DET}}. \tag{12.4}$$

Here, m_{ASIC} denotes the mass of the radioactive ASIC material ($m_{ASIC} = 500 \cdot 0.33\,\mathrm{mg}$) and m_{DET} the total detector mass in the LEGEND-1000 detector array ($m_{DET} = 500 \cdot 2\,\mathrm{kg}$) assuming 500 channels. Furthermore, a describes the specific activity (Bq/kg). The background indices of the ^{232}Th and the ^{238}U radionuclides are listed in **Tab.** 12.3. They were calculated using the specific activities (upper limits) of the ^{228}Th and ^{226}Ra contributions of the gamma counting measurements, see **Tab.** 12.2. The contributions of the other radionuclides were neglected since they are not relevant for the background in the ROI. Even though the upper limits of the assay are comparably high (driven by the sensitivity of the measurement method), the summed BI of the ^{232}Th and the ^{238}U contributions matches the design specification of LEGEND-1000, with an overall background goal of BI $< 1 \cdot 10^{-5}$ cts/(keV $\cdot$ kg $\cdot$ yr) [16].

12.3 LBNL ASIC

12.3.1 *Overview*

The LBNL ASIC is a single-channel, low-noise preamplifier based on 180 nm CMOS technology, cf. **Ch.** 10.2.3. The chip is currently being developed at LBNL to specifically meet the readout electronics requirements of LEGEND-1000, cf. **Ch.** 12.1. The circuit design incorporates a CSA and a differential driver generating differential output signals. A simplified block diagram of the circuit, including the detector and bias voltage section, is shown in **Fig.** 12.15.

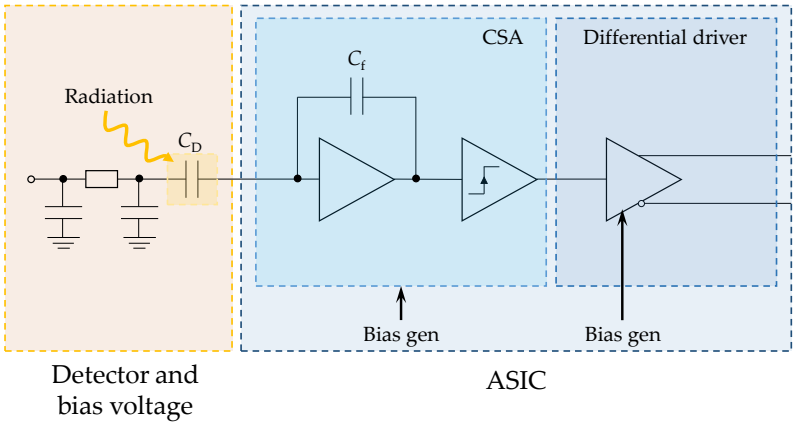

Figure 12.15: Simplified block diagram of the LBNL ASIC for LEGEND-1000. The diagram shows the detector and bias voltage section, as well as the charge sensitive amplifier (CSA) and the differential driver sections.

ASIC SPECIFICATIONS To provide for an excellent energy resolution and to enable low-energy analyses, a low electronic noise level of $\sim 20\,e^-$ RMS and a threshold of < 1 keV are targeted. Moreover, to be capable of studying background events anticipated at higher energies, a large dynamic range of ~ 10 MeV is envisioned. To this end, a feedback capacitance of $C_f = 500$ fF is implemented into the chip. Signals with fast rise times of $\mathcal{O}(10\,\text{ns})$ can be captured by a bandwidth of $20 - 50$ MHz. The input capacitance of the ASIC is optimized for the operation of detectors with capacitances in the range $1.0 \leqslant C_D \leqslant 5.0$ pF. To reduce the amount of radioactive impurities close to the detectors, the number of cables to the ASIC are minimized. In the final design stage, the chip will only require connections for power, ground, input, and output. The design is optimized to drive low-mass differential cables with a length of 10 m and a characteristic impedance of 50 Ω. The preamplifier is powered by a single voltage supply with on-chip LDO regulators, cf. **Ch.** 12.1. This also reduces the amount of heat dissipation in cryogenic liquid and the associated risk of bubble formation introducing microphonic noise. To reduce radioactive backgrounds potentially introduced by an external reset device, the LBNL ASIC has an internal reset mechanism realized via a CMOS transistor.

ASIC PROTOTYPE In September 2019, a first prototype of the LBNL ASIC has been produced[2]. In line with the stringent radiopurity requirements of $0\nu\beta\beta$ decay searches, the dimensions of the chip need to be as small as possible. Hence, the prototype was fabricated as a $1\,\text{mm} \times 1\,\text{mm} \times 8\,\mu\text{m}$ bare die. To test its performance, a dedicated electronics board accommodating the ASIC was used. The board made from low dielectric loss Rogers 4350 PCB material with ENIG traces has several 0603 footprints for bypass capacitors (filtering of voltage supply noise) and resistors (derivation of bias currents). On the board, the ASIC is epoxied to a ground pad and its contacts are ultrasonically wedge-bonded to the traces. An image of the ASIC and its mounting on the electronics board is shown in **Fig.** 12.16.

2 The ASIC prototype comprises several chip versions. In the scope of this work, the chiplet C1 was characterized. It derives the required bias currents externally and has no on-chip LDO regulators.

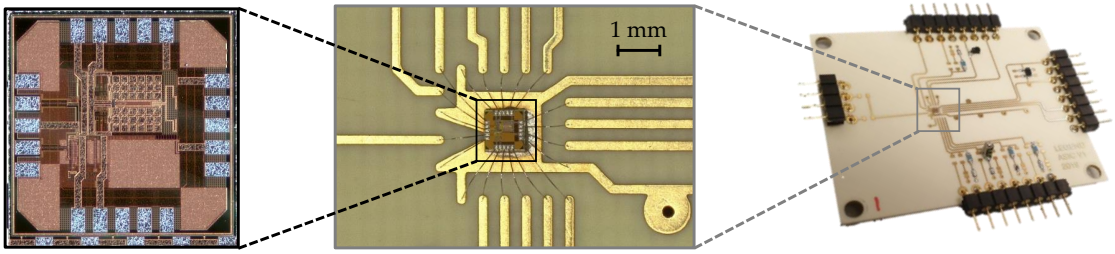

Figure 12.16: Close-up of the LBNL prototype ASIC for LEGEND-1000 (left). The chip is connected to the traces on a printed circuit board for testing purposes via several wire bonds (center). The board not only hosts the ASIC, but also bypass capacitors and resistors used to derive the bias currents (right).

VOLTAGES AND BIAS CURRENTS The prototype ASIC is powered by a main supply voltage in the range $V_{DDA} = 1.8 - 1.95\,V$ which is filtered with a bypass capacitor. A ground connection of $V_{SSA} = 0\,V$ is established. In addition, a common-mode voltage $V_{CM} = V_{DDA}/2$ is applied so that the baseline offset can be adjusted (for testing purposes). Just as the main supply voltage, it is filtered with a bypass capacitor. The investigated ASIC derives the required bias currents externally from the voltages V_{DDA} and V_{SSA}. Hence, additional external resistors are required on the electronics board. This is useful at an early development stage since it gives flexibility in optimizing the bias currents for subsequent design iterations. The bias current $I_{INP} = 8\,mA$ of the input stage of the CSA determines the operating point of the device. The linearity and dynamic range are controlled by the bias current $I_{CAS} = 0.5\,mA$ of the second CSA stage (cascode stage). The feedback stage of the CSA requires a bias current $I_{FB} = 100\,pA$ and defines the reset of the signals (discharge current of the feedback capacitor). The third stage (buffer stage) of the CSA with a bias current $I_{BUF} = 1\,mA$ drives the single-to-differential input and controls the DC level, gain, and bandwidth of the preamplifier. Finally, the differential driver converting the single-ended signal to a differential signal requires a bias current of $I_{S2D} = 30\,\mu A$. The ASIC can be tested without a detector by connecting an external pulse generator to its input. In this case, the input (pulser) capacitance emulating the detector capacitance is realized as stray capacitance between the traces on the board. The ASIC provides both a single-ended output (signal before the differential driver section), as well as a differential output.

12.3.2 *First measurement results*

In the framework of this thesis, first characterization measurements of the prototype ASIC have been carried out at LBNL in December 2019. To reduce the electronic noise in the system and to facilitate the submersion in cryogenic liquid, the electronics board together with the ASIC were installed in an aluminum box. A photograph of the assembly is shown in **Fig.** 12.17. For the characterization measurements, an arbitrary waveform generator (Agilent 33500B) was used for the generation of input signals. Power for the ASIC was provided by a standard power supply (Keithley 2230-30-1 DC). Output waveforms were acquired with an oscilloscope (Agilent MSO X 3054A). For the noise measurements, an MCA (labZY nano MCA) was used. In the following paragraphs, the characterization measurements to test performance metrics (rise time, dynamic range, electronic noise, etc.) will be discussed in detail. The ASIC prototype was characterized both at room temperature, and at cryogenic temperatures in LAr using short and long cables.

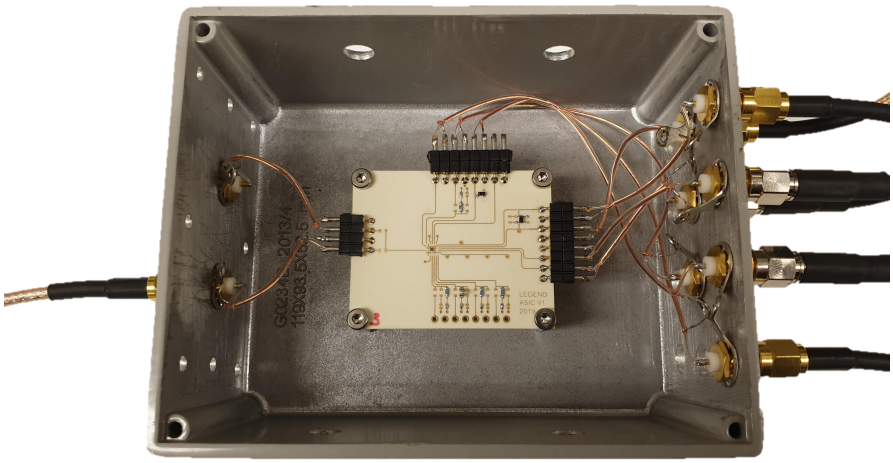

Figure 12.17: Photograph showing the electronics board hosting the LBNL ASIC assembled in an aluminum box.

WAVEFORM SHAPE AND POWER CONSUMPTION To test the functionality of the LBNL ASIC and to analyze the shape of the output signals, first characterization measurements were performed at room temperature. To reduce noise effects potentially introduced by the use of long cables, short coaxial cables (length of 1 m) between the ASIC and the DAQ system were used. The ASIC was operated using a supply voltage of $V_{DDA} = 1.90\,V$ ($I_{DDA} = 0.024\,A$) and a common-mode voltage of $V_{CM} = 0.95\,V$ ($I_{CM} \approx 0\,A$). This translates into a power consumption of $P = 45.6\,mW$. Bias resistor values haven been chosen based on prior calculations, and bias currents have not yet been tuned. An arbitrary waveform generator was used to generate input signals with 20 Hz frequency, 20 ms width, and 40 ns edge time. An example for the output waveform obtained with the ASIC prototype is shown in **Fig.** 12.18. The waveform features a fast rising edge (signal rise time $10\% - 90\%$ of $< 40\,ns$, limited by the edge time of the input pulse), followed by a linearly decaying tail that levels off exponentially.

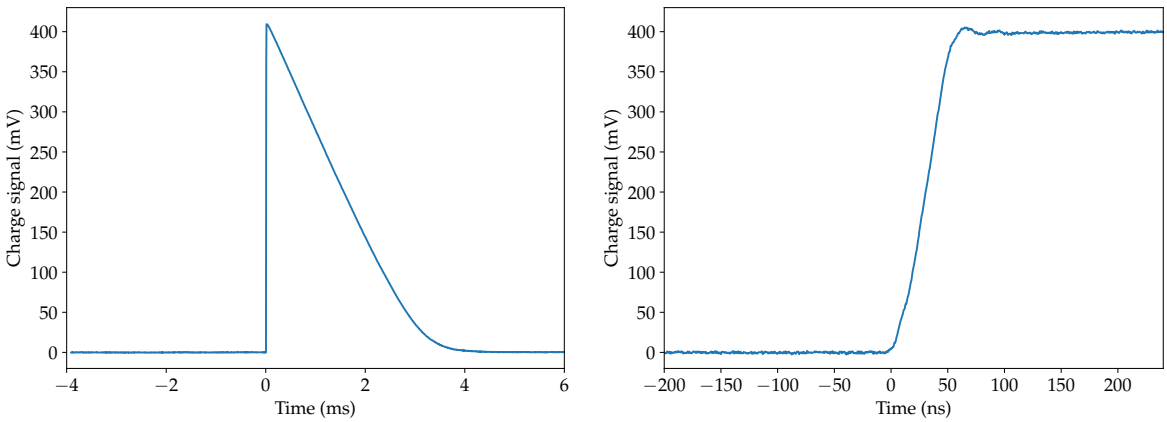

(a) Full waveform.

(b) Zoom of leading edge.

Figure 12.18: Waveform example obtained with the LBNL ASIC at room temperature. The waveform features (a) a linearly decaying tail that levels off exponentially, and (b) a fast rising edge.

DYNAMIC RANGE AND LINEARITY To determine the dynamic range of the ASIC and to test its linearity, output waveforms for input pulses with varying amplitudes were acquired. **Fig.** 12.19a shows waveform examples for different pulser input voltages V_{IN} (pulser termination of $50\,\Omega$). To investigate the linearity of the output voltage with respect to the input, the maximum signal amplitude V_{OUT} was determined for each waveform and plotted as a function of the input voltage,

see **Fig.** 12.19b. Besides a small deviation at lower input voltages, the system exhibits highly linear behavior over a large dynamic range. It should be noted here that at small input voltages, the normally linearly decaying waveform tail also shows slight non-linearities (see inset in **Fig.** 12.19a). These can probably be eliminated by adjusting the bias currents of the ASIC. To this end, more profound investigations are required.

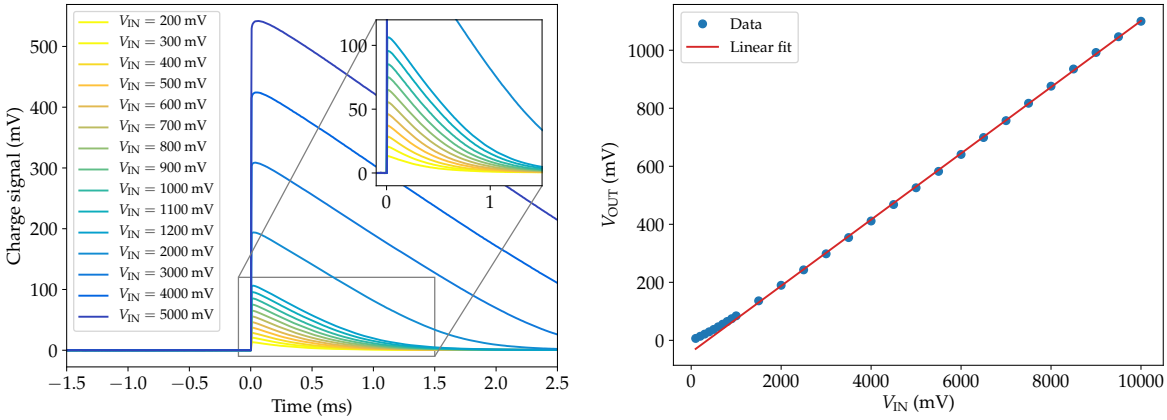

(a) Waveforms at varying input voltages.

(b) Linearity and dynamic range.

Figure 12.19: (a) Waveforms obtained with the LBNL ASIC at varying input voltages. (b) The maximum signal amplitude was used to determine the system linearity and the dynamic range.

ELECTRONIC NOISE The electronic noise performance of the LBNL ASIC was investigated for different input voltages at room temperature. The baseline noise was measured using an MCA with a trapezoidal filter with varying filter rise times and a fixed flat top time of 2 µs. Noise values were not converted into energy values due to the lack of knowledge of the pulser capacitance (stray capacitance between traces). A minimum noise level of about 3.2 ch FWHM was obtained for a filter rise time of 6 µs, see **Fig.** 12.20. It can be observed that the electronic noise is independent of the input voltages, i.e. the noise curves at different voltages are in good agreement with each other.

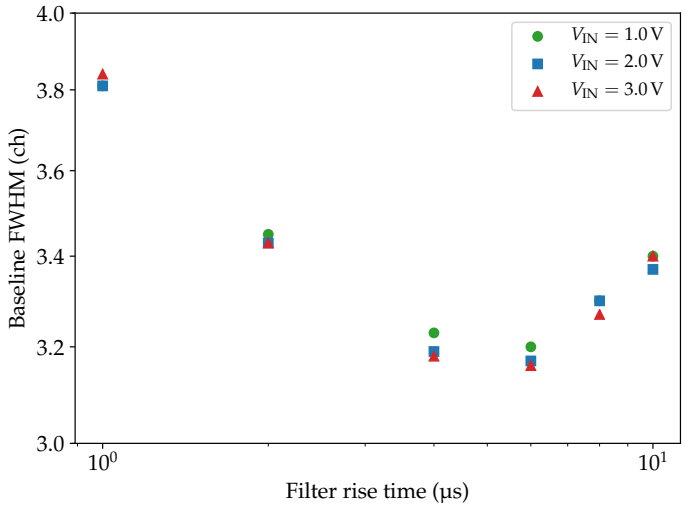

Figure 12.20: Noise performance of the LBNL ASIC at room temperature for varying input voltages.

SHORT VS LONG CABLES In the subsequent measurements, the cable lengths between the ASIC and the DAQ system were increased by a factor of ten (length of 10 m) to better reflect the conditions encountered in LEGEND-1000. The other operating conditions (bias voltage, bias currents, etc.) of

the ASIC were maintained. First, the power consumption of the system was determined. Even with the use of long cables, a very low power consumption comparable to the one with short cables was obtained. However, a non-degraded rising edge of the output signal was only obtained when the edge time of the input pulse was also increased by a factor of ten, i.e. from 40 ns to 400 ns. This behavior might be due to an improper termination of the waveform generator when using long cables and requires more detailed investigations. The increased input pulse edge time directly translates into a higher signal rise time (10% − 90%) of $\lesssim$ 400 ns. For reasons of better comparability, it was decided to perform the subsequent measurements still using 40 ns input pulse edge time. **Fig.** 12.21 shows waveforms for different input voltages for the case of short cables and long cables. In the case of short cables, for high input voltages, a slight overshoot at the end of the leading edge can be observed. When using long cables, the end of the leading edge is strongly distorted. However, these features are less pronounced for higher input pulse edge times.

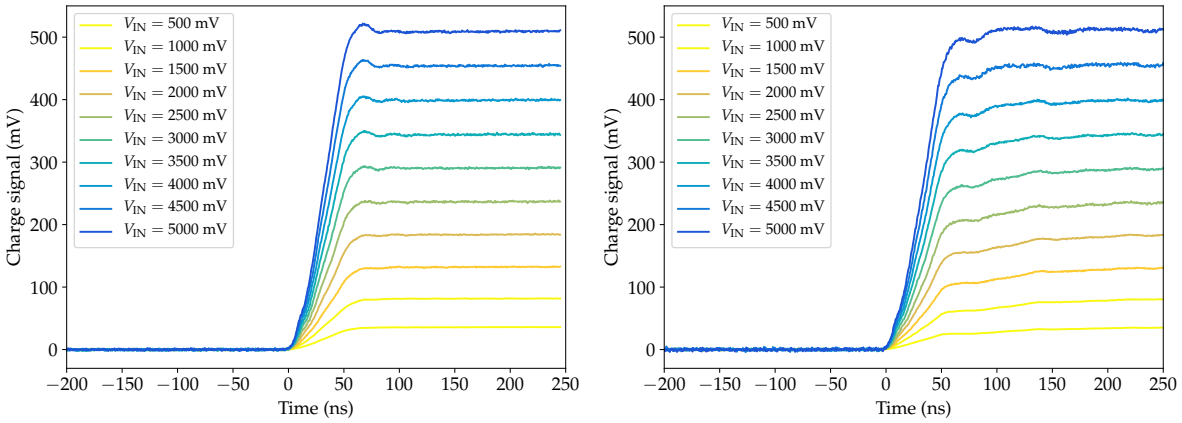

(a) Leading edge (short cables, 1 m).

(b) Leading edge (long cables, 10 m).

Figure 12.21: Waveforms (zoom on leading edge) obtained with the LBNL ASIC using (a) short cables and (b) long cables between the preamplifier and the DAQ system. Waveforms are illustrated for varying input voltages. The measurements were carried out at room temperature.

In the next step, the shapes of the differential output signals of the ASIC were analyzed. Measurements were again performed using short and long cables. Waveform examples for varying input pulse edge times are shown in **Fig.** 12.22. It can be observed that too small an input pulse edge time (improper termination) results in a considerable degradation of the leading edge. Waveforms with opposite polarity show a high symmetry with respect to their baselines.

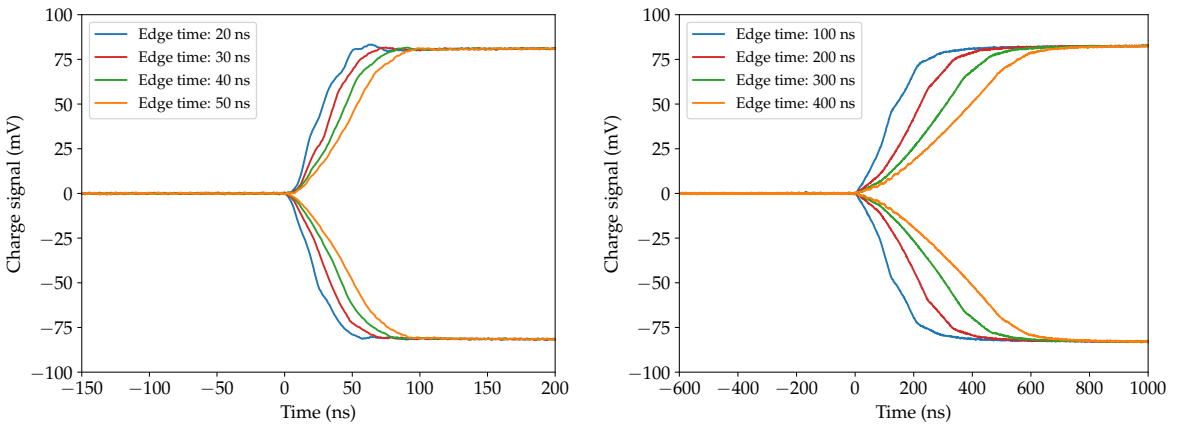

(a) Differential output (short cables, 1 m).

(b) Differential output (long cables, 10 m).

Figure 12.22: Differential signals (zoom on leading edge) obtained with the LBNL ASIC using (a) short cables and (b) long cables between the preamplifier and the DAQ systems. Waveforms are illustrated for varying input pulse edge times. The measurements were carried out at room temperature.

PERFORMANCE AT CRYOGENIC TEMPERATURES Finally, first bench tests were carried out to test the ASIC performance at cryogenic temperatures. To this end, the aluminum box including the electronics was dunked in a dewar filled with LAr. Long coaxial cables with a length of 10 m and a characteristic impedance of 50 Ω between the preamplifier and the DAQ system were used. Compared to the operation at room temperature, the power consumption at LAr temperature was slightly higher. The ASIC was operated at a supply voltage of $V_{DDA} = 1.90\,V$ ($I_{DDA} = 0.04\,A$) and a common-mode voltage of $V_{CM} = 0.95\,V$ ($I_{CM} \approx 0\,A$). This translates into a power consumption of $P = 76\,mW$. Just as for the measurements at room temperature, the signal rise time (10% – 90%) was limited by the input pulse edge time. A large dynamic range with a small deviation at lower input voltages was measured. **Fig.** 12.23 shows waveforms at room temperature and LAr temperature for varying input voltages. First, it can be observed that the rising edge at cryogenic temperatures appears to be sharper. This is due to a strong overshoot at the end of the leading and a subsequent ringing. The plots also show that the waveforms at LAr temperature have a much longer decay time (several tens of ms). In addition, a kink-like structure can be observed in the decaying tail. This might be explained by a charge carrier freeze-out in the MOSFET transistors at cryogenic temperatures [274, 275]. The differential signal output showed a slight asymmetry between the positive and negative rails.

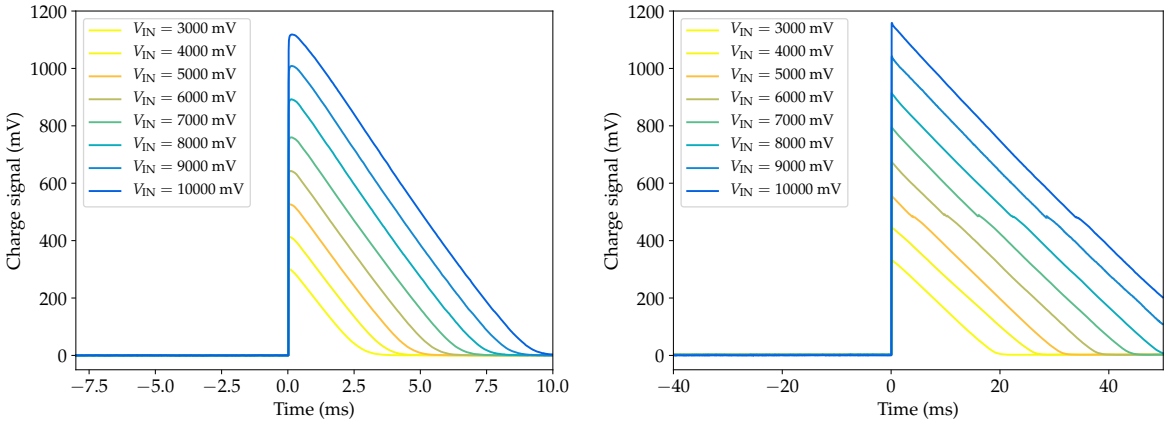

(a) Waveforms (room tepmerature).

(b) Waveforms (LAr temperature).

Figure 12.23: Waveforms obtained with the LBNL ASIC at (a) room temperature and (b) at cryogenic temperatures in LAr at varying input voltages.

OUTLOOK The results of the ASIC characterization measurements obtained within this work provide vital information for the design of a second iteration that is currently being developed at LBNL. Further (bench) tests are required to optimize the bias currents, and to better understand some of the waveform features observed in the measurements. Currently, a self-biased version (internally set biases) of the chip and an LDO regulator die are being investigated. From the analysis point of view, novel techniques have to be developed to correct for the linearly decaying tail that levels off exponentially. This is of particular interest so that PSD techniques such as the DCR PSD, cf. **Ch.** 5.3, for background rejection can be applied.

12.4 CONCLUSIONS

Signal readout electronics in close proximity to the detectors plays a major role in maximizing the experiment's discovery sensitivity. For LEGEND-1000, the baseline design foresees to use an ASIC-based readout scheme for the HPGe detectors. Within this work, two important contributions have been made to realize this ambitious project: 1) The characterization of a commercially available ASIC preamplifier together with a PPC germanium detector, and 2) the characterization of performance metrics of a first prototype ASIC for LEGEND-1000.

A dedicated vacuum test facility was constructed to investigate the commercially available

XGLab CUBE ASIC together with a PPC detector. The measurements demonstrated that low noise levels, excellent energy resolutions, and fast signal rise times can be obtained with this readout. Moreover, the viability of PSD techniques for the efficient rejection of background events was shown. Finally, an extensive radiopurity assay campaign demonstrated that the radioactive contaminations of the CUBE ASIC are compatible with the targeted background goal of LEGEND-1000. The work was published in [16].

The results obtained in the characterization measurements are very promising for a potential application of ASIC technology in LEGEND-1000. However, the investigated chip is not ideally suited for the final application in the experiment: Each of its three power supplies requires at least one bypass capacitor for filtering the voltage supply noise. This increases the amount of radioactive material close to the detectors considerably. Furthermore, the ASIC comprises neither an internal reset mechanism, nor a differential output required to reduce the noise associated with driving signals over long transmission lines. To specifically meet the electronics requirements of LEGEND-1000, a customized ASIC is currently being developed at LBNL. Within this work, a first prototype of the chip was characterized in bench tests. The measurements at room temperature and at cryogenic temperatures in LAr showed that the amplifier features fast rise times, a linear behavior over a large dynamic range, and a low power consumption. Further investigations are required to better characterize the electronic noise, and to optimize the bias currents of the CSA.

Part IV

CONCLUSIONS

13

CONCLUSIONS

The Large Enriched Germanium Experiment for Neutrinoless ββ Decay, LEGEND, will search for $0\nu\beta\beta$ decay in the isotope ^{76}Ge with an unprecedented sensitivity. The final phase of the experiment, LEGEND-1000, targets a signal discovery sensitivity on the decay half-life of $T^{0\nu}_{1/2} > 10^{28}$ yr by operating up to one tonne of germanium detectors for a time period of about ten years. To achieve this ambitious goal, an operation in the background-free regime is crucial, i.e. a background level of $BI < 10^{-5}$ cts/(keV · kg · yr) is envisioned. Consequently, the reduction of backgrounds is one of the main challenges to be addressed.

I CHARACTERIZATION OF POINT CONTACT GERMANIUM DETECTORS

In the first phase of the experiment, LEGEND-200, one of the main background contributions is anticipated to arise from alpha and beta surface events. To better understand these backgrounds, the response of a p-type point contact (PPC) germanium detector to alpha and beta particles was studied in detail within this work. The measurements in a vacuum test facility demonstrated that the passivated detector surface is prone to effects such as charge build-up. For both alpha and beta surface events, a radial-dependent energy degradation was observed that could be explained with the presence of (negative) surface charges at the passivation layer. The measurements also showed that independent of the sign of the charge build-up, surface alpha events exhibit a delayed charge recovery (DCR) effect that can be exploited to powerfully reject them. In dedicated characterization measurements with beta particles, two event populations could be identified. One population could be associated with events having small penetration depths that are sensitive to surface effects, whereas the other population with higher penetration depths was found to be mostly insensitive to these effects. For the surface beta events, no pronounced DCR effect was observed, and the signal waveforms did not show any noticeable features. Consequently, their discrimination at the passivated surface is expected to be challenging.

To better understand the results of the surface characterization measurements, an extensive simulation campaign was carried out. The study of charge collection efficiency maps provided vital information on the impact of surface charges on important pulse shape parameters. Moreover, it could be shown that surface effects are much less pronounced in the case of positive surface charges. Monte Carlo event simulations in combination with pulse shape simulations were capable of reproducing the measurement results qualitatively. In particular, the surface charge model as a foundation to explain the observations could be verified. The measurement and simulation results obtained within this work led to a significant improvement of the understanding of PPC detector surface effects. This serves as a basis to better assess the surface backgrounds in LEGEND-200. A publication of this work is to be submitted soon.

II DEVELOPMENT OF SIGNAL READOUT ELECTRONICS FOR LEGEND

Another major role in minimizing backgrounds and maximizing the experiment's discovery sensitivity plays signal readout electronics. By reducing electronic noise levels, the energy resolution, and pulse shape discrimination (PSD) capabilities for the rejection of backgrounds can be enhanced. To this end, the charge sensitive amplifier (CSA) needs to be placed as close as possible to the detector. However, this is in conflict with the stringent radiopurity requirements. In LEGEND-200, this is addressed by deploying a CSA consisting of two stages: a first low-mass front-end (LMFE) electronics stage very close to the detectors, and a second amplification stage farther away. First tests of the full readout chain were carried out as part of the Post-GERDA

test (PGT). Within this work, a dedicated full software framework has been developed to analyze the measurement data. The analysis revealed that most of the detectors operated in the PGT showed a very good performance, including an excellent energy resolution and appropriate PSD capabilities. Due to the improved noise situation compared to the GERDA experiment, the successful application of a drift time correction for charge trapping for the inverted coaxial point contact (ICPC) detector geometry could be demonstrated. This is of particular importance for the performance optimization of this detector type. Besides, the data analysis revealed a stable operation of the LMFE. The decay time remained stable over an extended period of time indicating a high stability of the feedback resistor and capacitor on the LMFE.

Alongside with the analysis of the PGT data, dedicated bench tests of a backup amplifier for LEGEND-200 were carried out at Lawrence Berkeley National Laboratory (LBNL). Performance metrics such as electronic noise, signal rise time, dynamic range, power consumption, etc. were studied and found to be compatible with the intended electronics requirements. Finally, the CSA was compared to the baseline amplifier and a similar performance was obtained.

To reach the targeted signal discovery sensitivity beyond 10^{28} yr on the decay half-life, LEGEND-1000 pursues an ambitious background goal. From the readout electronics point of view, this can be supported by using state-of-the-art application-specific integrated circuit (ASIC) technology. The technology enables the integration and miniaturization of all relevant readout electronics components into a single low-mass, low-background chip that can be placed in close proximity to the detector. In this work, a detailed investigation of the performance of a commercially available ASIC, the XGLab CUBE ASIC, was carried out. The chip was operated together with a PPC germanium detector. Dedicated measurements revealed that 1) low noise levels, 2) an excellent energy resolution over a wide energy range, and 3) very fast signal rise times can be obtained with an ASIC CSA. The PSD performance of the readout system was found to be comparable to the performance reported by the Majorana Demonstrator and GERDA experiments. Finally, the radiopurity of the CUBE preamplifier was analyzed by means of various assay techniques (gamma ray counting, mass spectroscopy, radon emanation techniques). In all measurements, upper limits for the radioactive contaminations were obtained whose corresponding upper limits on the background index meet the requirements of LEGEND-1000.

The investigated CUBE ASIC is not ideally suited for the final application in LEGEND. The bypass capacitors required for filtering the noise of the ASIC power supplies increase the amount of radioactive material close to the detectors. This can be alleviated by using a single internally filtered power supply or low-background bypass capacitors. To further reduce radioactive contaminations, the CSA reset mechanism needs to be integrated into the chip. A dedicated ASIC fulfilling these requirements is currently being developed at LBNL. Within this work, a first prototype of the LBNL ASIC was characterized. Bench tests provided first insights into performance metrics of the chip. The measurements demonstrated that the ASIC features fast signal rise times, a linear behavior over a large dynamic range, and a low power consumption. Further tests are required to optimize the bias settings, and to better understand several waveform features observed in the measurements. The results obtained in this work serve as a basis for future design iterations.

In summary, the results obtained within this work provide vital information to better assess the backgrounds to be encountered in LEGEND. The results of the surface characterization measurements of a PPC detector will be of key importance for the development of future means to further reduce surface backgrounds. A second major contribution was the development and characterization of signal readout electronics for LEGEND. The PGT demonstrated the successful operation of the whole signal readout chain for LEGEND-200. In particular, the data analysis revealed that the novel readout system including the LMFE and the preamplifier, as well as most of the detectors showed a very good performance. Finally, dedicated measurements provided valuable information about the operation of a germanium detector together with an ASIC-based readout system. The results serve as a basis for the design of future ASIC iterations for the final phase of LEGEND.

Part V

APPENDIX

A

INFORMATION ON SURFACE CHARACTERIZATION MEASUREMENTS

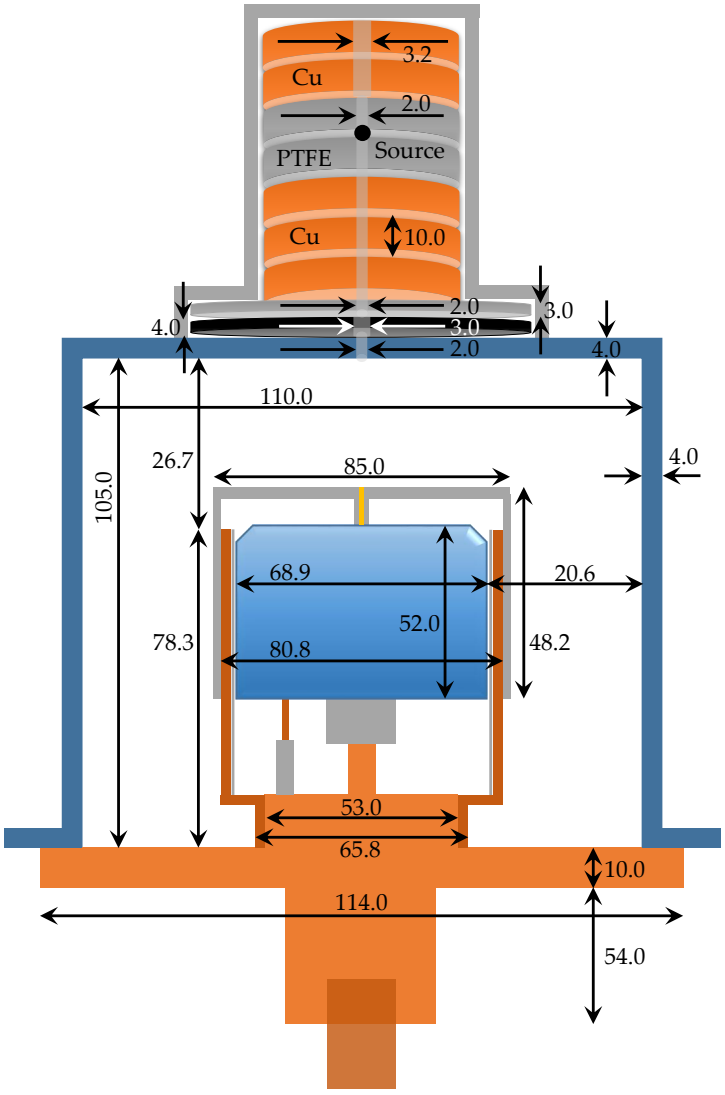

Figure A.1: Simplified sectional view of the PONaMa1 detector in the GALATEA scanning facility. The figure shows all relevant dimensions for the case of the surface alpha characterization measurements (^{241}Am source). Dimensions are in mm. The figure is not to scale.

Table A.1: Overview of the surface characterization measurements with the PONaMa1 detector in the GALATEA scanning facility. The third column indicates whether the measurement was a scan (S) or performed at a fixed position (F). In the latter case, the abbreviation BKG denotes a background measurement, the abbreviation BV a bias voltage scan, and the abbreviation TE a test measurement. The fourth column is the scan range (in terms of the collimator position). The last column indicates the measurement duration t per scan point.

No	Source/s	Scan [S] or fix [F]	Range (mm)	ϕ (°)	V_B (kV)	t (h)
1)	^{90}Sr	S	$0-40$	117	2.0	1.0
2)	^{90}Sr	S	$0-40$	297	2.0	1.0
3)	^{90}Sr	F (BKG)	52.5	297	2.0	3.0
4)	^{90}Sr	F (BV)	10	297	1.2, 1.5, 1.7, 1.9, 2.0	1.0
5)	^{90}Sr	S	$0-7.5$	297	2.0	1.0
6)	^{90}Sr	S	$0-40$	297	1.05	1.0
7)	^{90}Sr	F (BKG)	47	252	1.05	8.0
8)	^{90}Sr	S	$0-40$	252	1.05	1.0
9)	^{241}Am + ^{228}Th	F (TE)	47	252	1.05	0.5
10)	^{241}Am + ^{228}Th	F (BKG)	47	252	1.05	20.0
11)	^{241}Am + ^{228}Th	F (TE)	6	252	1.05	0.5
12)	^{241}Am + ^{228}Th	F (TE)	14	252	1.05	10.0
13)	^{241}Am + ^{228}Th	S	$0-38$	252	1.05	2.0
14)	^{241}Am + ^{228}Th	F (BV)	4	252	$0.4-1.8$	2.0
15)	^{241}Am + ^{228}Th	F	4	252	1.05	8.0
16)	^{241}Am + ^{228}Th	S	$0-36$	297	1.05	2.0
17)	^{241}Am + ^{228}Th	S	$0-36$	117	1.05	2.0
18)	^{90}Sr	S	$0-40$	72	1.05	0.2
19)	^{90}Sr	F (BKG)	50	72	1.05	2.0
20)	^{90}Sr	S	$0-40$	72	1.05	0.5
21)	^{90}Sr	S (TE)	$4-26$	72	1.05	0.5
22)	^{90}Sr	S (TE)	$0-36$	72	1.05	0.5
23)	^{90}Sr	S	$0-36$	72	1.05	0.5
24)	^{90}Sr	F (BKG)	50	72	1.05	30.0
25)	^{90}Sr	S	$0-38$	72	1.05	0.5
26)	^{90}Sr	S	$0-36$	72	1.05	0.3
27)	^{90}Sr	S	$0-36$	72	2.0	0.5
28)	^{90}Sr	F (BV)	10	72	$0.8-2.0$	0.5

B

PULSE SHAPE DISCRIMINATION (PSD) TECHNIQUES

In the following sections, the formal procedures of the A/E and AvsE pulse shape analysis (PSA) techniques will be discussed briefly. While the GERDA collaboration has made extensive use of the A/E PSA for the rejection of background events, the AvsE PSA has been deployed intensively by the MAJORANA DEMONSTRATOR collaboration. More detailed information on the particular methods can be found in [246, 269, 273, 276, 277].

B.1 A/E PULSE SHAPE ANALYSIS

The A/E pulse shape discriminator is defined as the ratio of the maximum amplitude A of the current pulse and the amplitude (energy) E of the charge pulse.

CORRECTION FOR ENERGY DEPENDENCE In a first step, the A/E vs E distribution (of all events) is corrected for a slight linear energy dependence. To this end, 31 energy values E_{SCS} from the Compton continuum in the energy range $1.01\,\text{MeV} \leqslant E \leqslant 2.16\,\text{MeV}$ are selected and the corresponding A/E values in the regions $E_{SCS} \pm 20\,\text{keV}$ are histogrammed. The resulting distributions are fit with a function composed of a Gaussian and an empirically found function modeling the low tail [269, 273]:

$$f(A/E) = A \exp\left(-\frac{(E-\mu_{SCS})^2}{2\sigma_{SCS}^2}\right) + m \cdot \frac{\exp(k(E-l)) + d}{\exp((E-l)/t) + l}. \tag{B.1}$$

Here, the Gaussian term is described in terms of the mean μ_{SCS} and the standard deviation σ_{SCS}, while the component approximating the tail is parameterized by the parameters m, d, k, l and t. An example for the fitted A/E distributions of three different energy value ranges $E_{SCS} \pm 20\,\text{keV}$ is shown in **Fig.** B.1a. It can be observed that with increasing energy E_{SCS}, the Gaussian means μ_{SCS} of the distributions are shifted towards smaller A/E values.

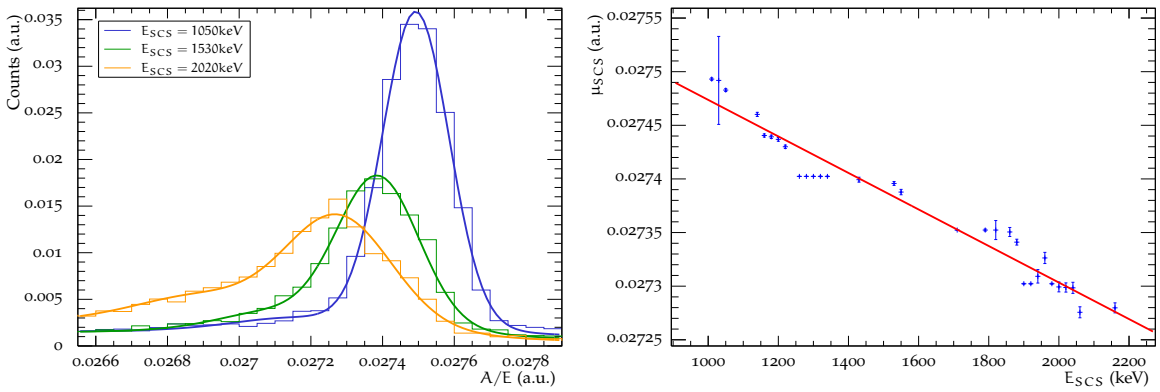

(a) A/E distributions (Compton continuum).

(b) Gaussian means vs energy.

Figure B.1: Linearization of the A/E parameter. (a) A/E distributions of events in different energy ranges $E_{SCS} \pm 20\,\text{keV}$ in the Compton continuum. (b) Relationship between the Gaussian means of the A/E distributions and the energy. The data were approximated with a linear function.

To quantify this behavior, the fitted Gaussian means μ_{SCS} are plotted as a function of the energy values E_{SCS}. As can be seen from **Fig.** B.1b, the tuples (E_{SCS}, μ_{SCS}) show a linear relationship which is approximated with a linear function of the form

$$\mu_{SCS} = \mu_{SCS,0} + aE_{SCS}. \tag{B.2}$$

Here, $\mu_{SCS,0}$ and a denote the fit parameters. Finally, all A/E values are corrected for the linear energy dependence according to

$$A/E_c = \frac{A/E}{\mu_{SCS,0} + aE_{SCS}}. \tag{B.3}$$

BACKGROUND SUBTRACTION AND SURVIVAL PROBABILITIES Before computing the survival probabilities of certain peaks/areas in the energy spectrum, the underlying background needs to be subtracted. To this end, signal and background regions are defined. For the FEPs and the SEP, the regions are defined as follows [273, 277]:

- Region 1: $[\mu_{FEP} - 1 \cdot 4.5\sigma,\ \mu_{FEP} + 1 \cdot 4.5\sigma]$ (peak region)
- Region 2: $[\mu_{FEP} - 2 \cdot 4.5\sigma,\ \mu_{FEP} - 1 \cdot 4.5\sigma]$ (left side band, LSB)
- Region 3: $[\mu_{FEP} + 1 \cdot 4.5\sigma,\ \mu_{FEP} + 2 \cdot 4.5\sigma]$ (right side band, RSB)

Here, μ_{FEP} denotes the peak position and σ the energy resolution of the FEP. The LSB and the RSB are located at energies below and above the peak energy, respectively. For the DEP, the ranges are slightly adjusted [273, 277]:

- Region 1: $[\mu_{DEP} - 1 \cdot 4.5\sigma,\ \mu_{DEP} + 1 \cdot 4.5\sigma]$ (peak region)
- Region 2: $[\mu_{DEP} - 2 \cdot 4.5\sigma,\ \mu_{DEP} - 1 \cdot 4.5\sigma]$ (LSB)
- Region 3: $[\mu_{DEP} + 1 \cdot 4.5\sigma,\ \mu_{DEP} + 2 \cdot 4.5\sigma]$ (RSB 1)
- Region 4: $[\mu_{DEP} + 2 \cdot 4.5\sigma,\ \mu_{DEP} + 3 \cdot 4.5\sigma]$ (RSB 2)

In both cases, the peak regions correspond to the signal regions while the LSBs and RSBs correspond to the background regions. For the actual background subtraction, the corrected A/E values in these energy ranges are histogrammed. The resulting distribution in the peak region is corrected for the background by subtracting the distributions of the LSB and RSB regions.

In the final step of the A/E PSA, the A/E cut value and the survival efficiencies are calculated. The cut value corresponds to the value for which 90% of the events in the DEP survive. It is obtained by integrating the background-corrected A/E distribution of the DEP up to a value of 10% of the total integral. Finally the, the survival probabilities are computed by dividing the number N^+ of accepted events in the background corrected A/E distributions by the total number N of events:

$$\varepsilon_{PSD} = \frac{N^+}{N}. \tag{B.4}$$

This procedure with the associated estimation of uncertainties is described in more detail in [273, 277].

B.2 AVSE PULSE SHAPE ANALYSIS

Another efficient PSD method to reject background events in HPGe detectors is the AvsE PSA. The formal procedure is very similar to the one of the A/E PSA, cf. **Ch.** B.1.

CORRECTION FOR ENERGY DEPENDENCE In a first step, the uncorrected AvsE parameter, cf. **Eq.** (12.3), is corrected for its (quadratic) energy dependence in a similar way as the A/E parameter. The quadratic correction parameters are obtained as follows: First, 22 energy values E_{SCS} are selected from the energy range $200\,\text{keV} \leqslant E \leqslant 2300\,\text{keV}$. The corresponding $AvsE_u = A \cdot E/E_u$ values in the regions $E_{SCS} \pm 25\,\text{keV}$ are histogrammed. The resulting AvsE distributions are fit with

a Gaussian. Just as for the A/E PSA, the Gaussian means μ_{SCS} are then plotted as a function of the energy values and fitted with a quadratic function of the form

$$\mu_{SCS} = p_0 + p_1 E + p_2 E^2, \tag{B.5}$$

where p_0, p_1 and p_2 are the fit parameters. Finally, the AvsE values are corrected for their quadratic energy dependence according to

$$\text{AvsE} = A \cdot \frac{E}{E_u} - (p_0 + p_1 E + p_2 E^2). \tag{B.6}$$

BACKGROUND SUBTRACTION AND SURVIVAL PROBABILITIES The background subtraction in the AvsE PSA is based on sideband-subtracted DEP data. In contrast to the A/E PSA, the signal and background regions are not based on dynamic ranges (based on the mean and standard deviation of the actual data), but on fixed energy ranges around the peak regions. As an example, the regions for the DEP are defined as

- Region 1: [1590keV, 1595keV] (peak region)
- Region 2: [1570keV, 1580keV] (LSB)
- Region 3: [1600keV, 1610keV] (RSB)

Another difference between the two PSA methods is that in the AvsE PSA, the background subtraction is done on energy spectrum data (not on $A \cdot E/E_u$ distribution data).

In the final step, the AvsE cut value and the survival efficiencies are calculated. Just as for the A/E PSA, the cut value j corresponds to the value for which 90% of the events in the DEP survive. It is obtained by varying j in

$$\text{AvsE} = -\left(A \cdot \frac{E}{E_u} - (p_0 + p_1 E + p_2 E^2)\right)/j. \tag{B.7}$$

Eventually, the survival probabilities are computed by dividing the number N^+ of accepted signal events by the total number N of events:

$$\varepsilon_{PSD} = \frac{N^+}{N}. \tag{B.8}$$

This procedure and the uncertainty estimation are described in more detail in [246].

LIST OF FIGURES

LIST OF TABLES

BIBLIOGRAPHY

[1] F. Reines and C. L. Cowan. "Detection of the Free Neutrino." In: *Phys. Rev.* 92.830 (1953). DOI: 10.1103/PhysRev.92.830.

[2] C. L. Cowan *et al.* "Detection of the free neutrino: a confirmation." In: *Science* 124.3212 (1956), pp. 103–104. DOI: 10.1126/science.124.3212.103.

[3] F. Reines *et al.* "Detection of the Free Antineutrino." In: *Phys. Rev.* 117.159 (1960). DOI: 10.1103/PhysRev.117.159.

[4] R. Davis. "A Review of the Homestake Solar Neutrino Experiment." In: *Prog. Part. Nucl. Phys.* 32 (1994), pp. 13–32. DOI: 10.1016/0146-6410(94)90004-3.

[5] Y. Fukuda *et al.* "Evidence for Oscillation of Atmospheric Neutrinos." In: *Phys. Rev. Lett.* 81.1562 (1998). DOI: 10.1103/PhysRevLett.81.1562.

[6] Q. R. Ahmad. "Direct Evidence for Neutrino Flavor Transformation from Neutral-Current Interactions in the Sudbury Neutrino Observatory." In: *Phys. Rev. Lett.* 89.011301 (2002). DOI: 10.1103/PhysRevLett.89.011301.

[7] Q. R. Ahmad. "Measurement of the Rate of $\nu_e + d \rightarrow p + p + e^-$ Interactions Produced by ^8B Solar Neutrinos at the Sudbury Neutrino Observatory." In: *Phys. Rev. Lett.* 87.071301 (2001). DOI: 10.1103/PhysRevLett.87.071301.

[8] M. Aker *et al.* "Improved Upper Limit on the Neutrino Mass from a Direct Kinematic Method by KATRIN." In: *Phys. Rev. Lett.* 123.221802 (2019). DOI: 10.1103/PhysRevLett.123.221802.

[9] M. J. Dolinski *et al.* "Neutrinoless Double-Beta Decay: Status and Prospects." In: *Annu. Rev. Nucl. Part. Sci.* 69 (2019), pp. 219–251. DOI: 10.1146/annurev-nucl-101918-023407.

[10] A. Giuliani *et al.* "Double Beta Decay." In: *APPEC Committee Report* 3 (2020). arXiv: 1910.04688v2.

[11] F. Edzards. "The Future of Neutrinoless Double Beta Decay Searches with Germanium Detectors." In: *J. Phys.: Conf. Ser.* 1690.012180 (2020). DOI: 10.1088/1742-6596/1690/1/012180.

[12] N. Abgrall *et al.* "The Large Enriched Germanium Experiment for Neutrinoless Double Beta Decay (LEGEND)." In: *Proceedings of the MEDEX'17 meeting*. 2017. DOI: 10.1063/1.5007652.

[13] J. Myslik. "LEGEND: The Large Enriched Germanium Experiment for Neutrinoless Double-Beta Decay." In: *Proceedings of the CIPANP 2018 meeting*. 2018. arXiv: 1810.00849.

[14] N. Abgrall *et al.* "The Large Enriched Germanium Experiment for Neutrinoless $\beta\beta$ Decay: LEGEND-200 at LNGS." In: *Proposal LNGS-P 58/18* (2018).

[15] N. Abgrall *et al.* "The MAJORANA DEMONSTRATOR Neutrinoless Double-Beta Decay Experiment." In: *Adv. High Energy Phys.* 2014.365432 (2014). DOI: 10.1155/2014/365432.

[16] F. Edzards *et al.* "Investigation of ASIC-based signal readout electronics for LEGEND-1000." In: *J. Instr.* 15.P09022 (2020). DOI: 10.1088/1748-0221/15/09/P09022.

[17] C. Cuesta *et al.* "Background model for the MAJORANA DEMONSTRATOR." In: *J. Phys.: Conf. Ser.* 888 (2017). DOI: 10.1088/1742-6596/888/1/012240.

[18] N. Abgrall *et al.* "The MAJORANA low-noise low-background front-end electronics." In: *Procedia Computer Science* 00 (2014), pp. 1–4.

[19] S. Riboldi *et al.* "A low-noise charge sensitive preamplifier for Ge spectroscopy operating at cryogenic temperature in the GERDA experiment." In: *IEEE Nuclear Science Symposuim Medical Imaging Conference*. 2010, pp. 1386–1388. DOI: 10.1109/NSSMIC.2010.5873998.

[20] S. Riboldi *et al.* "Improvement of the "CC2" charge sensitive preamplifier for the GERDA phase II experiment." In: *2012 IEEE Nuclear Science Symposium and Medical Imaging Conference Record*. 2012, pp. 782–785. DOI: 10.1109/NSSMIC.2012.6551209.

[21] R. J. Cooper *et al.* "A novel HPGe detector for gamma-ray tracking and imaging." In: *Nucl. Instr. Meth. Phys. Res. A* 665 (2011), pp. 25–32. DOI: 10.1016/j.nima.2011.10.008.

[22] L. Bombelli *et al.* ""CUBE", A low-noise CMOS preamplifier as alternative to JFET front-end for high-count rate spectroscopy." In: *2011 IEEE Nuclear Science Symposium Conference Record*. 2011, pp. 1972–1975. DOI: doi:10.1109/NSSMIC.2011.6154396.

[23] XGLab SRL. "CUBE - Charge Sensitive Preamplifier for Radiation Detectors." In: *XGLab CUBE product flyer* (2020). URL: https://www.xglab.it/wp-content/uploads/2020/04/fly_xgc_cube_2p_en_rev2.pdf (visited on 02/09/2021).

[24] S. Weinberg. "A Model of Leptons." In: *Phys. Rev. Lett.* 19.1264 (1967). DOI: 10.1103/PhysRevLett.19.1264.

[25] M. Goldhaber. "Helicity of Neutrinos." In: *Phys. Rev.* 109.1015 (1958). DOI: 10.1103/PhysRev.109.1015.

[26] J. A. Formaggio and G. P. Zeller. "From eV to EeV: Neutrino Cross Sections Across Energy Scales." In: *Rev. Mod. Phys.* 84.1307 (2012). DOI: 10.1103/RevModPhys.84.1307.

[27] K. S. McFarland. "Neutrino Interactions." In: *Lecture manuscript* (2008). arXiv: 0804.3899.

[28] W. Pauli. "Letter to Gauvereinstagung in Tuebingen: *'Sehr geehrte radioaktive Damen und Herren'*." In: *Collected Scientific Papers*. Vol. 2. R. Kronig and V. Weisskopf (Eds.), Interscience, 1964.

[29] J. Chadwick and E. S. Bieler. "The collisions of α particles with hydrogen nuclei." In: *The London, Edinburgh, and Dublin Philosophical Magazine and Journal of Science* 42.252 (1921), pp. 923–940. DOI: 10.1080/14786442108633834.

[30] J. Chadwick. "Possible Existence of a Neutron." In: *Nature* 129.312 (1932). DOI: 10.1038/129312a0.

[31] E. Fermi. "Versuch einer Theorie der β-Strahlen. I." In: *Zeitrschrift für Physik* 88 (1934), pp. 161–177. DOI: doi.org/10.1007/BF01351864.

[32] G. Danby *et al.* "Observation of High-Energy Neutrino Reactions and the Existence of Two Kinds of Neutrinos." In: *Phys. Rev. Lett.* 9.36 (1962). DOI: 10.1103/PhysRevLett.9.36.

[33] M. L. Perl *et al.* "Evidence for Anomalous Lepton Production in e^+-e^- Annihilation." In: *Phys. Rev. Lett.* 35.1489 (1975). DOI: 10.1103/PhysRevLett.35.1489.

[34] K. Kodama *et al.* "Observation of tau neutrino interactions." In: *Phys. Lett. B* 504 (3 2001), pp. 218–224. DOI: 10.1016/S0370-2693(01)00307-0.

[35] J. A. Bagger (editor). "Precision electroweak measurements on the Z resonance." In: *Physics Reports* 427.5 (2006), pp. 257–454. DOI: 10.1016/j.physrep.2005.12.006.

[36] M. Bardon *et al.* "Helicity of μ^- Mesons; Mott Scattering of Polarized Muons." In: *Phys. Rev. Lett.* 7.23 (1961). DOI: 10.1103/PhysRevLett.7.23.

[37] H. Albrecht *et al.* "Determination of the tau-neutrino helicity." In: *Phys. Lett. B* 250 (1-2 1990), pp. 164–171. DOI: 10.1016/0370-2693(90)91173-9.

[38] K. Abe *et al.* "Measurement of the τ Neutrino Helicity and Michel Parameters in Polarized e^+e^- Collisions." In: *Phys. Rev. Lett.* 78.4691 (1997). DOI: 10.1103/PhysRevLett.78.4691.

[39] M. Thomson. *Modern Particle Physics*. Cambridge, United Kingdom: Cambridge University Press, 2013.

[40] J. N. Bahcall *et al.* "Present Status of the Theoretical Predictions for the ^{37}Cl Solar-Neutrino experiment." In: *Phys. Rev. Lett.* 20.1209 (1968). DOI: 10.1103/PhysRevLett.20.1209.

[41] J. N. Bahcall and R. K. Ulrich. "Solar models, neutrino experiments, and helioseismology." In: *Rev. Mod. Phys.* 60.297 (1988). DOI: 10.1103/RevModPhys.60.297.

[42] R. Davis. "Solar Neutrinos. II. Experimental." In: *Phys. Rev. Lett.* 12.303 (1964). DOI: 10.1103/PhysRevLett.12.303.

[43] R. Davis *et al.* "Search for Neutrinos from the Sun." In: *Phys. Rev. Lett.* 20.1205 (1968). DOI: 10.1103/PhysRevLett.20.1205.

[44] B. T. Cleveland *et al.* "Measurement of the Solar Electron Neutrino Flux with the Homestake Chlorine Detector." In: *Astrophys. J.* 496.1 (1998), pp. 505–526. DOI: 10.1086/305343.

[45] P. Anselmann *et al.* "GALLEX solar neutrino observations: complete results for GALLEX II." In: *Phys. Lett. B* 357 (1-2 1995), pp. 237–247. DOI: 10.1016/0370-2693(95)00897-T. Erratum: *Phys. Lett. B* 361 (1-4 1995), pp. 235-236. DOI: 10.1016/0370-2693(95)01178-S.

[46] M. Altmann *et al.* "Complete results for five years of GNO solar neutrino observations." In: *Phys. Lett. B* 616 (3-4 2005), pp. 174–190. DOI: 10.1016/j.physletb.2005.04.068.

[47] A. I. Abazov *et al.* "Search for neutrinos from the Sun using the reaction $^{71}\mathrm{Ga}(\nu_e, e^-)^{71}\mathrm{Ge}$." In: *Phys. Rev. Lett.* 67.3332 (1991). DOI: 10.1103/PhysRevLett.67.3332.

[48] J. N. Abdurashitov *et al.* "Measurement of the Solar Neutrino Capture Rate by the Russian-American Gallium Solar Neutrino Experiment During One Half of the 22-Year Cycle of Solar Activity." In: *J. Exp. Theor. Phys.* 95 (2002), pp. 181–193. DOI: 10.1134/1.1506424.

[49] C. Arpesella *et al.* "First real time detection of ^{7}Be solar neutrinos by Borexino." In: *Phys. Lett. B* 658 (4 2008), pp. 101–108. DOI: 10.1016/j.physletb.2007.09.054.

[50] G. Alimonti *et al.* "The Borexino detector at the Laboratori Nazionali del Gran Sasso." In: *Nucl. Instr. Meth. Phys. Res. A* 600 (2009), pp. 568–593. DOI: 10.1016/j.nima.2008.11.076.

[51] G. Bellini *et al.* "Precision Measurement of the ^{7}Be Solar Neutrino Interaction Rate in Borexino." In: *Phys. Rev. Lett.* 107.141302 (2011). DOI: 10.1103/PhysRevLett.107.141302.

[52] D. Griffiths. *Introduction to Elementary Particles.* Second Edition. USA: WILEY-VCH, 2008.

[53] B. Pontecorvo. "Mesonium and Antimesonium." In: *J. Exp. Theor. Phys.* 6.2 (1958).

[54] Z. Maki *et al.* "Remarks on the Unified Model of Elementary Particles." In: *Prog. Theor. Phys.* 28 (5 1962), pp. 870–880. DOI: 10.1143/PTP.28.870.

[55] B. Pontecorvo. "Neutrino Experiments and the Problem of Conservation of Leptonic Charge." In: *J. Exp. Theor. Phys.* 26.5 (1968).

[56] N. Cabibbo. "Unitary Symmetry and Leptonic Decays." In: *Phys. Rev. Lett.* 10.531 (1963). DOI: 10.1103/PhysRevLett.10.531.

[57] M. Kobayashi and T. Maskawa. "CP-Violation in the Renormalizable Theory of Weak Interaction." In: *Prog. Theor. Phys.* 49 (2 1973), pp. 652–657. DOI: 10.1143/PTP.49.652.

[58] O. Cremonesi and M. Pavan. "Challenges in Double Beta Decay." In: *Adv. High Energy Phys.* 2014.951432 (2014). DOI: 10.1155/2014/951432.

[59] D. H. Perkins. *Particle Astrophysics.* 2nd ed. Oxford, United Kingdom: Oxford University Press, 2009.

[60] I. Esteban *et al.* "The fate of hints: updated global analysis of three-flavor neutrino oscillations." In: *J. High Energ. Phys.* 178 (2020). DOI: 10.1007/JHEP09(2020)178.

[61] K. Abe *et al.* "Solar neutrino results in Super-Kamiokande-III." In: *Phys. Rev. D* 83.052010 (2011). DOI: 10.1103/PhysRevD.83.052010.

[62] B. Aharmim *et al.* "Combined analysis of all three phases of solar neutrino data from the Sudbury Neutrino Observatory." In: *Phys. Rev. C* 88.025501 (2013). DOI: 10.1103/PhysRevC.88.025501.

[63] G. Bellini *et al.* "Neutrinos from the primary proton–proton fusion process in the Sun." In: *Nature* 512 (2014), pp. 383–386. DOI: 10.1038/nature13702.

[64] M. G. Aartsen *et al.* "Determining neutrino oscillation parameters from atmospheric muon neutrino disappearance with three years of IceCube DeepCore data." In: *Phys. Rev. D* 91.072004 (2015). DOI: 10.1103/PhysRevD.91.072004.

[65] K. Abe *et al.* "Atmospheric neutrino oscillation analysis with external constraints in Super-Kamiokande I-IV." In: *Phys. Rev. D* 97.072001 (2018). DOI: 10.1103/PhysRevD.97.072001.

[66] C. Patrignani *et al.* (Particle Data Group). "Review of Particle Physics." In: *Chinese Physics C* 40.100001 (2016). DOI: 10.1088/1674-1137/40/10/100001.

[67] A. Gando *et al.* "Reactor on-off antineutrino measurement with KamLAND." In: *Phys. Rev. D* 88.033001 (2013). DOI: 10.1103/PhysRevD.88.033001.

[68] G. Bak *et al.* "Measurement of Reactor Antineutrino Oscillation Amplitude and Frequency at RENO." In: *Phys. Rev. Lett.* 121.201801 (2018). DOI: 10.1103/PhysRevLett.121.201801.

[69] D. Adey *et al.* "Measurement of the Electron Antineutrino Oscillation with 1958 Days of Operation at Daya Bay." In: *Phys. Rev. Lett.* 121.241805 (2018). DOI: 10.1103/PhysRevLett.121.241805.

[70] H. de Kerret *et al.* "Double Chooz θ_{13} measurement via total neutron capture detection." In: *Nat. Phys.* 16 (2020), pp. 558–564. DOI: 10.1038/s41567-020-0831-y.

[71] K. Abe *et al.* "Constraint on the matter-antimatter symmetry-violating phase in neutrino oscillations." In: *Nature* 580 (2020), pp. 339–344. DOI: 10.1038/s41586-020-2177-0.

[72] M. A. Acero *et al.* "First measurement of neutrino oscillation parameters using neutrinos and antineutrinos by NOvA." In: *Phys. Rev. Lett.* 123.151803 (2019). DOI: 10.1103/PhysRevLett.123.151803.

[73] S. P. Mikheyev and A. Yu. Smirnov. "Resonant neutrino oscillations in matter." In: *Prog. Part. Nucl. Phys.* 23 (1989), pp. 41–136. DOI: 10.1016/0146-6410(89)90008-2.

[74] K. J. Kelly *et al.* "Neutrino mass ordering in light of recent data." In: *Phys. Rev. D* 103.013004 (2021). DOI: 10.1103/PhysRevD.103.013004.

[75] M. G. Aartsen *et al.* "Combined sensitivity to the neutrino mass ordering with JUNO, the IceCube Upgrade, and PINGU." In: *Phys. Rev. D* 101.032006 (2020). DOI: 10.1103/PhysRevD.101.032006.

[76] P. A. Zyla *et al.* (Particle Data Group). "The Review of Particle Physics." In: *Prog. Theor. Exp. Phys.* 083C01 (2020). DOI: 10.1093/ptep/ptaa104.

[77] C. S. Wu *et al.* "Experimental Test of Parity Conservation in Beta Decay." In: *Phys. Rev. Lett.* 105.1413 (1957). DOI: 10.1103/PhysRev.105.1413.

[78] R. Adhikari *et al.* "A White Paper on keV sterile neutrino Dark Matter." In: *JCAP* 01.025 (2017). DOI: 10.1088/1475-7516/2017/01/025.

[79] S. M. Bilenky and C. Giunti. "Neutrinoless double-beta decay: A probe of physics beyond the Standard Model." In: *Int. J. Mod. Phys. A* 30.1530001 (2015). DOI: 10.1142/S0217751X1530001X.

[80] P. Minkowski. "$\mu \to e\gamma$ at a rate of one out of 10^9 muon decays?" In: *Phys. Lett. B* 67 (4 1977), pp. 421–428. DOI: 10.1016/0370-2693(77)90435-X.

[81] M. Gell-Mann *et al.* "Complex Spinors and Unified Theories." In: *Conf. Proc. C*. Vol. 790927. 1979, pp. 315–321. arXiv: 1306.4669.

[82] R. N. Mohapatra and G. Senjanović. "Neutrino Mass and Spontaneous Parity Nonconservation." In: *Phys. Rev. Lett.* 44.912 (1980). DOI: 10.1103/PhysRevLett.44.912.

[83] T. Yanagida. "Horizontal Symmetry and Masses of Neutrinos." In: *Prog. Theor. Phys.* 64 (3 1980), pp. 1103–1105. DOI: 10.1143/PTP.64.1103.

[84] R. N. Mohapatra. "Theory of Neutrinos: A White Paper." In: *Rep. Prog. Phys.* 70.1757 (2007). DOI: 10.1088/0034-4885/70/11/R02.

[85] C. Karl. "Analysis of First Tritium Data of the KATRIN Experiment." MA thesis. Technische Universität München, 2018.

[86] L. Gastaldo *et al.* "The electron capture in ^{163}Ho experiment - ECHo." In: *Eur. Phys. J. Spec. Top.* 226 (2017), pp. 1623–1694. DOI: 10.1140/epjst/e2017-70071-y.

[87] A. Nucciotti *et al.* "Status of the HOLMES Experiment to Directly Measure the Neutrino Mass." In: *J. Low Temp. Phys.* 193 (2018), pp. 1137–1145. DOI: 10.1007/s10909-018-2025-x.

[88] C. Wiesinger (for the GERDA collaboration). "Post-upgrade performance of GERDA Phase II." In: *J. Phys.: Conf. Ser.* 1468 (2020). DOI: 10.1088/1742-6596/1468/1/012109.

[89] N. Aghanim *et al.* "Planck 2018 results. I. Overview and the cosmological legacy of Planck." In: *Astronomy&Astrophysics* 641.A1 (2020). DOI: 10.1051/0004-6361/201833880.

[90] M. Goeppert-Mayer. "Double Beta-Disintegration." In: *Phys. Rev.* 48.512 (1935). DOI: 10.1103/PhysRev.48.512.

[91] V. I. Tretyak and Y. G. Zdesenko. "Tables of double beta decay data - An update." In: *Atomic Data and Nuclear Data Tables* 80 (1 2002), pp. 83–116. DOI: 10.1006/adnd.2001.0873.

[92] J. Kotila and F. Iachello. "Phase space factors for double-β decay." In: *Phys. Rev. C* 85 (2012), p. 034316. DOI: 10.1103/PhysRevC.85.034316.

[93] J. Barea *et al.* "Nuclear matrix elements for double-β decay." In: *Phys. Rev. C* 87.014315 (2013). DOI: 10.1103/PhysRevC.87.014315.

[94] G. Benato. "Data Reconstruction and Analysis for the GERDA Experiment." PhD thesis. University of Zurich, 2015.

[95] J. Engel and J. Menéndez. "Status and future of nuclear matrix elements for neutrinoless double-beta decay: a review." In: *Rep. Prog. Phys.* 80.046301 (2017). DOI: 10.1088/1361-6633/aa5bc5.

[96] E. Caurier *et al.* "ββ decay and nuclear structure." In: *Int. J. Mod. Phys. E* 16.02 (2007), pp. 552–560. DOI: 10.1142/S0218301307005983.

[97] N. Yoshida and F. Iachello. "Two-neutrino double-β decay in the interacting boson-fermion model." In: *Prog. Theor. Exp. Phys.* 043D01 (2013). DOI: 10.1093/ptep/ptt007.

[98] J. Suhonen and O. Civitarese. "Probing the quenching of g_A by single and double beta decays." In: *Phys. Lett. B* 725 (1-3 2013), pp. 153–157. DOI: 10.1016/j.physletb.2013.06.042.

[99] P. Gysbers *et al.* "Discrepancy between experimental and theoretical β-decay rates resolved from first principles." In: *Nat. Phys.* 15 (2019), pp. 428–431. DOI: 10.1038/s41567-019-0450-7.

[100] J. M. Yao *et al.* "Ab Initio Treatment of Collective Correlations and the Neutrinoless Double Beta Decay of ^{48}Ca." In: *Phys. Rev. Lett.* 124.232501 (2020). DOI: 10.1103/PhysRevLett.124.232501.

[101] K. Zuber. *Neutrino Physics.* Series in High Energy Physics, Cosmology and Gravitation, 2003.

[102] R. Arnold *et al.* "Measurement of the double-beta decay half-life and search for the neutrinoless double-beta decay of ^{48}Ca with the NEMO-3 detector." In: *Phys. Rev. D* 96.112008 (2016). DOI: 10.1103/PhysRevD.93.112008.

[103] M. Agostini *et al.* "Results on ββ decay with emission of two neutrinos or Majorons in ^{76}Ge from GERDA Phase I." In: *Eur. Phys. J. C* 75.416 (2015). DOI: 10.1140/epjc/s10052-015-3627-y.

[104] O. Azzolini *et al.* "Evidence of Single State Dominance in the Two-Neutrino Double-β Decay of ^{82}Se with CUPID-0." In: *Phys. Rev. Lett.* 123.262501 (2019). DOI: 10.1103/PhysRevLett.123.262501.

[105] J. Argyriades *et al.* "Measurement of the two neutrino double beta decay half-life of Zr-96 with the NEMO-3 detector." In: *Nucl. Phys. A* 847 (3-4 2010), pp. 168–179. DOI: 10.1016/j.nuclphysa.2010.07.009.

[106] E. Armengaud *et al.* "Precise measurement of 2νββ decay of ^{100}Mo with the CUPID-Mo detection technology." In: *Eur. Phys. J. C* 80.674 (2020). DOI: 10.1140/epjc/s10052-020-8203-4.

[107] A. S. Barabash *et al.* "Final results of the Aurora experiment to study 2β decay of ^{116}Cd with enriched $^{116}CdWO_4$ crystal scintillators." In: *Phys. Rev. D* 98.092007 (2018). DOI: 10.1103/PhysRevD.98.092007.

[108] C. Alduino *et al.* "Measurement of the two-neutrino double-beta decay half-life of ^{130}Te with the CUORE-0 experiment." In: *Eur. Phys. J. C* 77.13 (2017). DOI: 10.1140/epjc/s10052-016-4498-6.

[109] J. B. Albert *et al.* "Improved measurement of the 2νββ half-life of ^{136}Xe with the EXO-200 detector." In: *Phys. Rev. C* 89.015502 (2014). DOI: 10.1103/PhysRevC.89.015502.

[110] R. Arnold *et al.* "Measurement of the 2νββ decay half-life of ^{150}Nd and a search for 0νββ decay processes with the full exposure from the NEMO-3 detector." In: *Phys. Rev. D* 94.072003 (2016). DOI: 10.1103/PhysRevD.94.072003.

[111] J. S. Coursey *et al. Atomic Weights and Isotopic Compositions with Relative Atomic Masses.* URL: https://www.nist.gov/pml/atomic-weights-and-isotopic-compositions-relative-atomic-masses (visited on 11/12/2020).

[112] NuDat 2.8. *Nuclear structure and decay data.* URL: https://www.nndc.bnl.gov/nudat2/chartNuc.jsp (visited on 11/12/2020).

[113] L. Coraggio *et al.* "Calculation of the neutrinoless double-β decay matrix element within the realistic shell model." In: *Phys. Rev. C* 101.044315 (2020). DOI: 10.1103/PhysRevC.101.044315.

[114] J. M. Yao *et al.* "Systematic study of nuclear matrix elements in neutrinoless double-β decay with a beyond-mean-field covariant density functional theory." In: *Phys. Rev. C* 91.024316 (2015). DOI: 10.1103/PhysRevC.91.024316.

[115] L. S. Song *et al.* "Nuclear matrix element of neutrinoless double-β decay: Relativity and short-range correlations." In: *Phys. Rev. C* 95.024305 (2017). DOI: 10.1103/PhysRevC.95.024305.

[116] J. Barea *et al.* "0νββ and 2νββ nuclear matrix elements in the interacting boson model with isospin restoration." In: *Phys. Rev. C* 91.034304 (2015). DOI: 10.1103/PhysRevC.91.034304.

[117] J. Hyvärinen and J. Suhonen. "Nuclear matrix elements for 0νββ decays with light or heavy Majorana-neutrino exchange." In: *Phys. Rev. C* 91.024613 (2015). DOI: 10.1103/PhysRevC.91.024613.

[118] M. T. Mustonen and J. Engel. "Large-scale calculations of the double-β decay of ^{76}Ge, ^{130}Te, ^{136}Xe, and ^{150}Nd in the deformed self-consistent Skyrme quasiparticle random-phase approximation." In: *Phys. Rev. C* 87.064302 (2013). DOI: 10.1103/PhysRevC.87.064302.

[119] N. L. Vaquero *et al.* "Shape and Pairing Fluctuation Effects on Neutrinoless Double Beta Decay Nuclear Matrix Elements." In: *Phys. Rev. Lett.* 111.142501 (2013). DOI: 10.1103/PhysRevLett.111.142501.

[120] D.-L. Fang *et al.* "0νββ-decay nuclear matrix element for light and heavy neutrino mass mechanisms from deformed quasiparticle random-phase approximation calculations for ^{76}Ge, ^{82}Se, ^{130}Te, ^{136}Xe, and ^{150}Nd with isospin restoration." In: *Phys. Rev. C* 97.045503 (2018). DOI: 10.1103/PhysRevC.97.045503.

[121] T. R. Rodríguez and G. Martínez-Pinedo. "Energy Density Functional Study of Nuclear Matrix Elements for Neutrinoless ββ Decay." In: *Phys. Rev. Lett.* 105.252503 (2010). DOI: 10.1103/PhysRevLett.105.252503.

[122] W. H. Furry. "On transition probabilities in double beta-disintegration." In: *Phys. Rev.* 56 (1939), pp. 1184–1193. DOI: 10.1103/PhysRev.56.1184.

[123] J. Schechter and J. W. F. Valle. "Neutrinoless double β-decay in SU(2)×U(1) theories." In: *Phys. Rev. D* 25.2951 (1982). DOI: 10.1103/PhysRevD.25.2951.

[124] S. M. Bilenky and C. Giunti. "Neutrinoless double-beta decay: A brief review." In: *Mod. Phys. Lett. A* 27.1230015 (2012). DOI: 10.1142/S0217732312300157.

[125] M. Fukugita and T. Yanagida. "Barygenesis without grand unification." In: *Phys. Lett. B* 174 (1 1986), pp. 45–47. DOI: 10.1016/0370-2693(86)91126-3.

[126] C. E. Aalseth *et al.* "Neutrinoless double beta decay and direct searches for neutrino mass." In: *APS summary report* (2004). arXiv: hep-ph/0412300.

[127] A. D. Sakharov. "Violation of CP invariance, C asymmetry, and baryon asymmetry of the universe." In: *Sov. Phys. Usp.* 34.392 (1991). DOI: 10.1070/pu1991v034n05abeh002497.

[128] S. Dell'Oro *et al.* "Neutrinoless Double Beta Decay: 2015 Review." In: *Adv. High Energy Phys.* 2016.2162659 (2016). DOI: 10.1155/2016/2162659.

[129] M. Agostini. "Signal and background studies for the search of neutrinoless double beta decay in GERDA." PhD thesis. Technische Universität München, 2013.

[130] M. Agostini *et al.* "Final Results of GERDA on the Search for Neutrinoless Double-β Decay." In: *Phys. Rev. Lett.* 125.252502 (2020). DOI: 10.1103/PhysRevLett.125.252502.

[131] J. Menéndez. "Neutrinoless ββ decay mediated by the exchange of light and heavy neutrinos: The role of nuclear structure correlations." In: *J. Phys. G: Nucl. Part. Phys.* 45.014003 (2018). DOI: 10.1088/1361-6471/aa9bd4.

[132] F. Vissani. "Signal of neutrinoless double beta decay, neutrino spectrum and oscillation scenarios." In: *J. High Energ. Phys.* 022 (1999). DOI: 10.1088/1126-6708/1999/06/022.

[133] M. Agostini *et al.* "Probing Majorana neutrinos with double-β decay." In: *Science* 365 (2019), pp. 1445–1448. DOI: 10.1126/science.aav8613.

[134] M. Agostini *et al.* "Discovery probability of next-generation neutrinoless double-β decay experiments." In: *Phys. Rev. D* 96.053001 (2017). DOI: 10.1103/PhysRevD.96.053001.

[135] N. Abgrall *et al. The Large Enriched Germanium Experiment for Neutrinoless ββ Decay - LEGEND-200 at LNGS.* Proposal LNGS-P 58/18. 2020.

[136] N. Abgrall *et al. The Large Enriched Germanium Experiment for Neutrinoless ββ Decay - LEGEND-1000 Preconceptual Design Report.* Tech. rep. 2021. arXiv: 2107.11462.

[137] R. G. H. Robertson. "Empirical Survey of Neutrinoless Double Beta Decay Matrix Elements." In: *Mod. Phys. Lett. A* 28.1350021 (2013). DOI: 10.1142/S0217732313500211.

[138] E. der Mateosian and M. Goldhaber. "Limits for Lepton-Conserving and Lepton-Nonconserving Double Beta Decay in ^{48}Ca." In: *Phys. Rev.* 146.810 (1966). DOI: 10.1103/PhysRev.146.810.

[139] V. R. Lazarenko and S. Yu. Luk'yanov. "An Attempt to Detect Double Beta Decay in ^{48}Ca." In: *J. Exp. Theor. Phys.* 22.3 (1966).

[140] E. Fiorini *et al.* "A search for lepton non-conservation in double beta decay with a germanium detector." In: *Phys. Lett. B* 25 (10 1967), pp. 602–603. DOI: 10.1016/0370-2693(67)90127-X.

[141] G. Benato. "Currently negligible, future worrisome backgrounds for $0\nu\beta\beta$ decay experiments." SnowMass Workshop: $0\nu\beta\beta$ decay beyond the tonne-scale. 2020.

[142] S. I. Alvis *et al.* "A Search for Neutrinoless Double-Beta Decay in ^{76}Ge with 26 kg yr of Exposure from the Majorana Demonstrator." In: *Phys. Rev. C* 100.025501 (2019). DOI: 10.1103/PhysRevC.100.025501.

[143] O. Azzolini *et al.* "Final result of CUPID-0 phase-I in the search for the ^{82}Se Neutrinoless Double Beta Decay." In: *Phys. Rev. Lett.* 123.032501 (2019). DOI: 10.1103/PhysRevLett.123.032501.

[144] R. Arnold *et al.* "Results of the search for neutrinoless double-β decay in ^{100}Mo with the NEMO-3 experiment." In: *Phys. Rev. D* 92.072011 (2015). DOI: 10.1103/PhysRevD.92.072011.

[145] B. Schmidt *et al.* "New limit from the search for $0\nu\beta\beta$-decay of ^{100}Mo with the CUPID-Mo experiment." In: *Neutrino 2020 poster*. 2020.

[146] D. Q. Adams *et al.* "Improved Limit on Neutrinoless Double-Beta Decay in ^{130}Te with CUORE." In: *Phys. Rev. Lett.* 124.122501 (2020). DOI: 10.1103/PhysRevLett.124.122501.

[147] G. Anton *et al.* "Search for Neutrinoless Double-β Decay with the Complete EXO-200 Dataset." In: *Phys. Rev. Lett.* 123.161802 (2019). DOI: 10.1103/PhysRevLett.123.161802.

[148] A. Gando *et al.* "Search for Majorana Neutrinos Near the Inverted Mass Hierarchy Region with KamLAND-Zen." In: *Phys. Rev. Lett.* 117.082503 (2016). DOI: 10.1103/PhysRevLett.117.082503.

[149] C. Wiesinger. "No neutrinos not found: First exploration of neutrinoless double beta decay half-lives beyond 10^{26} years." PhD thesis. Technische Universität München, 2020.

[150] O. Azzolini *et al.* "Analysis of cryogenic calorimeters with light and heat read-out for double beta decay searches." In: *Eur. Phys. J. C* 78.734 (2018). DOI: 10.1140/epjc/s10052-018-6202-5.

[151] CUPID Interest Group. *CUPID pre-CDR*. Tech. rep. 2019. arXiv: 1907.09376.

[152] V. Alenkov *et al.* "First results from the AMoRE-Pilot neutrinoless double beta decay experiment." In: *Eur. Phys. J. C* 79.791 (2019). DOI: 10.1140/epjc/s10052-019-7279-1.

[153] J. Paton. "Neutrinoless Double Beta Decay in the SNO+ Experiment." In: *NuPhys2018 Prospects in Neutrino Physics*. 2019. arXiv: 1904.01418.

[154] J. B. Albert *et al.* "Sensitivity and discovery potential of the proposed nEXO experiment to neutrinoless double-β decay." In: *Phys. Rev. C* 97.065503 (2018). DOI: 10.1103/PhysRevC.97.065503.

[155] V. Álvarez *et al.* "NEXT-100 Technical Design Report (TDR). Executive summary." In: *J. Inst.* 7.T06001 (2012). DOI: 10.1088/1748-0221/7/06/T06001.

[156] J. Martín-Albo *et al.* "Sensitivity of NEXT-100 to neutrinoless double beta decay." In: *J. High Energ. Phys.* 159 (2016). DOI: 10.1007/JHEP05(2016)159.

[157] S. Wang. "PandaX-III high pressure xenon TPC for Neutrinoless Double Beta Decay search." In: *Nucl. Instr. Meth. Phys. Res. A* 958.162439 (2020). DOI: 10.1016/j.nima.2019.162439.

[158] R. Arnold *et al.* "Technical design and performance of the NEMO-3 detector." In: *Nucl. Instr. Meth. Phys. Res. A* 536 (2005), pp. 79–122. DOI: 10.1016/j.nima.2004.07.194.

[159] A. S. Barabash *et al.* "Calorimeter development for the SuperNEMO double beta decay experiment." In: *Nucl. Instr. Meth. Phys. Res. A* 868 (2017), pp. 98–108. DOI: 10.1016/j.nima.2017.06.044.

[160] E. Fiorini *et al.* "An underground experiment on neutrinoless double beta-decay." In: *Lettere al Nuovo Cimento* 3 (1970), pp. 149–152. DOI: 10.1007/BF02755836.

[161] E. Fiorini *et al.* "Neutrinoless double-beta decay of ^{76}Ge." In: *Il Nuovo Cimento A* 13 (1973), pp. 747–763. DOI: 10.1007/BF02784100.

[162] F. T. Avignone III *et al.* "New Limits on the Neutrino Mass, Lepton Conservation, and No-Neutrino Double Beta Decay of ^{76}Ge." In: *Phys. Rev. Lett.* 50.721 (1983). DOI: 10.1103/PhysRevLett.50.721.

[163] A. Forster *et al.* "Low background study of the neutrinoless double beta decay of 76-Ge and upper limit for neutrino mass." In: *Phys. Lett. B* 138 (4 1984), pp. 301–303. DOI: 10.1016/0370-2693(84)91665-4.

[164] J. J. Simpson *et al.* "New Limit for Neutrinoless Double β Decay of ^{76}Ge." In: *Phys. Rev. Lett.* 53.141 (1984). DOI: 10.1103/PhysRevLett.53.141.

[165] E. Bellotti *et al.* "The Mont Blanc experiment on ^{76}Ge double beta decay." In: *AIP Conference Proceedings*. 1984, pp. 189–198. DOI: 10.1063/1.34487.

[166] E. Bellotti *et al.* "New limits on double beta decay of ^{76}Ge." In: *Phys. Lett. B* 146 (6 1984), pp. 450–456. DOI: 10.1016/0370-2693(84)90158-8.

[167] R. L. Brodzinski *et al.* "The ^{76}Ge double beta decay experiment at Homestake." In: *AIP Conference Proceedings*. 1985, pp. 50–59. DOI: 10.1063/1.35162.

[168] F. T. Avignone III *et al.* "Ultralow-Background Study of Neutrinoless Double β Decay of ^{76}Ge: New Limit on the Majorana Mass of ν_e." In: *Phys. Rev. Lett.* 54.2309 (1985). DOI: 10.1103/PhysRevLett.54.2309.

[169] A. Alessandrello *et al.* "Underground laboratory and Milano double beta decay experiment." In: *Nucl. Instr. Meth. Phys. Res. B* 17 (1986), pp. 411–417. DOI: 10.1016/0168-583X(86)90174-6.

[170] P. Fisher *et al.* "A search for double beta decay in ^{76}Ge." In: *Phys. Lett. B* 218 (2 1989), pp. 257–262. DOI: 10.1016/0370-2693(89)91429-9.

[171] A. A. Vasenko *et al.* "New results in the ITEP/YePI double beta-decay experiment with enriched germanium detectors." In: *Mod. Phys. Lett. A* 5.17 (1990), pp. 1299–1306. DOI: 10.1142/S0217732390001475.

[172] D. Reusser *et al.* "Final report on the search for neutrinoless double-β decay of ^{76}Ge from the Gotthard underground experiment." In: *Phys. Rev. D* 45.2548 (1992). DOI: 10.1103/PhysRevD.45.2548.

[173] A. Balysh *et al.* "The Heidelberg-Moscow double beta decay experiment with enriched ^{76}Ge. First results." In: *Phys. Lett. B* 283 (1-2 1992), pp. 32–36. DOI: 10.1016/0370-2693(92)91421-5.

[174] A. Balysh *et al.* "Sub-eV limit for the neutrino mass from ^{76}Ge double beta decay by the Heidelberg-Moscow experiment." In: *Phys. Lett. B* 356 (4 1995), pp. 450–455. DOI: 10.1016/0370-2693(95)00817-5.

[175] C. E. Aalseth *et al.* "Recent results from the IGEX double-beta decay experiment." In: *Nucl. Phys. B - Proceed. Suppl.* Vol. 48. 1-3. 1996, pp. 223–225. DOI: 10.1016/0920-5632(96)00244-7.

[176] M. Günther *et al.* "Heidelberg-Moscow ββ experiment with ^{76}Ge: Full setup with five detectors." In: *Phys. Rev. D* 55.1 (1997), pp. 54–67. DOI: 10.1103/PhysRevD.55.54.

[177] C. E. Aalseth *et al.* "Neutrinoless double-β decay of ^{76}Ge: First results from the International Germanium Experiment (IGEX) with six isotopically enriched detectors." In: *Phys. Rev. C* 59.4 (1999), pp. 2108–2113. DOI: 10.1103/PhysRevC.59.2108.

[178] D. González *et al.* "Current IGEX results for neutrinoless double-beta decay of ^{76}Ge." In: *Nucl. Phys. B - Proceed. Suppl.* Vol. 87. 1-3. 2000, pp. 278–280. DOI: 10.1016/S0920-5632(00)00679-4.

[179] H. V. Klapdor-Kleingrothaus *et al.* "Latest Results from the Heidelberg-Moscow Double-Beta-Decay Experiment." In: *Eur. Phys. J. A* 12 (2001), pp. 147–154. DOI: 10.1007/978-3-642-56643-1_47.

[180] H. V. Klapdor-Kleingrothaus *et al.* "Evidence for neutrinoless double beta decay." In: *Mod. Phys. Lett. A* 16.37 (2001), pp. 2409–2420. DOI: 10.1142/S0217732301005825.

[181] A. Morales and J. Morales. "The neutrinoless double beta decay: The case for germanium detectors." In: *Nucl. Phys. B - Proceed. Suppl.* Vol. 114. 2003, pp. 141–157. DOI: 10.1016/S0920-5632(02)01901-1.

[182] H. V. Klapdor-Kleingrothaus *et al.* "Data acquisition and analysis of the ^{76}Ge double beta experiment in Gran Sasso 1990-2003." In: *Nucl. Instr. Meth. Phys. Res. A* 552 (2004), pp. 371–406. DOI: 10.1016/j.nima.2003.12.013.

[183] A. M. Bakalyarov *et al.* "Results of the experiment on investigation of Germanium-76 double beta decay." In: *Phys. Part. Nucl. Lett.* 2 (2005), pp. 77–81. arXiv: hep-ex/0309016v1.

[184] H. V. Klapdor-Kleingrothaus and I. V. Krivosheina. "The evidence for the observation of $0\nu\beta\beta$ decay: The identification of $0\nu\beta\beta$ events from the full spectrum." In: *Mod. Phys. Lett. A* 21.20 (2006), pp. 1547–1566. DOI: 10.1142/S0217732306020937.

[185] M. Agostini *et al.* "Results on Neutrinoless Double-β Decay of ^{76}Ge from Phase I of the GERDA Experiment." In: *Phys. Rev. Lett.* 111.122503 (2013). DOI: 10.1103/PhysRevLett.111.122503.

[186] M. Agostini *et al.* "Background-free search for neutrinoless double-β decay of ^{76}Ge with GERDA." In: *Nature* 544 (2017), pp. 47–52. DOI: 10.1038/nature21717.

[187] C. E. Aalseth *et al.* "Search for Neutrinoless Double-β Decay in ^{76}Ge with the MAJORANA DEMONSTRATOR." In: *Phys. Rev. Lett.* 120.132502 (2018). DOI: 10.1103/physrevlett.120.132502.

[188] M. Agostini *et al.* "Improved limit on neutrinoless double beta decay of ^{76}Ge from GERDA Phase II." In: *Phys. Rev. Lett.* 120.132503 (2018). DOI: 10.1103/PhysRevLett.120.132503.

[189] B. J. Mount *et al.* "Double-β-decay Q values of ^{74}Se and ^{76}Ge." In: *Phys. Rev. C* 81.032501(R) (2010). DOI: 10.1103/PhysRevC.81.032501.

[190] E. E. Haller *et al.* "Physics of ultra-pure germanium." In: *Adv. Phys.* 30 (1981), pp. 93–138. DOI: 10.1080/00018738100101357.

[191] B. Schwingenheuer. "Status and prospects of searches for neutrinoless double beta decay." In: *Annalen Phys.* 525 (4 2013). DOI: 10.1002/andp.201200222.

[192] G. F. Knoll. *Radiation Detection and Measurement.* USA: Wiley, 2010.

[193] J. Ebert *et al.* "Results of a search for neutrinoless double-β decay using the COBRA demonstrator." In: *Phys. Rev. C* 94.024603 (2016). DOI: 10.1103/PhysRevC.94.024603.

[194] A. E. Chavarria *et al.* "A high-resolution CMOS imaging detector for the search of neutrinoless double β decay in ^{82}Se." In: *J. Inst.* 12.P03022 (2017). DOI: 10.1088/1748-0221/12/03/p03022.

[195] NIST. *Appendix for ESTAR, PSTAR, and ASTAR.* URL: https://physics.nist.gov/PhysRefData/Star/Text/appendix.html (visited on 12/28/2020).

[196] M. J. Berger *et al. Stopping-Power & Range Tables for Electrons, Protons, and Helium Ions.* URL: https://www.nist.gov/pml/stopping-power-range-tables-electrons-protons-and-helium-ions (visited on 09/08/2020).

[197] M. J. Berger *et al. XCOM: Photon Cross Sections Database.* URL: https://www.nist.gov/pml/xcom-photon-cross-sections-database (visited on 12/16/2020).

[198] R. L. Murray and K. E. Holbert. *Nuclear Energy. Chapter 5 - Radiation and Materials.* 8th ed. Butterworth-Heinemann, 2020. DOI: 10.1016/B978-0-12-812881-7.00005-8.

[199] K. Panas. "Development of Pulse Shape Discrimination Methods as Tools for Background Suppression in High Purity Germanium Detectors used in the GERDA Experiment." PhD thesis. Jagiellonian University Cracow, 2018.

[200] B. Lehnert. "Search for $2\nu\beta\beta$ Excited State Transitions and HPGe Characterization for Surface Events in GERDA Phase II." PhD thesis. Technische Universität Dresden, 2015.

[201] F. E. Emery and T. A. Rabson. "Average Energy Expended Per Ionized Electron-Hole Pair in Silicon and Germanium as a Function of Temperature." In: *Phys. Rev.* 140.A2089 (1965). DOI: 10.1103/PhysRev.140.A2089.

[202] Y. P. Varshni. "Temperature dependence of the energy gap in semiconductors." In: *Physica* 34.1 (1967), pp. 149–154. DOI: 10.1016/0031-8914(67)90062-6.

[203] R. K. Schaevitz *et al.* "Indirect absorption in germanium quantum wells." In: *AIP Advances* 1 (3 2011). DOI: 10.1063/1.3646149.

[204] C. R. Nave. *The Doping of Semiconductors.* URL: http://hyperphysics.phy-astr.gsu.edu/hbase/Solids/dope.html (visited on 09/05/2020).

[205] W. Shockley. "Currents to Conductors Induced by a Moving Point Charge." In: *J. Appl. Phys.* 9 (1938), pp. 635–636. DOI: 10.1063/1.1710367.

[206] S. Ramo. "Currents Induced by Electron Motion." In: *Proceedings of the IRE*. Vol. 27. 9. 1939, pp. 584–585. DOI: 10.1109/JRPROC.1939.228757.

[207] C. E. Aalseth *et al.* "The IGEX ^{76}Ge Neutrinoless Double-Beta Decay Experiment: Prospects for Next Generation Experiments." In: *Phys. Rev. D* 65.092007 (2002). DOI: 10.1103/PhysRevD.65.092007.

[208] H. V. Klapdor-Kleingrothaus *et al.* "Search for Neutrinoless Double Beta Decay with Enriched ^{76}Ge in Gran Sasso 1990-2003." In: *Phys. Lett. B* 586 (3-4 2004), pp. 198–212. DOI: 10.1016/j.physletb.2004.02.025.

[209] P. N. Luke *et al.* "Low capacitance large volume shaped-field germanium detector." In: *IEEE Transactions on Nuclear Science* 36 (1989), pp. 926–930. DOI: 10.1109/23.34577.

[210] C. E. Aalseth *et al.* "CoGeNT: A search for low-mass dark matter using p-type point contact germanium detectors." In: *Phys. Rev. D* 88.012002 (2013). DOI: 10.1103/PhysRevD.88.012002.

[211] G. K. Giovanetti *et al.* "A Dark Matter Search with MALBEK." In: *Phys. Proc.* 61 (2015), pp. 77–84. DOI: 10.1016/j.phpro.2014.12.014.

[212] D. Akimov *et al.* "Observation of coherent elastic neutrino-nucleus scattering." In: *Science* 357 (2017), pp. 1123–1126. DOI: 10.1126/science.aao0990.

[213] H. Bonet *et al.* "Constraints on Elastic Neutrino Nucleus Scattering in the Fully Coherent Regime from the CONUS Experiment." In: *Phys. Rev. Lett.* 126.041804 (2021). DOI: 10.1103/PhysRevLett.126.041804.

[214] M. Agostini *et al.* "Signal modeling of high-purity Ge detectors with a small read-out electrode and application to neutrinoless double beta decay search in Ge-76." In: *J. Inst.* 6.P03005 (2011). DOI: 10.1088/1748-0221/6/03/P03005.

[215] M. Agostini *et al.* "Characterization of 30 ^{76}Ge enriched Broad Energy Ge detectors for GERDA Phase II." In: *Eur. Phys. J. C* 79.978 (2019). DOI: 10.1140/epjc/s10052-019-7353-8.

[216] A. Domula *et al.* "Pulse shape discrimination performance of Inverted Coaxial Ge detectors." In: *Nucl. Instr. Meth. Phys. Res. A* 891 (2017), pp. 106–110. DOI: 10.1016/j.nima.2018.02.056.

[217] T. Comellato *et al.* "Charge-carrier collective motion in germanium detectors for $\beta\beta$-decay searches." In: *Eur. Phys. J. C* 81.76 (2021). DOI: 10.1140/epjc/s10052-021-08889-0.

[218] K.-H. Ackermann *et al.* "The GERDA experiment for the search of $0\nu\beta\beta$ decay in ^{76}Ge." In: *Eur. Phys. J. C* 73.2330 (2013). DOI: 10.1140/epjc/s10052-013-2330-0.

[219] M. Agostini *et al.* "Upgrade for Phase II of the GERDA experiment." In: *Eur. Phys. J. C* 78.388 (2018). DOI: 10.1140/epjc/s10052-018-5812-2.

[220] M. Gimmarchi *et al.* "Water purification in Borexino." In: *AIP Conference Proceedings*. Vol. 1549. 209. 2013. DOI: 10.1063/1.4818110.

[221] E. Aprile *et al.* "The XENON1T dark matter experiment." In: *Eur. Phys. J. C* 77.881 (2017). DOI: 10.1140/epjc/s10052-017-5326-3.

[222] M. Agostini *et al.* "Modeling of GERDA Phase II data." In: *J. High Energ. Phys.* 139 (2020). DOI: 10.1007/jhep03(2020)139.

[223] K. Freund *et al.* "The performance of the Muon Veto of the GERDA experiment." In: *Eur. Phys. J. C* 76.298 (2016). DOI: 10.1140/epjc/s10052-016-4140-7.

[224] M. Agostini *et al.* "Improvement of the energy resolution via an optimized digital signal processing in GERDA Phase I." In: *Eur. Phys. J. C* 75.6 (2015). DOI: 10.1140/epjc/s10052-015-3409-6.

[225] P. Barton *et al.* "Low-noise low-mass front end electronics for low-background physics experiments using germanium detectors." In: *IEEE Nuclear*. 2011, pp. 1976–1979. DOI: 10.1109/NSSMIC.2011.6154397.

[226] E. W. Hoppe *et al.* "Reduction of radioactive backgrounds in electroformed copper for ultra-sensitive radiation detectors." In: *Nucl. Instr. Meth. Phys. Res. A* 764 (2014), pp. 116–121. DOI: 10.1016/j.nima.2014.06.082.

[227] Y. Efremenko *et al.* "Use of poly(ethylene naphthalate) as a self-vetoing structural material." In: *J. Inst.* 14.P07006 (2019). DOI: 10.1088/1748-0221/14/07/P07006.

[228] J. Gruszko. "Surface Alpha Interactions in P-Type Point-Contact HPGe Detectors: Maximizing Sensitivity of ^{76}Ge Neutrinoless Double-Beta Decay Searches." PhD thesis. University of Washington, 2017.

[229] F. Edzards *et al. Surface characterization of p-type point contact germanium detectors.* Submitted to MDPI Particles. 2021. arXiv: 2105.14487.

[230] J. Gruszko. "L1000 Alpha Rate Prediction." 2020.

[231] J. Gruszko. "Surface Backgrounds in L1000." LEGEND Collaboration Meeting (remote). 2020.

[232] R. B. Firestone. *Table of Isotopes.* 8th ed. New York: Wiley, 1998.

[233] A. Lubashevskiy *et al.* "Mitigation of ^{42}Ar/^{42}K background for the GERDA Phase II experiment." In: *Eur. Phys. J. C* 78.15 (2018). DOI: 10.1140/epjc/s10052-017-5499-9.

[234] D. C. Radford. *`mjd_fieldgen` and `mjd_siggen` software.* July 30, 2020. URL: https://github.com/radforddc/icpc_siggen.

[235] I. J. Arnquist *et al. α-event Characterization and Rejection in Point-Contact HPGe Detectors.* Submitted to Eur. Phys. J. C. 2021. arXiv: 2006.13179.

[236] R. J. Cooper *et al.* "Effect of a surface channel on the performance of a P-type Point Contact HPGe detector." In: *Nucl. Instr. Meth. Phys. Res. A* 680 (2012), pp. 48–55. DOI: 10.1016/j.nima.2012.04.005.

[237] D. C. Radford. "Surface-Alpha Simulations with Charge Cloud Size." LEGEND Collaboration Meeting (remote). 2020.

[238] I. Abt *et al.* "The GALATEA test-facility for high purity germanium detectors." In: *Nucl. Instr. Meth. Phys. Res. A* 782 (2015), pp. 56–62. DOI: 10.1016/j.nima.2015.02.007.

[239] S. Irlbeck. "The GALATEA Test Facility and a First Study of α-induced Surface Events in a Germanium Detector." PhD thesis. Ludwig-Maximilians-Universität München, 2014.

[240] *Murtfeldt Plastics.* URL: https://www.murtfeldt.de/en/products/plastics/ (visited on 02/25/2021).

[241] M. Agostini *et al.* "GELATIO: a general framework for modular digital analysis of high-purity Ge detector signals." In: *J. Inst.* 6.P08013 (2011). DOI: 10.1088/1748-0221/6/08/p08013.

[242] P. Födisch *et al.* "Digital high-pass filter deconvolution by means of an infinite impulse response filter." In: *Nucl. Instr. Meth. Phys. Res. A* 830 (2016), pp. 484–496. DOI: 10.1016/j.nima.2016.06.019.

[243] A. Savitzky and M. J. E. Golay. "Smoothing and Differentiation of Data by Simplified Least Squares Procedures." In: *Anal. Chem.* 36.8 (1964), pp. 1627–1639. DOI: 10.1021/ac60214a047.

[244] R. D. Martin *et al.* "Determining the drift time of charge carriers in p-type point-contact HPGe detectors." In: *Nucl. Instr. Meth. Phys. Res. A* 678 (2012), pp. 98–104. DOI: 10.1016/j.nima.2012.02.047.

[245] D. C. Radford. "Drift-Time Correction for A/E." LEGEND Collaboration Meeting Seattle. 2019.

[246] S. I. Alvis *et al.* "Multi-site event discrimination for the MAJORANA DEMONSTRATOR." In: *Phys. Rev. C* 99.065501 (2019). DOI: 10.1103/physrevc.99.065501.

[247] S. Mertens *et al.* "Characterization of High Purity Germanium Point Contact Detectors with Low Net Impurity Concentration." In: *Nucl. Instr. Meth. Phys. Res. A* 921 (2019), pp. 81–88. DOI: 10.1016/j.nima.2018.09.012.

[248] P. Mullowney *et al.* "Computational models of germanium point contact detectors." In: *Nucl. Instr. Meth. Phys. Res. A* 662 (2012), pp. 33–44. DOI: 10.1016/j.nima.2011.09.061.

[249] D. C. Radford. "Attempt to Reproduce Measured Superpulses. Alphas on Ponama1 in GALATEA." 2020.

[250] C. Jacoboni *et al.* "Electron drift velocity and diffusivity in germanium." In: *Phys. Rev. B* 24 (1981), pp. 1014–1026. DOI: 10.1103/PhysRevB.24.1014.

[251] R. Henning. *PIRE GEMADARC Course on concepts of detector electronics - Lecture notes.* 2020. URL: http://pire.gemadarc.org/education/school20/#electronics.

[252] P. Barton *et al.* "Ultra-Low Noise Mechanically Cooled Germanium Detector." In: *Nucl. Instr. Meth. Phys. Res. A* 812 (2016), pp. 17–23. DOI: 10.1016/j.nima.2015.12.031.

[253] F. S. Goulding *et al. The Design and Performance of a High-resolution, High-rate Amplifier System for Nuclear Spectrometry.* Tech. rep. Lawrence Berkeley National Laboratory, 1967.

[254] T. Nashashibi and G. White. "A low noise FET with integrated charge restoration for radiation detectors." In: *IEEE Transactions on Nuclear Science*. 1990, pp. 452–456. DOI: 10.1109/23.106661.

[255] P. Horowitz and W. Hill. *The Art of Electronics.* Cambridge, United Kingdom: Cambridge University Press, 2015.

[256] H. Spieler. *Semiconductor Detector Systems.* Oxford: Clarendon Press, 2005.

[257] V. Radeka. "Low-Noise Techniques in Detectors." In: *Annual Review of Nuclear and Particle Science* 38.1 (1988), pp. 217–277. DOI: 10.1146/annurev.ns.38.120188.001245.

[258] U. Fano. "Ionization Yield of Radiations. II. The Fluctuations of the Number of Ions." In: *Phys. Rev.* 72.26 (1947). DOI: 10.1103/PhysRev.72.26.

[259] S. Croft and D. S. Bond. "A determination of the Fano factor for germanium at 77.4 K from measurements of the energy resolution of a 113 cm^3 HPGe gamma-ray spectrometer taken over the energy range from 14 to 6129 keV." In: *Appl. Rad. Isot. A* 42 (1991), pp. 1009–1014. DOI: 10.1016/0883-2889(91)90002-I.

[260] B. G. Lowe. "Measurements of Fano factors in silicon and germanium in the low-energy X-ray region." In: *Nucl. Instr. Meth. Phys. Res. A* 399 (1997), pp. 354–364. DOI: 10.1016/S0168-9002(97)00965-0.

[261] M. C. Lépy *et al.* "Experimental study of the response of semiconductor detectors to low-energy photons." In: *Nucl. Instr. Meth. Phys. Res. A* 439 (2000), pp. 239–246. DOI: 10.1016/S0168-9002(99)00932-8.

[262] T. Papp *et al.* "A new approach to the determination of the Fano factor for semiconductor detectors." In: *X-Ray Spectr.* 34 (2005), pp. 106–111. DOI: 10.1002/xrs.754.

[263] N. Abgrall *et al.* "The MAJORANA low-noise low-background front-end electronics." In: *Phys. Proc.* 61 (2015), pp. 654–657. DOI: 10.1016/j.phpro.2014.12.066.

[264] M. W. Lund *et al.* "Low noise JFETs for room temperature x-ray detectors." In: *Nucl. Instr. Meth. Phys. Res. A* 380 (1996), pp. 318–322. DOI: 10.1016/S0168-9002(96)00473-1.

[265] Axon' Cable S.A.S. *Axon Pico Coax Cable Datasheet.* Rev. H2. 2016.

[266] A. Lucchini. "Germanium detector readout electronics for LEGEND-200." MA thesis. Università degli Studi di Milano, 2018.

[267] F. Werner *et al.* "Performance verification of the FlashCam prototype camera for the Cherenkov Telescope Array." In: *Nucl. Instr. Meth. Phys. Res. A* 876 (2017), pp. 31–34. DOI: 10.1016/j.nima.2016.12.056.

[268] Y. Kermaïdic. "GERDA, MAJORANA and LEGEND - towards a background-free ton-scale Ge-76 experiment." Neutrino 2020 Conference. 2020.

[269] M. Agostini *et al.* "Pulse shape discrimination for GERDA Phase I data." In: *Eur. Phys. J. C* 73.2583 (2013). DOI: 10.1140/epjc/s10052-013-2583-7.

[270] M. Agostini *et al.* "The background in the $0\nu\beta\beta$ experiment GERDA." In: *Eur. Phys. J. C* 74.2764 (2014). DOI: 10.1140/epjc/s10052-014-2764-z.

[271] Analog Devices. *LTC6363.* URL: https://www.analog.com/en/products/ltc6363.html#product-overview (visited on 02/08/2021).

[272] Texas Instruments. *The Bypass Capacitor in High-Speed Environments.* Tech. rep. 1996. URL: https://www.ti.com/lit/an/scba007a/scba007a.pdf.

[273] V. E. Wagner. "Pulse Shape Analysis for the GERDA Experiment to Set a New Limit on the Half-life of $0\nu\beta\beta$ Decay of ^{76}Ge." PhD thesis. Heidelberg University, 2017.

[274] F. Balestra *et al.* "Influence of substrate freeze-out on the characteristics of MOS transistors at very low temperatures." In: *Solid-State Electronics* 30 (3 1987), pp. 321–327. DOI: 10.1016/0038-1101(87)90190-0.

[275] E. Simoen *et al.* "Freeze-out effects on NMOS transistor characteristics at 4.2 K." In: *IEEE Transactions on Electron Devices* 36.6 (1989), pp. 1155–1161. DOI: 10.1109/16.24362.

[276] D. Budjáš *et al.* "Pulse shape discrimination studies with a Broad-Energy Germanium detector for signal identification and background suppression in the GERDA double beta decay experiment." In: *J. Inst.* 4.P10007 (2009). DOI: 10.1088/1748-0221/4/10/p10007.

[277] D. Budjáš. "Germanium detector studies in the framework of the GERDA experiment." PhD thesis. Heidelberg University, 2015.